A NUMERICAL INVESTIGATION OF THE EVOLUTION OF SELF-PROPAGATING DETONATION IN ENERGETIC GRANULAR SOLIDS

A Dissertation

Submitted to the Graduate School
of the University of Notre Dame
In Partial Fulfillment of the Requirements
for the Degree of

Doctor of Philosophy

by

Keith Alan Gonthier, B.S., B.S.A.E., M.S.

Joseph M. Powers
Joseph M. Powers, Director

Department of Aerospace and Mechanical Engineering
Notre Dame, Indiana
November 1996

A NUMERICAL INVESTIGATION OF THE EVOLUTION OF SELF-PROPAGATING DETONATION IN ENERGETIC GRANULAR SOLIDS

Abstract

by

Keith Alan Gonthier

Two-phase continuum equations are numerically solved to predict the evolution of self-propagating detonation in an energetic granular solid. Deflagration-to-detonation transition (DDT) is considered whereby combustion is induced by weak, planar mechanical shock due to low velocity piston impact ($\sim 100\ m/s$). A new high-resolution numerical method is formulated for solving the non-strictly hyperbolic system of unsteady model equations. The numerical method, which is based on Godunov's approach, is able to accurately capture strong shocks without the generation of spurious oscillations, and can accurately resolve fine-scale detonation structure. The method is shown to be convergent, and the convergence rate is determined based on comparisons of numerical predictions with known theoretical results for several test problems. The numerical simulations predict most experimentally observed features characteristic of piston-initiated DDT in granular explosives. Experimentally observed time scales, wave speeds, and pressure magnitudes are correctly predicted. Several classes of steady two-phase detonation wave structures are predicted to evolve: Chapman-Jouguet (CJ) and weak detonation structures having a lead shock in the gas and an unshocked solid, CJ structures having a lead shock in the solid and an unshocked gas, and CJ structures having a shock in both the gas and solid. Which structure evolves is found to depend on the material compaction rate, the interphase drag rate, and the ambient mixture density. The results indicate that the CJ wave speed is not the unique wave speed for a self-propagating two-phase detonation. Numerically predicted structures agree well with results given by a strictly steady-state detonation wave analysis.

Dedication

This dissertation is dedicated to my wife Stephanie and my son Blake, and to my parents Ralph and Angelina, whose love and encouragement not only made this graduate experience enjoyable, but also possible.

TABLE OF CONTENTS

LIST OF FIGURES

LIST OF TABLES

LIST OF SYMBOLS

$\hat{\bullet}$	Accent denoting dimensional quantities
$\tilde{\bullet}$	Accent denoting averages for the approximate Riemann solution
$\bullet_a$	Subscript denoting ambient mixture quantities
$\bullet_{max}$	Subscript denoting a maximum of a quantity
$\bullet_o$	Subscript denoting ambient conditions
$\bullet_{CJ}$	Subscript denoting Chapman-Jouguet detonation quantities
$\bullet_L$, $\bullet_R$	Subscripts denoting left and right states for the Riemann problem
$\bullet_W$	Subscript denoting weak detonation quantities
$\bullet^\circ$	Superscript denoting equilibrium end state
$\bullet^-$, $\bullet^+$	1) Superscripts denoting quantities to the immediate left and right of ξ_s 2) Superscripts denoting quantities to the immediate left and right of the j^{th} wave associated with the Riemann solution

$\hat{a}$	Burn rate prefactor
$\hat{b}$	Gas virial coefficient
$\mathbf{b}$	Burn front
$\mathbf{c}$	Compaction wave
c_ϵ	Dimensionless velocity parameter
c_i	Frozen sound speed of i^{th} phase
$\mathbf{cp}$	Compression waves
c_{vi}	Specific heat at constant volume for i^{th} phase
$d\mathbf{f}^{(j+)}_{k-1/2}$	Jump in $\mathbf{f}$ across j^{th} forward propagating wave at $\xi_{k-1/2}$
$d\mathbf{f}^{(j-)}_{k+3/2}$	Jump in $\mathbf{f}$ across j^{th} backward propagating wave at $\xi_{k+3/2}$
$d\check{\mathbf{f}}^{(j+)}_{k-1/2}$	Flux-limited form of $d\mathbf{f}^{(j+)}_{k-1/2}$

$d\check{\mathbf{f}}^{(j-)}_{k+3/2}$	Flux-limited form of $d\mathbf{f}^{(j-)}_{k+3/2}$
e_i	Specific internal energy of i^{th} phase
f	Intragranular stress
$\mathbf{f}$	Flux vector
f_j	Components of $\mathbf{f}$
$\bar{\mathbf{f}}_{k\pm1/2}$, or $\mathbf{F}_{k\pm1/2}$	Average flux at $\xi_{k\pm1/2}$ over the time interval $[\tau^n, \tau^{n+1}]$
$\mathbf{f}^{(f)}_k$, $\mathbf{f}^{(b)}_k$	Flux vectors for forward and backward propagating waves at ξ_k
$\mathbf{g}$	Source vector
$\hat{h}$	Convective heat transfer coefficient
$\mathbf{h}_i$	Nonlinear vector function of $\mathbf{y}_i$
$\mathbf{h}_s$	Nonlinear vector function of $\mathbf{y}_s$
i	Index denoting phase properties; $i = 1$ for the gas, $i = 2$ for the solid
j	1) Index denoting vector components, $j = 1, \ldots, 9$ 2) Index denoting quantities associated with the characteristic fields, $j = 1, \ldots, 9$
k	Index denoting computational cell center, $k = 1, \ldots, N$
k_I	Ignition rate prefactor
$\mathbf{l}^{(j)}$, $\bar{\bar{\mathbf{L}}}$	Left eigenvectors and left eigenvector matrix of $\bar{\bar{\mathbf{A}}}$
l_{ig}, τ_{ig}	Estimate for the ignition length and time
l_{rxn}, τ_{rxn}	Estimate for the reaction zone length and reaction time
m	Burn rate exponent
n	Solid particle number density
p	Numerical convergence rate
$\mathbf{p}$	Characteristic variable vector, $\bar{\bar{\mathbf{R}}}^{-1}\mathbf{q}$
p_j	Components of $\mathbf{p}$
$q(\xi, \tau)$	Arbitrary scalar function of ξ and τ

$\hat{q}$	Chemical energy
$\mathbf{q}$	Conserved variable vector
$\mathbf{q}^*$	Constant reference state for the linear Riemann problem
q_j	Components of $\mathbf{q}$
$\check{\mathbf{q}}(\xi, \tau^n)$	Piecewise constant function at time τ^n
$\bar{\mathbf{q}}^n$, $\mathbf{Q}_k^n$	Averages of $\mathbf{q}$ within k^{th} computational cell at time τ^n
r	Particle radius
$\mathbf{r}^{(j)}$, $\tilde{\tilde{\mathbf{R}}}$	Right eigenvectors and right eigenvector matrix of $\tilde{\tilde{\mathbf{A}}}$
$\mathbf{r}_{IG}^{(7)}$	Compaction eigenvector for an ideal gas
s_i	Specific entropy of i^{th} phase
$\mathbf{s}$	Inert solid plug
t, τ	Time
u_i	Velocity of i^{th} phase relative to laboratory frame
v_i	Velocity of i^{th} phase relative to piston frame
v_p	Piston velocity
w_i	Velocity of i^{th} phase relative to steady wave frame
x	Position relative to laboratory frame
x_p	Piston position
$\mathbf{y}_i$	Primary variable vector for the i^{th} phase
$\mathbf{y}_s$	Dependent variable vector associated with $\mathcal{L}_s^{2\Delta\tau}$
z	Dummy integration variable

A, B, C	Generic chemical reactants and products
$\tilde{\tilde{\mathbf{A}}}$	Flux Jacobian matrix
A_1, A_2,	Coefficients of the cubic polynomial for ρ_1
A_3, A_4	
BKW	Commonly used product equation of state

C_d, C_e, C_I, C_m	Dimensionless phase interaction terms
C_D	Drag coefficient for gas flow around a sphere
CFL	Courant-Friedrichs-Lewy
CJ	Chapman-Jouguet
CPU	Central processing unit
D	Discontinuity propagation speed
$\mathbf{D}$	Detonation wave
DDT	Deflagration-to-detonation transition
E_i	Fractional error for i^{th} phase
FCT	Flux-corrected transport
F_i	Denotes the functional relationship $P_i\phi_i = F_i(\rho_i\phi_i, \phi_i, e_i)$
$F_{i_{\rho_i\phi_i}}$, $F_{i_{\phi_i}}$, $F_{i_{e_i}}$	$\left.\frac{\partial F_i}{\partial(\rho_i\phi_i)}\right\|_{\phi_i,e_i}$, $\left.\frac{\partial F_i}{\partial\phi_i}\right\|_{(\rho_i\phi_i),e_i}$, $\left.\frac{\partial F_i}{\partial e_i}\right\|_{(\rho_i\phi_i),\phi_i}$
$\mathbf{F}^{\dagger}_{k+1/2}$	Modified numerical flux at $\xi_{k+1/2}$ for a sonic rarefaction
$\mathbf{F}^{\ddagger}_{k+1/2}$	Modified numerical flux at $\xi_{k+1/2}$ for the singularities $\tilde{v}_2 - \tilde{v}_1 \mp \tilde{c}_1 = 0$
$\mathbf{F}^{(H)}_{k+1/2}$	Second-order TVD numerical flux
$\mathbf{F}^{(L)}_{k+1/2}$	Lower-order numerical flux given by the Riemann solution
$\mathbf{F}^{(2)}_{k+1/2}$	Second-order numerical flux obtained by flux-extrapolation
H_i	Total enthalpy of i^{th} phase
$H(I - I_{ig})$	Heaviside unit step function
HMX	Cyclotetramethylene tetranitramine
I	Ignition variable
IBVP	Initial-boundary-value problem
IVP	Initial-value problem
$\tilde{\tilde{\mathbf{I}}}$	Identity matrix
I_{ig}	Ignition constant
JWL	Commonly used product equation of state (Jones-Wilkins-Lee)

$L\{x,y\}$	Nonlinear flux-limiter
LSODE	Livermore Solver for Ordinary Differential Equations
M_i	Mach number of i^{th} phase relative to steady wave frame
N	Total number of computation cells
P	Arbitrary point in a two-phase mixture
P_i	Pressure of i^{th} phase
P_i^c	Characteristic pressure of i^{th} phase
PETN	Pentaerythritol tetranitrate
R	Retonation wave
$\Re$	Set of real numbers
Re	Reynolds number
$\hat{R}_i$	Ideal state constants for i^{th} phase
RDX	Cyclotrimethylene trinitramine
REV	Representative elementary volume
S	Strong detonation end state
SDT	Shock-to-detonation transition
T	Turning point
T_i	Temperature of i^{th} phase
T_I	Ignition temperature parameter
TVD	Total variation diminishing
$TV(q(\xi,\tau))$	Total variation in $q(\xi,\tau)$
$TV(Q^n)$	Total variation in the numerical approximation Q^n for q at time τ^n
W	Weak detonation end state
ZND	Zeldovich-von Neumann-Doering
$\alpha^{(j)}$	Eigenvector expansion coefficients for the Riemann solution
$\hat{\beta}$	Drag coefficient

γ_i	Specific heat ratio for i^{th} phase
ϵ	Perturbation parameter
ζ	Position relative to steady wave frame
η_i	$c_i^2 - (\Gamma_i - 1)\dfrac{P_i}{\rho_i}$
κ	CFL number
$\lambda^{(j)}$, $\tilde{\tilde{\mathbf{\Lambda}}}$	Eigenvalues and diagonal eigenvalue matrix of $\tilde{\tilde{\mathbf{A}}}$
$\hat{\mu}_c$	Compaction viscosity
μ_i	Specific volume of i^{th} phase
$\boldsymbol{\nu}_L$, $\boldsymbol{\nu}_R$	$\tilde{\tilde{\mathbf{R}}}^{-1}\mathbf{q}_L$, $\tilde{\tilde{\mathbf{R}}}^{-1}\mathbf{q}_R$
ν_{jL}, ν_{jR}	Components of $\boldsymbol{\nu}_L$ and $\boldsymbol{\nu}_R$
ξ	Position relative to piston frame
ξ_1, ξ_2	End points of control volume
ξ_k	Spatial position of k^{th} computational cell center $k\Delta\xi$
$\xi_{k\pm1/2}$	Spatial location of k^{th} computational cell boundaries $(k \pm \frac{1}{2})\Delta\xi$
ξ_s	Shock position
$\pi_{1,\ldots,16}$	Dimensionless parameters
ρ_i	Density of i^{th} phase
$\hat{\sigma}$	Non-ideal Tait parameter
τ_c	Time constant for τ_{ig}
τ^n	Time at the n^{th} time step
ϕ_i	Volume fraction of i^{th} phase
$\phi_{2\epsilon}$	Value of ϕ_2 at which combustion is terminated

Γ_i	Grüneisen coefficient for i^{th} phase
$\Delta\tau$	Small time increment
$\Delta\xi$	Small spatial increment
ΔV	Small volume element

Ω_k^{n+1}, Ψ_i^{n+1}, Υ_k^{n+1}	Integration constants associated with $\mathcal{L}_s^{2\Delta\tau}$
$d(\bullet)$	Differential operator
$\mathcal{L}_c^{\Delta\tau/2}$, $\mathcal{L}_c^{\Delta\tau}$	Convective numerical operators
$\mathcal{L}_s^{\Delta\tau/2}$, $\mathcal{L}_s^{2\Delta\tau}$	Source numerical operators
$\delta(\bullet)$	Difference operator $\bullet_R - \bullet_L$ for $\mathbf{q}_L$ close to $\mathbf{q}_R$
$\Delta(\bullet)$	Difference operator $\bullet_R - \bullet_L$ for arbitrary $\mathbf{q}_L$ and $\mathbf{q}_R$

ACKNOWLEDGMENTS

I would like to acknowledge several people who have contributed in various ways to this work. First, I would like to acknowledge my advisor, Prof. Joseph Powers, for his technical insight and guidance which were instrumental in completing this dissertation and in making my graduate career professionally rewarding. He was as much a friend as an advisor, sharing personal experiences and always willing to lend an open ear. For all of this, I thank him. I would also like to acknowledge the remaining members of my doctoral committee, Profs. Hafiz Atassi, Eric Jumper, and Flint Thomas, University of Notre Dame, and Prof. Herman Krier, University of Illinois at Urbana-Champaign, for taking the time to carefully review this dissertation.

I would like to acknowledge my colleague Capt. Matt Grismer, Wright-Patterson Air Force Base, for first introducing me to Godunov-based numerical methods, and for the many helpful time-saving computer tips he has given me in the past. I would like to thank my colleagues Prof. David Sawyers, Wilkes College, and Mr. Andy Smith for insights gained through the many informal discussions of our research. I would also like to thank the faculty and staff of the Department of Aerospace and Mechanical Engineering, University of Notre Dame, for their instruction, and their willingness to help solve various problems as they arose.

This research was funded by the NASA Lewis Research Center; the contract monitor was Dr. Robert Stubbs. Supplemental funding for this research was provided by the Department of Aerospace and Mechanical Engineering, University of Notre Dame, and the United States Air Force, Wright Laboratories, Eglin Air Force Base.

1

INTRODUCTION AND REVIEW

This study addresses the theory and modeling of detonation in granulated reactive solids. The main focus is on an analysis of detonation waves which evolve due to compression of the granulated solid by a moving piston. Since the solid reacts to form mostly gaseous products having distinct properties, we model these systems as consisting of two phases: gas and solid. In this chapter, we first briefly discuss practical motivations for the study of detonation in granulated material, introduce the model problem considered, and describe a two-phase detonation within the context of the model. Next, we survey relevant experimental, theoretical, and modeling research, and discuss basic concepts of detonation theory. Lastly, we define the specific objectives of this study, and outline the plan of this dissertation.

1.1 Motivation and Problem Description

Detonation is a rapid combustion process induced by the passage of a strong shock through a reactive material. The combustion process is self-sustaining, provided that the energy released by chemical reaction is sufficient to support the propagation of the shock through the material. Typical pressures generated by the detonation of energetic solids are near 20 GPa, and detonation wave speeds are near 7000 m/s. Though the energy per unit mass of these materials is comparable to ordinary solid fuels, the energy release rates are extremely fast resulting in energy fluxes at the detonation front near 1×10^5 GW/m^2. Various aerospace, mining, and defense related applications have evolved which utilize the large power generated by the detonation of energetic solids to perform specific tasks. However, with their use come hazards associated with the storage and handling of these materials.

Considerable research has been conducted during the past three decades addressing the evolution of detonation in granulated energetic material. This research has largely been motivated by concerns over the accidental detonation of damaged high-explosives or propellants in response to weak mechanical shock or thermal insult [2]. Here, damaged material refers to cast solid material which has been inadvertently fractured; thus, local granulated regions exist within the material.

Relative to granulated explosives, cast solid explosives are less susceptible to detonation by weak mechanical shock as only strong shocks provide sufficient energy to initiate chemical reaction. In contrast, experiments have shown that weak mechanical shock is often sufficient to trigger detonation in granulated explosives [79, 42]. In these systems, chemical reaction is initiated by the formation of local regions of intense thermal energy concentration, commonly termed "hot spots." Possible heating mechanisms include shock-void interaction, granule fracture, friction between granules, and adiabatic compression of gas trapped within the interstices of granules [56, 77]. Once reaction is initiated, and if the burning material is strongly confined (e.g., by the walls of the vessel containing the explosive), then the pressure-dependent reaction rate will accelerate, and the pressure of the combustion gases will quickly rise. The high gas pressurization rate may be sufficient to induce the formation of a relatively strong shock. If so, additional hot spots will form as the shock propagates, which will trigger additional reactive centers, which will in turn further strengthen the shock. Detonation results.

Experiments have also shown that granulated regions in damaged cast solid propellants can accelerate normal combustion rates by several orders of magnitude [43, 98]; this is of particular concern to the solid rocket propulsion community. In granulated regions, where the surface area of unburnt solid propellant is high, flame spread is significantly enhanced by the permeation of hot combustion gases through the granulated material; this mode of flame spread is commonly termed convective burning. The hot gases ignite the unburnt propellant granules, resulting in an increase in the total burning surface area; consequently, the production rate of combustion gases increases which leads to an increase in gas pressure. If the gas pressurization rate is sufficiently high to induce the formation of a shock, the propellant can undergo a transition to detonation in a manner similar to that described above. This sequence of events is a plausible scenario for the accidental detonation of solid propellants used in rocket motors which may have been damaged prior to, or during, motor operation.

Devices also exist which utilize the power generated by detonation to perform specific tasks within controlled environments. One such device is the Super*Zip separation joint which is regularly used on the Space Shuttle to release spacecraft from the Shuttle's cargo bay [13]. This device uses a detonating explosive cord as a mechanism to achieve planar separation. Since explosively actuated devices often play critical roles in space-related missions, one must strive for fail-proof designs. As such, detailed modeling could be a useful tool in optimizing the design of these devices.

Many questions exist concerning the evolution of detonation in granulated material: What are the most important heating mechanisms induced by weak mechanical shock? How do these mechanisms interact with the chemistry of the solid to initiate chemical reaction? Following initiation of reaction, what are the most important physical processes responsible for transition to detonation? How do the properties of the granulated region, such as the granule size distribution, affect localized heating, initiation of chemical reaction, and transition to detonation? What major factors influence the distance required for transition to detonation? How much granulation is necessary to effect transition to detonation? How much confinement is necessary to effect transition to detonation?

In this study, we continue a long-standing effort to address these and other questions. Specifically, we consider a paradigm problem for the initiation of detonation in

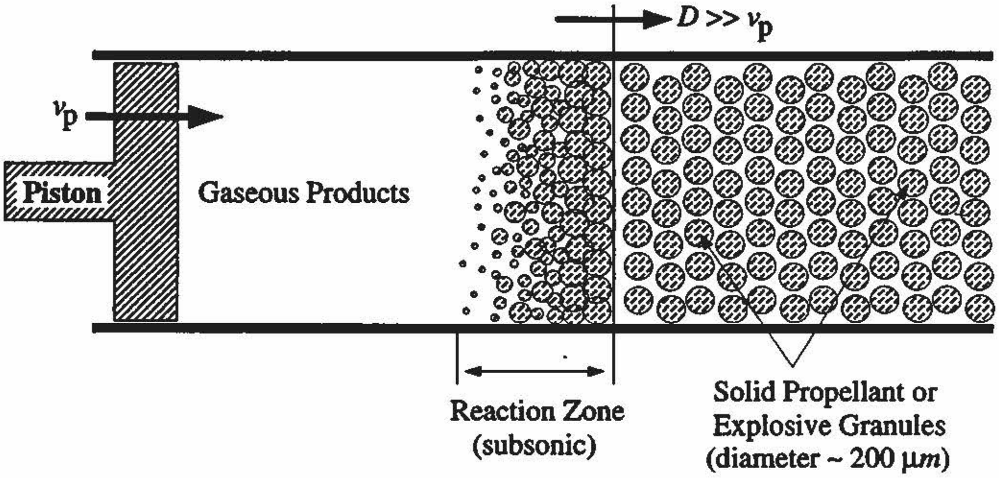

Figure 1.1: Schematic of the model problem.

damaged high-explosives by weak, planar mechanical shock. This problem, which is well-characterized by experiments [42, 79, 80, 105], involves the low velocity impact of a moving piston, having velocity v_p, with a stationary bed of granular explosive.

A simple schematic of the model problem is given in Fig. 1.1. In this figure, transition to detonation has already occurred, and the resulting detonation wave, composed of a thin lead shock followed by a thick reaction zone, is propagating to the right at speed D, where $D \gg v_p$, and is supersonic with respect to both the ambient gas and solid. As will be shown, the lead shock may be in the gas and/or solid depending on the relative rates of the various physical processes occurring within the reaction zone structure. In this study, we model shocks as discontinuities since the time scales associated with diffusive processes, which define a shock structure, are large compared to the time scales associated with detonation. Adiabatic compression of the ambient material by the lead shock provides sufficient energy to initiate chemical reaction. Due to reaction, solid particle mass, momentum, and energy are converted into gas mass, momentum, and energy. This conversion process sustains propagation of the wave through the material by means of acoustic energy transmission from the point of local reaction, through the subsonic region of the reaction zone, and to the lead shock. Other processes occurring within the reaction zone include momentum and energy exchange between the gas and solid due to drag interaction, thermal energy exchange between the gas and solid due to convective heat transfer, and material compaction due to mechanical stresses. At the end of the reaction zone, all of the solid is completely consumed by reaction. The reaction rate determines both the time required for complete reaction and the length of the reaction zone; a typical reaction time predicted by this study is 1 μs, and a typical reaction zone length is 10 mm.

For this study, we adopt a common terminology, and collectively term the sequence of events, whereby the low speed combustion wave initiated by weak mechanical shock (i.e., for approximately $v_p < 700\ m/s$) accelerates and undergoes a transition to detonation, as *deflagration-to-detonation transition* (DDT). This terminology is also commonly used to describe the transition process resulting from thermal energy input. The transition process whereby detonation is directly initiated by strong mechanical shock (i.e., for approximately $v_p > 700\ m/s$) is commonly termed shock-to-detonation transition (SDT). Though a distinction is often made in the literature between DDT and SDT, these processes are not mutually exclusive as a key component of DDT is the formation of a strong shock within the material due to the accelerating combustion wave, and the subsequent transition to detonation in a manner similar to SDT.

1.2 Literature Review

In this section, we survey selected experimental, theoretical, and modeling work relevant to this study.

1.2.1 Experimental

A number of experimental studies have been conducted for the purpose of identifying a mechanism for DDT in granulated energetic material. The earliest experiments are those of Griffiths and Groocock [43], and Bernecker and Price [14, 15, 97]. More recent experiments include those of Baer et al. [7], Bernecker and co-workers [16, 17, 105], Campbell, McAfee, and co-workers [24, 79, 80, 81], Green et al. [42], and Leubcke et al. [75].

In these experiments, explosive granules ($\sim$ 10 to 300 μm in diameter) are placed into a thick-walled steel tube which provides the confinement necessary for detonation. Typically, the inner diameter of the tube ($\sim$ 30 mm) is small compared to its length ($\sim$ 300 mm). Commonly tested solid high-explosives include HMX (cyclotetramethylene tetranitramine; $C_4H_8N_8O_8$), RDX (cyclotrimethylene trinitramine; $C_3H_6N_6O_6$), and PETN (pentaerythritol tetranitrate; $C_5H_8N_4O_{12}$). These secondary high-explosives are often used in various military and aerospace applications. The explosive granules are compressed into the tube in such a way as to locally maintain a nearly uniform solid volume fraction. Here, solid volume fraction is defined as the ratio of the volume occupied by the explosive granules to the total volume (Solid Volume Fraction = Solid Volume/Total Volume). The ends of the tube are sealed to provide additional confinement, and combustion is initiated at one end. Though various methods have been used to initiate combustion, the two most commonly used methods are 1) thermal energy input supplied by a chemical ignition device [7, 14, 15, 16, 17, 24, 43, 75, 81, 97], and 2) mechanical energy input supplied by driving a piston into the granular explosive bed [42, 79, 80, 105]. Transition to detonation is observed to depend on the chemical reactivity of the particular explosive, the initial solid volume fraction of the granular bed, the extent of confinement, and the piston velocity (for piston impact experiments).

Here, we primarily focus on experimental results for piston-initiated DDT. In these experiments, the piston, which is constrained to move within the tube, is fired at the explosive test bed using a driver explosive. It is possible to record piston velocities, mixture pressures, and solid volume fractions during DDT, and to track the propagation of strong compression waves within the granular bed. Typical piston velocities used in experiments are near 100 m/s, and ambient solid volume fractions are near 0.70.

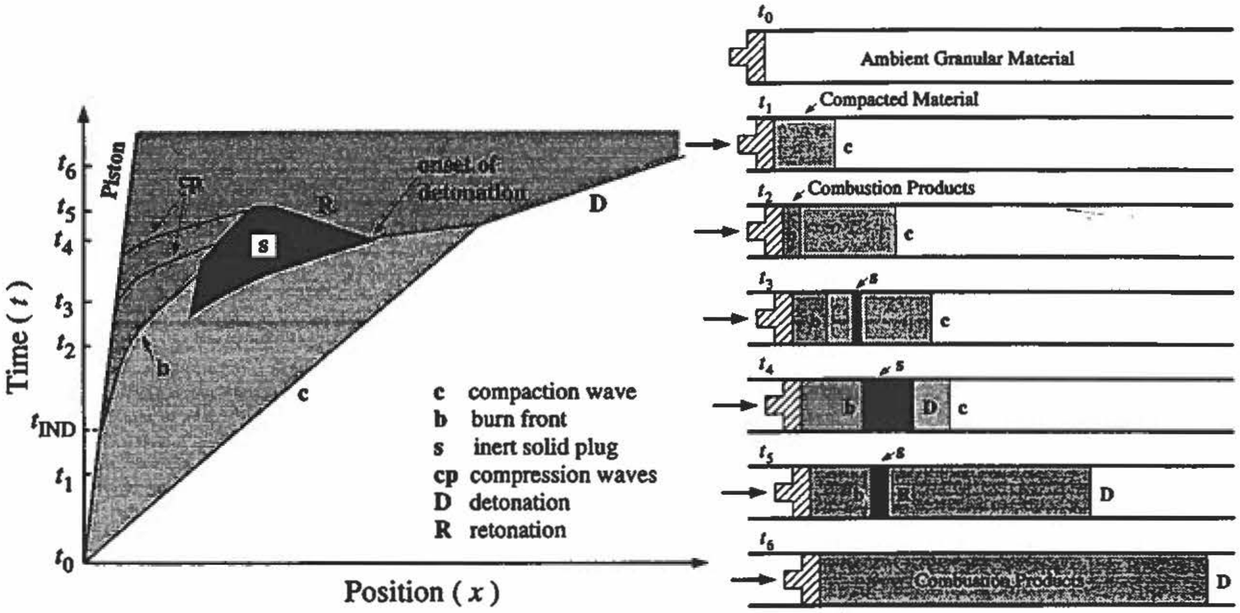

Figure 1.2: Results of a typical piston-initiated DDT experiment.

The transient events observed during a typical piston-initiated DDT experiment are qualitatively shown in the distance-time plane of Fig. 1.2. The piston impacts the explosive test bed at time t_0, and generates a compaction wave, labeled **c**, which propagates away from the piston at nearly constant speed ($\sim$ 400 m/s). Across the compaction wave, the solid volume fraction increases from its ambient value to near 0.90 (for ambient solid volume fractions near 0.70). Weakly exothermic chemical reaction is initiated due to local heating mechanisms as the material is compacted. Following an induction period, during which chemical reaction slowly intensifies, a burn front, labeled **b**, is seen to form near the piston surface; this occurs at time t_{IND}. Subsequently, the reaction rate increases near the piston surface, and the pressure of the gaseous reaction products rapidly increases due to confinement provided by the piston, the wall of the tube, and the low permeability of the compacted material. The resulting high gas pressurization rate causes the burn front to strengthen and accelerate. As the burn front accelerates through the compacted material, the material is further compacted resulting in the formation of an inert solid plug (i.e., solid volume fraction near unity), labeled **s**, slightly ahead of the burn front. The mechanism responsible for the formation of this plug is not clearly understood, but is believed to be associated with the coalescence of compression waves generated by the accelerating burn front [79, 109, 111]. The width of the solid plug rapidly increases with time as compression waves originating from behind the plug impinge upon the rear of the plug; these waves are labeled **cp**. Finally, a shock is generated at the front of the plug which initiates both a right-propagating detonation, labeled **D**, and a left-propagating detonation (referred to as a retonation), labeled **R**. For the case shown here, the propagation speed of the resulting detonation decreases slightly as the detonation overtakes the initial compaction front and propagates into the less dense ambient material.

A similar sequence of events has been observed in recent DDT experiments whereby combustion was directly initiated by gasless pyrotechnic ignitors [81, 75]. The purpose of these experiments was to identify the role of convective burning in DDT by eliminating pre-pressurization of the explosive bed due to gases generated by standard chemical ignitors. Results of these experiments, which support the earlier results obtained by Campbell [24], show that convective burning is restricted to a short region near the point of ignition. In these experiments, the high gas pressure generated by convective burning during the early stage of DDT was sufficient to choke the flow of gas through the bed, resulting in the formation and propagation of a compaction wave; subsequently, transition to detonation was seen to occur in a manner similar to that described above for piston-initiated DDT.

1.2.2 Theoretical and Modeling

Though experiments have provided much information about DDT in granular explosives, it is necessary to model the physical processes involved, and the coupling between these processes, in order to identify and better understand important mechanisms responsible for transition to detonation. To this end, a number of two-phase models have been formulated for analyzing the combustion of granular energetic solids. Most models are based on principles of continuum mixture theory; details of the theory are given in Chapter 2.

Relevant modeling studies include those of Krier and co-workers [22, 23, 41, 52, 60, 61, 62, 63, 92, 94, 95], Kuo, Summerfield, and co-workers [64, 65, 66, 67], Nunziato, Baer and co-workers [4, 5, 6, 7, 86], Saurel and co-workers [106, 107], and more recently those of Son, Bdzil, and co-workers [10, 59, 109, 110]. Reviews of other relevant literature can be found in many of these references. The work of Kuo et al. primarily addressed low speed, low pressure combustion, while the work of Krier et al., Nunziato et al., Saurel et al., and Son et al. addressed high speed, high pressure combustion associated with DDT. Also, Stewart et al. [111] recently formulated a simplified model for predicting DDT in granulated reactive material using a modified single phase state variable approach.

The two-phase continuum models used to study DDT are posed as coupled time-dependent systems of partial differential equations which track the evolution of mass, momentum, and energy of an inert gas and reactive solid particles in one spatial dimension. Some models include an additional partial differential equation to account for dynamic compaction of the solid particles [5, 94], while other models use an algebraic stress relation to account for compaction [22, 23]. Physical processes accounted for by most models include 1) convective transport in both the gas and solid, 2) mass, momentum, and energy transfer from the solid to the gas due to chemical reaction, 3) momentum and energy exchange between the gas and solid due to drag interaction, 4) thermal energy exchange between the gas and solid due to convective heat transfer, and 5) material compaction due to a stress imbalance between the gas pressure, solid pressure, and an intragranular stress. Though the various two-phase models have common features, they often differ in the functional forms of the evolution equations and constitutive models. These differences have been the focus of some debate; relevant issues are discussed in detail by Powers et al. [94] and are not considered in this dissertation.

A number of difficulties exist in the numerical modeling of DDT in these systems, of which accurately capturing strong shocks is the most challenging. To this end, traditional higher-order numerical methods (i.e., Lax-Wendroff methods) fail since they produce spurious oscillations near shocks, and are unstable as a consequence. Traditional lower-order methods (i.e., first-order upwind methods), while stable, are overly diffusive resulting in significantly smeared shocks; as such, the physical phenomena which are to be modeled within the reaction zone can be overwhelmed by the artificially large shock structure. Commonly used numerical methods for simulating DDT are based on the explicit use of artificial viscosity, and it is likely that this added numerical diffusion adversely affects their ability to accurately resolve fine scale detonation structure. Furthermore, the optimal amount of artificial viscosity needed to reasonably capture shocks is largely problem specific, and must be chosen by the modeler based on a trial and error procedure. Numerical methods used to simulate DDT must also be capable of handling mathematical stiffness which arises due to the disparate time scales associated with gas and solid convection, combustion, interphase drag, interphase heat transfer, and material compaction.

For certain conditions, this study has identified length scales associated with various physical phenomena occurring within the reaction zone structure which are as small as 30 μm. This poses an additional problem for numerical modeling as it would require approximately 1000 computational cells within a 10 mm reaction zone to accurately resolve such fine-scale structure. Obviously, the computational costs for such well-resolved simulations are prohibitively expensive.

Numerical simulations based on the two-phase continuum models have been modestly successful in predicting most experimentally observed features of DDT including 1) the formation and propagation of a lead compaction wave, 2) the initiation and subsequent acceleration of a burn front in the compacted material, and 3) the final transition to detonation. Also, some simulations have predicted the formation of a secondary compacted region reminiscent of the inert solid plug [5, 23, 109]. The predicted gas pressures, densities, and velocities at the end of the reaction zone, as well as the predicted compaction and detonation wave speeds, reasonably match experimental results.

However, much of the two-phase modeling effort has concentrated on predicting the transient events leading to detonation, with little emphasis given to an analysis of the fully-developed detonation structures; as such, detonation structures predicted by DDT simulations are not well-characterized. Here, detonation structure refers to the spatial variation in all two-phase variables, such as gas and solid density, velocity, pressure, etc., within the reaction zone. Furthermore, many DDT simulations are performed using coarse computational grids which place approximately 6-15 computational cells within the reaction zone; as such, fine-scale structures within the reaction zone are not accurately resolved. Results of these unsteady analyses have provided a weak foundation for the development of a steady two-phase detonation theory.

An analysis of detonation structure is of both practical and theoretical importance. From a practical perspective, it is the physical phenomena occurring within the detonation wave which are responsible for the peak stresses and wave speeds, and thus the power generated by detonation. From a theoretical perspective, one cannot understand all implications of a DDT theory without a careful examination of fully-resolved two-phase detonation structure. Also, an analysis of planar two-phase detonation structure provides the theoretical base necessary for the attack of more complicated multiple-dimensional problems.

A significant advancement in the theory of steady two-phase detonation is due to Powers, Stewart, and Krier [91, 92, 94, 95]. In their investigations, Powers, Stewart, and Krier formulated a new unsteady, two-phase continuum model appropriate for describing detonation in granulated material. Their model is based on principles of continuum mixture theory, and is believed to be an improvement over previous existing two-phase continuum models used to predict detonation in granulated material. Reference [94] gives a complete description of modeling improvements. Powers, Stewart, and Krier then used their model to analyze steady two-phase detonation structures admitted by the steady form of the model equations. A key contribution of their work was in placing two-phase detonation theory within the context of classical one-phase detonation theory [34]. As such, it is appropriate to briefly introduce relevant concepts from one-phase detonation theory before proceeding with a discussion of their results.

One-phase detonations are modeled by the reactive Euler equations of gas dynamics. Assuming a steady, one-dimensional detonation having a lead discontinuous shock followed by a zone of exothermic chemical reaction, the equations reduce to an autonomous system of ordinary differential equations expressed in a reference frame attached to the lead shock. Thus, the steady one-phase detonation problem is posed as an initial value problem, where the initial conditions are given by the shocked gas state.

The simplest theory, referred to as Chapman-Jouguet (CJ) theory, is based on an analysis of complete reaction end states, which are equilibria of the ordinary differential equations. Thus, results of this analysis are independent of reaction zone structure. For fixed ambient conditions, CJ theory predicts no equilibrium end states for wave speeds less than a minimum critical value. For a unique value of wave speed equal to this minimum value, referred to as the CJ wave speed, there is predicted a single equilibrium end state called the CJ state. For all wave speeds larger than the CJ wave speed, the theory predicts two equilibrium end states: a strong state and a weak state. The strong state has higher pressure than the CJ state, and the weak state has lower pressure. The gas velocity relative to the wave front is sonic for the CJ state, subsonic for strong states, and supersonic for weak states. As such, steady detonations terminating at either a CJ or weak state are not susceptible to degradation by rarefaction waves originating from behind the detonation which propagate at the local acoustic speed relative to the local flow velocity. The CJ theory hypothesizes that the CJ state is the unique end state for a steady self-propagating detonation, though self-propagating detonations terminating at weak states cannot be ruled out solely based on an equilibrium end state analysis. Here, a self-propagating detonation refers to one in which the energy released by combustion is sufficient to sustain propagation of the wave in the absence of external energy input. Strong detonations, being susceptible to degradation by rarefaction waves, require the support of a moving piston so that no rarefactions exist between the piston and the detonation end state; as such, a region of constant state exists between the piston and the end of the reaction zone. Strong detonations are not self-propagating. In fact, if the piston supporting a strong detonation was suddenly stopped, a rarefaction would be produced which would propagate to the detonation and weaken it to either a CJ or weak detonation.

Though the equilibrium analysis identifies CJ, strong, and weak detonation end states, one must consider detonation structure in order to determine whether a path exists connecting the shocked gas state to these end states. The simple Zeldovich [131], von Neumann [121], Doering [29] (ZND) theory, developed during the 1940's, considers the structure of a one-phase detonation wave resulting from a one-step, irreversible, exothermic chemical reaction ($A \rightarrow B$). Based on ZND theory, it can be shown that all self-propagating detonations having a lead shock propagate at the CJ speed, as no path exists leading from the shocked gas state to the weak state. Though weak detonations with a lead shock are not admitted by ZND theory, Fickett and Davis [34] show that they can be readily obtained by relaxing the simple restrictions of the theory. For example, replacing the one-step, irreversible, exothermic chemical reaction with a two-step, irreversible chemical reaction ($A \rightarrow B \rightarrow C$), where the first step is exothermic and the second step is endothermic, gives the possibility of obtaining weak detonations. In summary, ZND theory demonstrates how detonation structure can place constraints on the existence of steady detonation waves.

We now return to a discussion of the two-phase detonation theory developed by Powers, Stewart, and Krier. As shown in their work, the problem of determining steady two-phase detonation structure requires the solution of an autonomous system of four ordinary differential equations subject to initial conditions at the detonation front. In order to define the initial conditions, it is first necessary to specify the ambient state of the material, the detonation wave speed, and whether the gas and/or solid is shocked. The appropriate shocked state at the detonation front is then obtained from two-phase Rankine-Hugoniot relations. In their study, both an equilibrium end state analysis and a detonation structure analysis of the governing ordinary differential equations were performed.

The equilibrium end state analysis identified two-phase equivalents to the CJ, strong, and weak states predicted by one-phase theory. As in one-phase theory, the two-phase CJ state is predicted for a unique value of detonation wave speed. No equilibrium solutions are predicted for wave speeds less than this value. Two-phase strong and weak states are predicted for wave speeds in excess of this value. Once again, the strong state has higher pressure than the CJ state, and the weak state has lower pressure.

The steady structure analysis for two-phase detonations is considerably more complicated than for one-phase detonations. The added complexity is due to the presence of two phases, and interactions between the phases. In their analysis, Powers, Stewart, and Krier identified paths leading to both the CJ and strong end states for detonations having a lead shock in the gas and an unshocked solid; paths leading to the weak state were not identified. Moreover, they defined parametric conditions for the existence of this class of CJ detonations. Though only shocked gas/unshocked solid structures were predicted, it is likely that other steady structures exist which terminate at CJ, strong, or weak states, possibly having solid shocks, or even multiple shocks. However, due the complexity of the steady two-phase model, the identification of other steady structures is largely a trial and error process.

A comprehensive study of two-phase detonation structure should include both a steady and unsteady analysis. One could numerically solve the unsteady DDT problem, carefully examine the structure of the resulting fully-developed detonation waves, and compare the results to predictions obtained by the steady analysis. As such, one could determine if the steady structures identified by Powers, Stewart, and Krier evolve from DDT events, and identify other, more complicated, steady structures not predicted by the steady analysis. Also, an unsteady analysis can provide information about the stability of two-phase detonations. No such analyses have been reported in the two-phase detonation literature.

1.3 Objectives of this Study

The primary objective of this dissertation is to predict and analyze two-phase detonation structures by numerically simulating piston-initiated DDT, and to compare the predicted structures with results given by a steady-state detonation analysis. A secondary objective is to classify new steady detonation structures. We only consider detonations which are ultimately self-propagating; therefore, we specify piston velocities ($\sim 100\ m/s$) well below those required for piston-supported strong detonations ($\sim 2000\ m/s$). The steady analysis is a minor extension of the work performed by Powers, Stewart, and Krier [91, 95], whereas the unsteady analysis is a major new extension of their work. Specific objectives of the steady analysis are:

1. *To predict all self-propagating two-phase detonation structures.*

2. *To define parametric conditions for the existence of these structures.*

Specific objectives of the unsteady analysis are:

1. *To develop a modern high-resolution numerical method which can accurately resolve the fine scale structure of a two-phase detonation.*
2. *To determine if the detonation structures identified by the steady analysis evolve from a physically relevant ambient state.*
3. *To determine how DDT and detonation structure are affected by system parameters.*

The development of a new high-resolution numerical method is a major contribution of this dissertation.

The model used in this study is a variant of the unsteady, two-phase continuum model formulated by Powers, Stewart, and Krier [91, 94]. We have modified their model to include an additional evolution equation for an ignition variable, and have incorporated an intragranular stress relation which is better suited for describing dynamic compaction of granular explosives [93]. The equation for the ignition variable is used to model the induction period observed prior to the onset of full-scale combustion in piston-initiated DDT experiments. The use of such an equation is not standard in DDT modeling, though similar equations have been used to control the heat of reaction during the induction period [8, 59, 110]. The continuum model is representative of other two-phase continuum models commonly used to predict detonation in granulated material [5, 23], and is able to predict most events characteristic of DDT. Whenever possible, comparisons of model predictions with experimental data are given in this dissertation.

The plan of this dissertation is as follows. First, the unsteady model is presented in Chapter 2. The modeling approach is discussed, and the dimensional model equations are given. As this study considers detonation initiated by a moving piston, the model equations are transformed to a reference frame that moves with the piston. The equations are non-dimensionalized, and the non-dimensional parameters are discussed.

Next, a characteristics analysis of the non-dimensional model equations is given in Chapter 3. The purpose of this analysis is to classify the model equations, and to provide the mathematical framework needed for the construction of the high-resolution numerical method for solving the unsteady model equations. The equations are shown to admit discontinuous solutions, such as shocks and contact discontinuities, which are also discussed in this chapter.

The high-resolution numerical method is formulated in Chapter 4. The method is upwind, does not require the explicit use of artificial viscosity, can accurately capture shocks with minimal smearing, and can accurately resolve disparate time-scales associated with rate-dependent processes. The method is based on Godunov's methodology [40] which requires the solution of a two-phase Riemann problem at each computational cell boundary in order to advance the solution in time. Rather than exactly solving the two-phase Riemann problem, an approximate solution is used for increased computational efficiency. The approximate solution is constructed based on the exact solution of the linear two-phase Riemann problem. As such, the exact solution of the linear problem is first obtained, and its wave structure is analyzed. Such an analysis has not been previously reported for this class of DDT models. The initial and boundary conditions used in this study are also discussed in this chapter.

In Chapter 5, the numerical method is validated against three test problems for which analytical solutions are available: 1) an inert two-phase shock tube problem; 2) the evolution of an inert shock in both the gas and solid due to compression of the granular material by a moving piston; and 3) the evolution of an inert compaction wave due to compression of the granular material by a moving piston. Numerical convergence is demonstrated for each test problem, and the spatial convergence rate is determined. The reader who is primarily interested in the predictions of the physical system can bypass Chapters 4 and 5 without difficulty.

The steady analysis of two-phase detonation is given in Chapter 6. The steady problem is mathematically posed as an initial value problem, and the technique used to put the equations into a simplified form suitable for analysis is given. Detonation end states are analyzed, and detonation structure is investigated by numerically integrating the reduced system of ordinary differential equations. Two classes of self-propagating detonation structures are identified leading to states predicted by the end state analysis: 1) CJ structures having a single lead shock in the gas and an unshocked solid, and 2) weak structures having a single lead shock in the gas and an unshocked solid. The first class of structures has been previously predicted by Powers, Stewart, and Krier [91, 95]; the second class of structures has not been previously predicted. Existence criteria for each of these classes are determined based on the results of a parametric study.

The unsteady analysis of two-phase detonation is given in Chapter 7. For this analysis, we predict the evolution of detonation resulting from piston-initiated DDT, and analyze the effect of material compaction, interphase drag, and ambient mixture density (defined later) on DDT and detonation structure. The predicted fully-developed detonation structures are compared with results given by the steady analysis. In addition to predicting the evolution of CJ and weak structures identified by the steady analysis, we also predict the evolution of fully-developed CJ structures having an unshocked gas and a single lead shock in the solid, as well as fully-developed CJ structures having a shock in both the gas and solid. Previous DDT studies have not clearly demonstrated the existence of such structures.

Conclusions and recommendations for additional study are given in Chapter 8.

2

TWO-PHASE CONTINUUM MODEL

Modeling the detonation of granulated energetic material is complicated by issues common to one-phase combustion modeling (*i.e.*, multi-dimensionality, complex reaction kinetics, compressibility, etc.), and is further complicated due to the simultaneous existence of multiple phases, interactions between phases, and the motion of phase interfaces. Due to these complexities, modeling approaches have been developed which bypass the discrete nature of the flow enabling the dynamics of systems containing a large number of particles to be predicted. One such approach involves averaging the classical continuum equations for each phase over a representative volume of the mixture; a set of macroscopic multi-phase equations expressed in terms of averaged variables results [21, 30, 47, 48]. A second approach, which eliminates the need for formal averaging, uses principles of continuum mixture theory to formulate a set of macroscopic multi-phase equations [90, 116, 117, 126]. Both of these approaches, which are based on a hydrodynamic description of multi-phase granular flow, enable one to obtain tractable models which can be used as tools for engineering applications.

The two-phase continuum model used in this study, which is based on principles of continuum mixture theory, is described in this chapter. First, the dimensional model equations are given in Section 2.1. Second, since this study addresses the evolution of detonation resulting from compression of the material by a moving piston, the dimensional model equations are transformed to the accelerating reference frame of the piston in Section 2.2. Lastly, the model equations are non-dimensionalized in Section 2.3, and the non-dimensional parameters are discussed.

2.1 Model Equations

The model used in this study is a variant of the model formulated by Powers et al. [91, 94] using principles of continuum mixture theory. This theory treats the phases as overlapping continua; as such, each phase is assumed to simultaneously occupy the entire region located within, and including, the system boundaries. Associated with each phase are variables describing its thermodynamic state (i.e., density, pressure, temperature, internal energy, etc.), velocity, and volume fraction. Here, the volume fraction of a particular phase is defined as the ratio of the volume occupied by that phase to the total volume. These variables are not the same as those corresponding to a single phase system, but are loosely interpreted as "averaged" quantities which are representative of the mixture's local microstructural properties. Evolution equations, which are intuitive extensions of the classical continuity, momentum, and energy equations for a single phase system, are postulated governing changes in the mass, momentum, and energy of each phase. Also, an evolution equation is postulated for the volume fraction. Forcing terms in the mass, momentum, and energy equations for each phase account for interactions between phases including drag, heat transfer, and chemical reaction resulting in phase change. Forcing terms in the evolution equation for volume fraction account for changes in volume fraction due to both material compaction and chemical reaction.

In general, the constitutive relations for each phase, and the phase interaction terms, are posed based on the following axioms [11, 90].

1. *Phase Separation.* This axiom asserts that the thermodynamic state of a particular phase depends only on the properties of that phase. In other words, the thermodynamic state of a particular phase is independent of the thermodynamic states of other phases. However, the phase interaction terms can depend on the properties and thermodynamic state of all phases.

2. *Conservation.* This axiom requires that the mass, momentum, and energy of the mixture be conserved. Though the phase interaction processes partition the mass, momentum, and energy of the mixture between the various phases, the net effect of these processes must maintain global conservation.

3. *Dissipation.* This axiom requires that the change in mixture entropy due to any thermo-mechanical process (i.e., the phase interaction processes) be non-decreasing.

4. *Frame Indifference.* This axiom requires that the constitutive relations for each phase, and the phase interaction terms, be invariant under a Galilean coordinate transformation.

Though these axioms constrain the construction of multi-phase continuum models, they still allow for a wide variety of models. As such, models formulated using these axioms are not unique; differences in both the functional form of the model equations and the constitutive relations exist. Furthermore, Powers et al. [94] have shown that two-phase continuum models commonly used to predict detonation in granulated material, including the model used in this study, fail to satisfy the dissipation axiom in special cases. The problem of posing models which satisfy the dissipation axiom under all conditions is currently unresolved.

Implicit to the continuum mixture approach, though not often stated, is the assumption that a suitable representative elementary volume (REV) can be defined about every point within the mixture at every instant in time. The REV defines a volume, $\Delta\hat{V}$ (here we use over-hats "$\hat{\bullet}$" to identify dimensional quantities), about a point, **P**, for which the local microscopic properties of the mixture (i.e., phase density, volume fraction, etc.) can be averaged (Fig. 2.1). In order to obtain statistically meaningful averages, it is required that the characteristic length associated with the REV be much larger than the characteristic length associated with the lo-

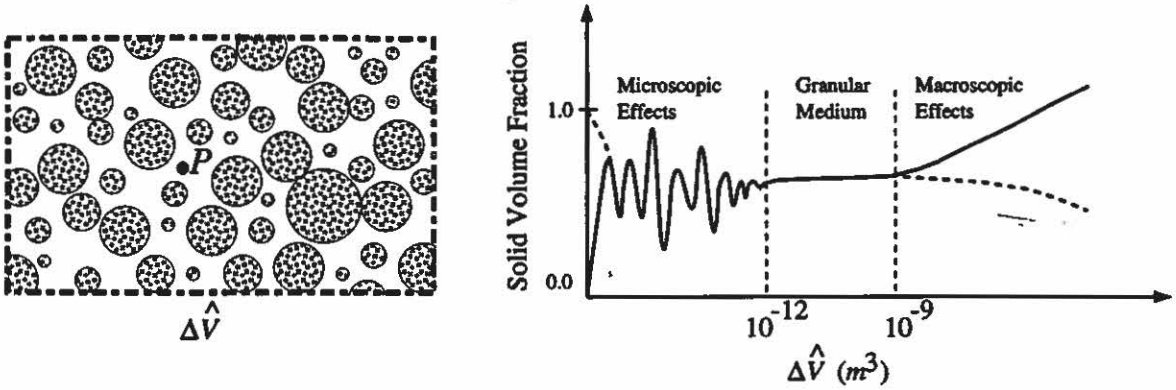

Figure 2.1: REV for a granular material.

cal microscopic structure. Furthermore, it is required that the characteristic length associated with the REV be much smaller than the characteristic length associated with macroscopic variations in the flow quantities. In other words, the REV should be insensitive to small changes in $\Delta\hat{V}$. This definition of a REV for a multi-phase mixture is analogous to the definition of a fluid particle in fluid mechanics.

This idea is illustrated in Fig. 2.1 for a dynamically evolving system of solid particles having radius 100 μm. These particles are similar in size to the particles considered in this study. If, at a fixed instant in time, the volume fraction of the particles contained within $\Delta\hat{V}$ is computed, and if the computation is repeated while continuously increasing $\Delta\hat{V}$, then a result similar to that shown in this figure is obtained. Here, microscopic effects dominate for approximately $\Delta\hat{V} < 10^{-12}\ m^3$, where this value is close to the volume of a single particle. For approximately $\Delta\hat{V} > 10^{-12}\ m^3$, there exist many solid particles within the volume enabling statistically meaningful solid volume fractions to be computed. However, the computed result may become increasingly sensitive to small changes in $\Delta\hat{V}$ as the volume approaches the characteristic volume (length) associated with macroscopic flow variations. Based on predictions of this study for the spatial variation in solid volume fraction within the reaction zone of a typical two-phase detonation (reaction zone length $\sim$ 10 mm), inhomogeneous effects associated with this macroscopic variation in volume fraction will occur for approximately $\Delta\hat{V} > 10^{-9}\ m^3$. Consequently, the two-phase continuum mixture approach is appropriate for REV's within the range $1 \times 10^{-12}\ m^3 \leq \Delta\hat{V} \leq 1 \times 10^{-9}\ m^3$. If a suitable REV cannot be identified at every point within the mixture at every instant in time, then the continuum mixture approach is invalid and other modeling techniques should be considered. This same result holds when using the formal averaging approach to derive macroscopic multi-phase equations.

The continuum model used in this study assumes the existence of reactive, spherical solid particles and an inert gas, both having fixed composition. This assumption is largely made for the sake of simplicity, as the solid particles will generally be of non-spherical shape, and the actual composition of the the reaction products, which is dependent upon many factors including the local pressure and temperature, may consist of a combination of solid, liquid, and gas species. Due to the large stresses generated by detonation ($\sim 10\ GPa$), we assume that each phase is compressible. Diffusive transport processes within each phase are ignored since the time scales associated with these processes ($\sim 1\ s$) are much larger than the time scales associated with detonation ($\sim 1\ \mu s$). Gravitational body forces are also ignored in this study since the magnitude of this force per unit volume ($\sim 10^3\ N/m^3$) is negligible compared to the force per unit volume characteristic of detonation ($\sim 10^{13}\ N/m^3$). Mass, momentum, and energy exchange between the gas and solid are modeled, as is dynamic compaction of the granular bed resulting from a mechanical stress imbalance. This study does not consider the effects of lateral boundaries on the two-phase flow; as such, the flow is assumed one-dimensional (in a macroscopic sense).

The dimensional model equations are given by the following:

$$\frac{\partial}{\partial \hat{t}}\left[\hat{\rho}_1\phi_1\right] + \frac{\partial}{\partial \hat{x}}\left[\hat{\rho}_1\phi_1\hat{u}_1\right] = \left(\frac{3}{\hat{r}}\right)\hat{\rho}_2\phi_2\hat{a}\hat{P}_1^m H(I - I_{ig}), \tag{2.1}$$

$$\begin{aligned}\frac{\partial}{\partial \hat{t}}\left[\hat{\rho}_1\phi_1\hat{u}_1\right] &+ \frac{\partial}{\partial \hat{x}}\left[\hat{\rho}_1\phi_1\hat{u}_1^2 + \hat{P}_1\phi_1\right] \\ &= \hat{u}_2\left(\frac{3}{\hat{r}}\right)\hat{\rho}_2\phi_2\hat{a}\hat{P}_1^m H(I - I_{ig}) + \hat{\beta}\frac{\phi_1\phi_2}{r}\left(\hat{u}_2 - \hat{u}_1\right),\end{aligned} \tag{2.2}$$

$$\begin{aligned}&\frac{\partial}{\partial \hat{t}}\left[\hat{\rho}_1\phi_1\left(\hat{e}_1+\frac{\hat{u}_1^2}{2}\right)\right]+\frac{\partial}{\partial \hat{x}}\left[\hat{\rho}_1\phi_1\hat{u}_1\left(\hat{e}_1+\frac{\hat{u}_1^2}{2}+\frac{\hat{P}_1}{\hat{\rho}_1}\right)\right]\\ &\qquad=\left(\hat{e}_2+\frac{\hat{u}_2^2}{2}\right)\left(\frac{3}{\hat{r}}\right)\hat{\rho}_2\phi_2\hat{a}\hat{P}_1^m H(I-I_{ig})+\hat{\beta}\frac{\phi_1\phi_2}{\hat{r}}\hat{u}_2\left(\hat{u}_2-\hat{u}_1\right)\\ &\qquad+\hat{h}\frac{\phi_1\phi_2}{\hat{r}^{1/3}}\left(\hat{T}_2-\hat{T}_1\right),\end{aligned}\tag{2.3}$$

$$\frac{\partial}{\partial \hat{t}}\left[\hat{\rho}_2\phi_2\right]+\frac{\partial}{\partial \hat{x}}\left[\hat{\rho}_2\phi_2\hat{u}_2\right]=-\left(\frac{3}{\hat{r}}\right)\hat{\rho}_2\phi_2\hat{a}\hat{P}_1^m H(I-I_{ig}),\tag{2.4}$$

$$\begin{aligned}&\frac{\partial}{\partial \hat{t}}\left[\hat{\rho}_2\phi_2\hat{u}_2\right]+\frac{\partial}{\partial \hat{x}}\left[\hat{\rho}_2\phi_2\hat{u}_2^2+\hat{P}_2\phi_2\right]\\ &\qquad=-\hat{u}_2\left(\frac{3}{\hat{r}}\right)\hat{\rho}_2\phi_2\hat{a}\hat{P}_1^m H(I-I_{ig})-\hat{\beta}\frac{\phi_1\phi_2}{\hat{r}}\left(\hat{u}_2-\hat{u}_1\right),\end{aligned}\tag{2.5}$$

$$\begin{aligned}&\frac{\partial}{\partial \hat{t}}\left[\hat{\rho}_2\phi_2\left(\hat{e}_2+\frac{\hat{u}_2^2}{2}\right)\right]+\frac{\partial}{\partial \hat{x}}\left[\hat{\rho}_2\phi_2\hat{u}_2\left(\hat{e}_2+\frac{\hat{u}_2^2}{2}+\frac{\hat{P}_2}{\hat{\rho}_2}\right)\right]\\ &\qquad=-\left(\hat{e}_2+\frac{\hat{u}_2^2}{2}\right)\left(\frac{3}{\hat{r}}\right)\hat{\rho}_2\phi_2\hat{a}\hat{P}_1^m H(I-I_{ig})-\hat{\beta}\frac{\phi_1\phi_2}{\hat{r}}\hat{u}_2\left(\hat{u}_2-\hat{u}_1\right)\\ &\qquad-\hat{h}\frac{\phi_1\phi_2}{\hat{r}^{1/3}}\left(\hat{T}_2-\hat{T}_1\right),\end{aligned}\tag{2.6}$$

$$\frac{\partial\phi_2}{\partial \hat{t}}+\hat{u}_2\frac{\partial\phi_2}{\partial \hat{x}}=\frac{\phi_1\phi_2}{\hat{\mu}_c}\left(\hat{P}_2-\hat{P}_1-\hat{f}\right)-\left(\frac{3}{\hat{r}}\right)\phi_2\hat{a}\hat{P}_1^m H(I-I_{ig}),\tag{2.7}$$

$$\frac{\partial\hat{n}}{\partial \hat{t}}+\frac{\partial}{\partial \hat{x}}\left[\hat{u}_2\hat{n}\right]=0,\tag{2.8}$$

$$\begin{aligned}&\frac{\partial I}{\partial \hat{t}}+\hat{u}_2\frac{\partial I}{\partial \hat{x}}\\ &\qquad=\hat{k}_I\left(1-I\right)\left[\frac{\hat{P}_1\phi_1+\hat{P}_2\phi_2-\hat{P}_{1o}\phi_{1o}-\hat{P}_{2o}\phi_{2o}}{\hat{P}_{1o}\phi_{1o}+\hat{P}_{2o}\phi_{2o}}\right]^2\exp\left[-\frac{\hat{T}_I}{\hat{T}_1\phi_1+\hat{T}_2\phi_2}\right],\end{aligned}\tag{2.9}$$

$$\hat{P}_1=\hat{P}_1(\hat{\rho}_1,\hat{T}_1),\tag{2.10}$$

$$\hat{e}_1=\hat{e}_1(\hat{\rho}_1,\hat{T}_1),\tag{2.11}$$

$$\hat{P}_2=\hat{P}_2(\hat{\rho}_2,\hat{T}_2),\tag{2.12}$$

$$\hat{e}_2=\hat{e}_2(\hat{\rho}_2,\hat{T}_2),\tag{2.13}$$

$$\hat{f}=\hat{f}(\phi_2),\tag{2.14}$$

$$\hat{n} = \frac{3\phi_2}{4\pi\hat{r}^3}, \tag{2.15}$$

$$\phi_1 + \phi_2 = 1. \tag{2.16}$$

In these equations, the subscripts "1" and "2" denote quantities associated with the gas and solid, respectively. Quantities labeled with subscript "o" are associated with the ambient state. The independent variables are time $\hat{t}$ and position $\hat{x}$. Dependent variables are as follows: the phase density $\hat{\rho}_i$ ($i = 1, 2$), defined as the mass of phase i per unit volume occupied by that phase; the phase pressure $\hat{P}_i$; the phase temperature $\hat{T}_i$; the particle velocity $\hat{u}_i$, measured with respect to a stationary reference frame; the specific internal energy $\hat{e}_i$; the volume fraction ϕ_i; the radius of the spherical solid particles $\hat{r}$; the number of particles per unit volume $\hat{n}$; the intragranular stress $\hat{f}$; and an ignition variable I which is discussed in a following paragraph. In Eqs. (2.1-2.9), $H(I - I_{ig})$ is the Heaviside unit step function, and I_{ig}, $\hat{a}$, m, $\hat{\beta}$, $\hat{h}$, $\hat{\mu}_c$, $\hat{k}_I$, and $\hat{T}_I$ are constant parameters which are described below. Equations (2.1-2.16) constitute a system of sixteen equations in sixteen unknowns; thus, the system of equations is mathematically closed and, in principle, can be solved provided that appropriate initial and boundary conditions are supplied. The initial and boundary conditions used in this study are discussed in Chapter 4.

Equations (2.1), (2.2), and (2.3) are evolution equations for the mass, momentum, and total energy of the gas. Equations (2.4), (2.5),and (2.6) are evolution equations for the mass, momentum, and total energy of the solid. Equations (2.7-2.9) are evolution equations for the solid volume fraction, the particle number density, and the ignition variable, respectively.

The forcing terms in Eqs. (2.1) and (2.4) account for the exchange of mass from the solid to the gas due to combustion. Here, mass exchange is modeled as a single, irreversible process (*solid → inert gas*), and all chemical reaction is assumed to occur on the particle surface. Combustion initiation occurs for $I \geq I_{ig}$, where I_{ig} is a constant ignition parameter. The combustion rate is modeled by a burn law which depends upon the gas pressure. The use of such a burn law is motivated by strand burn experiments. In these experiments, a cylindrical strand of solid propellant or explosive is burned within a pre-pressurized vessel. Combustion is initiated at one end of the strand, and a combustion wave develops which propagates along the length of the strand at nearly constant speed. The burn rate is inferred from the combustion wave speed, which is found to vary with initial pressure [125]. Values for the combustion rate parameters $\hat{a}$ and m are correlated to match the burn rate data.

The forcing terms in Eqs. (2.2) and (2.5) account for two forms of momentum exchange between the gas and solid. First, the gas is gaining that momentum associated with the solid which is being converted into gas due to combustion. Second, there is an exchange of momentum due to solid particle-gas drag interaction. The drag interaction is modeled by a drag law which states that the drag is proportional to the difference in velocity between the phases, and inversely proportional to the particle radius. In the drag law, $\hat{\beta}$ is defined as a drag coefficient.

The forcing terms in Eqs. (2.3) and (2.6) account for the exchange of energy between the gas and solid. Energy exchange associated with combustion, and with particle-gas drag work, are accounted for, as is thermal energy exchange between the gas and solid. The thermal energy exchange rate is assumed to be proportional to the temperature difference between the gas and the solid, and inversely proportional to the cube root of the particle radius; here, $\hat{h}$ is defined as a heat transfer coefficient.

Equation (2.7) is a dynamic compaction equation governing changes in solid volume fraction due to both compaction and combustion of the granular bed. This equation predicts that, in the absence of combustion, the solid volume fraction, ϕ_2, will equilibrate to a value such that the solid pressure, $\hat{P}_2$, equals the sum of the gas pressure, $\hat{P}_1$, and the intragranular stress, $\hat{f}$; the equilibration rate is governed by the parameter $\hat{\mu}_c$ which is referred to as the compaction viscosity. The use of this equation was first proposed by Baer and Nunziato [5]. Though this equation is not standard in multi-phase modeling, it does allow for the modeling of rate-dependent material compaction which is known to be important in the evolution of detonation in granulated material. Additionally, the use of this equation insures that the characteristic wave speeds associated with the model equations are real [91, 94], and that solutions of the governing partial differential equations are hyperbolic waves. The characteristic wave speeds of some two-phase models, particularly models which assume pressure equilibrium between the phases, have been shown to be imaginary, and are thus unable to properly model discontinuous solutions [30, 99].

Equation (2.8) expresses that the total number of particles in the system is conserved. Though not considered in this study, it is possible to model the coalescence and break-up of particles by including appropriate inhomogeneous terms in this equation.

Equation (2.9) is an *ad hoc* evolution equation for the ignition variable I. For this study, $0 \leq I \leq 1$, where $I_o = 0$ for the ambient state, and $I_{ig} = 0.5$. This equation is used to model the observed induction period occurring prior to the onset of full-scale combustion in piston-initiated DDT experiments [7, 24, 42, 79, 80, 105]. The forcing term in this equation models the ignition variable as an increasing function of pressure and temperature of the gas and solid. Consequently, in agreement with experiments, higher temperatures and pressures result in a decrease in the induction time. In this equation, $\hat{k}_I$ and $\hat{T}_I$ are ignition rate constants. Similar equations have been used in other two-phase combustion models as "switches" for controlling the amount of chemical energy released by combustion during the induction period [8, 59, 110].

Equations (2.10) and (2.11), and Eqs. (2.12) and (2.13) are functional dependencies for the thermal and caloric equations of state for the gas and the solid, respectively. At this juncture, we choose not to specify exact forms for the state relations as the formulation of the numerical method in Chapter 4 does not require us to do so. Furthermore, different state relations are used for various problems in this dissertation, the exact forms of which are given where appropriate. Equation (2.14) is a functional dependency for the intragranular stress which is assumed to be a monotonically increasing function of solid volume fraction. Equation (2.15) is the definition of the local particle number density expressed in terms of the solid volume fraction and the particle radius, and Eq. (2.16) is a mixture saturation condition (i.e., no voids are present within the mixture).

The phase interaction terms in Eqs. (2.1-2.6) have been constructed such that, for an isolated system, when Eqs. (2.1) and (2.4), Eqs. (2.2) and (2.5), and Eqs. (2.3) and (2.6) are respectively summed, homogeneous differential equations for the mixture mass, momentum, and total energy are obtained:

$$\frac{\partial}{\partial \hat{t}}\left[\hat{\rho}_1\phi_1+\hat{\rho}_2\phi_2\right]+\frac{\partial}{\partial \hat{x}}\left[\hat{\rho}_1\phi_1\hat{u}_1+\hat{\rho}_2\phi_2\hat{u}_2\right]=0, \tag{2.17}$$

$$\frac{\partial}{\partial \hat{t}}\left[\hat{\rho}_1\phi_1\hat{u}_1+\hat{\rho}_2\phi_2\hat{u}_2\right]+\frac{\partial}{\partial \hat{x}}\left[\hat{\rho}_1\phi_1\hat{u}_1^2+\hat{\rho}_2\phi_2\hat{u}_2^2+\hat{P}_1\phi_1+\hat{P}_2\phi_2\right]=0, \tag{2.18}$$

$$\begin{aligned}&\frac{\partial}{\partial \hat{t}}\left[\hat{\rho}_1\phi_1\left(\hat{e}_1+\frac{\hat{u}_1^2}{2}\right)+\hat{\rho}_2\phi_2\left(\hat{e}_2+\frac{\hat{u}_2^2}{2}\right)\right]\\&\quad+\frac{\partial}{\partial \hat{x}}\left[\hat{\rho}_1\phi_1\hat{u}_1\left(\hat{e}_1+\frac{\hat{u}_1^2}{2}+\frac{\hat{P}_1}{\hat{\rho}_1}\right)+\hat{\rho}_2\phi_2\hat{u}_2\left(\hat{e}_2+\frac{\hat{u}_2^2}{2}+\frac{\hat{P}_2}{\hat{\rho}_2}\right)\right]=0.\end{aligned} \tag{2.19}$$

Consequently, the total mass, momentum, and energy of the mixture are conserved.

In addition to mixture conservation constraints, it is desirable to construct the phase interaction terms such that, for a thermally isolated mixture, the change in total entropy of the mixture due to any thermodynamic process is non-negative. This is the basis of the dissipation axiom discussed at the beginning of this chapter. It is proposed that the mixture entropy satisfy the following evolution equation [90]:

$$\frac{\partial}{\partial \hat{t}}\left[\hat{\rho}_1\phi_1\hat{s}_1+\hat{\rho}_2\phi_2\hat{s}_2\right]+\frac{\partial}{\partial \hat{x}}\left[\hat{\rho}_1\phi_1\hat{u}_1\hat{s}_1+\hat{\rho}_2\phi_2\hat{s}_2\hat{u}_2\right]\geq 0, \tag{2.20}$$

where $\hat{s}_1$ and $\hat{s}_2$ are the specific entropy of the gas and solid, respectively. An expression for Eq. (2.20) can be obtained using the Gibbs relation for each phase $[\hat{T}_i d\hat{s}_i = d\hat{e}_i - (\hat{P}_i/\hat{\rho}_i^2)d\hat{\rho}_i,\ i=1,2]$ with Eqs. (2.3) and (2.6); the resulting expression is given by Powers et al. [94] and is not repeated here. This analysis enables the contribution of each thermodynamic process (i.e., mass transfer, momentum transfer, energy transfer, and compaction) to be identified. Powers et al. [94] have shown that many commonly used two-phase combustion models may not satisfy Eq. (2.20) under all circumstances. It is difficult to to construct physically relevant forms for the phase interaction terms which identically satisfy Eq. (2.20).

The phase interaction terms have also been constructed so that the ambient state of the material is an equilibrium state. Other reasons for having chosen these specific forms for the phase interaction terms are to achieve some degree of analytical simplicity, and to enable a steady two-phase detonation wave to be predicted. In spite of their relative simplicity, it is shown in Reference [95] that these forms do predict the same trends as more complicated empirical relations.

Equations (2.10-2.13) can be used to define expressions for the gas sound speed, $\hat{c}_1$, and the solid sound speed, $\hat{c}_2$. To this end, we solve Eqs. (2.11) and (2.13) for $\hat{T}_1$ and $\hat{T}_2$, respectively, and substitute the results into Eqs. (2.10) and (2.12) to obtain the following functional dependencies:

$$\hat{P}_1 = \hat{P}_1(\hat{\rho}_1, \hat{e}_1), \tag{2.21}$$

$$\hat{P}_2 = \hat{P}_2(\hat{\rho}_2, \hat{e}_2). \tag{2.22}$$

As shown in Appendix A, the gas and solid sound speed can be expressed in terms of thermodynamic derivatives obtained from these relations:

$$\hat{c}_1^2 \equiv \left.\frac{\partial \hat{P}_1}{\partial \hat{\rho}_1}\right|_{\hat{s}_1} = \frac{\hat{P}_1}{\hat{\rho}_1}\Gamma_1 + \left.\frac{\partial \hat{P}_1}{\partial \hat{\rho}_1}\right|_{\hat{e}_1}, \tag{2.23}$$

$$\hat{c}_2^2 \equiv \left.\frac{\partial \hat{P}_2}{\partial \hat{\rho}_2}\right|_{\hat{s}_2} = \frac{\hat{P}_2}{\hat{\rho}_2}\Gamma_2 + \left.\frac{\partial \hat{P}_2}{\partial \hat{\rho}_2}\right|_{\hat{e}_2}, \tag{2.24}$$

where Γ_1 and Γ_2 are the Grüneisen coefficients for the gas and solid, and are defined by

$$\Gamma_1 \equiv \frac{1}{\hat{\rho}_1} \left.\frac{\partial \hat{P}_1}{\partial \hat{e}_1}\right|_{\hat{\rho}_1}, \qquad \Gamma_2 \equiv \frac{1}{\hat{\rho}_2} \left.\frac{\partial \hat{P}_2}{\partial \hat{e}_2}\right|_{\hat{\rho}_1}. \tag{2.25}$$

Lastly, the construction of the numerical method in Chapter 4 requires that Eqs. (2.7) and (2.9) be expressed in divergence form. To this end, Eq. (2.4) is multiplied by ϕ_2, Eq. (2.7) is multiplied by $\hat{\rho}_2\phi_2$, and the two resulting expressions are added to obtain

$$\begin{aligned}&\frac{\partial}{\partial \hat{t}}\left[\hat{\rho}_2\phi_2^2\right]+\frac{\partial}{\partial \hat{x}}\left[\hat{\rho}_2\hat{u}_2\phi_2^2\right]\\&\quad=\frac{\hat{\rho}_2\phi_1\phi_2^2}{\hat{\mu}_c}\left(\hat{P}_2-\hat{P}_1-\hat{f}\right)-2\left(\frac{3}{\hat{r}}\right)\hat{\rho}_2\phi_2^2\hat{a}\hat{P}_1^m H(I-I_{ig}).\end{aligned}\tag{2.26}$$

Similarly, Eq. (2.4) is multiplied by I, Eq. (2.9) is multiplied by $\hat{\rho}_2\phi_2$, and the two resulting expressions are added to obtain

$$\begin{aligned}&\frac{\partial}{\partial \hat{t}}\left[\hat{\rho}_2\phi_2 I\right]+\frac{\partial}{\partial \hat{x}}\left[\hat{\rho}_2\phi_2\hat{u}_2 I\right]\\&\quad=\hat{k}_I\hat{\rho}_2\phi_2\left(1-I\right)\left[\frac{\hat{P}_1\phi_1+\hat{P}_2\phi_2-\hat{P}_{1o}\phi_{1o}-\hat{P}_{2o}\phi_{2o}}{\hat{P}_{1o}\phi_{1o}+\hat{P}_{2o}\phi_{2o}}\right]^2\exp\left[-\frac{\hat{T}_I}{\hat{T}_1\phi_1+\hat{T}_2\phi_2}\right]\\&\quad-\left(\frac{3}{\hat{r}}\right)\hat{\rho}_2\phi_2 I\hat{a}\hat{P}_1^m H(I-I_{ig}).\end{aligned}\tag{2.27}$$

As noted by LeVeque [72], spurious wave speeds for discontinuities may be introduced when manipulating partial differential equations in this manner. However, this is not a problem here since the solid mass equation, which can be derived from first principles, is used to express Eqs. (2.7) and (2.9) in the form of Eqs. (2.26) and (2.27), respectively. In fact, it is shown in the following chapter that Eqs. (2.7) and (2.9) are already in standard characteristic form, and that the characteristics are solid particle paths. Furthermore, the corresponding characteristic fields are linearly degenerate; consequently, discontinuities in these characteristic fields propagate at speed $\hat{u}_2$. This result is also obtained by the formal discontinuity analysis given in the following chapter based on integral conservation expressions for Eqs. (2.26) and (2.27).

Equations (2.1-2.6), (2.8), (2.26), and (2.27) form a quasilinear system of nine first-order partial differential equations expressed in standard divergence form.

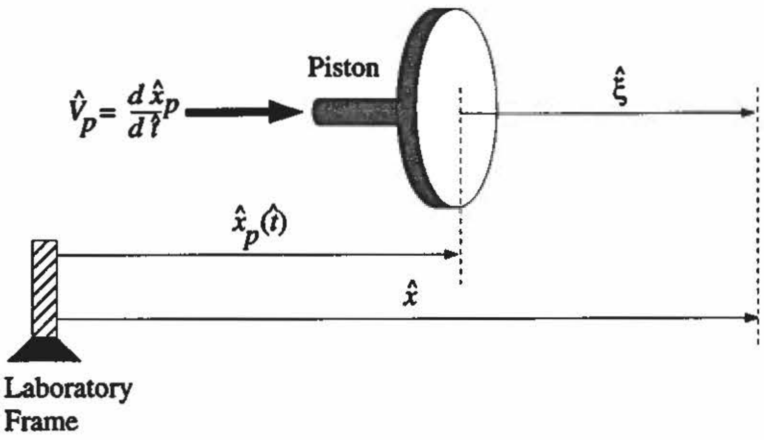

Figure 2.2: Schematic of the piston-attached coordinate system.

2.2 Transformation to the Piston-Attached Coordinate System

As this study models the transient development of planar two-phase detonation in response to energy input from a moving piston, it is convenient to transform the governing equations to a coordinate system which moves with the piston. The transformation from the laboratory coordinate system to the piston-attached coordinate system is illustrated in Fig. 2.2.

A general transformation of the independent variables $(\hat{x}, \hat{t}) \rightarrow (\hat{\xi}, \hat{\tau})$ is expressed by the following:

$$\hat{\xi} = \hat{\xi}(\hat{x}, \hat{t}), \qquad \hat{\tau} = \hat{\tau}(\hat{x}, \hat{t}). \tag{2.28}$$

Using this transformation, the following differential operators are derived by direct application of the chain rule:

$$\left.\frac{\partial}{\partial \hat{t}}\right|_{\hat{x}} = \left.\frac{\partial \hat{\xi}}{\partial \hat{t}}\right|_{\hat{x}} \left.\frac{\partial}{\partial \hat{\xi}}\right|_{\hat{\tau}} + \left.\frac{\partial \hat{\tau}}{\partial \hat{t}}\right|_{\hat{x}} \left.\frac{\partial}{\partial \hat{\tau}}\right|_{\hat{\xi}}, \tag{2.29}$$

$$\left.\frac{\partial}{\partial \hat{x}}\right|_{\hat{t}} = \left.\frac{\partial \hat{\xi}}{\partial \hat{x}}\right|_{\hat{t}} \left.\frac{\partial}{\partial \hat{\xi}}\right|_{\hat{\tau}} + \left.\frac{\partial \hat{\tau}}{\partial \hat{x}}\right|_{\hat{t}} \left.\frac{\partial}{\partial \hat{\tau}}\right|_{\hat{\xi}}. \tag{2.30}$$

If the piston position is a prescribed function of time, $\hat{x}_p(\hat{t})$, then its velocity is given by

$$\hat{v}_p(\hat{t}) \equiv \frac{d\hat{x}_p(\hat{t})}{d\hat{t}}. \tag{2.31}$$

For the transformation from the laboratory coordinate system to the piston-attached coordinate system, we have the following form for Eq. (2.28):

$$\hat{\xi} = \hat{x} - \hat{x}_p(\hat{t}), \qquad \hat{\tau} = \hat{t}. \tag{2.32}$$

Using these expressions, Eqs. (2.29) and (2.30) reduce to the following, respectively:

$$\left.\frac{\partial}{\partial \hat{t}}\right|_{\hat{x}} = -\hat{v}_p(\hat{\tau}) \left.\frac{\partial}{\partial \hat{\xi}}\right|_{\hat{\tau}} + \left.\frac{\partial}{\partial \hat{\tau}}\right|_{\hat{\xi}}, \tag{2.33}$$

$$\left.\frac{\partial}{\partial \hat{x}}\right|_{\hat{t}} = \left.\frac{\partial}{\partial \hat{\xi}}\right|_{\hat{\tau}}. \tag{2.34}$$

Additionally, both the gas velocity, $\hat{v}_1$, and the solid velocity, $\hat{v}_2$, measured relative to the piston-attached coordinate system are obtained by differentiating the first expression in Eq. (2.32) with respect to $\hat{t}$:

$$\hat{v}_i = \hat{u}_i - \hat{v}_p(\hat{\tau}) \qquad (i = 1, 2). \tag{2.35}$$

In this expression, $\hat{t}$ has been replaced in favor of $\hat{\tau}$.

Equations (2.33-2.35) are used to transform Eqs. (2.1-2.6), (2.8), (2.26), and (2.27) into the following equations valid in the piston-attached coordinate system:

$$\frac{\partial}{\partial \hat{\tau}}\left[\hat{\rho}_1\phi_1\right] + \frac{\partial}{\partial \hat{\xi}}\left[\hat{\rho}_1\phi_1\hat{v}_1\right] = \left(\frac{3}{\hat{r}}\right)\hat{\rho}_2\phi_2\hat{a}\hat{P}_1^m H(I - I_{ig}), \tag{2.36}$$

$$\begin{aligned} &\frac{\partial}{\partial \hat{\tau}}\left[\hat{\rho}_1\phi_1\hat{v}_1\right] + \frac{\partial}{\partial \hat{\xi}}\left[\hat{\rho}_1\phi_1\hat{v}_1^2 + \hat{P}_1\phi_1\right] \\ &\quad = \hat{v}_2\left(\frac{3}{\hat{r}}\right)\hat{\rho}_2\phi_2\hat{a}\hat{P}_1^m H(I - I_{ig}) + \hat{\beta}\frac{\phi_1\phi_2}{\hat{r}}\left(\hat{v}_2 - \hat{v}_1\right) - \hat{\rho}_1\phi_1\frac{d\hat{v}_p}{d\hat{\tau}}, \end{aligned} \tag{2.37}$$

$$\begin{aligned} &\frac{\partial}{\partial \hat{\tau}}\left[\hat{\rho}_1\phi_1\left(\hat{e}_1 + \frac{\hat{v}_1^2}{2}\right)\right] + \frac{\partial}{\partial \hat{\xi}}\left[\hat{\rho}_1\phi_1\hat{v}_1\left(\hat{e}_1 + \frac{\hat{v}_1^2}{2} + \frac{\hat{P}_1}{\hat{\rho}_1}\right)\right] \\ &\quad = \left(\hat{e}_2 + \frac{\hat{v}_2^2}{2}\right)\left(\frac{3}{\hat{r}}\right)\hat{\rho}_2\phi_2\hat{a}\hat{P}_1^m H(I - I_{ig}) + \hat{\beta}\frac{\phi_1\phi_2}{\hat{r}}\hat{v}_2\left(\hat{v}_2 - \hat{v}_1\right) \\ &\quad + \hat{h}\frac{\phi_1\phi_2}{\hat{r}^{1/3}}\left(\hat{T}_2 - \hat{T}_1\right) - \hat{\rho}_1\phi_1\hat{v}_1\frac{d\hat{v}_p}{d\hat{\tau}}, \end{aligned} \tag{2.38}$$

$$\frac{\partial}{\partial \hat{\tau}}\left[\hat{\rho}_2\phi_2\right] + \frac{\partial}{\partial \hat{\xi}}\left[\hat{\rho}_2\phi_2\hat{v}_2\right] = -\left(\frac{3}{\hat{r}}\right)\hat{\rho}_2\phi_2\hat{a}\hat{P}_1^m H(I - I_{ig}), \tag{2.39}$$

$$\begin{aligned}&\frac{\partial}{\partial\hat{\tau}}\left[\hat{\rho}_2\phi_2\hat{v}_2\right]+\frac{\partial}{\partial\hat{\xi}}\left[\hat{\rho}_2\phi_2\hat{v}_2^2+\hat{P}_2\phi_2\right]\\&\qquad=-\hat{v}_2\left(\frac{3}{\hat{r}}\right)\hat{\rho}_2\phi_2\hat{a}\hat{P}_1^m H(I-I_{ig})-\hat{\beta}\frac{\phi_1\phi_2}{\hat{r}}\left(\hat{v}_2-\hat{v}_1\right)-\hat{\rho}_2\phi_2\frac{d\hat{v}_p}{d\hat{\tau}},\end{aligned}\tag{2.40}$$

$$\begin{aligned}&\frac{\partial}{\partial\hat{\tau}}\left[\hat{\rho}_2\phi_2\left(\hat{e}_2+\frac{\hat{v}_2^2}{2}\right)\right]+\frac{\partial}{\partial\hat{\xi}}\left[\hat{\rho}_2\phi_2\hat{v}_2\left(\hat{e}_2+\frac{\hat{v}_2^2}{2}+\frac{\hat{P}_2}{\hat{\rho}_2}\right)\right]\\&\qquad=-\left(\hat{e}_2+\frac{\hat{v}_2^2}{2}\right)\left(\frac{3}{\hat{r}}\right)\hat{\rho}_2\phi_2\hat{a}\hat{P}_1^m H(I-I_{ig})-\hat{\beta}\frac{\phi_1\phi_2}{\hat{r}}\hat{v}_2\left(\hat{v}_2-\hat{v}_1\right)\\&\qquad-\hat{h}\frac{\phi_1\phi_2}{\hat{r}^{1/3}}\left(\hat{T}_2-\hat{T}_1\right)-\hat{\rho}_2\phi_2\hat{v}_2\frac{d\hat{v}_p}{d\hat{\tau}},\end{aligned}\tag{2.41}$$

$$\begin{aligned}&\frac{\partial}{\partial\hat{\tau}}\left[\hat{\rho}_2\phi_2^2\right]+\frac{\partial}{\partial\hat{\xi}}\left[\hat{\rho}_2\hat{v}_2\phi_2^2\right]\\&\qquad=\frac{\hat{\rho}_2\phi_1\phi_2^2}{\hat{\mu}_c}\left(\hat{P}_2-\hat{P}_1-\hat{f}\right)-2\left(\frac{3}{\hat{r}}\right)\hat{\rho}_2\phi_2^2\hat{a}\hat{P}_1^m H(I-I_{ig}),\end{aligned}\tag{2.42}$$

$$\frac{\partial\hat{n}}{\partial\hat{\tau}}+\frac{\partial}{\partial\hat{\xi}}\left[\hat{v}_2\hat{n}\right]=0,\tag{2.43}$$

$$\begin{aligned}&\frac{\partial}{\partial\hat{\tau}}\left[\hat{\rho}_2\phi_2 I\right]+\frac{\partial}{\partial\hat{\xi}}\left[\hat{\rho}_2\phi_2\hat{v}_2 I\right]\\&\qquad=\hat{k}_I\hat{\rho}_2\phi_2\left(1-I\right)\left[\frac{\hat{P}_1\phi_1+\hat{P}_2\phi_2-\hat{P}_{1o}\phi_{1o}-\hat{P}_{2o}\phi_{2o}}{\hat{P}_{1o}\phi_{1o}+\hat{P}_{2o}\phi_{2o}}\right]^2\exp\left[-\frac{\hat{T}_I}{\hat{T}_1\phi_1+\hat{T}_2\phi_2}\right]\\&\qquad-\left(\frac{3}{\hat{r}}\right)\hat{\rho}_2\phi_2 I\hat{a}\hat{P}_1^m H(I-I_{ig}).\end{aligned}\tag{2.44}$$

Here, the momentum equations, Eqs. (2.37) and (2.40), and the total energy equations, Eqs. (2.38) and (2.41), contain additional terms which account for the acceleration of the piston-attached coordinate system. The remaining equations, including Eqs. (2.10-2.16), Eqs. (2.23), and (2.24), are unaffected by the transformation.

2.3 Non-Dimensional Model Equations

The model equations can be non-dimensionalized by redefining both the independent and dependent variables in terms of the following dimensionless variables:

$$\xi = \frac{\hat{\xi}}{\hat{r}_o}, \quad \tau = \frac{\hat{\tau}}{\hat{r}_o/\hat{c}_{2o}}, \quad v_i = \frac{\hat{v}_i}{\hat{c}_{2o}}, \quad P_i = \frac{\hat{P}_i}{\hat{\rho}_{io}\hat{c}_{2o}^2}, \quad \rho_i = \frac{\hat{\rho}_i}{\hat{\rho}_{io}}, \quad e_i = \frac{\hat{e}_i}{\hat{c}_{2o}^2},$$

$$T_i = \frac{\hat{T}_i}{\hat{c}_{2o}^2/\hat{c}_{vio}}, \quad r = \frac{\hat{r}}{\hat{r}_o}, \quad n = \frac{\hat{n}}{1/\frac{4}{3}\pi\hat{r}_o^3}, \quad f = \frac{\hat{f}}{\hat{\rho}_{2o}\hat{c}_{2o}^2}, \qquad i = 1,2 \tag{2.45}$$

where $\hat{c}_{vio} = \left.\frac{\partial \hat{e}_i}{\partial \hat{T}_i}\right|_o$ are the specific heats at constant volume. The following non-dimensional equations result:

$$\frac{\partial}{\partial\tau}\left[\rho_1\phi_1\right] + \frac{\partial}{\partial\xi}\left[\rho_1\phi_1 v_1\right] = \frac{\pi_1}{\pi_5}\frac{\rho_2\phi_2 P_1^{\pi_4}}{r} H(I - \pi_{10}), \tag{2.46}$$

$$\begin{aligned}\frac{\partial}{\partial\tau}\left[\rho_1\phi_1 v_1\right] &+ \frac{\partial}{\partial\xi}\left[\rho_1\phi_1 v_1^2 + P_1\phi_1\right] \\ &= \frac{\pi_1}{\pi_5}\frac{v_2\rho_2\phi_2 P_1^{\pi_4}}{r} H(I - \pi_{10}) + \frac{\pi_2}{\pi_5}\frac{\phi_1\phi_2}{r}\left(v_2 - v_1\right) - \rho_1\phi_1\frac{dv_p}{d\tau},\end{aligned} \tag{2.47}$$

$$\begin{aligned}\frac{\partial}{\partial\tau}\left[\rho_1\phi_1\left(e_1 + \frac{v_1^2}{2}\right)\right] &+ \frac{\partial}{\partial\xi}\left[\rho_1\phi_1 v_1\left(e_1 + \frac{v_1^2}{2} + \frac{P_1}{\rho_1}\right)\right] \\ &= \frac{\pi_1}{\pi_5}\left(e_2 + \frac{v_2^2}{2}\right)\frac{\rho_2\phi_2 P_1^{\pi_4}}{r} H(I - \pi_{10}) + \frac{\pi_2}{\pi_5}\frac{\phi_1\phi_2}{r} v_2\left(v_2 - v_1\right) \\ &+ \frac{\pi_3}{\pi_5}\frac{\phi_1\phi_2}{r^{1/3}}\left(\pi_6 T_2 - T_1\right) - \rho_1\phi_1 v_1\frac{dv_p}{d\tau},\end{aligned} \tag{2.48}$$

$$\frac{\partial}{\partial\tau}\left[\rho_2\phi_2\right] + \frac{\partial}{\partial\xi}\left[\rho_2\phi_2 v_2\right] = -\pi_1\frac{\rho_2\phi_2 P_1^{\pi_4}}{r} H(I - \pi_{10}), \tag{2.49}$$

$$\begin{aligned}\frac{\partial}{\partial\tau}\left[\rho_2\phi_2 v_2\right] &+ \frac{\partial}{\partial\xi}\left[\rho_2\phi_2 v_2^2 + P_2\phi_2\right] \\ &= -\pi_1\frac{v_2\rho_2\phi_2 P_1^{\pi_4}}{r} H(I - \pi_{10}) - \pi_2\frac{\phi_1\phi_2}{r}\left(v_2 - v_1\right) - \rho_2\phi_2\frac{dv_p}{d\tau},\end{aligned} \tag{2.50}$$

$$\begin{aligned}\frac{\partial}{\partial\tau}\left[\rho_2\phi_2\left(e_2 + \frac{v_2^2}{2}\right)\right] &+ \frac{\partial}{\partial\xi}\left[\rho_2\phi_2 v_2\left(e_2 + \frac{v_2^2}{2} + \frac{P_2}{\rho_2}\right)\right] \\ &= -\pi_1\left(e_2 + \frac{v_2^2}{2}\right)\frac{\rho_2\phi_2 P_1^{\pi_4}}{r} H(I - \pi_{10}) - \pi_2\frac{\phi_1\phi_2}{r} v_2\left(v_2 - v_1\right) \\ &- \pi_3\frac{\phi_1\phi_2}{r^{1/3}}\left(\pi_6 T_2 - T_1\right) - \rho_2\phi_2 v_2\frac{dv_p}{d\tau},\end{aligned} \tag{2.51}$$

$$\begin{aligned}&\frac{\partial}{\partial \tau}\left[\rho_2\phi_2^2\right] + \frac{\partial}{\partial \xi}\left[\rho_2 v_2 \phi_2^2\right] \\ &\qquad = \pi_7\rho_2\phi_1\phi_2^2\left(P_2 - \pi_5 P_1 - f\right) - 2\pi_1\frac{\rho_2\phi_2^2 P_1^{\pi_4}}{r}H(I - \pi_{10}),\end{aligned} \tag{2.52}$$

$$\frac{\partial n}{\partial \tau} + \frac{\partial}{\partial \xi}\left[v_2 n\right] = 0, \tag{2.53}$$

$$\begin{aligned}&\frac{\partial}{\partial \tau}\left[\rho_2\phi_2 I\right] + \frac{\partial}{\partial \xi}\left[\rho_2\phi_2 v_2 I\right] \\ &\quad = \pi_8\rho_2\phi_2\left(1 - I\right)\left[\frac{\pi_5 P_1\phi_1 + P_2\phi_2 - \pi_5 P_{1o}\phi_{1o} - P_{2o}\phi_{2o}}{\pi_5 P_{1o}\phi_{1o} + P_{2o}\phi_{2o}}\right]^2 \exp\left[-\frac{\pi_9}{T_1\phi_1 + \pi_6 T_2\phi_2}\right] \\ &\quad -\pi_1\frac{\rho_2\phi_2 I P_1^{\pi_4}}{r}H(I - \pi_{10}),\end{aligned} \tag{2.54}$$

$$P_1 = P_1(\rho_1, T_1), \tag{2.55}$$

$$e_1 = e_1(\rho_1, T_1), \tag{2.56}$$

$$P_2 = P_2(\rho_2, T_2), \tag{2.57}$$

$$e_2 = e_2(\rho_2, T_2), \tag{2.58}$$

$$f = f(\phi_2), \tag{2.59}$$

$$n = \frac{\phi_2}{r^3}, \tag{2.60}$$

$$\phi_1 + \phi_2 = 1, \tag{2.61}$$

$$c_1^2 = \frac{P_1}{\rho_1}\Gamma_1 + \left.\frac{\partial P_1}{\partial \rho_1}\right|_{e_1}, \tag{2.62}$$

$$c_2^2 = \frac{P_2}{\rho_2}\Gamma_2 + \left.\frac{\partial P_2}{\partial \rho_2}\right|_{e_2}, \tag{2.63}$$

$$\Gamma_1 = \frac{1}{\rho_1}\left.\frac{\partial P_1}{\partial e_1}\right|_{\rho_1}, \tag{2.64}$$

$$\Gamma_2 = \frac{1}{\rho_2}\left.\frac{\partial P_2}{\partial e_2}\right|_{\hat{\rho}_1}. \tag{2.65}$$

Non-dimensional parameters contained in these equations are defined by the following:

$$\pi_1 = 3\hat{a}\hat{\rho}_{1o}^{m}\hat{c}_{2o}^{2m-1}, \quad \pi_2 = \frac{\hat{\beta}}{\hat{\rho}_{2o}\hat{c}_{2o}}, \quad \pi_3 = \frac{\hat{h}\hat{r}_o^{2/3}}{\rho_{2o}\hat{c}_{v1o}\hat{c}_{2o}}, \quad \pi_4 = m, \quad \pi_5 = \frac{\hat{\rho}_{1o}}{\hat{\rho}_{2o}},$$

$$\pi_6 = \frac{\hat{c}_{v1o}}{\hat{c}_{v2o}}, \quad \pi_7 = \frac{\hat{\rho}_{2o}\hat{c}_{2o}\hat{r}_o}{\hat{\mu}_c}, \quad \pi_8 = \frac{\hat{k}_I\hat{r}_o}{\hat{c}_{2o}}, \quad \pi_9 = \frac{\hat{T}_I\hat{c}_{v1o}}{\hat{c}_{2o}^2}, \quad \pi_{10} = I_{ig}.$$

The parameters π_1, π_2, π_3, π_7, and π_8 are ratios of the characteristic time associated with combustion, interphase drag, interphase heat transfer, material compaction, and ignition to the time required for acoustic waves in the ambient solid to propagate a distance of one particle radius. For this investigation, values for chosen these parameters vary substantially from case to case; thus, no simplifications are made based upon dimensional arguments. The parameters π_5 and π_6 are a consequence of the different characteristic densities, pressures, and temperatures used to non-dimensionalize the gas and solid thermodynamic variables. Though the value for π_5 is small for this study (~ 0.005), simplifications are not made based on the smallness of this parameter because the gas density for detonation conditions is several orders of magnitude higher than its ambient value; thus, the characteristic value used here for the gas density is misleading. The parameter π_6 is order one for this study. The parameter π_9 is a non-dimensional ignition parameter, and the parameters π_4 and π_{10} are defined for convenience.

3

CHARACTERISTICS ANALYSIS

A characteristics analysis of the model equations is given in this chapter. The purpose of this analysis is two-fold: 1) to classify the model equations and to characterize the solution behavior; and 2) to form the mathematical framework necessary for the construction of the high-resolution numerical method. Furthermore, results of this analysis are used to formulate appropriate boundary conditions for the problems investigated in this study. In Section 3.1, the model equations are classified, and the characteristic fields are identified. In Section 3.2, two-phase Rankine-Hugoniot relations are derived from the integral form of the model equations, and discontinuities admitted by the Rankine-Hugoniot relations are discussed.

3.1 Mathematical Classification

The model equations used in this study are most fundamentally posed as a system of integro-differential conservation relations:

$$\frac{d}{d\tau}\int_{\xi_1}^{\xi_2} \mathbf{q}(\xi,\tau)d\xi = \mathbf{f}(\mathbf{q}(\xi_1,\tau)) - \mathbf{f}(\mathbf{q}(\xi_2,\tau)) + \int_{\xi_1}^{\xi_2} \mathbf{g}(\mathbf{q}(\xi,\tau))d\xi, \tag{3.1}$$

where

$$\begin{aligned}\mathbf{q} = &\left[\rho_1\phi_1,\ \rho_1\phi_1 v_1,\ \rho_1\phi_1\left(e_1 + \frac{v_1^2}{2}\right),\ \rho_2\phi_2,\ \rho_2\phi_2 v_2,\right.\\ &\left.\rho_2\phi_2\left(e_2 + \frac{v_2^2}{2}\right),\ \rho_2\phi_2^2,\ n,\ \rho_2\phi_2 I\right]^T, \qquad (3.2)\\ \mathbf{f}(\mathbf{q}) = &\left[\rho_1\phi_1 v_1,\ \rho_1\phi_1 v_1^2 + P_1\phi_1,\ \rho_1\phi_1 v_1\left(e_1 + \frac{v_1^2}{2} + \frac{P_1}{\rho_1}\right),\ \rho_2\phi_2 v_2,\right.\\ &\left.\rho_2\phi_2 v_2^2 + P_2\phi_2,\ \rho_2\phi_2 v_2\left(e_2 + \frac{v_2^2}{2} + \frac{P_2}{\rho_2}\right),\ \rho_2 v_2\phi_2^2,\ v_2 n,\ \rho_2\phi_2 v_2 I\right]^T, \qquad (3.3)\end{aligned}$$

$$
\begin{aligned}
\mathbf{g}(\mathbf{q}) = \Bigg[& C_m,\ C_m v_2 + C_d - \rho_1\phi_1 \frac{dv_p}{d\tau},\ C_m\left(e_2 + \frac{v_2^2}{2}\right) + C_d v_2 + C_e \\
& -\rho_1\phi_1 v_1 \frac{dv_p}{d\tau},\ -\pi_5 C_m, -\pi_5 C_m v_2 - \pi_5 C_d - \rho_2\phi_2 \frac{dv_p}{d\tau}, \\
& -\pi_5 C_m\left(e_2 + \frac{v_2^2}{2}\right) - \pi_5 C_d v_2 - \pi_5 C_e - \rho_2\phi_2 v_2 \frac{dv_p}{d\tau}, \\
& \pi_7 \rho_2 \phi_1 \phi_2^2 \left(P_2 - \pi_5 P_1 - f\right) - 2\pi_5\phi_2 C_m,\ 0,\ \rho_2\phi_2 C_I - \pi_5 I C_m \Bigg]^T, \qquad (3.4)
\end{aligned}
$$

and

$$
\begin{aligned}
C_m &= \left(\frac{\pi_1}{\pi_5}\right) \frac{\rho_2\phi_2 P_1^{\pi_4}}{r} H(T_2 - \pi_8), \\
C_d &= \left(\frac{\pi_2}{\pi_5}\right) \frac{\phi_1\phi_2}{r} \left(v_2 - v_1\right), \\
C_e &= \left(\frac{\pi_3}{\pi_5}\right) \frac{\phi_1\phi_2}{r^{1/3}} \left(\pi_6 T_2 - T_1\right), \\
C_I &= \pi_8 \left(1 - I\right) \left[\frac{\pi_5 P_1\phi_1 + P_2\phi_2 - \pi_5 P_{1o}\phi_{1o} - P_{2o}\phi_{2o}}{\pi_5 P_{1o}\phi_{1o} + P_{2o}\phi_{2o}}\right]^2 \exp\left[-\frac{\pi_9}{T_1\phi_1 + \pi_6 T_2\phi_2}\right].
\end{aligned}
\qquad (3.5)
$$

Here, $\mathbf{q} \in \Re^9$ is the vector of conserved quantities, $\mathbf{f} \in \Re^9$ is the flux vector, and $\mathbf{g} \in \Re^9$ is the source vector ($\Re$ is the set of real numbers). Both $\mathbf{f}$ and $\mathbf{g}$ are vector valued functions of $\mathbf{q}$. The term $\frac{dv_p}{d\tau}$ in Eq. (3.4) is a known function of time.

Denoting the components of $\mathbf{q}$ by q_j ($j = 1, \ldots, 9$), Eq. (3.1) expresses that the time rate of change in the conserved quantity q_j within the fixed spatial interval $[\xi_1, \xi_2]$, where $\xi_1 < \xi_2$, equals the sum of the net flux of q_j into the interval, and the net production of q_j within the interval. Obviously, the conserved quantities for the mass, momentum, and energy of the gas and solid (q_1, q_2, q_3, q_4, q_5, and q_6, respectively) have physical meaning, as does the conserved quantity for the particle number density (q_8). However, the conserved quantities $\rho_2\phi_2^2$ and $\rho_2\phi_2 I$ (q_7 and q_8, respectively) have no physical meaning, and are treated in a conservative fashion solely for utility.

Assuming that $\mathbf{q}$ is continuous on the interval $[\xi_1, \xi_2]$, then

$$
\mathbf{f}(\mathbf{q}(\xi_1, \tau)) - \mathbf{f}(\mathbf{q}(\xi_2, \tau)) = -\int_{\xi_1}^{\xi_2} \frac{\partial \mathbf{f}(\mathbf{q})}{\partial \xi} d\xi.
$$

Substituting this expression into Eq. (3.1), moving the time derivative inside the integral (since both ξ_1 and ξ_2 are fixed), and collecting terms gives

$$\int_{\xi_1}^{\xi_2} \left[\frac{\partial \mathbf{q}}{\partial \tau} + \frac{\partial \mathbf{f}(\mathbf{q})}{\partial \xi} - \mathbf{g}(\mathbf{q}) \right] d\xi = 0. \tag{3.6}$$

This equation is generally satisfied only if the integrand identically vanishes. Thus, the following quasilinear system of partial differential equations are obtained:

$$\frac{\partial \mathbf{q}}{\partial \tau} + \frac{\partial \mathbf{f}(\mathbf{q})}{\partial \xi} = \mathbf{g}(\mathbf{q}). \tag{3.7}$$

This is the differential form of the model equations presented in the previous chapter.

We now perform a standard analysis [130] applicable to systems of first-order quasilinear partial differential equations in two independent variables to determine the mathematical classification of the model equations. The analysis requires that Eq. (3.7) be expressed in the following non-divergence form obtained by carrying out the differentiation of $\mathbf{f}$ with respect to ξ:

$$\frac{\partial \mathbf{q}}{\partial \tau} + \bar{\bar{\mathbf{A}}}(\mathbf{q}) \frac{\partial \mathbf{q}}{\partial \xi} = \mathbf{g}(\mathbf{q}), \tag{3.8}$$

where $\bar{\bar{\mathbf{A}}}$ is the 9×9 flux Jacobian matrix defined by

$$\bar{\bar{\mathbf{A}}} \equiv \frac{\partial \mathbf{f}}{\partial \mathbf{q}}. \tag{3.9}$$

If we denote the components of $\mathbf{f}$ by f_j $(j = 1, \ldots, 9)$, then $\bar{\bar{\mathbf{A}}}$ is given by

$$\bar{\bar{\mathbf{A}}} = \begin{bmatrix} \partial f_1/\partial q_1 & \partial f_1/\partial q_2 & \cdots & \partial f_1/\partial q_9 \\ \partial f_2/\partial q_1 & \partial f_2/\partial q_2 & \cdots & \partial f_2/\partial q_9 \\ \vdots & \vdots & & \vdots \\ \partial f_9/\partial q_1 & \partial f_9/\partial q_2 & \cdots & \partial f_9/\partial q_9 \end{bmatrix}. \tag{3.10}$$

For the construction of $\bar{\bar{\mathbf{A}}}$, it is necessary to first express ϕ_1, ρ_1, v_1, e_1, ϕ_2, ρ_2, v_2, e_2, n, and I as functions of $\mathbf{q}$. In particular, we have that

$$\begin{aligned} &\phi_1 = 1 - \frac{q_7}{q_4}, && \rho_1 = \frac{q_1}{1 - q_7/q_4}, && v_1 = \frac{q_2}{q_1}, && e_1 = \frac{q_3}{q_1} - \frac{1}{2}\left(\frac{q_2}{q_1}\right)^2, \\ &\phi_2 = \frac{q_7}{q_4}, && \rho_2 = \frac{q_4^2}{q_7}, && v_2 = \frac{q_5}{q_4}, && e_2 = \frac{q_6}{q_4} - \frac{1}{2}\left(\frac{q_5}{q_4}\right)^2, \\ &n = q_8, && I = \frac{q_9}{q_4}. \end{aligned} \tag{3.11}$$

Solving Eqs. (2.56) and (2.58) for T_1 and T_2, respectively, and substituting the results into Eqs. (2.55) and (2.57) gives the following functional dependencies for P_1 and P_2:

$$P_1 = P_1\left(\rho_1(\mathbf{q}), e_1(\mathbf{q})\right), \tag{3.12}$$

$$P_2 = P_2\left(\rho_2(\mathbf{q}), e_2(\mathbf{q})\right). \tag{3.13}$$

Given the expressions for ρ_1, e_1, ρ_2, and e_2 in Eq. (3.11), and using the functional dependencies of Eqs. (3.12) and (3.13), the derivatives $\left.\frac{\partial P_1}{\partial q_j}\right|_{q_{j'}(j' \neq j)}$ and $\left.\frac{\partial P_2}{\partial q_j}\right|_{q_{j'}(j' \neq j)}$ $(j, j' = 1, \ldots, 9)$, which are needed for the construction of $\bar{\bar{\mathbf{A}}}$, can be computed by direct application of the chain rule:

$$\left.\frac{\partial P_1}{\partial q_j}\right|_{q_{j'}(j' \neq j)} = \left.\frac{\partial P_1}{\partial \rho_1}\right|_{e_1} \left.\frac{\partial \rho_1}{\partial q_j}\right|_{q_{j'}(j' \neq j)} + \left.\frac{\partial P_1}{\partial e_1}\right|_{\rho_1} \left.\frac{\partial e_1}{\partial q_j}\right|_{q_{j'}(j' \neq j)}, \tag{3.14}$$

$$\left.\frac{\partial P_2}{\partial q_j}\right|_{q_{j'}(j' \neq j)} = \left.\frac{\partial P_2}{\partial \rho_2}\right|_{e_1} \left.\frac{\partial \rho_2}{\partial q_j}\right|_{q_{j'}(j' \neq j)} + \left.\frac{\partial P_2}{\partial e_2}\right|_{\rho_2} \left.\frac{\partial e_2}{\partial q_j}\right|_{q_{j'}(j' \neq j)}. \tag{3.15}$$

Explicit expressions for the derivatives $\left.\frac{\partial P_1}{\partial \rho_1}\right|_{e_1}$ and $\left.\frac{\partial P_1}{\partial e_1}\right|_{\rho_1}$, and $\left.\frac{\partial P_2}{\partial \rho_2}\right|_{e_1}$ and $\left.\frac{\partial P_2}{\partial e_2}\right|_{\rho_2}$ can be obtained when the gas and solid state relations are specified.

After performing the required calculations, the following expression is obtained for $\bar{\bar{\mathbf{A}}}$:

$$\bar{\bar{\mathbf{A}}} = \left[\begin{array}{ccc} 0 & 1 & 0 \\ c_1^2 - v_1^2 - (H_1 - v_1^2)\,\Gamma_1 & 2v_1 - v_1\Gamma_1 & \Gamma_1 \\ v_1\left(c_1^2 - H_1\right) - v_1\left(H_1 - v_1^2\right)\Gamma_1 & H_1 - v_1^2\Gamma_1 & v_1 + v_1\Gamma_1 \\ 0 & 0 & 0 \\ 0 & 0 & 0 \\ 0 & 0 & 0 \\ 0 & 0 & 0 \\ 0 & 0 & 0 \\ 0 & 0 & 0 \end{array} \right.$$

$$\left.\begin{array}{cccccc}
0 & 0 & 0 & 0 & 0 & 0 \\
-\rho_1\eta_1/\rho_2 & 0 & 0 & \rho_1\eta_1/\left(\rho_2\phi_2\right) & 0 & 0 \\
-v_1\rho_1\eta_1/\rho_2 & 0 & 0 & v_1\rho_1\eta_1/\left(\rho_2\phi_2\right) & 0 & 0 \\
0 & 1 & 0 & 0 & 0 & 0 \\
c_2^2 - v_2^2 - \left(H_2 - v_2^2\right)\Gamma_2 + \eta_2 & 2v_2 - v_2\Gamma_2 & \Gamma_2 & -\eta_2/\phi_2 & 0 & 0 \\
v_2\left(c_2^2 - v_2^2\right) - v_2\left(H_2 - v_2^2\right)\Gamma_2 + v_2\eta_2 & H_2 - v_2^2\Gamma_2 & v_2 + v_2\Gamma_2 & -v_2\eta_2/\phi_2 & 0 & 0 \\
-\phi_2 v_2 & \phi_2 & 0 & v_2 & 0 & 0 \\
-v_2 n/\left(\rho_2\phi_2\right) & n/\left(\rho_2\phi_2\right) & 0 & 0 & v_2 & 0 \\
-v_2 I & I & 0 & 0 & 0 & v_2
\end{array}\right] \tag{3.16}$$

In Eq. (3.16), the total enthalpies H_1 and H_2 are defined by

$$H_1 \equiv e_1 + \frac{v_1^2}{2} + \frac{P_1}{\rho_1}, \qquad H_2 \equiv e_2 + \frac{v_2^2}{2} + \frac{P_2}{\rho_2}. \tag{3.17}$$

Additionally, the following variables have been introduced for compactness:

$$\eta_1 \equiv c_1^2 - \left(\Gamma_1 + 1\right)\frac{P_1}{\rho_1}, \qquad \eta_2 \equiv c_2^2 - \left(\Gamma_2 + 1\right)\frac{P_2}{\rho_2}. \tag{3.18}$$

Here, it is noted that for a calorically perfect ideal gas and solid, $c_i^2 = \gamma_i \dfrac{P_i}{\rho_i}$ and $\Gamma_i = \gamma_i - 1$ $(i = 1, 2)$, where γ_i is the specific heat ratio; consequently, $\eta_{1,2} \equiv 0$. Terms in Eq. (3.16) corresponding to the derivatives of the mass, momentum, and energy flux components with respect to the conserved mass, momentum, and energy variables for each phase are similar in form to the derivatives given by Glaister [37] for a single phase system.

The classification of Eq. (3.8) requires that the eigenvalues and eigenvectors of $\bar{\bar{\mathbf{A}}}$ be computed. The eigenvalues and right eigenvectors of $\bar{\bar{\mathbf{A}}}$, $\lambda^{(j)}$ $(j = 1, \ldots, 9)$ and $\mathbf{r}^{(j)}$, respectively, are solutions of the eigenvalue problem

$$\bar{\bar{\mathbf{A}}} \cdot \mathbf{r}^{(j)} = \lambda^{(j)}\mathbf{r}^{(j)}. \tag{3.19}$$

Using matrix notation, the right eigenvalue problem can be concisely expressed as

$$\bar{\bar{\mathbf{A}}}\bar{\bar{\mathbf{R}}} = \bar{\bar{\mathbf{R}}}\bar{\bar{\mathbf{\Lambda}}}, \tag{3.20}$$

where $\bar{\bar{\mathbf{R}}}$ is the 9×9 matrix whose columns consist of the right eigenvectors, and $\bar{\bar{\mathbf{\Lambda}}}$ is the 9×9 diagonal matrix of eigenvalues, i.e.

$$\tilde{\tilde{\mathbf{R}}} \equiv \left[\mathbf{r}^{(1)}|\mathbf{r}^{(2)}|\cdots|\mathbf{r}^{(9)}\right], \qquad \tilde{\tilde{\mathbf{\Lambda}}} \equiv \begin{bmatrix} \lambda^{(1)} & 0 & \cdots & 0 \\ 0 & \lambda^{(2)} & \cdots & 0 \\ \vdots & \vdots & \ddots & \vdots \\ 0 & 0 & \cdots & \lambda^{(9)} \end{bmatrix}. \tag{3.21}$$

The eigenvalues are found to be

$$\begin{aligned} &\lambda^{(1)} = v_1, && \lambda^{(2)} = v_1 + c_1, && \lambda^{(3)} = v_1 - c_1, \\ &\lambda^{(4)} = v_2, && \lambda^{(5)} = v_2 + c_2, && \lambda^{(6)} = v_2 - c_2, \\ &\lambda^{(7)} = v_2, && \lambda^{(8)} = v_2, && \lambda^{(9)} = v_2, \end{aligned} \tag{3.22}$$

and the right eigenvectors are found to be

$$\mathbf{r}^{(1)} = \left[1,\ v_1,\ H_1 - c_1^2/\Gamma_1,\ 0,\ 0,\ 0,\ 0,\ 0,\ 0\right]^T, \tag{3.23}$$

$$\mathbf{r}^{(2)} = [1,\ v_1 + c_1,\ H_1 + v_1 c_1,\ 0,\ 0,\ 0,\ 0,\ 0,\ 0]^T, \tag{3.24}$$

$$\mathbf{r}^{(3)} = [1,\ v_1 - c_1,\ H_1 - v_1 c_1,\ 0,\ 0,\ 0,\ 0,\ 0,\ 0]^T, \tag{3.25}$$

$$\mathbf{r}^{(4)} = \left[0,\ 0,\ 0,\ 1,\ v_2,\ H_2 - c_2^2/\Gamma_2,\ \phi_2,\ 0,\ 0\right]^T, \tag{3.26}$$

$$\mathbf{r}^{(5)} = [0,\ 0,\ 0,\ 1,\ v_2 + c_2,\ H_2 + v_2 c_2,\ \phi_2,\ n/\left(\rho_2 \phi_2\right),\ I]^T, \tag{3.27}$$

$$\mathbf{r}^{(6)} = [0,\ 0,\ 0,\ 1,\ v_2 - c_2,\ H_2 - v_2 c_2,\ \phi_2,\ n/\left(\rho_2 \phi_2\right),\ I]^T, \tag{3.28}$$

$$\begin{aligned} \mathbf{r}^{(7)} = \Bigg[& \frac{\rho_1 \eta_1}{\rho_2 \phi_2 \left((v_2 - v_1)^2 - c_1^2\right)},\ \frac{\rho_1 \eta_1 v_2}{\rho_2 \phi_2 \left((v_2 - v_1)^2 - c_1^2\right)}, \\ & \frac{\rho_1 \eta_1 \left(H_1 + v_1 v_2 - v_1^2\right)}{\rho_2 \phi_2 \left((v_2 - v_1)^2 - c_1^2\right)},\ 0,\ 0,\ \frac{\eta_2}{\phi_2 \Gamma_2},\ 1,\ 0,\ 0 \Bigg]^T, \end{aligned} \tag{3.29}$$

$$\mathbf{r}^{(8)} = [0,\ 0,\ 0,\ 0,\ 0,\ 0,\ 0,\ 1,\ 0]^T, \tag{3.30}$$

$$\mathbf{r}^{(9)} = [0,\ 0,\ 0,\ 0,\ 0,\ 0,\ 0,\ 0,\ 1]^T. \tag{3.31}$$

The left eigenvectors of $\tilde{\tilde{\mathbf{A}}}$, $\mathbf{l}^{(j)}$ $(j = 1, \ldots, 9)$, are solutions of the eigenvalue problem

$$\mathbf{l}^{(j)} \cdot \tilde{\tilde{\mathbf{A}}} = \lambda^{(j)} \mathbf{l}^{(j)}. \tag{3.32}$$

Using matrix notation, the left eigenvalue problem can be concisely expressed as

$$\tilde{\tilde{\mathbf{L}}} \tilde{\tilde{\mathbf{A}}} = \tilde{\tilde{\mathbf{\Lambda}}} \tilde{\tilde{\mathbf{L}}}, \tag{3.33}$$

where $\bar{\bar{\mathbf{L}}}$ is the 9×9 matrix whose rows consists of the left eigenvectors, i.e.

$$\bar{\bar{\mathbf{L}}} \equiv \begin{bmatrix} \mathbf{l}^{(1)} \\ \mathbf{l}^{(2)} \\ \vdots \\ \mathbf{l}^{(9)} \end{bmatrix}. \tag{3.34}$$

Solving each of Eqs. (3.20) and (3.33) for $\bar{\bar{\mathbf{A}}}$, and equating the resulting expressions gives

$$\bar{\bar{\mathbf{R}}}\bar{\bar{\Lambda}}\bar{\bar{\mathbf{R}}}^{-1} = \bar{\bar{\mathbf{L}}}^{-1}\bar{\bar{\Lambda}}\bar{\bar{\mathbf{L}}}.$$

This equation is identically satisfied if we take $\bar{\bar{\mathbf{L}}} = \bar{\bar{\mathbf{R}}}^{-1}$. Consequently, the left eigenvectors are orthonormal to the right eigenvectors since

$$\bar{\bar{\mathbf{L}}}\bar{\bar{\mathbf{R}}} = \bar{\bar{\mathbf{R}}}\bar{\bar{\mathbf{L}}} = \bar{\bar{\mathbf{I}}},$$

where $\bar{\bar{\mathbf{I}}}$ is the 9×9 identity matrix. The left eigenvectors are given by

$$\mathbf{l}^{(1)} = \frac{1}{c_1^2}\left[\left(H_1 - v_1^2\right)\Gamma_1,\ v_1\Gamma_1,\ -\Gamma_1,\ 0,\ 0,\ 0,\ 0,\ 0,\ 0\right], \tag{3.35}$$

$$\begin{aligned}\mathbf{l}^{(2)} = \frac{1}{2c_1^2}\Bigl[&-\left(H_1 - v_1^2\right)\Gamma_1 + c_1\left(c_1 - v_1\right),\ c_1 - v_1\Gamma_1,\ \Gamma_1, \\ &\frac{\rho_1\eta_1 c_1}{\rho_2\left(v_2 - \left(v_1 + c_1\right)\right)},\ 0,\ 0,\ -\frac{\rho_1\eta_1 c_1}{\rho_2\phi_2\left(v_2 - \left(v_1 + c_1\right)\right)},\ 0,\ 0\Bigr],\end{aligned} \tag{3.36}$$

$$\begin{aligned}\mathbf{l}^{(3)} = \frac{1}{2c_1^2}\Bigl[&-\left(H_1 - v_1^2\right)\Gamma_1 + c_1\left(c_1 + v_1\right),\ -c_1 - v_1\Gamma_1,\ \Gamma_1, \\ &-\frac{\rho_1\eta_1 c_1}{\rho_2\left(v_2 - \left(v_1 - c_1\right)\right)},\ 0,\ 0,\ \frac{\rho_1\eta_1 c_1}{\rho_2\phi_2\left(v_2 - \left(v_1 - c_1\right)\right)},\ 0,\ 0\Bigr],\end{aligned} \tag{3.37}$$

$$\mathbf{l}^{(4)} = \frac{1}{c_2^2}\left[0,\ 0,\ 0,\ \left(H_2 - v_2^2\right)\Gamma_2 - \eta_2,\ v_2\Gamma_2,\ -\Gamma_2,\ \eta_2/\phi_2,\ 0,\ 0\right], \tag{3.38}$$

$$\begin{aligned}\mathbf{l}^{(5)} = \frac{1}{2c_2^2}\Bigl[&0,\ 0,\ 0,\ -\left(H_2 - v_2^2\right)\Gamma_2 + c_2\left(c_2 - v_2\right) + \eta_2,\ c_2 - v_2\Gamma_2, \\ &\Gamma_2,\ -\eta_2/\phi_2,\ 0,\ 0\Bigr],\end{aligned} \tag{3.39}$$

$$\begin{aligned}\mathbf{l}^{(6)} = \frac{1}{2c_2^2}\Bigl[&0,\ 0,\ 0,\ -\left(H_2 - v_2^2\right)\Gamma_2 + c_2\left(c_2 + v_2\right) + \eta_2,\ -c_2 - v_2\Gamma_2, \\ &\Gamma_2,\ -\eta_2/\phi_2,\ 0,\ 0\Bigr],\end{aligned} \tag{3.40}$$

$$\mathbf{l}^{(7)} = \left[0,\ 0,\ 0,\ -\phi_2,\ 0,\ 0,\ 1,\ 0,\ 0\right], \tag{3.41}$$

$$\mathbf{l}^{(8)} = \frac{n}{\rho_2\phi_2c_2^2}\Big[0,\ 0,\ 0,\ \left(H_2 - v_2^2\right)\Gamma_2 - c_2^2 - \eta_2,\ v_2\Gamma_2,\ -\Gamma_2,$$
$$\eta_2/\phi_2,\ \rho_2\phi_2c_2^2/n,\ 0\Big], \tag{3.42}$$

$$\mathbf{l}^{(9)} = [0,\ 0,\ 0,\ -I,\ 0,\ 0,\ 0,\ 0,\ 1]. \tag{3.43}$$

Each grouping $(\lambda, \mathbf{r}, \mathbf{l})^{(j)}$ $(j = 1, \ldots, 9)$ is associated with a different mode of wave propagation. In particular, $(\lambda, \mathbf{r}, \mathbf{l})^{(1)}$, $(\lambda, \mathbf{r}, \mathbf{l})^{(2)}$, and $(\lambda, \mathbf{r}, \mathbf{l})^{(3)}$ are associated with the propagation of entropy waves, forward traveling acoustic waves, and backward traveling acoustic waves in the gas, respectively; $(\lambda, \mathbf{r}, \mathbf{l})^{(4)}$, $(\lambda, \mathbf{r}, \mathbf{l})^{(5)}$, and $(\lambda, \mathbf{r}, \mathbf{l})^{(6)}$ are associated with the propagation of entropy waves, forward traveling acoustic waves, and backward traveling acoustic waves in the solid, respectively; and $(\lambda, \mathbf{r}, \mathbf{l})^{(7)}$, $(\lambda, \mathbf{r}, \mathbf{l})^{(8)}$, and $(\lambda, \mathbf{r}, \mathbf{l})^{(9)}$ are associated with the propagation of infinitesimal disturbances in the volume fraction, the particle number density, and the ignition variable, respectively.

Following Zauderer [130], a system of equations having the form of Eq. (3.8) is classified as strictly hyperbolic if for each ξ, τ, and $\mathbf{q}$, the eigenvalues of $\bar{\bar{\mathbf{A}}}$ are real and distinct; in this case, the right eigenvectors are linearly independent. If the eigenvalues are real but not distinct, then the system of equations is non-strictly hyperbolic provided that the right eigenvectors are linearly independent. In the event that the eigenvalues are real but not distinct, and the right eigenvectors are not linearly independent, then the system of equations is parabolic.

Since the eigenvalues given by Eq. (3.22) are real but not distinct, the model equations constitute a non-strictly hyperbolic system provided that the right eigenvectors [Eqs. (3.23-3.30)] are linearly independent. Linear independence requires that the right eigenvector matrix $\bar{\bar{\mathbf{R}}}$ be non-singular or, equivalently, that its inverse exists [1]. Inspection of $\bar{\bar{\mathbf{R}}}^{-1}$ $(= \bar{\bar{\mathbf{L}}})$, whose rows consist of the left eigenvectors [Eqs. (3.35-3.42)], indicates that the right eigenvectors are linearly independent except at the singular points $\phi_2 = 0$ and $v_2 = v_1 \pm c_1$.

For $\phi_2 = 0$, it is seen that the forward and backward acoustic eigenvectors for the solid, $\mathbf{r}^{(5)}$ and $\mathbf{r}^{(6)}$ respectively, degenerate (upon proper scaling) into the particle number density eigenvector $\mathbf{r}^{(8)}$:

$$\lim_{\phi_2 \to 0}\left[\frac{\rho_2\phi_2}{n}\mathbf{r}^{(5)}\right] = \lim_{\phi_2 \to 0}\left[\frac{\rho_2\phi_2}{n}\mathbf{r}^{(6)}\right] = \mathbf{r}^{(8)}. \tag{3.44}$$

The time-dependent analysis performed in this study does not formally consider the limit $\phi_2 \to 0$; rather, the singularity is avoided by terminating combustion when the solid volume fraction reaches a specified minimum value. As such, the solid particles are assumed to have an inert core of small diameter. It is noted that this complete combustion singularity also exists in the steady-state model given in Chapter 6 and, within the context of that model, is shown to be inconsequential.

For $v_2 = v_1 + c_1$ and $v_2 = v_1 - c_1$, it is seen that the compaction eigenvector $\mathbf{r}^{(7)}$ degenerates (upon proper scaling) into the forward and backward acoustic eigenvectors of the gas, $\mathbf{r}^{(2)}$ and $\mathbf{r}^{(3)}$, respectively:

$$\lim_{v_2 \to v_1 + c_1}\left[\frac{\rho_2\phi_2\left((v_2 - v_1)^2 - c_1^2\right)}{\rho_1\eta_1}\mathbf{r}^{(7)}\right] = \mathbf{r}^{(2)}, \tag{3.45}$$

$$\lim_{v_2 \to v_1 - c_1}\left[\frac{\rho_2\phi_2\left((v_2 - v_1)^2 - c_1^2\right)}{\rho_1\eta_1}\mathbf{r}^{(7)}\right] = \mathbf{r}^{(3)}. \tag{3.46}$$

Inspection of Eqs. (3.36) and (3.37) shows that the sonic singularities, corresponding to $v_2 = v_1 \pm c_1$, are removed for $\eta_1 \equiv 0$; as mentioned earlier, this condition results if a calorically perfect ideal equation of state is used for the gas. In this case, $\mathbf{r}^{(7)}$ reduces to

$$\mathbf{r}^{(7)}_{IG} = [0,\ 0,\ 0,\ 0,\ 0,\ \eta_2/(\phi_2\Gamma_2),\ 1,\ 0,\ 0]^T.$$

Thus, for $\eta_1 \neq 0$, the model equations constitute a non-strictly hyperbolic system of equations which contain a parabolic degeneracy on the manifolds $\phi_2 = 0$ and $v_2 = v_1 \pm c_1$ in phase space.

Similar singularities have been identified in the two-phase model proposed by Baer and Nunziato [5]; a detailed discussion is given by Embid and Baer [31]. The physical interpretation of these singular points is unclear. Embid and Baer suggest that the sonic singularities arise since, at the pore level, two-phase granular flow is analogous to flow in a moving duct of variable cross-sectional area; a choked flow condition is reached when the relative flow is sonic. Furthermore, it is suggested by Embid and Baer that nonlinear resonant interactions between the compaction mode, $(\lambda, \mathbf{r}, \mathbf{l})^{(7)}$, and the related gas acoustic mode, $(\lambda, \mathbf{r}, \mathbf{l})^{(2)}$ or $(\lambda, \mathbf{r}, \mathbf{l})^{(3)}$, may occur near these singular points; such resonant interactions are discussed by Isaacson and Temple [53] for a general inhomogeneous system of conservation laws. Based on this premise, Embid et al. [32], and Embid and Majda [33] developed and analyzed an asymptotic model describing transition to detonation in granulated reactive solids. It is demonstrated in Reference [33] that the asymptotic model does predict the development of resonant gas acoustic hot spots which may influence the DDT process.

When the model equations are hyperbolic (i.e., for $\phi_2 \neq 0$ and $v_2 \neq v_1 \pm c_1$), it is possible to express them in characteristic form [130]. As such, the governing partial differential equations can be reduced to ordinary differential equations describing the evolution of the two-phase system along characteristic curves in the ξ-τ plane. The characteristic form of the governing equations is summarized in Appendix B.

Having identified the characteristic fields, it is possible to classify them as genuinely nonlinear or linearly degenerate [68, 69, 87]. As shown in Appendix C, the gas entropy field, $(\lambda, \mathbf{r}, \mathbf{l})^{(1)}$, the solid entropy field, $(\lambda, \mathbf{r}, \mathbf{l})^{(4)}$, the compaction field, $(\lambda, \mathbf{r}, \mathbf{l})^{(7)}$, the number density field, $(\lambda, \mathbf{r}, \mathbf{l})^{(8)}$, and the ignition field, $(\lambda, \mathbf{r}, \mathbf{l})^{(9)}$, are linearly degenerate fields. The gas acoustic fields, $(\lambda, \mathbf{r}, \mathbf{l})^{(2)}$ and $(\lambda, \mathbf{r}, \mathbf{l})^{(3)}$, and the solid acoustic fields, $(\lambda, \mathbf{r}, \mathbf{l})^{(5)}$ and $(\lambda, \mathbf{r}, \mathbf{l})^{(6)}$, are genuinely nonlinear fields provided that $\left.\frac{\partial^2 P_1}{\partial \mu_1^2}\right|_{s_1} \neq 0$ and $\left.\frac{\partial^2 P_2}{\partial \mu_2^2}\right|_{s_2} \neq 0$, where μ_1 and μ_2 are the non-dimensional specific volume of the gas and solid. Each of these conditions is identical to the requirement for genuinely nonlinear acoustic fields for the Euler equations of gas dynamics [28, 132]. For the gas and solid equations of state used in this study, $\left.\frac{\partial^2 P_1}{\partial \mu_1^2}\right|_{s_1} > 0$ and $\left.\frac{\partial^2 P_2}{\partial \mu_2^2}\right|_{s_2} > 0$, respectively; consequently, the state relations satisfy the standard convexity condition of gas dynamics [28], and the gas and solid acoustic fields are genuinely nonlinear. Both shock waves and rarefaction waves can occur in genuinely nonlinear fields. Though neither shocks nor rarefaction waves can occur in linearly degenerate fields, contact discontinuities are admitted [72]. Discontinuous solutions of the model equations are discussed in the following section.

Lastly, it is mentioned that the initial value problem for strictly hyperbolic systems is well-posed (i.e., a unique solution exists which depends continuously on the initial data), and the solution behavior is well-characterized [54, 68, 130]. However, the same cannot be generally said for non-strictly hyperbolic systems having parabolic degeneracies [57, 58, 114]. For such systems, a general criterion for well-posedness does not exists, and the solution behavior can be very complicated. Some of these issues relevant to the solution of the two-phase Riemann problem are discussed in the following chapter.

3.2 Discontinuous Solutions

Continuous single-valued solutions of hyperbolic equations may not exist for all time [54, 68, 123]. In order to assure that the solutions remain single-valued, discontinuities are introduced at locations where the continuous solutions become multi-valued; the resulting piecewise continuous solutions are referred to as a weak solutions [54]. Weak solutions of the two-phase model equations are addressed in this section. The analysis given here closely follows that given in Reference [123] for systems of conservation laws having the form of Eq. (3.7) for arbitrary $\mathbf{q}$, $\mathbf{f}$, and $\mathbf{g}$.

Here, we consider a discontinuity propagating to the right at speed $D \equiv \dfrac{d\xi_s}{d\tau}$; a simple illustration is given in Fig. 3.1. The discontinuity is located at $\xi_s(\tau)$, where $\xi_1 < \xi_s(\tau) < \xi_2$. The locations ξ_1 and ξ_2 are assumed fixed for purposes of this analysis. The differential form of the conservation equations [Eq. (3.7)] is formally valid only in regions where $\mathbf{q}$ has continuous first derivatives, i.e. in the regions $\xi_1 < \xi_s^-(\tau)$ and $\xi_s^+(\tau) < \xi_2$, where $\xi_s^-(\tau)$ and $\xi_s^+(\tau)$ are the locations immediately to the left and

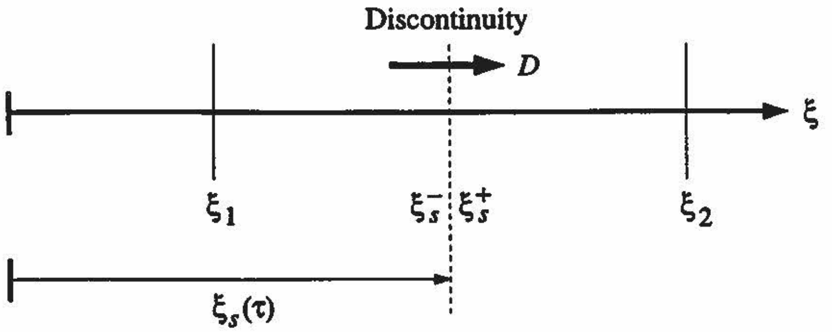

Figure 3.1: Illustration of a propagating discontinuity in the two-phase material.

right of the discontinuity, respectively. Therefore, it is necessary to consider the more fundamental integral form of the equations in order to properly define expressions which connect the continuous solutions at the discontinuity. The integral form of the equations only requires that $\mathbf{q}$ be integrable and, therefore, places no restrictions on the differentiability of $\mathbf{q}$.

To this end, we return to the integral form of model equations given by Eq. (3.1). With the assumption that both $\mathbf{q}$ and its first derivatives are continuous over the intervals $\xi_1 \leq \xi < \xi_s(\tau)$ and $\xi_s(\tau) < \xi \leq \xi_2$, and that their limits are bounded as $\xi \to \xi_s(\tau)$ from either side of the discontinuity, Eq. (3.1) can be rewritten as

$$\begin{aligned}\frac{d}{d\tau}\int_{\xi_1}^{\xi_s(\tau)} \mathbf{q}(\xi,\tau)d\xi + \frac{d}{d\tau}\int_{\xi_s(\tau)}^{\xi_2} \mathbf{q}(\xi,\tau)d\xi &= \mathbf{f}(\mathbf{q}(\xi_1,\tau)) - \mathbf{f}(\mathbf{q}(\xi_2,\tau)) \\ &+ \int_{\xi_1}^{\xi_s(\tau)} \mathbf{g}(\mathbf{q}(\xi,\tau))d\xi + \int_{\xi_s(\tau)}^{\xi_2} \mathbf{g}(\mathbf{q}(\xi,\tau))d\xi.\end{aligned} \tag{3.47}$$

Using Leibnitz's rule, the terms on the left hand side of this equation can be expressed as

$$\begin{aligned}\frac{d}{d\tau}\int_{\xi_1}^{\xi_s(\tau)} \mathbf{q}(\xi,\tau)d\xi &= \mathbf{q}(\xi_s^-,\tau)D + \int_{\xi_1}^{\xi_s(\tau)} \frac{\partial}{\partial\tau}\mathbf{q}(\xi,\tau)d\xi, \\ \frac{d}{d\tau}\int_{\xi_s(\tau)}^{\xi_2} \mathbf{q}(\xi,\tau)d\xi &= -\mathbf{q}(\xi_s^+,\tau)D + \int_{\xi_s(\tau)}^{\xi_2} \frac{\partial}{\partial\tau}\mathbf{q}(\xi,\tau)d\xi,\end{aligned}$$

where $\mathbf{q}(\xi_s^\pm,\tau)$ are the values of $\mathbf{q}(\xi,\tau)$ as $\xi \to \xi_s^\pm(\tau)$. Substituting these expressions into Eq. (3.47), and taking the limit as $\xi_1 \to \xi_s^-$ and $\xi_2 \to \xi_s^+$, results in the following (since all of the remaining integrals vanish in this limit):

$$[\mathbf{q}]_-^+ D = [\mathbf{f}]_-^+, \tag{3.48}$$

where the notation $[\;]_-^+$ denotes a jump in the enclosed quantity across the discontinuity, i.e.

$$[\mathbf{q}]_-^+ = \mathbf{q}(\xi_s^-, \tau) - \mathbf{q}(\xi_s^+, \tau),$$
$$[\mathbf{f}]_-^+ = \mathbf{f}(\mathbf{q}(\xi_s^-, \tau)) - \mathbf{f}(\mathbf{q}(\xi_s^+, \tau)).$$

Equation (3.48) constitutes a coupled system of nonlinear algebraic equations which must be satisfied across any *mathematically* admissible discontinuity. These algebraic jump relations are commonly referred to as Rankine-Hugoniot relations. It is noted that the expressions given by Eq. (3.48) are trivially satisfied for $\mathbf{q}(\xi_s^-, \tau) = \mathbf{q}(\xi_s^+, \tau)$.

Substituting the expressions given by Eqs. (3.2) and (3.3) into Eq. (3.48), expanding the resulting expressions, and regrouping terms gives the following Rankine-Hugoniot relations for the two-phase system:

$$[\rho_1 \phi_1 (v_1 - D)]_-^+ = 0, \tag{3.49}$$

$$\left[\rho_1 \phi_1 (v_1 - D)^2 + P_1 \phi_1\right]_-^+ = 0, \tag{3.50}$$

$$\left[\rho_1 \phi_1 (v_1 - D) \left(e_1 + \frac{(v_1 - D)^2}{2} + \frac{P_1}{\rho_1}\right)\right]_-^+ = 0, \tag{3.51}$$

$$[\rho_2 \phi_2 (v_2 - D)]_-^+ = 0, \tag{3.52}$$

$$\left[\rho_2 \phi_2 (v_2 - D)^2 + P_2 \phi_2\right]_-^+ = 0, \tag{3.53}$$

$$\left[\rho_2 \phi_2 (v_2 - D) \left(e_2 + \frac{(v_2 - D)^2}{2} + \frac{P_2}{\rho_2}\right)\right]_-^+ = 0, \tag{3.54}$$

$$\left[\rho_2 \phi_2^2 (v_2 - D)\right]_-^+ = 0, \tag{3.55}$$

$$[n (v_2 - D)]_-^+ = 0, \tag{3.56}$$

$$[\rho_2 \phi_2 I (v_2 - D)]_-^+ = 0. \tag{3.57}$$

In order to completely determine the jumps in all gas and solid quantities across a discontinuity propagating at speed D, the gas and solid state to either side of the discontinuity must be known, and the two-phase Rankine-Hugoniot relations must be supplemented by the state relations $P_1 = P_1(\rho_1, e_1)$ and $P_2 = P_2(\rho_2, e_2)$, and the saturation condition $\phi_1 + \phi_1 = 1$. Weak solutions of the model equations satisfy Eq. (3.7) in continuous regions, and satisfy Eqs. (3.49-3.58) across discontinuities.

Weak solutions of hyperbolic systems are not unique. For example, in gas dynamics it is possible to obtain two mathematically correct weak solutions for an expanding gas resulting from certain discontinuous initial data [132]: 1) a continuous rarefaction wave, and 2) a discontinuous "rarefaction shock." In order to determine the physically relevant solution, one must appeal to the second law of thermodynamics which asserts that the change in entropy resulting from any physically admissible thermodynamic process be non-negative. For the continuous rarefaction, it is determined that the gas entropy is constant throughout the wave; consequently, the second law of thermodynamics is trivially satisfied for this case. However, for the rarefaction shock, it is determined that the change in gas entropy across the shock is negative; consequently, the second law is violated and the rarefaction shock is non-physical. Thus, it is necessary to supplement the Rankine-Hugoniot relations with a criterion for identifying *physically* admissible discontinuities. One hopes that the use of such a criterion will identify a unique solution of the initial-value problem; in practice this is usually the case.

A similar entropy criterion has been proposed Embid and Baer [31] for determining physically relevant discontinuities admitted by Eqs. (3.49-3.56). This criterion asserts that the entropy of the mixture be non-decreasing across a discontinuity. Using an approach similar to that used above to define the two-phase Rankine-Hugoniot relations, it is possible to obtain the following entropy criterion from Eq. (2.20):

$$[\rho_1 \phi_1 s_1 (v_1 - D) + \rho_2 \phi_2 s_2 (v_2 - D)]_-^+ \geq 0. \tag{3.58}$$

This criterion does not require that the entropy of each phase be non-decreasing across a discontinuity. Rather, it only requires that the sum of the change in gas and solid entropy be non-decreasing.

A brief discussion of discontinuities admitted by Eqs. (3.49-3.58) will now be given.

To this end, two broad classes of discontinuities are identified: 1) discontinuities across which there exists no jump in volume fraction, (i.e., $[\phi_1]_-^+ = [\phi_2]_-^+ = 0$), and 2) discontinuities across which there does exists a jump in volume fraction (i.e., $[\phi_1]_-^+ = -[\phi_2]_-^+ \neq 0$). For purposes of this discussion, it is assumed that the ignition variable is everywhere continuous (i.e., $[I]_-^+ = 0$).

3.2.1 Discontinuities With a Continuous Volume Fraction

For $\phi_2^- = \phi_2^+ = \phi_2$ (thus, $\phi_1^- = \phi_1^+ = \phi_1$), Eqs. (3.49-3.58) reduce to the following:

$$[\rho_1 (v_1 - D)]_-^+ = 0, \tag{3.59}$$

$$\left[\rho_1 (v_1 - D)^2 + P_1\right]_-^+ = 0, \tag{3.60}$$

$$\left[\rho_1 (v_1 - D) \left(e_1 + \frac{(v_1 - D)^2}{2} + \frac{P_1}{\rho_1}\right)\right]_-^+ = 0, \tag{3.61}$$

$$[\rho_2 (v_2 - D)]_-^+ = 0, \tag{3.62}$$

$$\left[\rho_2 (v_2 - D)^2 + P_2\right]_-^+ = 0, \tag{3.63}$$

$$\left[\rho_2 (v_2 - D) \left(e_2 + \frac{(v_2 - D)^2}{2} + \frac{P_2}{\rho_2}\right)\right]_-^+ = 0, \tag{3.64}$$

$$[\phi_2]_-^+ = 0, \tag{3.65}$$

$$[n (v_2 - D)]_-^+ = 0, \tag{3.66}$$

$$[I]_-^+ = 0, \tag{3.67}$$

$$\phi_1 [\rho_1 s_1 (v_1 - D)]_-^+ + \phi_2 [\rho_2 s_2 (v_2 - D)]_-^+ \geq 0. \tag{3.68}$$

Since Eqs. (3.59-3.61) are decoupled from Eqs. (3.62-3.64), they can be independently solved for the jumps in the gas and solid quantities across the discontinuity, respectively, provided that the wave speed, the state to either side of the discontinuity, and the state relations $P_1 = P_1(\rho_1, e_1)$ and $P_2 = P_2(\rho_2, e_2)$ are specified. Furthermore, each set of decoupled equations is identical to the classical Rankine-Hugoniot relations for a single phase system [28]. Once Eqs. (3.62-3.64) are solved for the jump in v_2, then Eq. (3.66) can be solved for the jump in n. The entropy condition, Eq. (3.68), is used to determine if the discontinuity is physically admissible.

Type	*Gas*	*Solid*	*Admissibility Condition* [based on Eq. (3.68)]
(i)	shock	continuous	$D > v_1^+ + c_1^+$
(ii)	continuous	shock	$D > v_2^+ + c_2^+$
(iii)	contact discontinuity	continuous	$D = v_1^- = v_1^+$
(iv)	continuous	contact discontinuity	$D = v_2^- = v_2^+$
(v)	shock	shock	$D > \max[v_1^+ + c_1^+, v_2^+ + c_2^+]$
(vi)	shock	contact discontinuity	$D = v_2^- = v_2^+ > v_1^+ + c_1^+$
(vii)	contact discontinuity	shock	$D = v_1^- = v_1^+ > v_2^+ + c_2^+$
(viii)	contact discontinuity	contact discontinuity	$D = v_1^- = v_1^+ = v_2^- = v_2^+$

TABLE 3.1: DISCONTINUITIES HAVING A CONTINUOUS VOLUME FRACTION ADMITTED BY THE TWO-PHASE RANKINE-HUGONIOT RELATIONS

The different types of discontinuities admitted by Eqs. (3.59-3.68) are listed in TABLE 3.1. Each of these discontinuities is of classical type since the jump relations for the gas and solid are identical to the classical Rankine-Hugoniot relations for a single-phase system. Also listed in TABLE 3.1 are admissibility conditions for each type of discontinuity based on Eq. (3.68). For the purpose of discussing these discontinuities, we assume that the discontinuity is propagating to the right, and that the right-hand state is known; similar results hold for a left-propagating discontinuity with the state to the left of the discontinuity known.

First, there exist discontinuities associated with one phase only; as such, quantities associated with the second phase remain continuous. These discontinuities include compression shocks [types (i) and (ii)] and contact discontinuities [types (iii) and (iv)] which are identical to those predicted in gas dynamics. Across a compression shock, there exists an increase in the magnitude of all thermodynamic variables, and the velocity, of the shocked phase. Quantities associated with a shocked gas are nontrivial solutions of Eqs. (3.59-3.61), and quantities associated with a shocked solid are nontrivial solutions of Eqs. (3.62-3.66). Results from classical shock wave theory show that the inequalities $[\rho_i s_i(v_i - D)]_-^+ > 0$ (here, $i = 1, 2$ correspond to shocks in the gas and solid, respectively) are satisfied for right-propagating shocks having speeds $D > v_i^+ + c_i^+$ [28, 132]. Consequently, for shocks in the gas, the first term in Eq. (3.68) is positive (since ϕ_1 is non-negative), and the second term vanishes since the solid flow is continuous. A similar result holds for shocks in the solid.

Contact discontinuities, which separate states having different density and temperature, propagate at speed $D = v_i$ ($i = 1, 2$); consequently, there is no gas/solid mass flux through a gas/solid contact discontinuity. For contact discontinuities in the gas, $D = v_1$, Eqs. (3.59) and (3.61) are trivially satisfied, and Eq. (3.60) reduces to $[P_1]_-^+ = 0$. Similarly, for contact discontinuities in the solid, $D = v_2$, Eqs. (3.62), (3.64), and (3.66) are trivially satisfied, and Eq. (3.63) reduces to $[P_2]_-^+ = 0$. Thus, pressure and velocity are constant across contact discontinuities. Furthermore, for contact discontinuities in the gas, the first term in Eq. (3.68) is trivially satisfied since $D = v_1$, as is the second term in this equation since the solid flow is continuous. A similar result holds for contact discontinuities in the solid.

There also exist discontinuities which affect both the gas and solid. In particular, it is possible to have compound discontinuities consisting of 1) a shock in each phase [type (v)], 2) a shock in one phase and a contact discontinuity in the other [types (vi) and (vii)], or 3) a contact discontinuity in each phase [type (viii)]. In each case, Eq. (3.68) is satisfied since each term in this equation is either zero for a contact discontinuity or positive for a shock. Boundary and initial conditions necessary for the evolution of these discontinuities are unknown. Though such discontinuities do not violate the entropy criterion, the existence of these waves is dependent upon their hydrodynamic stability.

Lastly, since the equations of state used in this study satisfy the convexity condition described in Appendix C, the classical entropy criterion proposed by Lax [69] can be used to identify physically inadmissible discontinuities. This criterion asserts

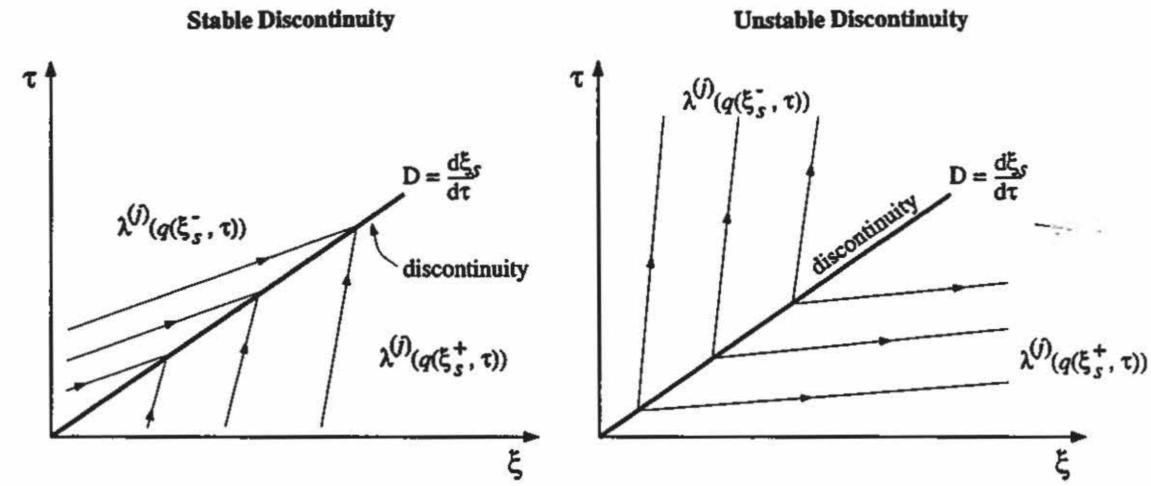

Figure 3.2: Examples of a stable and unstable discontinuity in the j^{th} characteristic field.

that a discontinuity in the j^{th} characteristic field is physically admissible if

$$\lambda^{(j)}(\mathbf{q}(\xi_s^-,\tau)) \geq D \geq \lambda^{(j)}(\mathbf{q}(\xi_s^+,\tau)), \tag{3.69}$$

where the $\lambda^{(j)}$ $(j = 1,\ldots,9)$ are given by Eqs. (3.22). The equality corresponds to contact discontinuities occurring in linearly degenerate fields. This criterion is based on stability arguments. A discontinuity in the j^{th} characteristic field is deemed stable if the characteristics to the left and right of the discontinuity converge into the discontinuity; otherwise, the discontinuity is deemed unstable. Based on this reasoning, rarefaction shocks are unstable, and compression shocks are stable. This idea is illustrated in Fig. 3.2 for a discontinuity in the j^{th} characteristic field. We use this entropy criterion with the high-resolution numerical method formulated in the following chapter to identify physically inadmissible rarefaction shocks predicted by the approximate solution of the two-phase Riemann problem.

3.2.2 Discontinuities With a Jump in Volume Fraction

Here, we consider discontinuities for which $[\phi_2]_-^+ \neq 0$. As shown in the following chapter, these discontinuities naturally arise from two-phase Riemann problems having an initial discontinuity in volume fraction. To analyze these discontinuities, Eq.

(3.52) is first used to re-express Eq. (3.55) as

$$\left\{\rho_2^-\phi_2^-\left(v_2^- - D\right) - \rho_2^+\phi_2^+\left(v_2^+ - D\right)\right\}[\phi_2]_-^+ = 0.$$

From this expression it is seen that if $[\phi_2]_-^+ \neq 0$, then $\rho_2^-\phi_2^-(v_2^- - D) = \rho_2^+\phi_2^+(v_2^+ - D)$. This requirement is satisfied for $D = v_2^- = v_2^+ = v_2$; consequently, discontinuities for which $[\phi_2]_-^+ \neq 0$ propagate at the local particle velocity of the solid. Though not given here, a similar analysis can be performed to show that discontinuities for which $[I]_-^+ \neq 0$ also propagate at the local particle velocity of the solid.

For $D = v_2$, Eqs. (3.49-3.58) reduce to the following:

$$[\rho_1\phi_1(v_1 - v_2)]_-^+ = 0, \tag{3.70}$$

$$\left[\rho_1\phi_1(v_1 - v_2)^2 + P_1\phi_1\right]_-^+ = 0, \tag{3.71}$$

$$\left[\rho_1\phi_1(v_1 - v_2)\left(e_1 + \frac{(v_1 - v_2)^2}{2} + \frac{P_1}{\rho_1}\right)\right]_-^+ = 0, \tag{3.72}$$

$$[v_2]_-^+ = 0, \tag{3.73}$$

$$[P_2\phi_2]_-^+ = 0, \tag{3.74}$$

$$[\rho_1\phi_1(v_1 - v_2)s_1]_-^+ \geq 0. \tag{3.75}$$

Discontinuities admitted by these relations are of non-classical type since Eqs. (3.70-3.74) depend upon volume fraction. Inspection of Eqs. (3.73) and (3.74) indicates that a non-classical contact discontinuity is associated with the solid. Though v_2 is constant across this discontinuity, a jump in P_2 is predicted. Furthermore, the change in P_2 is inversely proportional to the change in ϕ_2 since $\frac{P_2^+}{P_2^-} = \frac{\phi_2^-}{\phi_2^+}$. This result differs from classical theory in that no jump in pressure is predicted across a classical contact discontinuity. Given the change in P_2, the jumps in ρ_2 and e_2 are constrained by the solid state relation $P_2 = P_2(\rho_2, e_2)$.

It is seen from Eqs. (3.70-3.72) that the jump in gas quantities across the discontinuity is dependent upon both the wave speed, v_2, and the jump in ϕ_1. A simple solution of these equations is obtained if a calorically perfect, ideal equation of state is used for the gas. The solution is given by

$$[\rho_1\phi_1]_-^+ = 0, \qquad [v_1]_-^+ = 0, \qquad [P_1\phi_1]_-^+ = 0, \qquad [e_1]_-^+ = 0.$$

As such, $\frac{\rho_1^+}{\rho_1^-} = \frac{P_1^+}{P_1^-} = \frac{\phi_1^-}{\phi_1^+}$, $v_1 = v_1^- = v_1^+$, and $e_1 = e_1^- = e_1^+$. Given the change in ϕ_1 across the discontinuity (i.e., $\frac{\phi_1^-}{\phi_1^+}$), and the gas state to either side of the discontinuity, then the gas state to the opposite side is fixed. For instance, given the ideal state relation $P_1 = (\gamma_1 - 1)\rho_1 e_1$, we have that

$$\frac{P_1^+}{P_1^-} = \frac{(\gamma_1 - 1)\rho_1^+ e_1^+}{(\gamma_1 - 1)\rho_1^- e_1^-} = \frac{\rho_1^+ e_1}{\rho_1^- e_1} = \frac{\rho_1^+}{\rho_1^-} = \frac{\phi_1^-}{\phi_1^+}.$$

Here, we have used the result $e_1 = e_1^- = e_1^+$. This solution will not generally exists for arbitrary state relations. For this solution, Eq. (3.75) reduces to $(v_1 - v_2)[s_1]_-^+ \geq 0$. Since the jump in s_1 is dependent upon the jump in both ρ_1 and P_1, and since the quantity $(v_1 - v_2)$ may be either positive or negative, this inequality will not be satisfied for all possible conditions. If this inequality is not satisfied, then the discontinuity is physically inadmissible, and an alternative solution should be considered.

The gas may also be associated with non-classical shocks and contact discontinuities. The gas shocks are non-trivial solutions of Eqs. (3.70-3.72). Since the shocked state is also dependent upon the jump in ϕ_1, Eq. (3.75) will not be satisfied for all possible conditions. For non-classical gas contact discontinuities, $v_1 = v_2$, Eq. (3.70) and (3.72) are trivially satisfied, and Eq. (3.71) reduces to $[P_1\phi_1]_-^+ = 0$. Equation (3.75) is trivially satisfied in this case.

4

NUMERICAL METHOD

A high-resolution numerical method for solving the unsteady two-phase model equations is formulated in this chapter. Due to the hyperbolicity of the model equations, a minimum requirement of any numerical method used to solve these equations is the ability to accurately capture discontinuities. Several shock-capturing methods have been developed for solving the Euler equations of gas dynamics which have nominally second-order (or higher) spatial accuracy in regions of continuous flow, and can accurately capture discontinuities without the generation of spurious oscillations. Numerical methods having this property are collectively termed high-resolution methods. Many of the high-resolution methods for the Euler equations are based on Godunov's approach which requires the exact or approximate solution of Riemann problems in order to advance the solution in time. The method formulated in this chapter is also based on Godunov's approach, and is similar to the well-developed methods for the Euler equations.

This chapter is divided into three sections. In Section 4.1, the upwind numerical method used to solve the equations governing nonlinear convection in the gas and solid is formulated. Since this transport mechanism is responsible for the evolution of discontinuities in the gas and solid, it is important that the upwind method accurately predict convection effects. This is especially important for problems involving local processes such as combustion, interphase drag, interphase heat transfer, and material compaction. Spurious oscillations near discontinuities can greatly affect these local processes resulting in severe numerical inaccuracies. In Section 4.2, the numerical method used to solve the equations governing the local phase interaction processes is formulated, and the numerical splitting technique used to couple this method with the upwind method for non-linear convection is given. Lastly, the initial and boundary conditions used in this study are given in Section 4.3.

4.1 Numerical Solution of Two-Phase Convection

In this section, a numerical method for solving the following initial-value problem (IVP) for $\mathbf{q} \in \Re^9$ is formulated:

$$\frac{\partial \mathbf{q}}{\partial \tau} + \frac{\partial \mathbf{f}(\mathbf{q})}{\partial \xi} = 0, \tag{4.1}$$

$$\mathbf{q}(\xi, 0) = \mathbf{q}_o(\xi), \tag{4.2}$$

where $\mathbf{f}: \Re^9 \to \Re^9$, $\xi \in (-\infty, \infty)$, and $\tau \in [0, \infty)$. This system of equations, obtained by setting $\mathbf{g}(\mathbf{q}) \equiv 0$ in Eq. (3.7), governs nonlinear convection in the gas and solid. The initial-boundary-value problem (IBVP) for $\xi \in [0, \infty)$ involving the moving piston is addressed in Section 4.3.

A variety of high-resolution numerical methods have been developed for solving nonlinear hyperbolic systems of conservation laws having the general form of Eq. (4.1). These methods are typically based on either 1) the explicit use of artificial viscosity [70, 120], 2) flux-corrected transport (FCT) [19, 20, 129], or 3) Godunov's methodology [12, 40]. A description of the artificial viscosity and FCT methods is given in the cited references, and is not given here. Godunov's methodology, which forms the basis of the numerical method used in this study, is discussed in the following subsection. The reader is referred to Reference [113] for a comprehensive discussion of the merits of these various methods.

Regardless of the numerical method used to solve Eq. (4.1), it is required that it be expressed in the following conservative form so that the correct propagation speeds of discontinuities are predicted [72]:

$$\mathbf{Q}_k^{n+1} = \mathbf{Q}_k^n - \frac{\Delta \tau}{\Delta \xi} \left[\mathbf{F}_{k+1/2}(\mathbf{Q}^n) - \mathbf{F}_{k-1/2}(\mathbf{Q}^n) \right]. \tag{4.3}$$

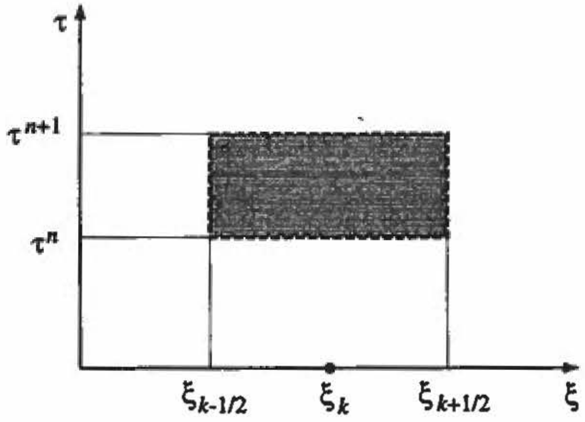

Figure 4.1: Computational rectangle in the ξ-τ plane.

Here, it is assumed that the spatial domain is discretized into uniformly spaced nodes located at the points ξ_k $(k = 1, 2, \ldots)$. Each node is located at the center of a computational cell of width $\Delta\xi$. The location of the left and right boundaries of the k^{th} cell are denoted as $\xi_{k-1/2}$ and $\xi_{k+1/2}$, respectively. The vector quantities $\mathbf{Q}_k^n$ and $\mathbf{Q}_k^{n+1}$ are numerical approximations for $\mathbf{q}$ at times τ^n and $\tau^{n+1} = \tau^n + \Delta\tau$, respectively, where $\Delta\tau$ is a small time increment. The vector quantities $\mathbf{F}_{k\pm1/2}$, which are dependent upon $\mathbf{Q}^n$, are numerical approximations for $\mathbf{f}$ at the cell boundaries $\xi_{k\pm1/2}$. The three classes of high-resolution methods mentioned above differ only in the way $\mathbf{F}_{k+1/2}$ is defined. Numerical methods which can be expressed in the form of Eq. (4.3) fall into the general category of finite-volume methods.

To illustrate the conservative character of Eq. (4.3), we integrate Eq. (4.1) over the domain $[\xi_{k-1/2}, \xi_{k+1/2}] \times [\tau^n, \tau^{n+1}]$ shown in Figure 4.1 to obtain

$$\begin{aligned}\int_{\xi_{k-1/2}}^{\xi_{k+1/2}} \mathbf{q}(\xi, \tau^{n+1})d\xi - \int_{\xi_{k-1/2}}^{\xi_{k+1/2}} \mathbf{q}(\xi, \tau^n)d\xi \\ + \int_{\tau^n}^{\tau^{n+1}} \mathbf{f}(\mathbf{q}(\xi_{k+1/2}, \tau))d\tau - \int_{\tau^n}^{\tau^{n+1}} \mathbf{f}(\mathbf{q}(\xi_{k-1/2}, \tau))d\tau = 0.\end{aligned} \tag{4.4}$$

Here, the spatial increment $\xi_{k-1/2} \leq \xi \leq \xi_{k+1/2}$ defines a single computational cell centered about the location ξ_k. Next, we define the quantities $\bar{\mathbf{q}}_k^{n+1}$ and $\bar{\mathbf{q}}_k^n$ to be the spatially averaged values of $\mathbf{q}$ contained within the computational cell at times τ^{n+1} and τ^n, respectively, and $\bar{\mathbf{f}}_{k-1/2}$ and $\bar{\mathbf{f}}_{k+1/2}$ to be the temporally averaged fluxes through the left and right computational cell boundaries during the time interval $[\tau^n, \tau^{n+1}]$, respectively:

$$\bar{\mathbf{q}}_k^{n+1} \equiv \frac{1}{\Delta\xi}\int_{\xi_{k-1/2}}^{\xi_{k+1/2}} \mathbf{q}(\xi, \tau^{n+1})d\xi, \qquad \bar{\mathbf{q}}_k^{n} \equiv \frac{1}{\Delta\xi}\int_{\xi_{k-1/2}}^{\xi_{k+1/2}} \mathbf{q}(\xi, \tau^{n})d\xi,$$
$$\bar{\mathbf{f}}_{k-1/2} \equiv \frac{1}{\Delta\tau}\int_{\tau^n}^{\tau^{n+1}} \mathbf{f}(\mathbf{q}(\xi_{k-1/2}, \tau))d\tau, \qquad \bar{\mathbf{f}}_{k+1/2} \equiv \frac{1}{\Delta\tau}\int_{\tau^n}^{\tau^{n+1}} \mathbf{f}(\mathbf{q}(\xi_{k+1/2}, \tau))d\tau. \tag{4.5}$$

Substituting these definitions into Eq. (4.4) and rearranging terms gives

$$\bar{\mathbf{q}}_k^{n+1} = \bar{\mathbf{q}}_k^{n} - \frac{\Delta\tau}{\Delta\xi}\left[\bar{\mathbf{f}}_{k+1/2} - \bar{\mathbf{f}}_{k-1/2}\right]. \tag{4.6}$$

Comparing this expression with Eq. (4.3), it is seen that $\mathbf{Q}_k^n$ and $\mathbf{Q}_k^{n+1}$ can be interpreted as averages of the conserved quantities contained within the k^{th} cell at times τ^{n+1} and τ^n, respectively. Similarly, $\mathbf{F}_{k-1/2}$ and $\mathbf{F}_{k+1/2}$ can be interpreted as average fluxes through the computational cell boundaries over the time interval $[\tau^n, \tau^{n+1}]$.

4.1.1 Godunov's Methodology and the Two-Phase Riemann Problem

The methodology formulated by Godunov [40] directly accounts for local wave propagation information within the framework of a conservative numerical method; as such, it constitutes an upwind conservative method. Here, an upwind method refers to one in which the solution is computed in a directionally-biased manner based on the direction of flow of characteristic information [72]. Though Godunov's methodology was originally developed for the Euler equations, it can be generalized to hyperbolic systems of conservation laws such as that given by Eq. (4.1).

In Godunov's methodology, local wave propagation information is provided by the solution of Riemann problems at computational cell boundaries. Mathematically, the two-phase Riemann problem is defined as the IVP given by Eq. (4.1) with the discontinuous initial data

$$\mathbf{q}_o(\xi) = \begin{cases} \mathbf{q}_L & \text{for } \xi < 0 \\ \mathbf{q}_R & \text{for } \xi > 0, \end{cases} \tag{4.7}$$

where $\mathbf{q}_L$ and $\mathbf{q}_R$ are constant states to the left and right of the discontinuity. Physically, this problem can be realized in part by partitioning a two-phase mixture in a tube using a thin diaphragm. The thermodynamic state to the left of the diaphragm is prepared in such a way that it is different from the state to the right. For instance, the two-phase mixture to the left of the diaphragm can be pressurized and heated, and the mixture to the right of the diaphragm can be maintained at the ambient pressure and temperature. Also, it is possible to prepare the mixtures such that they have different solid volume fractions and/or particle sizes. The diaphragm is then suddenly removed, resulting in a series of waves being formed which act to drive the system to a new equilibrium. This problem is a two-phase equivalent of the classical gas shock-tube problem [28]. The physical problem would certainly involve phase interaction processes such as drag, heat transfer, and material compaction, and would also involve diffusive transport of mass, momentum, and energy within each phase; however, the mathematical problem posed here ignores these processes. Though the mathematical solution of this problem has not been studied in detail, a few general comments can be made concerning its behavior. As such, we first discuss the solution of the two-phase Riemann problem in the following four paragraphs, and give the details of Godunov's methodology at the end of this subsection.

The various waves which comprise a typical solution of the two-phase Riemann problem are shown in the ξ-τ diagram of Fig. 4.2. Here, it is assumed that both the gas and solid pressure associated with the state $\mathbf{q}_L$ are higher than that associated with the state $\mathbf{q}_R$. The initial discontinuity is located at $\xi = 0$, and the solution evolves for $\tau > 0$. The resulting waves separate regions having different constant states. Due to the absence of phase interaction processes, physical diffusion, and physical boundaries, the solution has a self-similar form; e.g., it can be expressed as a function of the similarity variable ξ/τ. Associated with each phase is a shock, a contact discontinuity (entropy wave), and a rarefaction (expansion wave). The shocks,

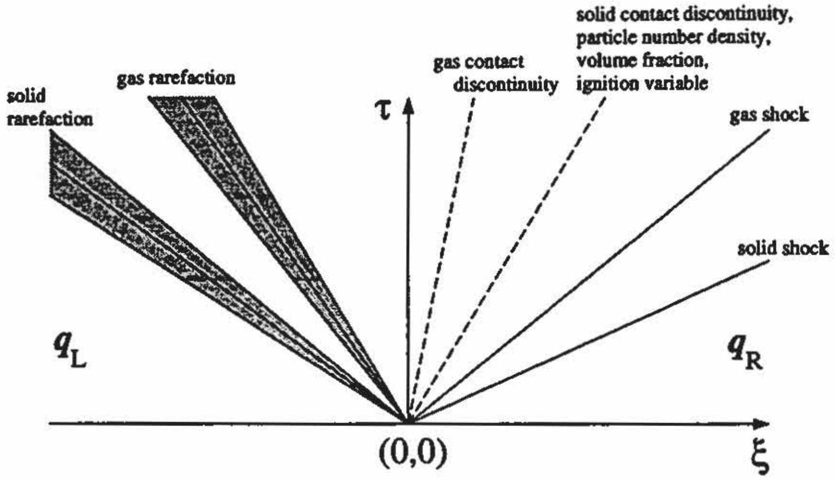

Figure 4.2: Sketch of a typical solution of the two-phase Riemann problem.

which are driven by the high pressure state $\mathbf{q}_L$, propagate to the right into the low pressure region. The shocks are followed by right-propagating contact discontinuities which separate regions having different entropy. Since the gas and solid entropy are constant through their respective rarefactions, the gas and solid entropy to the left of their respective contact discontinuities are associated with the state $\mathbf{q}_L$, while the gas and solid entropy to the right of the contact discontinuities are associated with the shocked gas and solid states. Also, a discontinuity in particle number density advects with the solid contact discontinuity, as does the initial discontinuity in the volume fraction and the ignition variable (if a jump in the volume fraction and the ignition variable is prescribed across the initial discontinuity). Rarefactions, which propagate to the left into the high pressure region, continuously expand the gas and solid from the state $\mathbf{q}_L$ to the constant states to the left of their respective contact discontinuities.

An exact solution of the two-phase Riemann problem for a calorically perfect ideal gas and solid $[\hat{P}_1 = \hat{\rho}_1\hat{R}_1\hat{T}_1$, $\hat{e}_1 = \hat{c}_{v1}\hat{T}_1$; $\hat{P}_2 = \hat{\rho}_2\hat{R}_2\hat{T}_2$, $\hat{e}_2 = \hat{c}_{v2}\hat{T}_2]$ is shown in Fig. 4.3. These state relations were chosen solely for simplicity, as the exact solution can be easily constructed for this case [51]. The initial conditions and model parameters used to construct this solution are given in TABLE 4.1. No jump in volume fraction

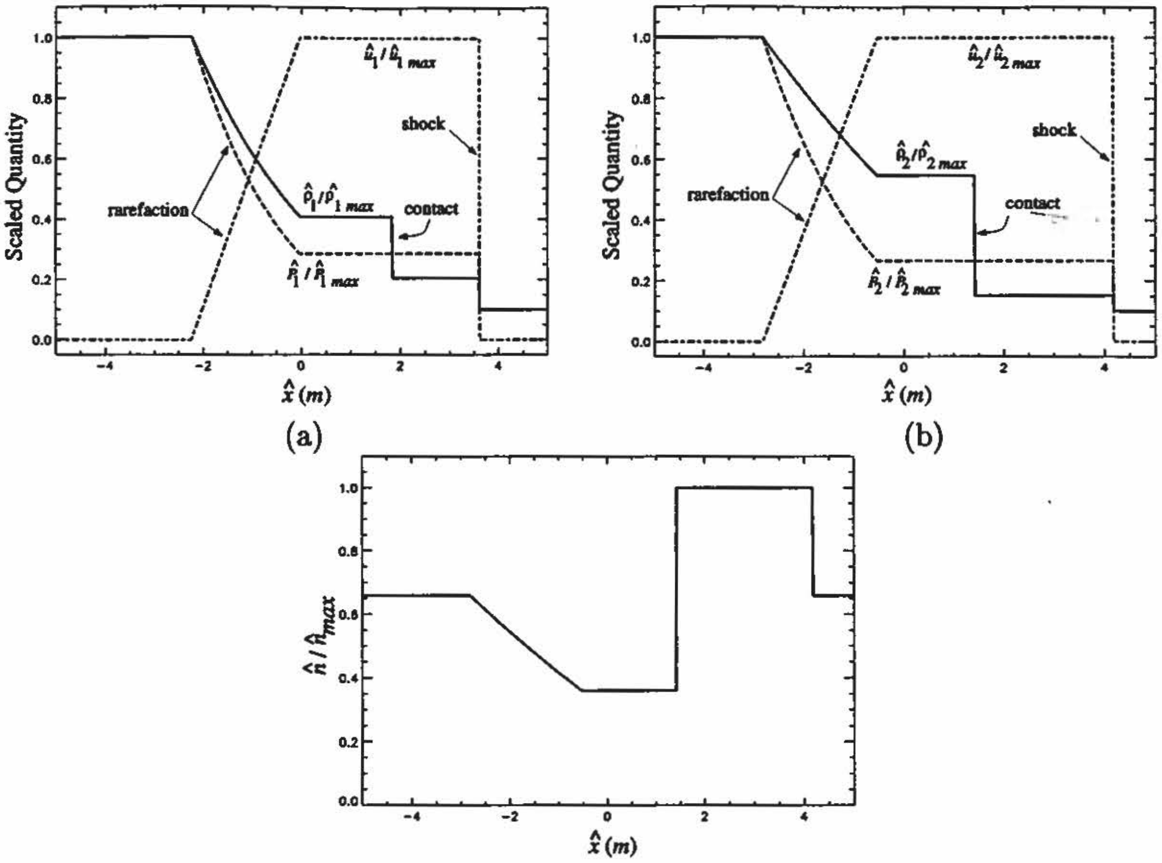

(a) (b)

(c)

Figure 4.3: Exact solution of the two-phase Riemann problem for a calorically perfect ideal gas and solid at $\hat{\tau} = 6\ ms$: (a) gas quantities; (b) solid quantities; and (c) particle number density. ($\hat{\rho}_{1max} = \hat{\rho}_{2max} = 10\ kg/m^3$, $\hat{P}_{1max} = \hat{P}_{2max} = 1\ MPa$, $\hat{u}_{1max} = 307.3\ m/s$, $\hat{u}_{2max} = 237.4\ m/s$, $\hat{n}_{max} = 1.81 \times 10^{11}$ particles/m^3.)

was prescribed across the initial discontinuity; as such, volume fraction is constant for all time, and the gas and solid evolution equations decouple. Factoring ϕ_1 and ϕ_2 from the gas and solid evolution equations of Eq. (4.1) results in equations for each phase which are identical to the Euler equations. Thus, the solution of the Riemann problem for each phase is given by the classical solution of the Riemann problem for a single-phase system [28]. The initial discontinuity, which separates the high pressure region on the left from the low pressure region on the right, was located at $\hat{x} = 0\ m$ at $\hat{\tau} = 0\ ms$ (it is assumed that $\hat{x} = \hat{\xi}$ for present purposes).

The solution for each phase, shown in Figs. 4.3(a,b) at time $\hat{\tau} = 6\ ms$, consists

Parameter or Initial Condition	Value	Units
$\hat{c}_{v1}$	7.18×10^2	$J/(kg\ K)$
$\hat{c}_{v2}$	2.39×10^2	$J/(kg\ K)$
$\hat{R}_1$	2.87×10^2	$J/(kg\ K)$
$\hat{R}_2$	2.87×10^2	$J/(kg\ K)$
$\hat{u}_{1L}$	0	m/s
$\hat{u}_{2L}$	0	m/s
$\hat{u}_{1R}$	0	m/s
$\hat{u}_{2R}$	0	m/s
$\hat{\rho}_{1L}/\hat{\rho}_{1R}$	1.00×10^1	
$\hat{\rho}_{2L}/\hat{\rho}_{2R}$	1.00×10^1	
ϕ_{2L}/ϕ_{2R}	1.00×10^0	
$\hat{P}_{1L}/\hat{P}_{1R}$	1.00×10^1	
$\hat{P}_{2L}/\hat{P}_{2R}$	1.00×10^1	
$\hat{n}_L/\hat{n}_R$	1.00×10^0	

TABLE 4.1: PARAMETER VALUES AND INITIAL CONDITIONS USED FOR THE SHOCK TUBE PROBLEM

of a right-propagating shock, followed by a right-propagating contact discontinuity, and a left-propagating rarefaction. Across the gas shock, there exists a jump in $\hat{\rho}_1$, $\tilde{u}_1$, $\hat{P}_1$, and $\hat{T}_1$ (the solution for $\hat{T}_1$ is not shown in the figure). Across the solid shock there exists a jump in $\tilde{\rho}_2$, $\tilde{u}_2$, $\tilde{P}_2$, $\tilde{T}_2$, and $\tilde{n}$ (the solution for $\hat{T}_2$ is not shown in the figure). Though there is no change in pressure and velocity across the contact discontinuities, there is a jump in $\hat{\rho}_1$ and $\hat{T}_1$ across the gas contact discontinuity, and in $\hat{\rho}_2$, $\hat{T}_2$, and $\tilde{n}$ across the solid contact discontinuity. The jumps in the thermodynamic quantities across the contact discontinuities are associated with changes in entropy; thus, contact discontinuities are also referred to as entropy waves. The gas and solid rarefactions, which propagate to the left at the local gas and solid sound speed, respectively, have a continuous structure. Since the leading edge of the rarefaction propagates to the left faster than the trailing edge, the width of these waves grows with time. All gas and solid thermodynamic variables, and the gas and solid velocity, vary continuously through their respective rarefactions; also, the particle number density continuously varies through the solid rarefaction. If an initial discontinuity in volume fraction had been prescribed, then it would have simply advected with the solid contact discontinuity. In this event, the gas and solid evolution equations do not decouple, and Eqs. (3.70-3.75) predict a jump in $\hat{\rho}_1$, $\hat{P}_1$, and $\hat{P}_2$ across the solid contact discontinuity.

The order of the gas waves relative to the solid waves for the Riemann problem can change depending upon the states $\mathbf{q}_L$ and $\mathbf{q}_R$. However, the order of the waves associated with each phase is maintained in that the contact discontinuity will always separate the shock and rarefaction. In general, the relative movement of the gas waves with respect to the solid waves poses no special problems, but more work needs to be done to verify this claim; this is beyond the scope of this investigation. It is plausible, however, that certain initial conditions might result in the evolution of the compound discontinuities discussed in Section 3.2 (e.g., if both the gas shock and solid contact discontinuity propagate at the same speed). Furthermore, if the solid contact discontinuity is located within the gas rarefaction wave, then the sonic condition $v_2 = v_1 - c_1$ is locally satisfied at the point where the two waves intersect, and the model equations become parabolic (for a non-ideal gas). As such, the wave structure associated with the solution of the Riemann problem may be considerably more complicated than illustrated here. In particular, it is noted that for arbitrary $\mathbf{q}_L$ and $\mathbf{q}_R$, a single wave will generally evolve in each of the characteristic fields identified in Appendix B; such is the case shown in Figs. 4.2 and 4.3. However, in contrast to results for strictly hyperbolic systems [68], Keyfitz and Kranzer [58] have shown that the Riemann problem for a class of non-strictly hyperbolic systems containing parabolic degeneracies can admit multiple waves in a single characteristic field. A similar result may hold for Eq. (4.1) for certain values of $\mathbf{q}_L$ and $\mathbf{q}_R$.

The basic premise of Godunov's methodology is to use the wave propagation information provided by the solution of a Riemann problem at each computational cell boundary in order to advance the solution over a small time interval $\Delta\tau$. The method consists of three steps for computing the updated average solution $\bar{\mathbf{q}}_k^{n+1}$ $(k = 1, 2, \ldots)$ within each computational cell from the known average solution $\bar{\mathbf{q}}_k^n$ [51].

1. *Projection step.* The initial data $\bar{\mathbf{q}}_k^n$ is used to define a piecewise constant function $\check{\mathbf{q}}(\xi, \tau^n)$ having the value $\bar{\mathbf{q}}_k^n$ over the interval $\xi_{k-1/2} < \xi < \xi_{k+1/2}$. Thus, the function $\check{\mathbf{q}}(\xi, \tau^n)$ defines a sequence of Riemann problems at computational cell boundaries (Figure 4.4a).

2. *Evolution step*: Using $\check{\mathbf{q}}(\xi, \tau^n)$ as initial data, the system of conservation laws given by Eq. (4.1) is solved exactly for $\tau^n < \tau \leq \tau^{n+1}$ to obtain $\check{\mathbf{q}}(\xi, \tau^{n+1})$ (Figure 4.4b). Here, the exact global solution is simply the sequence of exact solutions of the local Riemann problems defined at the cell boundaries.

3. *Reconstruction step.* The updated solution $\bar{\mathbf{q}}_k^{n+1}$ is obtained by averaging the exact solution at τ^{n+1} over the spatial interval $\xi_{k-1/2} < \xi < \xi_{k+1/2}$:

$$\bar{\mathbf{q}}_k^{n+1} = \frac{1}{\Delta\xi} \int_{\xi_{k-1/2}}^{\xi_{k+1/2}} \check{\mathbf{q}}(\xi, \tau^{n+1}) d\xi. \tag{4.8}$$

   The updated values are then used to define a new piecewise constant function in the projection step, and the process is repeated.

In practice, the averages defined by Eq. (4.8) need not be computed explicitly. Rather, the updated averages can be computed from Eq. (4.6) provided that expressions for the average fluxes $\bar{\mathbf{f}}_{k+1/2}$ are known. The average fluxes are easily determined since the solution of each Riemann problem is constant along the rays $\xi/\tau = \text{constant}$. Thus, with the solution $\check{\mathbf{q}}(\xi_{k+1/2}, \tau^{n+1})$ known, then $\bar{\mathbf{f}}_{k+1/2}$ is simply given by $\mathbf{f}(\check{\mathbf{q}}(\xi_{k+1/2}, \tau^{n+1}))$.

Lastly, we note that the evolution step is computationally expensive since it requires that a nonlinear algebraic system of equations be solved iteratively at each

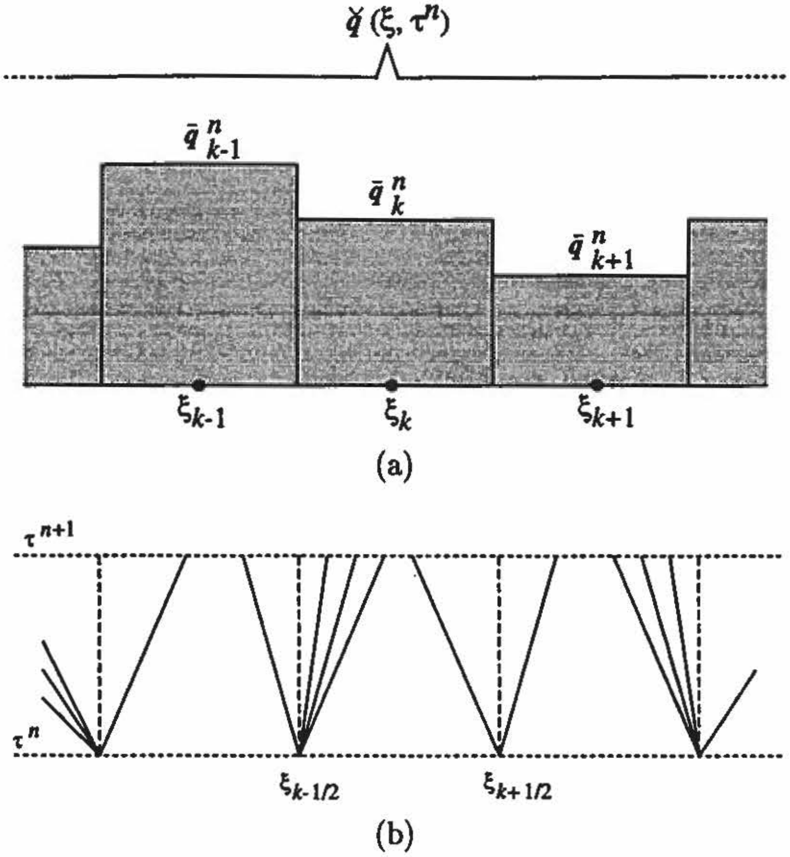

Figure 4.4: Sketch of the *projection step* and *evolution step* of Godunov's methodology: (a) piecewise distribution of $\check{\mathbf{q}}$ at τ^n; (b) evolution of the solution at the computational cell boundaries over the time interval $[\tau^n, \tau^{n+1}]$.

computational cell boundary. Furthermore, much of the detail provided by the exact solution of the Riemann problem is significantly smeared due to the averaging step. These extravagancies have motivated the use of approximate Riemann solutions for approximating the fluxes $\bar{\mathbf{f}}_{k+1/2}$, resulting in more computationally efficient numerical methods.

4.1.2 Approximate Solution of the Two-Phase Riemann Problem

An approximate solution of the two-phase Riemann problem is formulated in this subsection. In addition to having increased computational efficiency, the use of an approximate Riemann solution in this study is warranted since the exact solution of the two-phase Riemann problem for non-ideal state relations has not been previously determined. Here, the approach used by Roe and Pike [103] to formulate an approximate Riemann solution for the Euler equations for ideal state relations, and that used by Glaister [37, 38] to formulate an approximate Riemann solution for the Euler equations for non-ideal state relations is adopted.

The approximate solution of the two-phase Riemann problem is closely coupled to the exact solution of the linearized two-phase Riemann problem. As such, we first consider the case where the initial data $\mathbf{q}_L$ and $\mathbf{q}_R$ in Eq. (4.7) are close to a constant reference state $\mathbf{q}^*$. This assumption will be later relaxed to account for arbitrary $\mathbf{q}_L$ and $\mathbf{q}_R$.

For $\mathbf{q}_L$ and $\mathbf{q}_R$ close to $\mathbf{q}^*$, we can linearize Eq. (3.8) by assuming an expansion of the form

$$\mathbf{q}(\xi,\tau) = \mathbf{q}^* + \epsilon\mathbf{q}_{(1)}(\xi,\tau) + \epsilon^2\mathbf{q}_{(2)}(\xi,\tau) + \ldots, \tag{4.9}$$

where $0 < \epsilon \ll 1$. The following linear system of equations are obtained at lowest order in ϵ:

$$\epsilon\frac{\partial\mathbf{q}_{(1)}}{\partial\tau} + \epsilon\tilde{\bar{\mathbf{A}}}(\mathbf{q}^*)\frac{\partial\mathbf{q}_{(1)}}{\partial\xi} = 0, \tag{4.10}$$

or, since $\epsilon\mathbf{q}_{(1)} = \mathbf{q} - \mathbf{q}^* + O(\epsilon^2)$,

$$\frac{\partial\mathbf{q}}{\partial\tau} + \tilde{\bar{\mathbf{A}}}(\mathbf{q}^*)\frac{\partial\mathbf{q}}{\partial\xi} = 0, \tag{4.11}$$

where $\tilde{\bar{\mathbf{A}}}(\mathbf{q}^*)$ is the Jacobian matrix evaluated at the constant reference state. This equation, with the initial data of Eq. (4.7), can be solved using standard techniques applicable to linear hyperbolic systems [72, 123, 130].

The solution of the linear Riemann problem is obtained by re-expressing Eqs. (4.7) and (4.11) in terms of the characteristic variables defined by

$$\mathbf{p} \equiv \tilde{\bar{\mathbf{R}}}^{-1}\mathbf{q}, \tag{4.12}$$

where $\tilde{\bar{\mathbf{R}}}^{-1}$ is the inverse of the right eigenvector matrix [Eq. (3.21)] evaluated at the reference state. To this end, we first post-multiply Eq. (3.20) by $\tilde{\bar{\mathbf{R}}}^{-1}$ to obtain the expression

$$\tilde{\tilde{\mathbf{A}}} = \tilde{\tilde{\mathbf{R}}}\tilde{\tilde{\mathbf{\Lambda}}}\tilde{\tilde{\mathbf{R}}}^{-1}, \tag{4.13}$$

where $\tilde{\tilde{\mathbf{\Lambda}}}$ is the diagonal eigenvalue matrix [Eq. (3.21)] evaluated at the reference state. Next, we substitute the expression given by Eq. (4.13) into Eq. (4.11), and pre-multiply the result by $\tilde{\tilde{\mathbf{R}}}^{-1}$ to obtain

$$\tilde{\tilde{\mathbf{R}}}^{-1}\frac{\partial \mathbf{q}}{\partial \tau} + \tilde{\tilde{\mathbf{\Lambda}}}\tilde{\tilde{\mathbf{R}}}^{-1}\frac{\partial \mathbf{q}}{\partial \xi} = 0. \tag{4.14}$$

Since $\tilde{\tilde{\mathbf{R}}}^{-1}$ is constant, we obtain the following equation expressed in terms of the characteristic variables:

$$\frac{\partial \mathbf{p}}{\partial \tau} + \tilde{\tilde{\mathbf{\Lambda}}}\frac{\partial \mathbf{p}}{\partial \xi} = 0. \tag{4.15}$$

The initial condition for this equation is

$$\mathbf{p}(\xi, 0) = \begin{cases} \boldsymbol{\nu}_L \equiv \tilde{\tilde{\mathbf{R}}}^{-1}\mathbf{q}_L & \text{for } \xi < 0 \\ \boldsymbol{\nu}_R \equiv \tilde{\tilde{\mathbf{R}}}^{-1}\mathbf{q}_R & \text{for } \xi > 0. \end{cases} \tag{4.16}$$

Since $\tilde{\tilde{\mathbf{\Lambda}}}$ is a diagonal matrix, Eq. (4.15) consists of nine decoupled linear advection equations each having the form

$$\frac{\partial p_j}{\partial \tau} + \lambda^{(j)}\frac{\partial p_j}{\partial \xi} = 0, \tag{4.17}$$

where p_j $(j = 1, \ldots, 9)$ are the components of $\mathbf{p}$. The solution of each advection equation, subject to the initial condition of Eq. (4.16), is given by

$$p_j(\xi, \tau) = \begin{cases} \nu_{jL} & \text{if } \xi - \lambda^{(j)}\tau < 0 \\ \nu_{jR} & \text{if } \xi - \lambda^{(j)}\tau > 0, \end{cases} \tag{4.18}$$

where ν_{jL} and ν_{jR} are the j^{th} components of $\boldsymbol{\nu}_L$ and $\boldsymbol{\nu}_R$, respectively. Thus, by Eq. (4.12), we obtain the following solution for $\mathbf{q}(\xi, \tau)$:

$$\mathbf{q}(\xi, \tau) = \tilde{\tilde{\mathbf{R}}}\mathbf{p}(\xi, \tau) = \sum_{j=1}^{9} p_j(\xi, \tau)\mathbf{r}^{(j)}. \tag{4.19}$$

Once again, we note that the right eigenvectors $\mathbf{r}^{(j)}$ $(j = 1, \ldots, 9)$ [Eqs. (3.23-3.31)] are evaluated at the reference state $\mathbf{q}^*$.

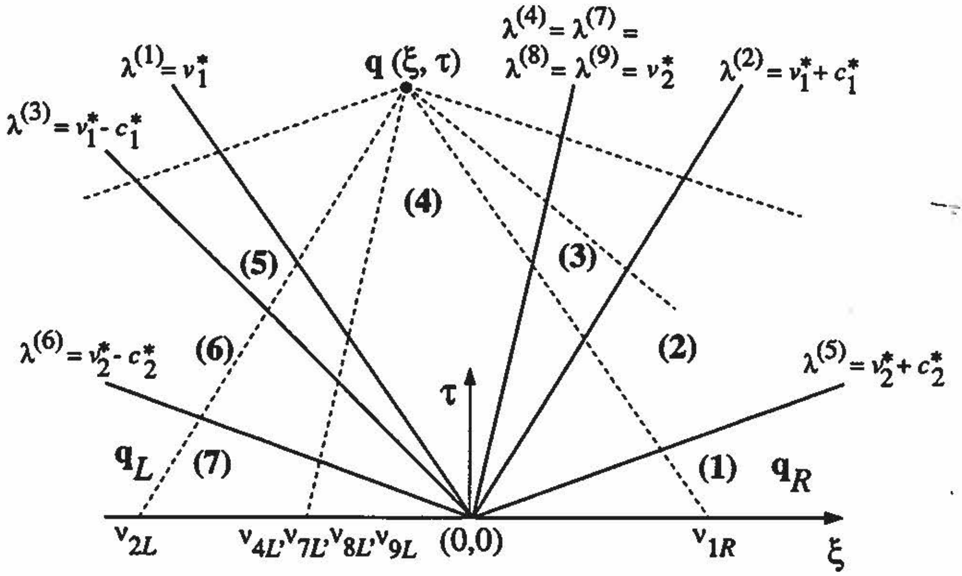

Figure 4.5: Sketch of a typical solution of the linear two-phase Riemann problem.

The solution of the linear Riemann problem is illustrated in the ξ-τ plane of Fig. 4.5. The initial disturbance, located at $(\xi, \tau) = (0, 0)$, generates a wave of infinitesimal strength in each characteristic field for $\tau > 0$. The resulting waves simply advect along their respective characteristics (identified by the solid lines) at speeds $\lambda^{(j)}$ $(j = 1, \ldots, 9)$. For this problem, the characteristics associated with each field are parallel since the $\lambda^{(j)}$ are constant. The waves include a gas entropy wave $[\lambda^{(1)}]$, gas acoustic waves $[\lambda^{(2)}$ and $\lambda^{(3)}]$, a solid entropy wave $[\lambda^{(4)}]$, and solid acoustic waves $[\lambda^{(5)}$ and $\lambda^{(6)}]$. Also, disturbances in the volume fraction $[\lambda^{(7)}]$, the particle number density $[\lambda^{(8)}]$, and the ignition variable $[\lambda^{(9)}]$ advect with the solid entropy wave; consequently, these four waves may be treated as a single compound wave. As identified in this figure, the waves separate seven regions of uniform state. The solution $\mathbf{q}(\xi, \tau)$ in each of these regions is constant, and is easily constructed by extrapolating the characteristics passing through the point (ξ, τ) backwards in time to $\tau = 0$.

We illustrate this idea for a point located in region (4) in Fig. 4.5; for clarity, only a few of the characteristics are extrapolated to $\tau = 0$ (identified by the dashed lines).

If the j^{th} characteristic through the point (ξ, τ) intersects the line $\tau = 0$ at $\xi > 0$, then p_j in Eq. (4.19) equals ν_{jR}; otherwise, p_j equals ν_{jL}. For the point located in region (4), Eq. (4.19) gives

$$\begin{aligned}\mathbf{q}(\xi, \tau) = \nu_{1R}\mathbf{r}^{(1)} + \nu_{2L}\mathbf{r}^{(2)} + \nu_{3R}\mathbf{r}^{(3)} + \nu_{4L}\mathbf{r}^{(4)} + \nu_{5L}\mathbf{r}^{(5)} \\ + \nu_{6R}\mathbf{r}^{(6)} + \nu_{7L}\mathbf{r}^{(7)} + \nu_{8L}\mathbf{r}^{(8)} + \nu_{9L}\mathbf{r}^{(9)}.\end{aligned} \tag{4.20}$$

It is useful to consider the jump in the dependent vector $\mathbf{q}$ across each of the waves identified in Fig. 4.5. Writing out the solution given by Eq. (4.19) in each of the constant regions identified in Fig. 4.5, and using the definitions for the eigenvector expansion coefficients p_j, given by Eq. (4.18), it can be shown that the jump in $\mathbf{q}$ across the j^{th} wave is given by

$$[\mathbf{q}]_j \equiv \left(\mathbf{q}^+ - \mathbf{q}^-\right)_j = \left(\nu_{jR} - \nu_{jL}\right)\mathbf{r}^{(j)}, \tag{4.21}$$

where $\mathbf{q}^-$ and $\mathbf{q}^+$ are the states immediately to the left and right of the wave, respectively. The jump in $\mathbf{q}$ across the entire wave system equals the sum of the jumps across each wave:

$$\begin{aligned}\mathbf{q}_R - \mathbf{q}_L &= \sum_{j=1}^{9} [\mathbf{q}]_j \\ &= \sum_{j=1}^{9} \left(\nu_{jR} - \nu_{jL}\right)\mathbf{r}^{(j)}.\end{aligned} \tag{4.22}$$

It is convenient to express the solution $\mathbf{q}(\xi, \tau)$ in terms of these jumps:

$$\begin{aligned}\mathbf{q}(\xi, \tau) &= \mathbf{q}_L + \sum_{\lambda^{(j)} < \xi/\tau} \left(\nu_{jR} - \nu_{jL}\right)\mathbf{r}^{(j)} \\ &= \mathbf{q}_R - \sum_{\lambda^{(j)} \geq \xi/\tau} \left(\nu_{jR} - \nu_{jL}\right)\mathbf{r}^{(j)}.\end{aligned} \tag{4.23}$$

Furthermore, since $\tilde{\tilde{\mathbf{A}}}$ is constant for this problem, then $\mathbf{f} = \tilde{\tilde{\mathbf{A}}}\mathbf{q}$, and the jump in $\mathbf{f}$ across the j^{th} wave is given by

$$\begin{aligned}[\mathbf{f}]_j \equiv \left(\mathbf{f}^+ - \mathbf{f}^-\right)_j &= \tilde{\tilde{\mathbf{A}}}\,[\mathbf{q}]_j \\ &= \left(\nu_{jR} - \nu_{jL}\right)\tilde{\tilde{\mathbf{A}}}\mathbf{r}^{(j)} \\ &= \left(\nu_{jR} - \nu_{jL}\right)\lambda^{(j)}\mathbf{r}^{(j)}.\end{aligned} \tag{4.24}$$

From Eq. (4.21) and the last expression of Eq. (4.24), it is seen that $[\mathbf{f}]_j = \lambda^{(j)}[\mathbf{q}]_j$; thus, the Rankine-Hugoniot relations are identically satisfied across each wave. Furthermore, the compound wave propagating at speed $\lambda_{cw} \equiv v_2$ poses no special difficulty since the Rankine-Hugoniot relations are identically satisfied across this wave:

$$\begin{aligned}
[\mathbf{f}]_{cw} &= (\nu_{4R} - \nu_{4L})\,\lambda^{(4)}\mathbf{r}^{(4)} + (\nu_{7R} - \nu_{7L})\,\lambda^{(7)}\mathbf{r}^{(7)} \\
&\quad + (\nu_{8R} - \nu_{8L})\,\lambda^{(8)}\mathbf{r}^{(8)} + (\nu_{9R} - \nu_{9L})\,\lambda^{(9)}\mathbf{r}^{(9)} \\
&= \lambda_{cw}\left[(\nu_{4R} - \nu_{4L})\,\mathbf{r}^{(4)} + (\nu_{7R} - \nu_{7L})\,\mathbf{r}^{(7)} + (\nu_{8R} - \nu_{8L})\,\mathbf{r}^{(8)} + (\nu_{9R} - \nu_{9L})\,\mathbf{r}^{(9)}\right] \\
&= \lambda_{cw}\,[\mathbf{q}]_{cw}\,.
\end{aligned} \tag{4.25}$$

The jump in $\mathbf{f}$ across the entire wave system equals the sum of the jumps across each wave:

$$\begin{aligned}
\mathbf{f}_R - \mathbf{f}_L &= \sum_{j=1}^{9} [\mathbf{f}]_j \\
&= \sum_{j=1}^{9} (\nu_{jR} - \nu_{jL})\,\lambda^{(j)}\mathbf{r}^{(j)}.
\end{aligned} \tag{4.26}$$

From these relations, the following solution for $\mathbf{f}(\xi, \tau)$ is obtained:

$$\begin{aligned}
\mathbf{f}(\xi, \tau) &= \mathbf{f}_L + \sum_{\lambda^{(j)} < \xi/\tau} (\nu_{jR} - \nu_{jL})\,\lambda^{(j)}\mathbf{r}^{(j)} \\
&= \mathbf{f}_R - \sum_{\lambda^{(j)} \geq \xi/\tau} (\nu_{jR} - \nu_{jL})\,\lambda^{(j)}\mathbf{r}^{(j)}.
\end{aligned} \tag{4.27}$$

Following Roe and Pike [103] and Glaister [37, 38], the eigenvector coefficients ν_{jL} and ν_{jR} $(j = 1, \ldots, 9)$ are not directly computed using the definitions given in Eq. (4.16). Rather, the differences $\nu_{jR} - \nu_{jL}$ are approximated by the coefficients $\alpha^{(j)}$ $(j = 1, \ldots, 9)$ which are determined such that each component of the vector equation

$$\delta(\mathbf{q}) = \sum_{j=1}^{9} \alpha^{(j)}\mathbf{r}^{(j)}, \tag{4.28}$$

is satisfied to within $O[\delta(q_j)^2] \sim O(\epsilon^2)$, and that each component of the vector equation

$$\delta(\mathbf{f}) = \sum_{j=1}^{9} \alpha^{(j)}\lambda^{(j)}\mathbf{r}^{(j)}, \tag{4.29}$$

is satisfied to within $O[\delta(f_j)^2] \sim O(\epsilon^2)$, where the difference operator is defined by $\delta(\bullet) \equiv (\bullet)_R - (\bullet)_L$. In the limit as $\mathbf{q}_L \to \mathbf{q}_R$, Eqs. (4.22) and (4.26) reduce to Eqs. (4.28) and (4.29), respectively. Expressions for $\alpha^{(j)}$ $(j = 1, \ldots, 9)$, which are derived in Appendix G, are given by the following:

$$\alpha^{(1)} = \delta(\rho_1\phi_1) - \frac{1}{c_1^2}\delta(P_1\phi_1) - \frac{\rho_1\eta_1}{c_1^2}\delta(\phi_1), \tag{4.30}$$

$$\alpha^{(2)} = \frac{1}{2c_1^2}\delta(P_1\phi_1) + \frac{\rho_1\phi_1}{2c_1}\delta(v_1) + \left(\frac{v_2 - v_1}{v_2 - (v_1 + c_1)}\right)\frac{\rho_1\eta_1}{2c_1^2}\delta(\phi_1), \tag{4.31}$$

$$\alpha^{(3)} = \frac{1}{2c_1^2}\delta(P_1\phi_1) - \frac{\rho_1\phi_1}{2c_1}\delta(v_1) + \left(\frac{v_2 - v_1}{v_2 - (v_1 - c_1)}\right)\frac{\rho_1\eta_1}{2c_1^2}\delta(\phi_1), \tag{4.32}$$

$$\alpha^{(4)} = \delta(\rho_2\phi_2) - \frac{1}{c_2^2}\delta(P_2\phi_2), \tag{4.33}$$

$$\alpha^{(5)} = \frac{1}{2c_2^2}\delta(P_2\phi_2) + \frac{\rho_2\phi_2}{2c_2}\delta(v_2), \tag{4.34}$$

$$\alpha^{(6)} = \frac{1}{2c_2^2}\delta(P_2\phi_2) - \frac{\rho_2\phi_2}{2c_2}\delta(v_2), \tag{4.35}$$

$$\alpha^{(7)} = \rho_2\phi_2\delta(\phi_2), \tag{4.36}$$

$$\alpha^{(8)} = \delta(n) - \frac{n}{\rho_2\phi_2 c_2^2}\delta(P_2\phi_2), \tag{4.37}$$

$$\alpha^{(9)} = \rho_2\phi_2\delta(I) + I\delta(\rho_2\phi_2) - \frac{I}{c_2^2}\delta(P_2\phi_2). \tag{4.38}$$

Here, it is again noted that these expressions are to be evaluated at the constant reference state $\mathbf{q}^*$. The expressions for $\alpha^{(2)}$ [Eq. (4.31)] and $\alpha^{(3)}$ [Eq. (4.32)] are singular when $v_2 = v_1 + c_1$ and $v_2 = v_1 - c_1$, respectively; also, the expression for $\alpha^{(8)}$ [Eq. (4.37)] is singular when $\phi_2 = 0$. These points correspond to the sonic and complete combustion singularities discussed in Chapter 3. At these points, the model equations become parabolic, and the eigenvector expansions given by Eqs. (4.28) and (4.29) [also, Eqs. (4.22) and (4.26)] are no longer valid. The methodology used to suppress numerical instabilities at these points is discussed at the end of this section.

Before proceeding to develop an approximate solution of the nonlinear two-phase Riemann problem for arbitrary $\mathbf{q}_L$ and $\mathbf{q}_R$, the solution of the linear problem is re-expressed in a form which better facilitates the derivation of the approximate solution. To this end, the solution of the linear problem is re-expressed in terms of the quantities ϕ_1, v_1, e_1, ϕ_2, v_2, e_2, n, I, and the new quantities $(\rho_1\phi_1)$, $(P_1\phi_1)$, $(\rho_2\phi_2)$, $(P_2\phi_2)$. These latter quantities are the partial density and partial pressure of the gas and solid, respectively. Also, the derivatives $F_{i_{\rho_i\phi_i}} \equiv \left.\frac{\partial F_i}{\partial(\rho_i\phi_i)}\right|_{\phi_i,e_i}$, $F_{i_{\phi_i}} \equiv \left.\frac{\partial F_i}{\partial\phi_i}\right|_{(\rho_i\phi_i),e_i}$, and $F_{i_{e_i}} \equiv \left.\frac{\partial F_i}{\partial e_i}\right|_{(\rho_i\phi_i),\phi_i}$ $(i = 1, 2)$ are introduced, where the F_i denote the functional relationships $P_i\phi_i = F_i(\rho_i\phi_i, \phi_i, e_i)$ obtained from the gas and solid state relations. The solution of the linear Riemann problem expressed in terms of these quantities is summarized in Appendix E.

An approximate solution of the nonlinear two-phase Riemann problem for arbitrary $\mathbf{q}_L$ and $\mathbf{q}_R$ will now be formulated. Following Roe [100] and Glaister [37], it is desirable to construct the approximate solution such that the following criteria are satisfied.

1. The approximate solution reduces to the exact solution of the linear Riemann problem as $\mathbf{q}_R \rightarrow \mathbf{q}_L \rightarrow \mathbf{q}$.
2. The approximate solution is derived from a hyperbolic system of equations.
3. The Rankine-Hugoniot relations are satisfied across all discontinuities.

In essence, these criteria stipulate that the approximate solution be consistent with the solution of the original system of hyperbolic equations.

The solution of the linear Riemann problem satisfies the above criteria. As such, it is plausible to use this solution as a basis for constructing the approximate solution. To this end, we require that the approximate solution have the same functional form as the solution of the linear Riemann problem summarized in Appendix E, evaluated at an average state $\tilde{\mathbf{q}}$ which is different from the reference state $\mathbf{q}^*$. The problem then reduces to one of properly defining $\tilde{\mathbf{q}}$ as a function of the arbitrary initial data $\mathbf{q}_L$ and $\mathbf{q}_R$. In particular, we seek to define $\tilde{\mathbf{q}}$ in terms of the average quantities $\widetilde{\rho_1\phi_1}$, $\tilde{v}_1$, $\tilde{e}_1$, $\tilde{H}_1$, $\tilde{F}_{1_{\rho1\phi1}}$, $\tilde{F}_{1_{\phi1}}$, $\tilde{F}_{1_{e1}}$, $\widetilde{\rho_2\phi_2}$, $\tilde{\phi}_2$, $\tilde{v}_2$, $\tilde{e}_2$, $\tilde{H}_2$, $\tilde{F}_{2_{\rho2\phi2}}$, $\tilde{F}_{2_{\phi2}}$, $\tilde{F}_{2_{e2}}$, $\tilde{n}$, and $\tilde{I}$, which are functions of $\mathbf{q}_L$ and $\mathbf{q}_R$, such that the following algebraic equations are identically satisfied [average quantities are denoted by $(\tilde{\bullet})$ throughout this analysis]:

$$\Delta(\mathbf{q}) = \sum_{j=1}^{9} \tilde{\alpha}^{(j)} \tilde{\mathbf{r}}^{(j)}, \tag{4.39}$$

$$\Delta(\mathbf{f}) = \sum_{j=1}^{9} \tilde{\alpha}^{(j)} \tilde{\lambda}^{(j)} \tilde{\mathbf{r}}^{(j)}, \tag{4.40}$$

where

$$\tilde{\lambda}^{(1),(2),\ldots,(9)} = \tilde{v}_1,\ \tilde{v}_1 + \tilde{c}_1,\ \tilde{v}_1 - \tilde{c}_1,\ \tilde{v}_2, \tilde{v}_2 + \tilde{c}_2,\ \tilde{v}_2 - \tilde{c}_2,\ \tilde{v}_2,\ \tilde{v}_2,\ \tilde{v}_2, \tag{4.41}$$

$$\begin{aligned}
\tilde{\mathbf{r}}^{(1)} &= \left[1,\ \tilde{v}_1,\ \tilde{H}_1 - \tilde{c}_1^2/\tilde{\Gamma}_1,\ 0,\ 0,\ 0,\ 0,\ 0,\ 0\right]^T, &(4.42)\\
\tilde{\mathbf{r}}^{(2)} &= \left[1,\ \tilde{v}_1 + \tilde{c}_1,\ \tilde{H}_1 + \tilde{v}_1\tilde{c}_1,\ 0,\ 0,\ 0,\ 0,\ 0,\ 0\right]^T, &(4.43)\\
\tilde{\mathbf{r}}^{(3)} &= \left[1,\ \tilde{v}_1 - \tilde{c}_1,\ \tilde{H}_1 - \tilde{v}_1\tilde{c}_1,\ 0,\ 0,\ 0,\ 0,\ 0,\ 0\right]^T, &(4.44)\\
\tilde{\mathbf{r}}^{(4)} &= \left[0,\ 0,\ 0,\ 1,\ \tilde{v}_2,\ \tilde{H}_2 - \tilde{c}_2^2/\tilde{\Gamma}_2,\ \tilde{\phi}_2,\ 0,\ 0\right]^T, &(4.45)\\
\tilde{\mathbf{r}}^{(5)} &= \left[0,\ 0,\ 0,\ 1,\ \tilde{v}_2 + \tilde{c}_2,\ \tilde{H}_2 + \tilde{v}_2\tilde{c}_2,\ \tilde{\phi}_2,\ \tilde{n}/\widetilde{\rho_2\phi_2},\ \tilde{I}\right]^T, &(4.46)\\
\tilde{\mathbf{r}}^{(6)} &= \left[0,\ 0,\ 0,\ 1,\ \tilde{v}_2 - \tilde{c}_2,\ \tilde{H}_2 - \tilde{v}_2\tilde{c}_2,\ \tilde{\phi}_2,\ \tilde{n}/\widetilde{\rho_2\phi_2},\ \tilde{I}\right]^T, &(4.47)\\
\tilde{\mathbf{r}}^{(7)} &= \Bigg[-\frac{\tilde{F}_{1_{\phi 1}}}{\widetilde{\rho_2\phi_2}\left((\tilde{v}_2 - \tilde{v}_1)^2 - \tilde{c}_1^2\right)},\ -\frac{\tilde{F}_{1_{\phi 1}}\tilde{v}_2}{\widetilde{\rho_2\phi_2}\left((\tilde{v}_2 - \tilde{v}_1)^2 - \tilde{c}_1^2\right)},\\
&\qquad -\frac{\tilde{F}_{1_{\phi 1}}\left(\tilde{H}_1 + \tilde{v}_1\tilde{v}_2 - \tilde{v}_1^2\right)}{\widetilde{\rho_2\phi_2}\left((\tilde{v}_2 - \tilde{v}_1)^2 - \tilde{c}_1^2\right)},\ 0,\ 0,\ -\frac{\tilde{F}_{2_{\phi 2}}}{\widetilde{\rho_2\phi_2}\tilde{\Gamma}_2},\ 1,\ 0,\ 0\Bigg]^T, &(4.48)\\
\tilde{\mathbf{r}}^{(8)} &= [0,\ 0,\ 0,\ 0,\ 0,\ 0,\ 0,\ 1,\ 0]^T, &(4.49)\\
\tilde{\mathbf{r}}^{(9)} &= [0,\ 0,\ 0,\ 0,\ 0,\ 0,\ 0,\ 0,\ 1]^T, &(4.50)\\
\tilde{\alpha}^{(1)} &= \Delta\left(\rho_1\phi_1\right) - \frac{1}{\tilde{c}_1^2}\Delta\left(P_1\phi_1\right) + \frac{\tilde{F}_{1_{\phi 1}}}{\tilde{c}_1^2}\Delta(\phi_1), &(4.51)\\
\tilde{\alpha}^{(2)} &= \frac{1}{2\tilde{c}_1^2}\Delta\left(P_1\phi_1\right) + \frac{\widetilde{\rho_1\phi_1}}{2\tilde{c}_1}\Delta(v_1) - \left(\frac{\tilde{v}_2 - \tilde{v}_1}{\tilde{v}_2 - (\tilde{v}_1 + \tilde{c}_1)}\right)\frac{\tilde{F}_{1_{\phi 1}}}{2\tilde{c}_1^2}\Delta(\phi_1), &(4.52)\\
\tilde{\alpha}^{(3)} &= \frac{1}{2\tilde{c}_1^2}\Delta\left(P_1\phi_1\right) - \frac{\widetilde{\rho_1\phi_1}}{2\tilde{c}_1}\Delta(v_1) - \left(\frac{\tilde{v}_2 - \tilde{v}_1}{\tilde{v}_2 - (\tilde{v}_1 - \tilde{c}_1)}\right)\frac{\tilde{F}_{1_{\phi 1}}}{2\tilde{c}_1^2}\Delta(\phi_1), &(4.53)\\
\tilde{\alpha}^{(4)} &= \Delta\left(\rho_2\phi_2\right) - \frac{1}{\tilde{c}_2^2}\Delta\left(P_2\phi_2\right), &(4.54)\\
\tilde{\alpha}^{(5)} &= \frac{1}{2\tilde{c}_2^2}\Delta\left(P_2\phi_2\right) + \frac{\widetilde{\rho_2\phi_2}}{2\tilde{c}_2}\Delta(v_2), &(4.55)
\end{aligned}$$

$$\tilde{\alpha}^{(6)} = \frac{1}{2\tilde{c}_2^2}\Delta\left(P_2\phi_2\right) - \frac{\widetilde{\rho_2\phi_2}}{2\tilde{c}_2}\Delta(v_2), \tag{4.56}$$

$$\tilde{\alpha}^{(7)} = \widetilde{\rho_2\phi_2}\Delta(\phi_2), \tag{4.57}$$

$$\tilde{\alpha}^{(8)} = \Delta(n) - \frac{\tilde{n}}{\widetilde{\rho_2\phi_2}\tilde{c}_2^2}\Delta\left(P_2\phi_2\right), \tag{4.58}$$

$$\tilde{\alpha}^{(9)} = \widetilde{\rho_2\phi_2}\Delta(I) + \tilde{I}\Delta(\rho_2\phi_2) - \frac{\tilde{I}}{\tilde{c}_2^2}\Delta(P_2\phi_2), \tag{4.59}$$

and $\tilde{c}_1^2$, $\tilde{c}_2^2$, $\widetilde{P_1\phi_1}$, $\widetilde{P_2\phi_2}$, $\tilde{\Gamma}_1$, and $\tilde{\Gamma}_2$ are given by

$$\tilde{c}_1^2 = \frac{\widetilde{P_1\phi_1}}{\widetilde{\rho_1\phi_1}^{\,2}}\tilde{F}_{1_{e1}} + \tilde{F}_{1_{\rho1\phi1}}, \qquad \tilde{c}_2^2 = \frac{\widetilde{P_2\phi_2}}{\widetilde{\rho_2\phi_2}^{\,2}}\tilde{F}_{2_{e2}} + \tilde{F}_{2_{\rho2\phi2}}, \tag{4.60}$$

$$\widetilde{P_1\phi_1} = \widetilde{\rho_1\phi_1}\left(\tilde{H}_1 - \tilde{e}_1 - \frac{\tilde{v}_1^2}{2}\right), \qquad \widetilde{P_2\phi_2} = \widetilde{\rho_2\phi_2}\left(\tilde{H}_2 - \tilde{e}_2 - \frac{\tilde{v}_2^2}{2}\right), \tag{4.61}$$

$$\tilde{\Gamma}_1 = \frac{1}{\widetilde{\rho_1\phi_1}}\tilde{F}_{1_{e1}}, \qquad \tilde{\Gamma}_2 = \frac{1}{\widetilde{\rho_2\phi_2}}\tilde{F}_{2_{e2}}. \tag{4.62}$$

Here, the difference operator is defined by $\Delta(\bullet) \equiv (\bullet)_R - (\bullet)_L$, where the difference $\mathbf{q}_R - \mathbf{q}_L$ is not necessarily small [as opposed to the difference operator $\delta(\bullet)$ defined for the linear Riemann problem]. If suitable averages can be defined, then the approximate solutions $\mathbf{q}(\xi,\tau)$ and $\mathbf{f}(\xi,\tau)$ are given by

$$\begin{aligned} \mathbf{q}(\xi,\tau) &= \mathbf{q}_L + \sum_{\tilde{\lambda}^{(j)}<\xi/\tau} \tilde{\alpha}^{(j)}\tilde{\mathbf{r}}^{(j)} \\ &= \mathbf{q}_R - \sum_{\tilde{\lambda}^{(j)}\geq\xi/\tau} \tilde{\alpha}^{(j)}\tilde{\mathbf{r}}^{(j)}, \end{aligned} \tag{4.63}$$

$$\begin{aligned} \mathbf{f}(\xi,\tau) &= \mathbf{f}_L + \sum_{\tilde{\lambda}^{(j)}<\xi/\tau} \tilde{\alpha}^{(j)}\tilde{\lambda}^{(j)}\tilde{\mathbf{r}}^{(j)} \\ &= \mathbf{f}_R - \sum_{\tilde{\lambda}^{(j)}\geq\xi/\tau} \tilde{\alpha}^{(j)}\tilde{\lambda}^{(j)}\tilde{\mathbf{r}}^{(j)}. \end{aligned} \tag{4.64}$$

Equations (4.39) and (4.40), and Eqs. (4.63) and (4.64) are analogous to Eqs. (4.28) and (4.29), and Eqs. (4.23) and (4.27), respectively.

In order to define the desired average quantities, it is necessary to solve the nonlinear algebraic problem given by Eqs. (4.39) and (4.40). Though the solution of this problem is nontrivial, closed form expressions can be obtained for the average quantities. The derivation of these quantities is given in Appendix F; the results are summarized below (where $i = 1, 2$):

$$\widetilde{\rho_i\phi_i} \equiv \sqrt{\rho_{iL}\phi_{iL}\rho_{iR}\phi_{iR}}, \tag{4.65}$$

$$\tilde{v}_i \equiv \frac{\sqrt{\rho_{iL}\phi_{iL}}v_{iL} + \sqrt{\rho_{iR}\phi_{iR}}v_{iR}}{\sqrt{\rho_{iL}\phi_{iL}} + \sqrt{\rho_{iR}\phi_{iR}}}, \tag{4.66}$$

$$\tilde{e}_i \equiv \frac{\sqrt{\rho_{iL}\phi_{iL}}e_{iL} + \sqrt{\rho_{iR}\phi_{iR}}e_{iR}}{\sqrt{\rho_{iL}\phi_{iL}} + \sqrt{\rho_{iR}\phi_{iR}}}, \tag{4.67}$$

$$\tilde{H}_i \equiv \frac{\sqrt{\rho_{iL}\phi_{iL}}H_{iL} + \sqrt{\rho_{iR}\phi_{iR}}H_{iR}}{\sqrt{\rho_{iL}\phi_{iL}} + \sqrt{\rho_{iR}\phi_{iR}}}, \tag{4.68}$$

$$\tilde{\phi}_2 \equiv \frac{\sqrt{\rho_{2L}\phi_{2L}}\phi_{2L} + \sqrt{\rho_{2R}\phi_{2R}}\phi_{2R}}{\sqrt{\rho_{2L}\phi_{2L}} + \sqrt{\rho_{2R}\phi_{2R}}}, \tag{4.69}$$

$$\tilde{n} \equiv \frac{\sqrt{\rho_{2L}\phi_{2L}}n_{2R} + \sqrt{\rho_{2R}\phi_{2R}}n_{2L}}{\sqrt{\rho_{2L}\phi_{2L}} + \sqrt{\rho_{2R}\phi_{2R}}}, \tag{4.70}$$

$$\tilde{I} \equiv \frac{\sqrt{\rho_{2L}\phi_{2L}}I_{2L} + \sqrt{\rho_{2R}\phi_{2R}}I_{2R}}{\sqrt{\rho_{2L}\phi_{2L}} + \sqrt{\rho_{2R}\phi_{2R}}}, \tag{4.71}$$

$$\tilde{F}_{i_{\rho_i\phi_i}} \equiv \begin{cases} \Big(\frac{1}{4}\left[F_i(\rho_{iR}\phi_{iR}, \phi_{iR}, e_{1R}) + F_i(\rho_{iR}\phi_{iR}, \phi_{iR}, e_{iL}) + F_i(\rho_{iR}\phi_{iR}, \phi_{iL}, e_{iL})\right. \\ \left.+F_i(\rho_{iR}\phi_{iR}, \phi_{iL}, e_{iR})\right] - \frac{1}{4}\left[F_i(\rho_{iL}\phi_{iL}, \phi_{iR}, e_{iR}) + F_i(\rho_{iL}\phi_{iL}, \phi_{iL}, e_{iR})\right. \\ \left.+F_i(\rho_{iL}\phi_{iL}, \phi_{iR}, e_{iL}) + F_i(\rho_{iL}\phi_{iL}, \phi_{iL}, e_{iL})\right]\Big) /\Delta(\rho_i\phi_i) & \text{if } \Delta(\rho_i\phi_i) \neq 0, \\ \\ \frac{1}{4}\left[\frac{\partial F_i}{\partial(\rho_i\phi_i)}(\rho_i\phi_i, \phi_{iR}, e_{1R}) + \frac{\partial F_i}{\partial(\rho_i\phi_i)}(\rho_i\phi_i, \phi_{iR}, e_{iL}) + \frac{\partial F_i}{\partial(\rho_i\phi_i)}(\rho_i\phi_i, \phi_{iL}, e_{iR})\right. \\ \left.+\frac{\partial F_i}{\partial(\rho_i\phi_i)}(\rho_i\phi_i, \phi_{iL}, e_{iL})\right], & \text{if } \Delta(\rho_i\phi_i) = 0, \end{cases} \tag{4.72}$$

$$\tilde{F}_{i_{\phi_i}} \equiv \begin{cases} \Big(\frac{1}{2}\left[F_i(\rho_{iR}\phi_{iR}, \phi_{iR}, e_{1R}) + F_i(\rho_{iL}\phi_{iL}, \phi_{iR}, e_{iL})\right] + \frac{1}{2}\left[F_i(\rho_{iR}\phi_{iR}, \phi_{iL}, e_{iR})\right. \\ \left.+F_i(\rho_{iL}\phi_{iL}, \phi_{iL}, e_{iL})\right]\Big) /\Delta(\phi_i) & \text{if } \Delta(\phi_i) \neq 0, \\ \\ \frac{1}{2}\left[\frac{\partial F_i}{\partial\phi_i}(\rho_{iR}\phi_{iR}, \phi_i, e_{1R}) + \frac{\partial F_i}{\partial\phi_i}(\rho_{iL}\phi_{iL}, \phi_i, e_{iL})\right] & \text{if } \Delta(\phi_i) = 0, \end{cases} \tag{4.73}$$

$$\tilde{F}_{i_{e_i}} \equiv \begin{cases} \Big(\frac{1}{4}\left[F_i(\rho_{iR}\phi_{iR}, \phi_{iR}, e_{1R}) + F_i(\rho_{iL}\phi_{iL}, \phi_{iL}, e_{iR}) + F_i(\rho_{iR}\phi_{iR}, \phi_{iL}, e_{iR}) \right. \\ \left. +F_i(\rho_{iL}\phi_{iL}, \phi_{iR}, e_{iR})\right] - \frac{1}{4}\left[F_i(\rho_{iR}\phi_{iR}, \phi_{iL}, e_{iL}) + F_i(\rho_{iR}\phi_{iR}, \phi_{iR}, e_{iL}) \right. \\ \left. +F_i(\rho_{iL}\phi_{iL}, \phi_{iR}, e_{iL}) + F_i(\rho_{iL}\phi_{iL}, \phi_{iL}, e_{iL})\right] \Big) /\Delta(e_i) \quad \text{if } \Delta(e_i) \neq 0, \\ \\ \frac{1}{4}\left[\frac{\partial F_i}{\partial e_i}(\rho_{iR}\phi_{iR}, \phi_{iR}, e_i) + \frac{\partial F_i}{\partial e_i}(\rho_{iR}\phi_{iR}, \phi_{iL}, e_i) + \frac{\partial F_i}{\partial e_i}(\rho_{iL}\phi_{iL}, \phi_{iR}, e_i) \right. \\ \left. + \frac{\partial F_i}{\partial e_i}(\rho_{iL}\phi_{iL}, \phi_{iL}, e_i)\right], \qquad \text{if } \Delta(e_i) = 0. \end{cases} \tag{4.74}$$

The averages defined by Eqs. (4.65-4.71) are similar in form to the "square root" averages defined in References [37, 100]. Though the average derivatives defined by Eqs. (4.72-4.74) appear complicated, it is shown in Appendix F that they can be substantially reduced when the functional form of the equations of state are specified, and that the reduced expressions are physically reasonable. Though not applicable to this study, the expressions for the average derivatives may be difficult and/or computationally expensive to evaluate for thermodynamic data given in tabular form. Furthermore, the average derivatives require function evaluations for artificial states constructed from the initial data $\mathbf{q}_L$ and $\mathbf{q}_R$, and it is possible that these states lie outside the range of validity of the thermodynamic data. Glaister [39] has recently addressed similar weaknesses for his approximate Riemann solution, and has modified his solution to overcome these shortcomings. Though not implemented for this study, it is possible that similar modifications can be made for the approximate solution outlined here.

It is easy to verify that the three criteria stated above are satisfied by the approximate solution. First, the averages defined by Eqs. (4.65-4.74) satisfy the property that $\tilde{\mathbf{q}} \to \mathbf{q}$ as $\mathbf{q}_L \to \mathbf{q}_R \to \mathbf{q}$; consequently, the approximate solution properly reduces to the exact solution of the linear Riemann problem in this limit. Second, since the approximate solution was constructed to have the same mathematical structure as the exact solution of the linear Riemann problem, the approximate solution can be considered to be associated with an equivalent linear, constant coefficient system of hyperbolic equations (provided that $\tilde{v}_2 \neq \tilde{v}_1 \pm \tilde{c}_1$ and $\tilde{\phi}_2 \neq 0$). As such, the approximate solution has the same physical interpretation as the solution of the linear Riemann problem, and consists of (at most) nine discontinuous waves separating seven regions of constant state. Third, the jumps in $\mathbf{q}$ and $\mathbf{f}$ across the j^{th} wave are given by

$$[\mathbf{q}]_j = \tilde{\alpha}^{(j)}\tilde{\mathbf{r}}^{(j)}, \tag{4.75}$$

$$[\mathbf{f}]_j = \tilde{\alpha}^{(j)}\tilde{\lambda}^{(j)}\tilde{\mathbf{r}}^{(j)}. \tag{4.76}$$

Thus, the Rankine-Hugoniot relations are satisfied across the discontinuities since

$$[\mathbf{f}]_j = \tilde{\lambda}^{(j)}[\mathbf{q}]_j.$$

A consequence of this property is that, in the event that $\mathbf{q}_L$ and $\mathbf{q}_R$ can be connected by a single shock or contact discontinuity, then the approximate solution agrees with the exact solution of the nonlinear Riemann problem [37, 103]. Lastly, we note that for $\Delta(\phi_1) = 0$ [or $\Delta(\phi_2) = 0$], the governing equations for the gas and solid, given by Eq. (3.7), decouple. Similarly, the approximate Riemann solution given here decouples for the gas and solid, and the resulting approximate solution for each phase reduces to the approximate solution given by Glaister [37] for a single phase non-ideal system.

The implementation of the approximate Riemann solution within the framework of Godunov's methodology is now described. First, the states $\mathbf{q}_L = \mathbf{Q}_k^n$ and $\mathbf{q}_R = \mathbf{Q}_{k+1}^n$ are defined to the left and right of the computational cell boundary located at $\xi_{k+1/2}$; this step is the *projection step* of Godunov's methodology. The solution is then allowed to evolve over a small time increment $\Delta\tau$, and the numerical flux $\mathbf{F}_{k+1/2}$ is computed from the approximate Riemann solution; this step is the *evolution step* of Godunov's methodology. The numerical flux is given by Eq. (4.64) evaluated at $\xi = 0$:

$$\begin{aligned}\mathbf{F}_{k+1/2} &= \mathbf{f}(\mathbf{Q}_k^n) + \left[\sum_{\tilde{\lambda}^{(j)}<0} \tilde{\alpha}^{(j)}\tilde{\lambda}^{(j)}\tilde{\mathbf{r}}^{(j)}\right]_{k+1/2} \\ &= \mathbf{f}(\mathbf{Q}_{k+1}^n) - \left[\sum_{\tilde{\lambda}^{(j)}\geq 0} \tilde{\alpha}^{(j)}\tilde{\lambda}^{(j)}\tilde{\mathbf{r}}^{(j)}\right]_{k+1/2} .\end{aligned} \tag{4.77}$$

These two expressions can be averaged to obtain a third expression for $\mathbf{F}_{k+1/2}$:

$$\mathbf{F}_{k+1/2} = \frac{\mathbf{f}(\mathbf{Q}_k^n) + \mathbf{f}(\mathbf{Q}_{k+1}^n)}{2} - \frac{1}{2}\left[\sum_{j=1}^{9} \tilde{\alpha}^{(j)}|\tilde{\lambda}^{(j)}|\tilde{\mathbf{r}}^{(j)}\right]_{k+1/2} . \tag{4.78}$$

The time increment $\Delta\tau$ is chosen such that waves associated with neighboring Riemann problems do not interact. This restriction leads in a natural way to the Courant-Friedrichs-Lewy (CFL) condition

$$\max_j \left|\frac{\tilde{\lambda}^{(j)}\Delta\tau}{\Delta\xi}\right|_{k+1/2} \leq \kappa; \qquad j = 1, \ldots, 9; \qquad k = 1, 2, \ldots . \tag{4.79}$$

Here, the constant κ, commonly termed the CFL number, lies in the range $0 \leq \kappa \leq 0.5$. The value $\kappa = 0.4$ was used for all computations performed in this study. Once the numerical flux is computed at each cell boundary, the solution at time $\tau^{n+1} = \tau^n + \Delta\tau$ is obtained from Eq. (4.3); this step is the *reconstruction step* of Godunov's methodology. The process is then repeated to further advance the solution in time.

The approximate solution has two deficiencies which must be addressed. First, since all waves are approximated by discontinuities, rarefaction waves, which have a continuous structure, are not accurately represented. This deficiency poses no difficulty except for the case when a gas or solid sonic point exists within a gas or solid rarefaction wave, respectively. Second, the approximate solution is not uniformly valid since the eigenvector expansions given by Eqs. (4.39) and (4.40) break down near the singularities $\tilde{v}_2 = \tilde{v}_1 \pm \tilde{c}_1$ and $\phi_2 = 0$. Numerical experiments have shown this deficiency to result in severe numerical instabilities near these points.

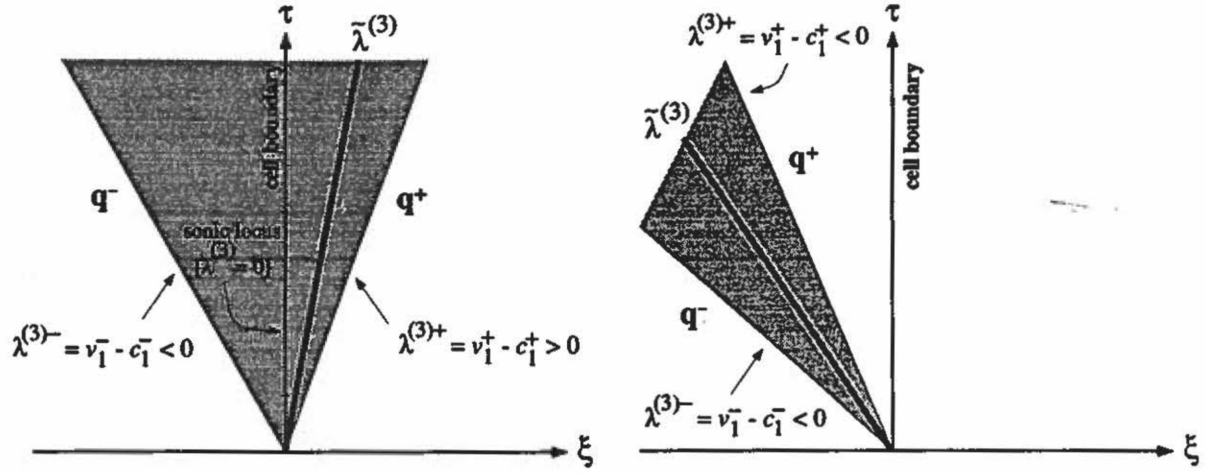

(a) (b)

Figure 4.6: Illustration of a (a) "sonic" rarefaction and a (b) "normal" rarefaction occurring in the gas acoustic field associated with backward propagating waves.

Both a "sonic" rarefaction and a "normal" rarefaction in the backward propagating gas acoustic field are illustrated in Fig. 4.6. Similar rarefactions may also exist in the forward propagating gas acoustic field, and in the solid acoustic fields. Here, a normal rarefaction refers to any rarefaction that is not a sonic rarefaction. The gas rarefaction shocks associated with the approximate Riemann solution are indicated by bold lines in this figure. These waves propagate at speed $\tilde{\lambda}^{(3)} = \tilde{v}_1 - \tilde{c}_1$. The predicted constant states immediately to the left and right of the rarefaction shocks are denoted as $\mathbf{q}^-$ and $\mathbf{q}^+$, respectively (quantities associated with each of these states are labeled with superscript "$-$" and "$+$"). The rarefaction shocks approximate the continuous rarefaction structures denoted by the shaded regions in this figure. As such, $\mathbf{q}^-$ and $\mathbf{q}^+$ are approximations for the constant states to the left and right of the continuous structures. As seen in Fig. 4.6(a), a sonic rarefaction occurs if $v_1^- - c_1^- < 0 < v_1^+ - c_1^+$; consequently, the sonic condition $v_1 = c_1$ is locally satisfied along the characteristic ray $\dfrac{\xi}{\tau} = 0$. For this case, the flux through the computational cell boundary located at $\xi = 0$ is not accurately predicted by the approximate Riemann solution. The flux predicted by the approximate solution is associated with the state $\mathbf{q}^-$ immediately to the left of the rarefaction shock, whereas the correct flux is associated with the constant state along the characteristic ray $\frac{\xi}{\tau} = 0$. This difficulty does not exist for the case illustrated in Fig. 4.6(b) since both the predicted and correct flux at the cell boundary are associated with the state $\mathbf{q}^+$. As might be expected, entropy violating rarefaction shocks are predicted by the numerical method when sonic rarefactions occur in the solution of the local Riemann problems. Although normal rarefactions are also approximated by rarefaction shocks, this approximation has no adverse effect on the global solution.

Various techniques can be used to modify the numerical flux at computational cell boundaries where a sonic rarefaction is predicted [45, 101]. Here, we use the technique proposed by Harten and Hyman [45], which is discussed in detail by LeVeque [72]. To this end, the entropy criterion given by Eq. (3.69) is used to detect sonic rarefactions in both the gas and solid; i.e., if $\lambda^{(j)-} < 0 < \lambda^{(j)+}$. If a sonic rarefaction is detected in the p^{th} characteristic field, then we replace the single jump $\tilde{\alpha}^{(p)}\mathbf{r}^{(p)}$ propagating at speed $\tilde{\lambda}^{(p)}$ with two jumps propagating at speeds $\lambda^{(p)-}$ and $\lambda^{(p)+}$. The jumps across these newly defined waves are constructed such that conservation is maintained across the entire wave system [i.e., such that Eqs. (4.39) and (4.40) are satisfied]. This idea can be conceptualized using Fig. 4.6(a). In this figure, the rarefaction shock propagating at speed $\tilde{\lambda}^{(3)}$ is replaced by two waves propagating at speeds $\lambda^{(3)-}$ and $\lambda^{(3)+}$. The shaded region between these two waves is associated with a new constant state which is defined in such a way that conservation is maintained. This new state provides a better estimate for the flux through the computational cell boundary located at $\xi = 0$, thereby eliminating the prediction of entropy violating rarefaction shocks. The modified flux, denoted by superscript "†", is given by

$$\mathbf{F}^{\dagger}_{k+1/2} = \frac{\mathbf{f}(\mathbf{Q}^n_k) + \mathbf{f}(\mathbf{Q}^n_{k+1})}{2} - \frac{1}{2}\left[\sum_{\substack{j=1\\ j\neq p}}^{9} \tilde{\alpha}^{(j)}\left|\tilde{\lambda}^{(j)}\right|\tilde{\mathbf{r}}^{(j)} + 2\left(\bar{\bar{\lambda}}^{(p)+} - \bar{\bar{\lambda}}^{(p)-}\right)\tilde{\alpha}^{(p)}\tilde{\mathbf{r}}^{(p)}\right]_{k+1/2}, \tag{4.80}$$

where

$$\bar{\bar{\lambda}}^{(p)-} = \lambda^{(p)-}\left(\frac{\lambda^{(p)+} - \tilde{\lambda}^{(p)}}{\lambda^{(p)+} - \lambda^{(p)-}}\right), \qquad \bar{\bar{\lambda}}^{(p)+} = \lambda^{(p)+}\left(\frac{\tilde{\lambda}^{(p)} - \lambda^{(p)-}}{\lambda^{(p)+} - \lambda^{(p)-}}\right).$$

Within the context of the approximate Riemann solution, the sonic singularities $\tilde{v}_2 = \tilde{v}_1 \pm \tilde{c}_1$ occur when the discontinuity in volume fraction, propagating at speed $\tilde{v}_2$, impinges upon either a gas shock or rarefaction, propagating at speed $\tilde{v}_1 + \tilde{c}_1$ or $\tilde{v}_1 - \tilde{c}_1$. For such cases, there may exist complicated wave interactions which are not predicted by the approximate solution. As shown by Keyfitz and Kranzer [58] , these interactions may result in a series of additional waves being produced, with the solution of the Riemann problem consisting of multiple waves in a single characteristic field. For the approximate solution formulated in this chapter, it was implicitly assumed that a physically relevant unique solution exists which consists of at most nine waves, one associated with each characteristic field; as such, this assumption may be invalid near the sonic singularities. In order to properly address this issue, a more detailed analysis of the Riemann problem would be required. Here, we accept some uncertainty and choose to only suppress numerical instabilities which are known to occur near these singularities. Also, we note that if no jump in volume fraction exists [i.e., $\Delta(\phi_2) = \Delta(\phi_2) = 0$], then the sonic singularities are inconsequential since the quantities $\tilde{\alpha}^{(2)}\tilde{\mathbf{r}}^{(2)}$, $\tilde{\alpha}^{(3)}\tilde{\mathbf{r}}^{(3)}$, and $\tilde{\alpha}^{(7)}\tilde{\mathbf{r}}^{(7)}$ remain well-defined. This result is easily seen from the definitions given in Eqs. (4.42-4.59).

General modifications to the Godunov methodology which are needed to suppress numerical instabilities resulting from a loss of hyperbolicity are discussed by Bell et al. [12]. To avoid numerical difficulties near the singularities $v_2 = v_1 \pm c_1$, we adopt a technique which is similar to that proposed in Reference [12]. In particular, we assume that a sonic singularity exists if the following criterion is satisfied:

$$|\tilde{v}_2 - (\tilde{v}_1 \pm \tilde{c}_1)| < c_\epsilon, \tag{4.81}$$

where c_ϵ is a small positive constant. The value $c_\epsilon = 0.017$ ($\hat{c}_\epsilon = 50\ m/s$) was used for all computations performed in this study. In such instances, we collapse the waves propagating at speed $\tilde{v}_2$ and $\tilde{v}_1 + \tilde{c}_1$ or $\tilde{v}_1 - \tilde{c}_1$ (whichever wave is involved) into a single wave propagating at speed $\tilde{\lambda}^{(\ddagger)} = (\tilde{v}_2 + \tilde{v}_1 \pm \tilde{c}_1)/2$. The jump across this wave, $\tilde{\alpha}^{(\ddagger)}\tilde{\mathbf{r}}^{(\ddagger)}$, is then defined in terms of both the difference $\mathbf{Q}_{k+1}^n - \mathbf{Q}_k^n$ and the jumps across the waves not associated with the sonic singularity. For example, if the singularity is associated with the gas wave propagating at speed $\tilde{\lambda}^{(3)} = \tilde{v}_1 - \tilde{c}_1$, then the following quantities are defined:

$$\begin{aligned}
\tilde{\lambda}^{(\ddagger)} &\equiv \frac{\tilde{v}_2 + \tilde{v}_1 - \tilde{c}_1}{2}, \\
\tilde{\alpha}^{(\ddagger)} &\equiv \left\| \Delta(\mathbf{q}) - \tilde{\alpha}^{(1)}\tilde{\mathbf{r}}^{(1)} - \tilde{\alpha}^{(2)}\mathbf{r}^{(2)} - \tilde{\alpha}^{(5)}\tilde{\mathbf{r}}^{(5)} - \tilde{\alpha}^{(6)}\tilde{\mathbf{r}}^{(6)} \right\|, \\
\tilde{\mathbf{r}}^{(\ddagger)} &\equiv \frac{\Delta(\mathbf{q}) - \tilde{\alpha}^{(1)}\tilde{\mathbf{r}}^{(1)} - \tilde{\alpha}^{(2)}\mathbf{r}^{(2)} - \tilde{\alpha}^{(5)}\tilde{\mathbf{r}}^{(5)} - \tilde{\alpha}^{(6)}\tilde{\mathbf{r}}^{(6)}}{\left\| \Delta\mathbf{q} - \tilde{\alpha}^{(1)}\tilde{\mathbf{r}}^{(1)} - \tilde{\alpha}^{(2)}\mathbf{r}^{(2)} - \tilde{\alpha}^{(5)}\tilde{\mathbf{r}}^{(5)} - \tilde{\alpha}^{(6)}\tilde{\mathbf{r}}^{(6)} \right\|},
\end{aligned} \tag{4.82}$$

where $\| \bullet \|$ is the Euclidean norm. Consequently,

$$\mathbf{Q}_{k+1}^n - \mathbf{Q}_k^n = \sum_{j=1,2,5,6,\ddagger} \tilde{\alpha}^{(j)}\tilde{\mathbf{r}}^{(j)} \tag{4.83}$$

by construction. The following modified numerical flux, denoted by superscript "‡", is proposed:

$$\mathbf{F}_{k+1/2}^{\ddagger} = \frac{\mathbf{f}(\mathbf{Q}_k^n) + \mathbf{f}(\mathbf{Q}_{k+1}^n)}{2} - \frac{1}{2}\left[\sum_{j=1,2,5,6,\ddagger} \tilde{\alpha}^{(j)} |\tilde{\lambda}^{(j)}| \tilde{\mathbf{r}}^{(j)} \right]_{k+1/2}. \tag{4.84}$$

A similar result holds if the singularity is associated with the gas wave propagating at speed $\tilde{\lambda}^{(2)} = \tilde{v}_1 + \tilde{c}_1$. Though the Rankine-Hugoniot relations are not identically satisfied by this newly defined wave (i.e., $[\mathbf{f}]_\ddagger \neq \tilde{\lambda}^{(\ddagger)}[\mathbf{q}]_\ddagger$), they are nearly satisfied; this has been numerically verified. Comparisons of numerical predictions with exact steady solutions for two-phase detonation structures possessing these sonic singularities indicate that this error is inconsequential.

In order to suppress numerical instabilities near $\phi_2 = 0$, it is necessary to constrain ϕ_2 to be greater than a constant minimum value $\phi_{2\epsilon}$. The value $\phi_{2\epsilon} = 1 \times 10^{-5}$ was used for all computations performed in this study. As discussed in Section 4.3, this is achieved by terminating combustion for $\phi_2 \leq \phi_{2\epsilon}$.

4.1.3 Higher-Order Spatial and Temporal Accuracy

The upwind numerical method outlined in the previous subsection has only nominal first-order spatial accuracy, and has first-order temporal accuracy. First-order spatial accuracy is characteristic of all Godunov-based methods for which the initial state within each computational cell is assumed constant in the *projection step*. In this subsection, the approaches used to increase both the spatial and temporal accuracy of the method are given.

Two techniques are commonly used to extend the spatial accuracy of Godunov-based numerical methods [51]: *variable extrapolation* and *flux extrapolation*. Both of these techniques extrapolate information from cells neighboring each grid point in the computational domain in order to locally define a higher-order numerical flux at each cell boundary. The variable extrapolation technique achieves increased accuracy by directly relaxing the constant state assumption used in the *projection step* of Godunov's methodology. This technique allows for a linear or parabolic variation in the initial state within each computational cell, subject to the constraint that the average value of the initial state satisfies Eq. (4.8). A comprehensive description of the variable extrapolation technique is given in Reference [51]. The flux extrapolation technique, which is used in this study, is described below.

The basic premise of the flux extrapolation technique is to define a higher-order numerical flux by extrapolating the exact fluxes $\mathbf{f}_k = \mathbf{f}(\mathbf{Q}_k^n)$, evaluated at the cell center locations ξ_k, to the cell boundaries. To this end, we decompose $\mathbf{f}_k$ into the following:

$$\mathbf{f}_k = \mathbf{f}_k^{(f)} + \mathbf{f}_k^{(b)}, \tag{4.85}$$

where $\mathbf{f}_k^{(f)}$ and $\mathbf{f}_k^{(b)}$ are fluxes associated with forward and backward propagating waves, respectively. As shown in Fig. 4.7, the fluxes $\mathbf{f}_k^{(f)}$ are then extrapolated forward using first-order upwind differencing to estimate $\mathbf{f}^{(f)}$ at the cell boundary located at

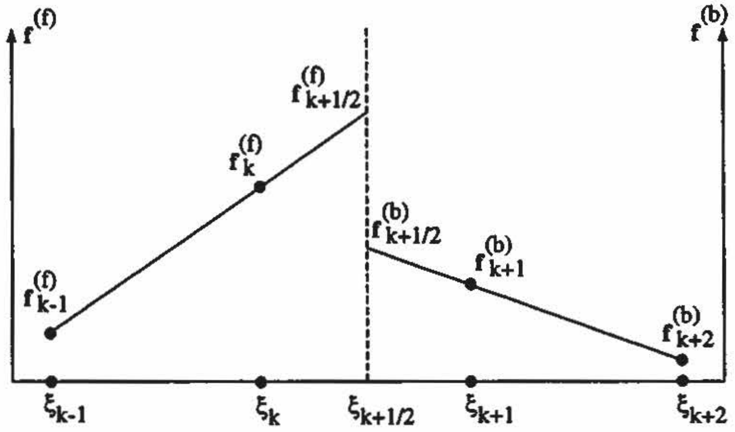

Figure 4.7: Illustration of the flux extrapolation technique used to define the second-order numerical flux.

$\xi_{k+1/2}$:

$$\mathbf{f}^{(f)}_{k+1/2} = \mathbf{f}^{(f)}_{k} + \frac{1}{2}\left(\mathbf{f}^{(f)}_{k} - \mathbf{f}^{(f)}_{k-1}\right). \tag{4.86}$$

Similarly, the fluxes $\mathbf{f}^{(b)}$ are extrapolated backwards using first-order upwind differencing to estimate $\mathbf{f}^{(b)}$ at the cell boundary located at $\xi_{k+1/2}$:

$$\mathbf{f}^{(b)}_{k+1/2} = \mathbf{f}^{(b)}_{k+1} - \frac{1}{2}\left(\mathbf{f}^{(b)}_{k+2} - \mathbf{f}^{(b)}_{k+1}\right). \tag{4.87}$$

The higher-order numerical flux, denoted by superscript "(2)", is defined as

$$\begin{aligned}\mathbf{F}^{(2)}_{k+1/2} &= \mathbf{f}^{(f)}_{k+1/2} + \mathbf{f}^{(b)}_{k+1/2} \\ &= \mathbf{f}^{(f)}_{k} - \mathbf{f}^{(b)}_{k+1} + \frac{1}{2}\left[\left(\mathbf{f}^{(f)}_{k} - \mathbf{f}^{(f)}_{k-1}\right) - \left(\mathbf{f}^{(b)}_{k+2} - \mathbf{f}^{(b)}_{k+1}\right)\right].\end{aligned} \tag{4.88}$$

The use of this flux in Eq. (4.3) results in a spatially second-order accurate method. Higher-order spatial accuracy (> 2) can be obtained through the use of high-order upwind differencing in the extrapolation steps.

It now remains to express the second-order flux in terms of the information provided by the approximate Riemann solution. To this end, the following contributions from forward and backward propagating waves to the flux difference $\mathbf{f}_R - \mathbf{f}_L$ given by Eq. (4.40) are defined:

$$\mathbf{f}^{(f)}_{k+1} - \mathbf{f}^{(f)}_{k} = \left[\sum_{\tilde{\lambda}^{(j)}<0} \tilde{\alpha}^{(j)}\tilde{\lambda}^{(j)}\tilde{\mathbf{r}}^{(j)}\right]_{k+1/2} = \sum_{j=1}^{9} d\mathbf{f}^{(j+)}_{k+1/2}, \tag{4.89}$$

$$\mathbf{f}^{(b)}_{k+1} - \mathbf{f}^{(b)}_{k} = \left[\sum_{\tilde{\lambda}^{(j)}>0} \tilde{\alpha}^{(j)}\tilde{\lambda}^{(j)}\tilde{\mathbf{r}}^{(j)}\right]_{k+1/2} = \sum_{j=1}^{9} d\mathbf{f}^{(j-)}_{k+1/2}, \tag{4.90}$$

where

$$d\mathbf{f}^{(j\pm)}_{k+1/2} = \tilde{\alpha}^{(j)}\tilde{\lambda}^{(j\pm)}\tilde{\mathbf{r}}^{(j)}, \tag{4.91}$$

and

$$\tilde{\lambda}^{(j\pm)} = \frac{\tilde{\lambda}^{(j)} \pm |\tilde{\lambda}^{(j)}|}{2}. \tag{4.92}$$

Using these definitions, the second expression in Eq. (4.88) can be re-expressed as the following after performing some simple algebra:

$$\mathbf{F}^{(2)}_{k+1/2} = \mathbf{F}^{(L)}_{k+1/2} + \frac{1}{2}\sum_{j=1}^{9}\left(d\mathbf{f}^{(j+)}_{k-1/2} - d\mathbf{f}^{(j-)}_{k+3/2}\right), \tag{4.93}$$

where $\mathbf{F}^{(L)}_{k+1/2}$ denotes the lower-order numerical flux defined in Eqs. (4.77) and (4.78). Thus, the second-order flux can be interpreted as the sum of a lower-order flux and a corrective flux, the latter given by the summation terms in Eq. (4.93). The corrective flux is often termed the anti-diffusive flux since it counteracts the numerical diffusion inherent in the lower-order flux to give a spatially second-order accurate method.

Though Eq. (4.93) is a fully upwind numerical flux, additional modification of this flux is needed to suppress the generation of spurious oscillations near discontinuities; such oscillations are characteristic of higher-order numerical methods. This modification requires that the corrective flux terms in Eq. (4.93) be limited in a nonlinear manner based on some measure of the local variation in the predicted solution. The variation in the flux differences $d\mathbf{f}^{(j\pm)}$ at neighboring cell boundaries provide such a measure. The corrective flux is limited such that 1) sufficient numerical diffusion exists in the numerical flux to prevent the generation of spurious oscillations in regions where the solution is rapidly changing (i.e., near discontinuities), and 2) no numerical diffusion exists in the numerical flux in regions of continuous flow resulting in spatially second-order accurate predictions. This idea forms the basis of second-order accurate total variation diminishing (TVD) numerical methods [26, 51, 72, 113].

Total variation diminishing numerical methods are designed to mimic the TVD property of scalar conservation laws [46, 51, 113]. Here, the total variation TV in the solution $q(\xi, \tau)$ of the scalar conservation law $\dfrac{\partial q}{\partial \tau} + \dfrac{\partial f(u)}{\partial \xi} = 0$ is defined as

$$TV\left(q(\xi, \tau))\right) = \int \left| \frac{\partial q(\xi, \tau)}{\partial \xi} \right| d\xi. \tag{4.94}$$

An important property of this scalar conservation law is that the total variation in the solution of the initial-value problem is bounded in time by the initial data $q(\xi, 0)$, i.e.

$$TV\left(q(\xi, \tau)\right) \leq TV\left(q(\xi, 0)\right), \tag{4.95}$$

for all $\tau > 0$. The discrete forms of Eqs. (4.94) and (4.95) are

$$TV(Q^n) = \sum_k \left| Q_k^n - Q_{k-1}^n \right|, \tag{4.96}$$

$$TV(Q^{n+1}) \leq TV(Q^n), \tag{4.97}$$

where Q^n and Q^{n+1} are numerical approximations of the scalar q at times τ^n and τ^{n+1}, respectively. Thus, it is easy to conceptualize that oscillations near discontinuities for this scalar conservation law locally violate the discrete form of the TVD principle [Eq. (4.97)]. If the numerical method for predicting Q^{n+1} is TVD, then no new extrema are generated, and the value of local maxima (minima) are non-increasing (non-decreasing). Though the TVD property only formally holds for scalar conservation laws and one-dimensional systems of linear hyperbolic equations, in practice this concept has been successfully used to develop high-resolution TVD numerical methods for coupled nonlinear systems of conservation laws.

Using the methodology of Chakravarthy and Osher [26] for obtaining second-order TVD methods, the corrective flux terms in Eq. (4.93) are modified as follows:

$$\mathbf{F}_{k+1/2}^{(H)} = \mathbf{F}_{k+1/2}^{(L)} + \frac{1}{2} \sum_{j=1}^{9} \left(d\breve{\mathbf{f}}_{k-1/2}^{(j+)} - d\breve{\breve{\mathbf{f}}}_{k+3/2}^{(j-)} \right), \tag{4.98}$$

where

$$d\breve{\mathbf{f}}_{k-1/2}^{(j+)} = L \left\{ \left[\tilde{\lambda}^{(j+)} \tilde{\alpha}^{(j)} \right]_{k-1/2}, \left[\tilde{\lambda}^{(j+)} \tilde{\alpha}^{(j)} \right]_{k+1/2} \right\} \tilde{\mathbf{r}}_{k+1/2}^{(j)}, \tag{4.99}$$

$$d\breve{\check{\mathbf{f}}}^{(j-)}_{k+3/2} = L\left\{\left[\tilde{\lambda}^{(j-)}\tilde{\alpha}^{(j)}\right]_{k+3/2}, \left[\tilde{\lambda}^{(j-)}\tilde{\alpha}^{(j)}\right]_{k+1/2}\right\}\tilde{\mathbf{r}}^{(j)}_{k+1/2}. \tag{4.100}$$

Here, the operator $L\{x, y\}$ is a nonlinear flux limiter which limits the amount of numerical diffusion in $\mathbf{F}^{(H)}_{k+1/2}$ based on the approximate Riemann solution at cell boundaries located immediately to the left ($\xi_{k-1/2}$) and right ($\xi_{k+3/2}$) of the boundary located at $\xi_{k+1/2}$. The flux limiter used in this study is referred to as Van Leer's limiter [113, 119] which is given by

$$L\{x, y\} = \frac{xy + |xy|}{x + y}. \tag{4.101}$$

Other limiters exist [51] which could be used in place of Van Leer's limiter; such limiters include that of Van Albada [118], that of Roe [102], and that of Sweby [113]. Which limiter is used is, to a certain extent, a matter of personal preference since they all reasonably capture discontinuities without the generation of spurious oscillations (though certain limiters may be more computationally expensive to use due to logical evaluations in the computer algorithm). Van Leer's limiter was chosen for this study based on numerical simulations which have shown that it can accurately capture discontinuities in both the gas and solid.

The use of the flux given by Eq. (4.98) in Eq. (4.3) results in an explicit TVD numerical method which has nominally second-order spatial accuracy in smooth regions of the flow, first order spatial accuracy near discontinuities, and first order temporal accuracy. Though the non-TVD second-order flux given by Eq. (4.93) results in an unconditionally unstable method, the TVD flux given by Eq. (4.98) results in a conditionally stable method provided that an additional constraint on the time step $\Delta\tau$ is satisfied (i.e., in addition to the CFL condition) [26]. Thus, it is desirable to increase the temporal accuracy of the method in order to obtain better stability properties and to eliminate the need to satisfy an additional time step constraint. To this end, the following two-step Runge-Kutta predictor/corrector algorithm is used to advance the solution from τ^n to $\tau^{n+1} = \tau^n + \Delta\tau$ [50]:

$$\begin{aligned} \bar{\mathbf{Q}}_k &= \mathbf{Q}_k^n - \frac{\Delta\tau}{2\Delta\xi}\left[\mathbf{F}_{k+1/2}^{(H)}(\mathbf{Q}^n) - \mathbf{F}_{k-1/2}^{(H)}(\mathbf{Q}^n)\right], \\ \mathbf{Q}_k^{n+1} &= \mathbf{Q}_k^n - \frac{\Delta\tau}{\Delta\xi}\left[\mathbf{F}_{k+1/2}^{(H)}(\bar{\mathbf{Q}}) - \mathbf{F}_{k-1/2}^{(H)}(\bar{\mathbf{Q}})\right]. \end{aligned} \tag{4.102}$$

Here, the first step is the predictor step whereby the solution is allowed to evolve over the time interval $\frac{\Delta\tau}{2}$, and the second step is the corrector step in which the updated solution is computed using the numerical flux of Eq. (4.98) evaluated in terms of the intermediate solution $\bar{\mathbf{Q}}$. Both the predictor and corrector steps are expressed in the conservative form of Eq. (4.3); as such, conservation is maintained. The resulting method is second-order accurate in time.

4.2 Numerical Solution of the Full Two-Phase Equations

In this section, the numerical solution of the full two-phase model equations [Eq. (3.7)] is considered. In addition to being able to accurately predict the effects of gas and solid convection, it is necessary that the numerical method accurately predict the effects of phase interaction processes, and the influence of these processes on convection.

The numerical approach used in this study to solve the full model equations is based on the following time-step splitting procedure [112, 128]:

$$\mathbf{Q}^{n+1} = \mathcal{L}_c^{\Delta\tau/2}\mathcal{L}_s^{\Delta\tau}\mathcal{L}_c^{\Delta\tau/2}\mathbf{Q}^n.$$

Here, $\mathbf{Q}^n$ and $\mathbf{Q}^{n+1}$ are the numerical solution at times τ^n and τ^{n+1}, respectively, $\mathcal{L}_c^{\Delta\tau/2}$ is the convective numerical operator, and $\mathcal{L}_s^{\Delta\tau}$ is the source numerical operator. The convective operator solves the convection problem using the high-resolution TVD method formulated in the previous section, and the source operator, which is described below, solves the phase interaction terms using a high-order time accurate stiff ordinary differential equation solver. During the convection steps, the phase interaction processes are suppressed [i.e., $\mathbf{g}(\mathbf{q}) = 0$ in Eq. (3.7)]; likewise, gas and solid convection are suppressed during the source step [i.e., $\dfrac{\partial \mathbf{f}(\mathbf{q})}{\partial \xi} = 0$ in Eq. (3.7)]. The splitting procedure requires that the convection step be performed over one-half of the time step $\Delta\tau$, and that the source step be performed over the full time step, where $\Delta\tau$ is chosen based upon the CFL condition given by Eq. (4.79). However, in practice the integration time increment used in the time-step splitting procedure is increased to $2\Delta\tau$ for better computational efficiency. This results in the modified procedure

$$\mathbf{Q}_k^{n+2} = \mathcal{L}_c^{\Delta\tau}\mathcal{L}_s^{2\Delta\tau}\mathcal{L}_c^{\Delta\tau}\mathbf{Q}_k^n. \tag{4.103}$$

Provided that the ordinary differential equation solver is at least second-order accurate in time, the splitting procedure given by Eq. (4.103) results in a approximation which is nominally second order accurate in both space and time.

To account for phase interaction processes, the following system of ordinary differential equations, obtained by setting $\dfrac{\partial \mathbf{f}}{\partial \xi} = 0$ in Eq. (3.7), must be solved over the time interval $2\Delta\tau$ at each computational grid point:

$$\frac{d}{d\tau}[\rho_1\phi_1] = C_m, \tag{4.104}$$

$$\frac{d}{d\tau}[\rho_1\phi_1 v_1] = v_2 C_m + C_d - \rho_1\phi_1\frac{dv_p}{d\tau}, \tag{4.105}$$

$$\frac{d}{d\tau}\left[\rho_1\phi_1\left(e_1 + \frac{v_1^2}{2}\right)\right] = \left(e_2 + \frac{v_2^2}{2}\right)C_m + v_2 C_d + C_e - \rho_1\phi_1 v_1\frac{dv_p}{d\tau}, \tag{4.106}$$

$$\frac{d}{d\tau}[\rho_2\phi_2] = -\pi_5 C_m, \tag{4.107}$$

$$\frac{d}{d\tau}[\rho_2\phi_2 v_2] = -\pi_5 v_2 C_m - \pi_5 C_d - \rho_2\phi_2\frac{dv_p}{d\tau}, \tag{4.108}$$

$$\frac{d}{d\tau}\left[\rho_2\phi_2\left(e_2 + \frac{v_2^2}{2}\right)\right] = -\pi_5\left(e_2 + \frac{v_2^2}{2}\right)C_m - \pi_5 v_2 C_d - \pi_5 C_e - \rho_2\phi_2 v_2\frac{dv_p}{d\tau}, \tag{4.109}$$

$$\frac{d}{d\tau}\left[\rho_2\phi_2^2\right] = \pi_7\rho_2\phi_1\phi_2^2\left(P_2 - \pi_5 P_1 - f\right) - 2\pi_5\phi_2 C_m, \tag{4.110}$$

$$\frac{dn}{d\tau} = 0, \tag{4.111}$$

$$\frac{d}{d\tau}[\rho_2\phi_2 I] = \rho_2\phi_2 C_I - \pi_5 I C_m. \tag{4.112}$$

The definitions for C_m, C_d, C_e, and C_I appearing in these equations are given in Eq. (3.5). Also, since the motion of the piston is a prescribed function of time, the piston acceleration terms in these equations are treated as time dependent forcing terms.

Equations (4.104-4.112) can be reduced to a non-autonomous system of five ordinary differential equations having the form

$$\frac{d\mathbf{y}_s}{d\tau} = \mathbf{h}_s(\mathbf{y}_s, \tau), \tag{4.113}$$

where $\mathbf{y}_s = [\rho_2, \phi_2, v_2, e_2, I]^T$, and $\mathbf{h}_s$ is a nonlinear vector function of $\mathbf{y}_s$; the explicit dependence of $\mathbf{h}_s$ on τ is due to the piston acceleration terms. To this end, the gas quantities ρ_1, ϕ_1, v_1, and e_1 are first expressed in terms of ρ_2, ϕ_2, v_2, and e_2. Multiplying Eq. (4.104) by π_5, and adding the resulting expression to Eq. (4.107) gives a homogeneous ordinary differential equation for the mixture mass. This equation is directly integrated, and the initial condition applied, to obtain the algebraic expression

$$\pi_5 \rho_1 \phi_1 + \rho_2 \phi_2 = \Omega_k^{n+1}, \tag{4.114}$$

where

$$\Omega_k^{n+1} = [\pi_5 \rho_1 \phi_1 + \rho_2 \phi_2]_k^{n+1}$$

is the constant of integration obtained using the data $\mathbf{Q}_k^{n+1}$ provided by the preceding convection step in Eq. (4.103). Here, the notation subscript "k" is used to indicate that this constant depends upon the grid cell location ξ_k.

Next, Eq. (4.105) is multiplied by π_5, and the resulting expression is added to Eq. (4.108) to obtain

$$\frac{d}{d\tau}\left[\pi_5 \rho_1 \phi_1 v_1 + \rho_2 \phi_2 v_2\right] = -\left(\pi_5 \rho_1 \phi_1 + \rho_2 \phi_2\right) \frac{dv_p}{d\tau}. \tag{4.115}$$

Thus, the momentum of the mixture within each computational cell, measured relative to the piston-attached reference frame, changes due to piston acceleration. If the piston velocity is constant, then the mixture momentum is unchanged. Since the coefficient of the piston acceleration term is constant, as seen from Eq. (4.114), this equation can be directly integrated, and the initial condition applied, to give the algebraic relation

$$\pi_5\rho_1\phi_1 v_1 + \rho_2\phi_2 v_2 = \Psi_k^{n+1} - \Omega_k^{n+1}\left[v_p(\tau) - v_p(\tau^n)\right], \tag{4.116}$$

where

$$\Psi_k^{n+1} = \left[\pi_5\rho_1\phi_1 v_1 + \rho_2\phi_2 v_2\right]_k^{n+1}.$$

In this relation, the initial condition on the piston velocity $v_p(\tau^n)$ is evaluated at the old time since it is held fixed during the convection step.

Lastly, Eq. (4.106) is multiplied by π_5, and the resulting expression is added to Eq. (4.109) to obtain

$$\frac{d}{d\tau}\left[\pi_5\rho_1\phi_1\left(e_1 + \frac{v_1^2}{2}\right) + \rho_2\phi_2\left(e_2 + \frac{v_2^2}{2}\right)\right] = -\left(\pi_5\rho_1\phi_1 v_1 + \rho_2\phi_2 v_2\right)\frac{dv_p}{d\tau}. \tag{4.117}$$

Using the expression given by Eq. (4.116), this equation can be directly integrated to give the algebraic relation

$$\begin{aligned}\pi_5\rho_1\phi_1\left(e_1 + \frac{v_1^2}{2}\right) + \rho_2\phi_2\left(e_2 + \frac{v_2^2}{2}\right) &= \Upsilon_k^{n+1} - \Psi_k^{n+1}\left(v_p(\tau) - v_p(\tau^n)\right) \\ &\quad + \Omega_k^{n+1}\frac{\left[v_p(\tau) - v_p(\tau^n)\right]^2}{2},\end{aligned} \tag{4.118}$$

where

$$\Upsilon_k^{n+1} = \left[\pi_5\rho_1\phi_1\left(e_1 + \frac{v_1^2}{2}\right) + \rho_2\phi_2\left(e_2 + \frac{v_2^2}{2}\right)\right]_k^{n+1}.$$

The algebraic relations given by Eqs. (4.114), (4.116), (4.118), and the saturation condition $\phi_1 = 1 - \phi_2$ are sufficient to express the gas variables as algebraic functions of the desired solid variables. Using the relation $\phi_1 = 1 - \phi_2$, ρ_1 can be directly computed from Eq. (4.114). With both ϕ_1 and ρ_1 known, an expression for v_1 can be obtained from Eq. (4.116). With ϕ_1, ρ_1, and v_1 known, an expression for e_1 can be obtained from Eq. (4.118). Also, the homogeneous ordinary differential equation given by Eq. (4.111) can be directly integrated to give

$$n = n_k^{n+1}; \tag{4.119}$$

thus, the particle number density is constant during the source step.

Equations (4.107-4.110) and (4.112) must now be expressed in the desired vector form. Multiplying Eq. (4.107) by ϕ_2, subtracting the result from Eq. (4.110), and simplifying gives

$$\frac{d\phi_2}{d\tau} = \pi_7\phi_1\phi_2\left(P_2 - \pi_5 P_1 - f\right) - \pi_5\phi_2 C_m. \tag{4.120}$$

Multiplying Eq. (4.120) by ρ_2, subtracting the result from Eq. (4.107), and simplifying gives

$$\frac{d\rho_2}{d\tau} = -\pi_7\rho_2\phi_1\left(P_2 - \pi_5 P_1 - f\right). \tag{4.121}$$

Next, Eq. (4.107) is multiplied by v_2, and the resulting expression is subtracted from Eq. (4.108) to get

$$\frac{dv_2}{d\tau} = -\pi_5\frac{C_d}{\rho_2\phi_2} - \frac{dv_p}{d\tau}. \tag{4.122}$$

Likewise, Eq. (4.107) is multiplied by $e_2 + \frac{v_2^2}{2}$, Eq. (4.122) is multiplied by $\rho_2\phi_2 v_2$, and both of the resulting expressions are subtracted from Eq. (4.109) to get

$$\frac{de_2}{d\tau} = -\pi_5\frac{C_e}{\rho_2\phi_2}. \tag{4.123}$$

Equations (4.120-4.123) show that combustion locally changes the solid volume fraction, compaction changes both the solid volume fraction and the solid density, drag changes the solid velocity, and heat transfer changes the solid internal energy. Obviously, the gas quantities also change due to these processes.

Lastly, we multiply Eq. (4.107) by I, subtract the result from Eq. (4.112), and simplify to get

$$\frac{dI}{d\tau} = C_I. \tag{4.124}$$

Equation (4.113) is in a suitable form to be numerically solved using standard ordinary differential equation solvers. For this study, an implicit stiff solver contained in the software package LSODE (Livermore Solver for Ordinary Differential Equations) [49] was used to numerically integrate these equations. The solver uses a method

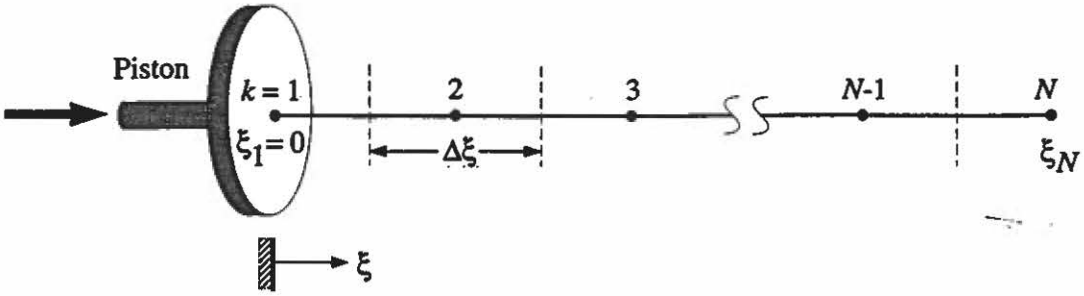

Figure 4.8: Illustration of the computational grid used in piston-initiated DDT simulations.

based on backward differentiation formulæ, and internally generates a full Jacobian matrix (i.e., $\dfrac{\partial \mathbf{h}_s}{\partial \mathbf{y}_s}$) using finite differencing. The solver achieves high-order time accurate approximations by adapting the integration time step such that the truncation error of the scheme meets a user specified tolerance. For the computations performed in this study, an absolute tolerance of 1.0×10^{-9} was used for each component of $\mathbf{y}_s$.

4.3 Initial and Boundary Conditions for the Piston Problem

In this section, the initial and boundary conditions used for the piston problem are given, and the implementation of the boundary conditions within the framework of the time-step splitting procedure is discussed. Here, the computational domain is discretized into uniformly spaced nodes located at the positions $\xi_k = (k-1)\Delta\xi$ $(k = 1, 2, \ldots, N)$, where $\Delta\xi = \xi_N/(N-1)$. An illustration of the computational domain is given in Fig. 4.8.

The computational domain is everywhere initialized to a constant ambient state having zero velocity. The piston is continuously accelerated from rest to a constant velocity of 100 m/s in 2 μs; the piston velocity is given by

$$\hat{v}_p(\hat{\tau}) = \begin{cases} (100\ m/s)\ \sin\left[\dfrac{\pi}{2}\left(\dfrac{\hat{\tau}}{2\ \mu s}\right)\right] & \text{for } 0 < \hat{\tau} \leq 2\ \mu s \\ 100\ m/s & \text{for } \hat{\tau} > 2\ \mu s, \end{cases} \tag{4.125}$$

This rapid acceleration is chosen so that the piston attains its maximum velocity over a time interval which is short relative to the time required for the piston-initiated det-

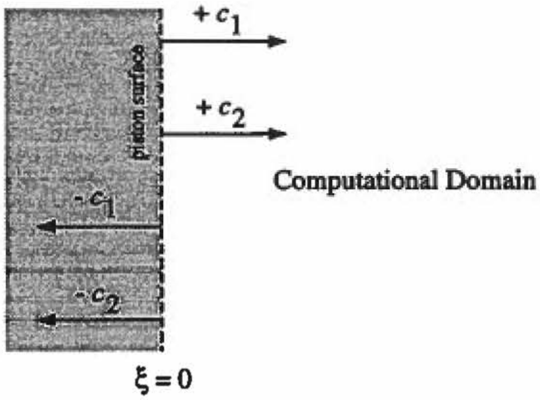

Figure 4.9: Gas and solid characteristics at the piston surface.

onation wave to become fully developed. A maximum piston velocity of 100 m/s is chosen since much of the experimental and numerical deflagration-to-detonation transition (DDT) data reported in the literature have been obtained for piston velocities close to this value [8, 24, 109, 110, 111].

The time-dependent boundary conditions which must be satisfied at the piston surface are easily obtained by requiring the velocity of both the gas and solid, measured relative to the piston, to vanish at this boundary:

$$v_1(0,\tau) = v_2(0,\tau) = 0. \tag{4.126}$$

This requirement is equivalent to enforcing a zero mass flux condition at the piston surface. It is shown in Fig. 4.9 that, for zero gas and solid velocity, only two of the characteristics emanating from the piston surface propagate information into the computational domain. These two characteristics are associated with forward propagating gas and solid acoustic waves. As such, the two conditions given in Eq. (4.126) are the only conditions which can be explicitly enforced at this boundary [35]; all other conditions are a consequence of these two conditions, and must be derived from Eq. (3.7).

In order to determine the equations which must be solved at the piston surface, each component of the derivative $\dfrac{\partial \mathbf{f}}{\partial \xi}$ in Eq. (3.7) is first expanded, and the resulting terms, as well as the source terms in Eq. (3.7), are evaluated for $v_1 = v_2 = 0$. The following evolution equations are obtained for the components q_j $(j = 1, \ldots, 9)$ of the conserved vector $\mathbf{q}$:

$$\frac{\partial q_1}{\partial \tau} + \rho_1 \phi_1 \frac{\partial v_1}{\partial \xi} = C_m, \tag{4.127}$$

$$\frac{\partial q_2}{\partial \tau} = 0, \tag{4.128}$$

$$\frac{\partial q_3}{\partial \tau} + \rho_1 \phi_1 \left(e_1 + \frac{P_1}{\rho_1} \right) \frac{\partial v_1}{\partial \xi} = e_2 C_m + C_e, \tag{4.129}$$

$$\frac{\partial q_4}{\partial \tau} + \rho_2 \phi_2 \frac{\partial v_2}{\partial \xi} = -\pi_5 C_m, \tag{4.130}$$

$$\frac{\partial q_5}{\partial \tau} = 0, \tag{4.131}$$

$$\frac{\partial q_6}{\partial \tau} + \rho_2 \phi_2 \left(e_2 + \frac{P_2}{\rho_2} \right) \frac{\partial v_2}{\partial \xi} = -\pi_5 e_2 C_m - \pi_5 C_e, \tag{4.132}$$

$$\frac{\partial q_7}{\partial \tau} + \rho_2 \phi_2^2 \frac{\partial v_2}{\partial \xi} = \pi_7 \rho_2 \phi_1 \phi_2^2 \left(P_2 - \pi_5 P_1 - f \right) - 2\pi_5 \phi_2 C_m, \tag{4.133}$$

$$\frac{\partial q_8}{\partial \tau} + n \frac{\partial v_2}{\partial \xi} = 0, \tag{4.134}$$

$$\frac{\partial q_9}{\partial \tau} + \rho_2 \phi_2 I \frac{\partial v_2}{\partial \xi} = \rho_2 \phi_2 C_I - \pi_5 I C_m. \tag{4.135}$$

These equations are identical to those which result using the general methodology of Thompson [115] for determining time-dependent boundary conditions for hyperbolic systems.

Equations (4.127-4.135) can be easily solved within the framework of the time-step splitting procedure given by Eq. (4.103) to update the conserved variables at the piston surface in time. For the convective step, the left hand side of Eqs. (4.127-4.135) are numerically solved using a first-order Euler method in time, where the spatial derivatives are discretized using one-sided, second-order differencing. For the source step, the spatial derivatives in Eqs. (4.127-4.135) are set equal to zero, and the resulting system of ordinary differential equations are numerically solved using the package LSODE. To this end, an analysis similar to that used in the preceding section to obtain Eq. (4.113) can be performed to express the resulting differential equations in the form

$$\frac{d}{d\tau}\begin{bmatrix}\rho_2\\ \phi_2\\ v_2\\ e_2\\ I\end{bmatrix}=\begin{bmatrix}-\pi_7\rho_2\phi_1\left(P_2-\pi_5P_1-f\right)\\ \pi_7\phi_1\phi_2\left(P_2-\pi_5P_1-f\right)-\pi_5\phi_2C_m\\ 0\\ -\pi_5\dfrac{C_e}{\rho_2\phi_2}\\ C_I\end{bmatrix}. \tag{4.136}$$

Here, the gas quantities are expressed in terms of the solid variables using the algebraic relations given by Eqs. (4.114), (4.116), and (4.118), evaluated for $v_1 = v_2 = 0$ and $\phi_1 = 1 - \phi_2$.

The upstream boundary condition applied at the location ξ_N is simply

$$\mathbf{Q}_N^{n+2} = \mathbf{Q}_{N-1}^{n+2}. \tag{4.137}$$

Thus, time is restricted such that there is insufficient time for waves generated by the moving piston to reach this boundary.

5

VALIDATION OF THE NUMERICAL METHOD

Comparisons are given in this chapter between numerical predictions and known solutions to three different test cases in order to validate the numerical method. The three test cases include: 1) an inert two-phase shock tube problem; 2) the evolution of an inert shock in both the gas and solid due to compression of the granular material by a moving piston; and 3) the evolution of an inert compaction wave due to compression of the granular material by a moving piston. The first two cases consider gas and solid convection only, whereas the third case couples gas and solid convection with interphase drag, interphase heat transfer, and material compaction. In addition to these test cases, further validation of the numerical method is provided in Chapter 7 whereby numerically predicted two-phase detonation structures are compared with results from the steady-state analysis given in Chapter 6. All computations performed as part of this dissertation were done on an IBM RS 6000 Model 350 workstation.

5.1 Inert Two-Phase Shock Tube Problem

The shock tube problem provides a stringent test for numerical methods used to solve hyperbolic systems of conservation laws since it generally requires the resolution of both contact discontinuities and shocks. As discussed in the previous chapter, the two-phase shock tube problem, also known as the Riemann problem, involves the breakup of a single initial discontinuity separating constant left (L) and right (R) states into self-similar waves consisting of a shock, a rarefaction, and a contact discontinuity in both the gas and the solid. This problem considers convection only; consequently, $\mathbf{g}(\mathbf{q}) = 0$ in Eq. (3.7).

For this simulation, the model equations valid in a fixed laboratory reference frame were solved, where position and velocity are denoted by $\hat{x}$ and $\hat{u}_i$ $(i = 1, 2)$, respectively. Ideal equations of state were used for both the gas and solid $[\hat{P}_1 = \hat{\rho}_1 \hat{R}_1 \hat{T}_1,\ \hat{e}_1 = \hat{c}_{v1} \hat{T}_1;\ \hat{P}_2 = \hat{\rho}_2 \hat{R}_2 \hat{T}_2,\ \hat{e}_2 = \hat{c}_{v2} \hat{T}_2]$ so that the numerical predictions could be compared to existing closed-form analytical solutions. To this end, no jump in volume fraction was prescribed across the initial discontinuity; as such, volume fraction remains constant for all time, and the analytical solution for each phase is simply given by the classical solution to the shock tube problem for a single phase system [28]. Values chosen for the model parameters and the initial conditions are given in TABLE 4.1. Different values for $\hat{c}_{v1}$ and $\hat{c}_{v2}$ were used so that differences in the gas and solid solutions exist. The computational domain used for this simulation $(-5\ m \leq \hat{x} \leq 5\ m)$ was discretized into $N = 200$ uniformly spaced nodes, with the initial discontinuity located at the center of the domain $(\hat{x} = 0\ m)$. The computational run time for this simulation was approximately two minutes.

Shown in Fig. 5.1 is a comparison between the numerically predicted solution and the exact solution at $\hat{\tau} = 6\ ms$. Here, the exact solution is the same solution shown in Fig. 4.3 which was discussed in detail in subsection 5.1.1; consequently, the discussion given here is intentionally brief. For each phase the solution consists of a right-propagating shock wave, followed by a slower right-propagating contact discontinuity, and a left-propagating rarefaction. As a consequence of choosing $\hat{c}_{v2} < \hat{c}_{v1}$, the solid shock and rarefaction propagate faster than those of the gas, while the solid contact discontinuity propagates more slowly than that of the gas. The numerical predictions agree well with the exact solution; both the wave speeds and the magnitudes of the jumps are correctly predicted. Furthermore, the numerical method is able to capture the discontinuities without the generation of spurious oscillations. The shocks are spread over approximately three computational cells, while the contact discontinuities are spread over approximately seven cells. Typically, a larger number of cells are

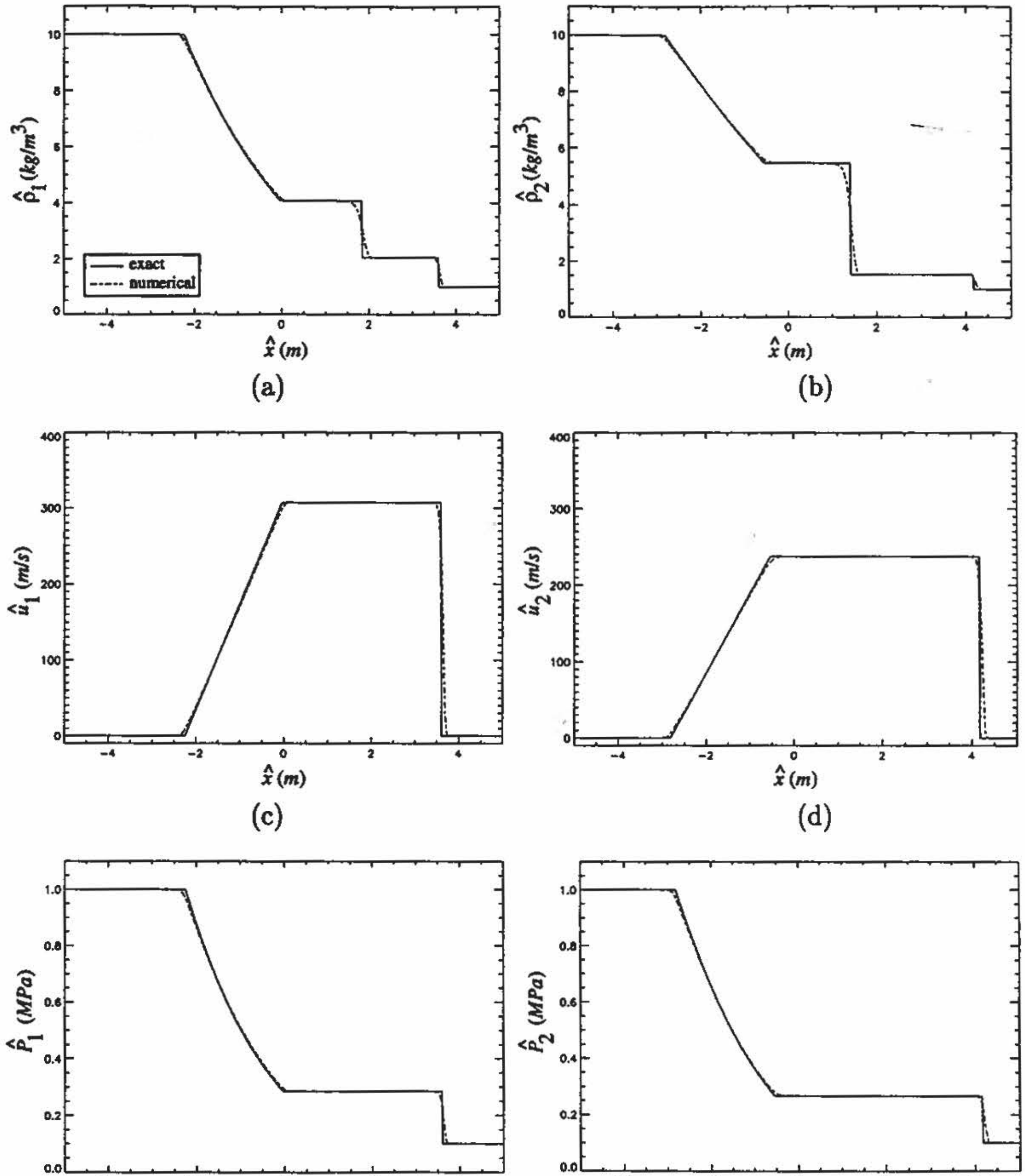

(a) (b)

(c) (d)

(e) (f)

Figure 5.1: Comparison of the predicted and exact solutions for the inert shock-tube problem at $\hat{\tau} = 6\,ms$: (a,b) gas and solid density; (c,d) gas and solid velocity; (e,f) gas and solid pressure; (g,h) gas and solid temperature; and (i) particle number density.

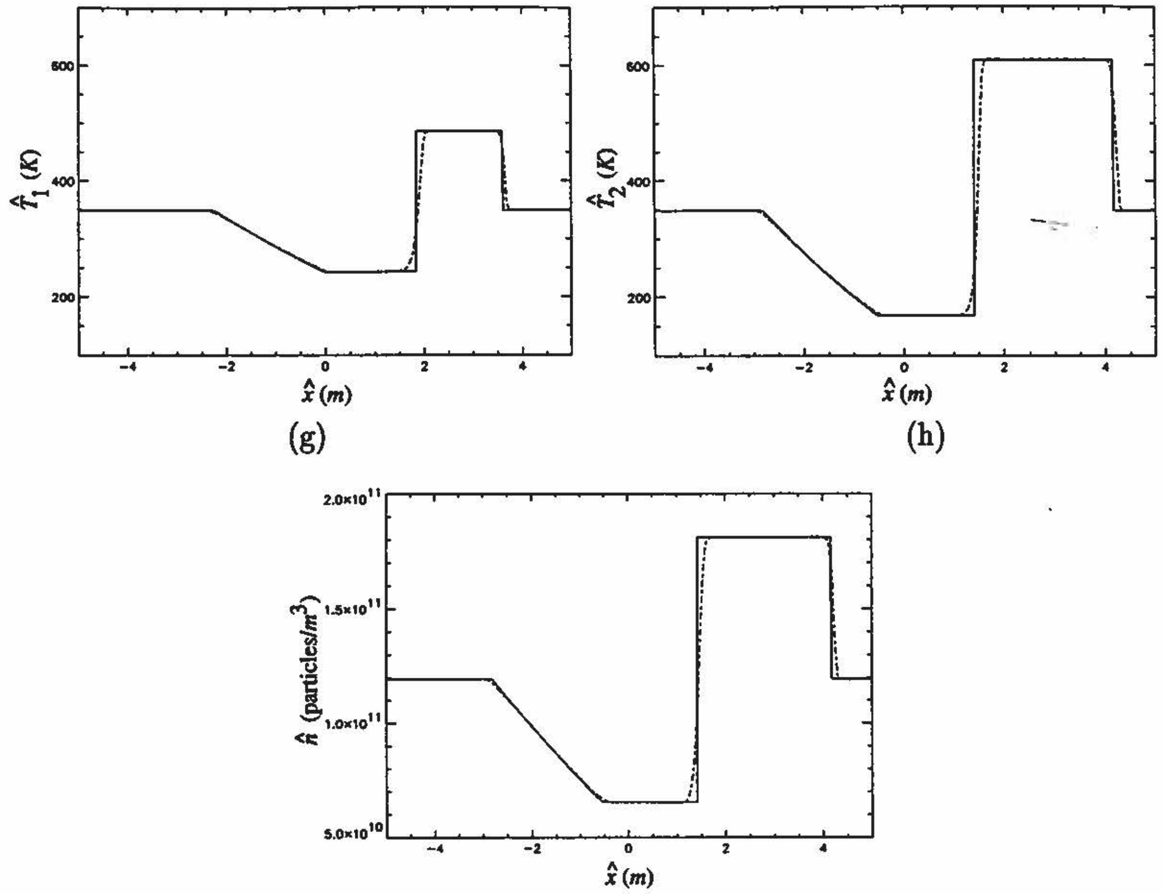

(g) (h)

(i)

Figure 5.1 (Continued)

required by shock-capturing methods to capture discontinuities associated with linearly degenerate characteristic fields (i.e., contact discontinuities). This is due to the absence of a "steepening" mechanism for linearly degenerate fields, such as provided by the coalescence of acoustic waves in genuinely nonlinear acoustic fields [113]. Consequently, numerically predicted spatial profiles for contact discontinuities do not steepen as time evolves.

To investigate the convergence rate of the numerical method, it is necessary to define the error associated with the numerical predictions. Here, the convergence rate is defined as the change in this error with respect to a change in grid resolution; thus, it provides a measure of the spatial accuracy of the method. For the test cases given in this chapter, the error E_i $(i = 1, 2)$ at $\hat{\tau}^n$ is based on either the gas or solid pressure, and is defined by

$$E_i(\hat{\tau}^n) = \sum_{k=1}^{N} \frac{|\hat{P}_{i_k}(\hat{\tau}^n) - \hat{P}_i(\xi_k, \hat{\tau}^n)|}{\hat{P}_i^c}, \tag{5.1}$$

where $\hat{P}_{i_k}(\hat{\tau}^n)$ is the numerically predicted pressure at the nodal location $\tilde{\xi}_k$, $\hat{P}_i(\xi_k, \hat{\tau}^n)$ is the pressure given by the exact solution at this same location, and $\hat{P}_i^c$ is a characteristic pressure used to non-dimensionalize the error. This error is the fractional error used by Woodward and Collela [127] and by Grismer [44] to demonstrate the convergence properties of similar high-resolution numerical methods for the Euler equations. Based on this error, the convergence rate of the numerical method is estimated by decreasing the size of the spatial increment $\Delta\xi$, and determining the corresponding change in the error. Assuming that the error is proportional to the spatial increment raised to some power (i.e., $E_i \propto \Delta\xi^p$), we obtain the proportionality

$$\log(E_i) \propto p \log(\Delta\xi),$$

or, since the spatial increment is proportional to the inverse of the maximum number of nodes N,

$$\log(E_i) \propto p \log\left(\frac{1}{N}\right). \tag{5.2}$$

The convergence rate, given by the exponent p, is estimated by the slope of the best fit line through the data points $(E_i, 1/N)$ plotted in the $\log(1/N)$-$\log E_i$ plane.

Convergence data obtained for the inert shock tube problem are plotted in Fig. 5.2. For simplicity, it was assumed that $\hat{R}_1 = \hat{R}_2 = 287\ J/(kg\ K)$ and $\hat{c}_{v1} = \hat{c}_{v2} = 717.5\ J/(kg\ K)$ for this convergence study. Consequently, identical solutions are obtained for the gas and solid (thus, $E = E_1 = E_2$), both of which are given by the gas phase solution shown in Fig. 5.1. The data were obtained using computational grids for which N was within the range $1000 \leq N \leq 15000$. The characteristic pressure used to non-dimensionalize the error was $\hat{P}_1^c = \hat{P}_2^c = 0.1\ MPa$, the pressure associated with the state to the left of the initial discontinuity. Results of this study show the

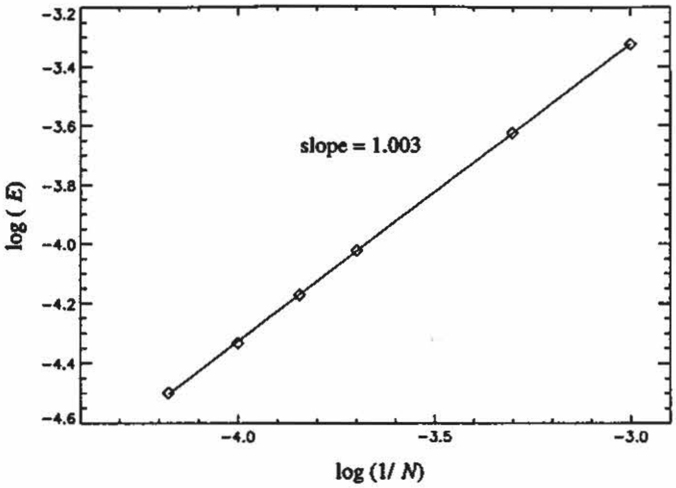

Figure 5.2: Numerical convergence data for the inert shock tube problem.

convergence rate to be $p = 1.003$. The convergence rates reported in References [44, 127], based on the exact solution of the inert shock tube problem for an ideal gas, were also near unity. Though these high-resolution shock-capturing methods have higher spatial accuracy than nominally first-order methods (i.e., the Lax-Friedrichs scheme, Godunov's method, etc.), the accuracy is less than second-order. This result is somewhat expected since these methods reduce to nominally first-order accuracy near discontinuities due to the flux-limiting procedure. For the range of nodal points used in this study, machine round-off error was insignificant.

5.2 Inert Shock Problem

This test case concerns the evolution of a shock in both the gas and solid due to compression of the granular material by a moving piston. Once again, only gas and solid convection are considered. Though phase interaction processes are ignored, the source vector $\mathbf{g}(\mathbf{q})$ is nonzero for early time due to the piston acceleration terms. Here, the piston velocity was prescribed by Eq. (4.125). The virial equation of state given in Appendix G was used for the gas, and the non-ideal Tait equation of state given in Appendix H was used for the solid. Since these state relations are used for the two-phase detonation analyses given in the following chapters, this test demonstrates the

Parameter or Ambient Condition	Value	Units
$\hat{b}$	7.60×10^{-4}	m^3/kg
$\hat{R}_1$	8.50×10^{2}	$J/(kg\ K)$
$\hat{c}_{v1}$	2.40×10^{3}	$J/(kg\ K)$
$\hat{c}_{v2}$	1.50×10^{3}	$J/(kg\ K)$
$\hat{\sigma}$	8.98×10^{6}	m^2/s^2
$\hat{q}$	0	J/kg
γ_2	5.00×10^{0}	
$\hat{r}_o$	1.00×10^{-4}	m
$\hat{T}_o$	3.00×10^{2}	K
$\hat{\rho}_{1o}$	1.00×10^{1}	kg/m^3
$\hat{\rho}_{2o}$	1.71×10^{3}	kg/m^3
ϕ_{2o}	7.00×10^{-1}	

TABLE 5.1: PARAMETER VALUES AND AMBIENT CONDITIONS USED FOR THE INERT SHOCK PROBLEM

ability of the numerical method to accurately capture shocks for the two-phase model system of interest in this research. Values for the parameters and ambient conditions are given in TABLE 5.1. The computational domain used for this simulation ($0\ cm \leq \hat{\xi} \leq 20\ cm$) was discretized into $N = 200$ nodes. The computational run time was approximately two minutes.

The numerically predicted velocity and pressure history for the gas and solid are shown in Fig. 5.3. Here, $\hat{\xi}$ is position measured relative to the piston surface. Initially, a smooth but rapid increase in the velocity and pressure is predicted in both the gas and solid due to the sudden acceleration of the piston. Though not shown here, there also exist rapid increases in the density and temperature of each phase, and and in the particle number density. The volume fraction, however, remains constant since the physical mechanisms which effect changes in volume fraction (i.e., material compaction and combustion) have been ignored. The coalescence of acoustic waves in

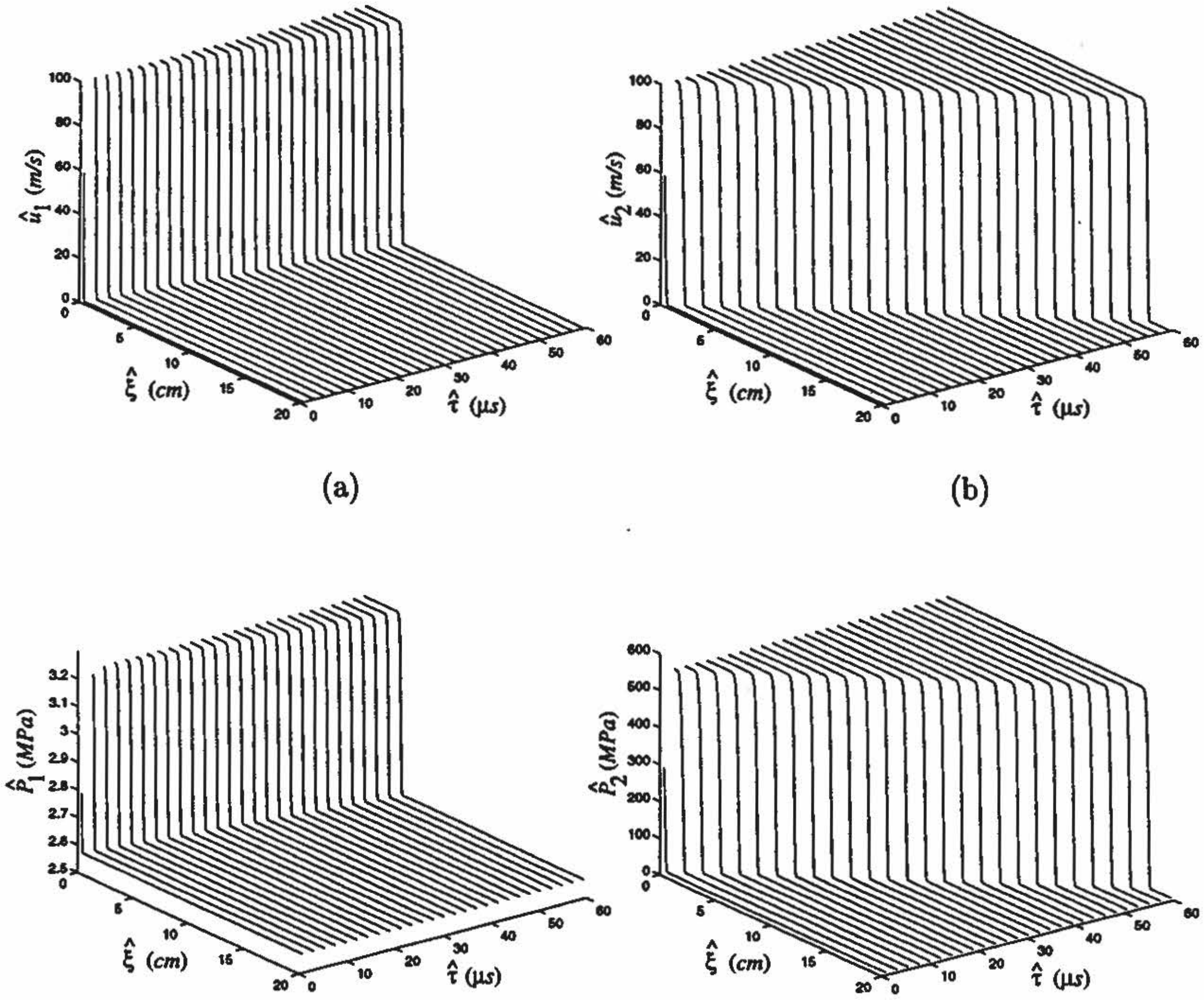

(a)

(b)

(c)

(d)

Figure 5.3: Predicted time histories for the inert shock problem: (a,b) gas and solid velocity, and (c,d) gas and solid pressure.

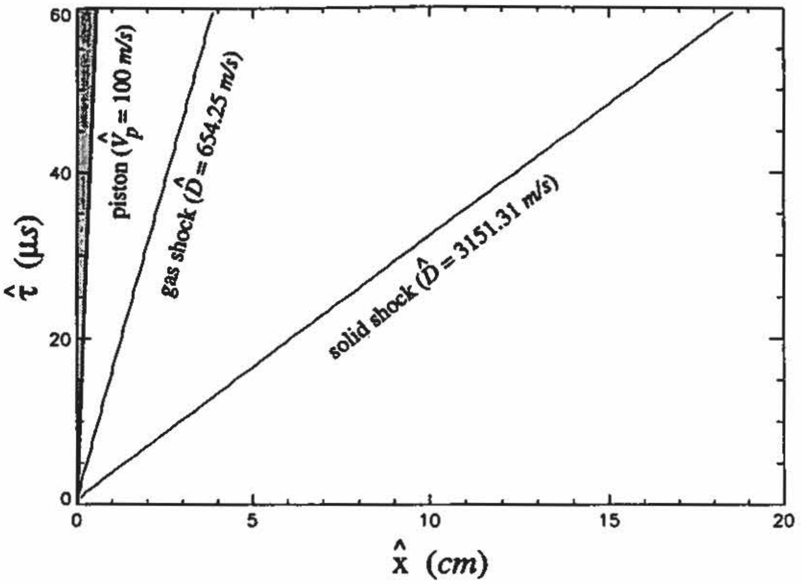

Figure 5.4: Predicted gas and solid shock trajectories for the inert shock problem.

the gas and solid causes the continuous spatial profiles to rapidly steepen, resulting in the formation of shocks. For this simulation, the steepening process occurs on the same time scale as that required for the piston to reach its constant maximum speed ($\sim 2\ \mu s$). Once formed, the shocks propagate away from the piston with uniform speed, creating an ever-widening steady region of shocked flow. The speeds of the gas and solid shocks are computed from the slopes of the shock trajectories in the $\hat{\xi}$-$\hat{\tau}$ plane using a least-squares curve-fitting technique; the trajectories are shown in Fig. 5.4. The numerically predicted speeds for the gas and solid shocks are 654.25 m/s and 3151.31 m/s, respectively.

This problem admits a simple analytical solution for the jumps in the gas and solid variables across their respective fully-developed shocks, as well as for the shock speeds. Given the ambient conditions and the piston velocity, exact values for the shocked thermodynamic variables and the wave speeds are obtained from the Rankine-Hugoniot relations given by Eqs. (3.59-3.68). Since the volume fraction is constant for all time, this analysis reduces to a classical shock wave analysis for each phase [28]. Comparisons of the numerically predicted solution at $\hat{\tau} = 60\ \mu s$ and the exact

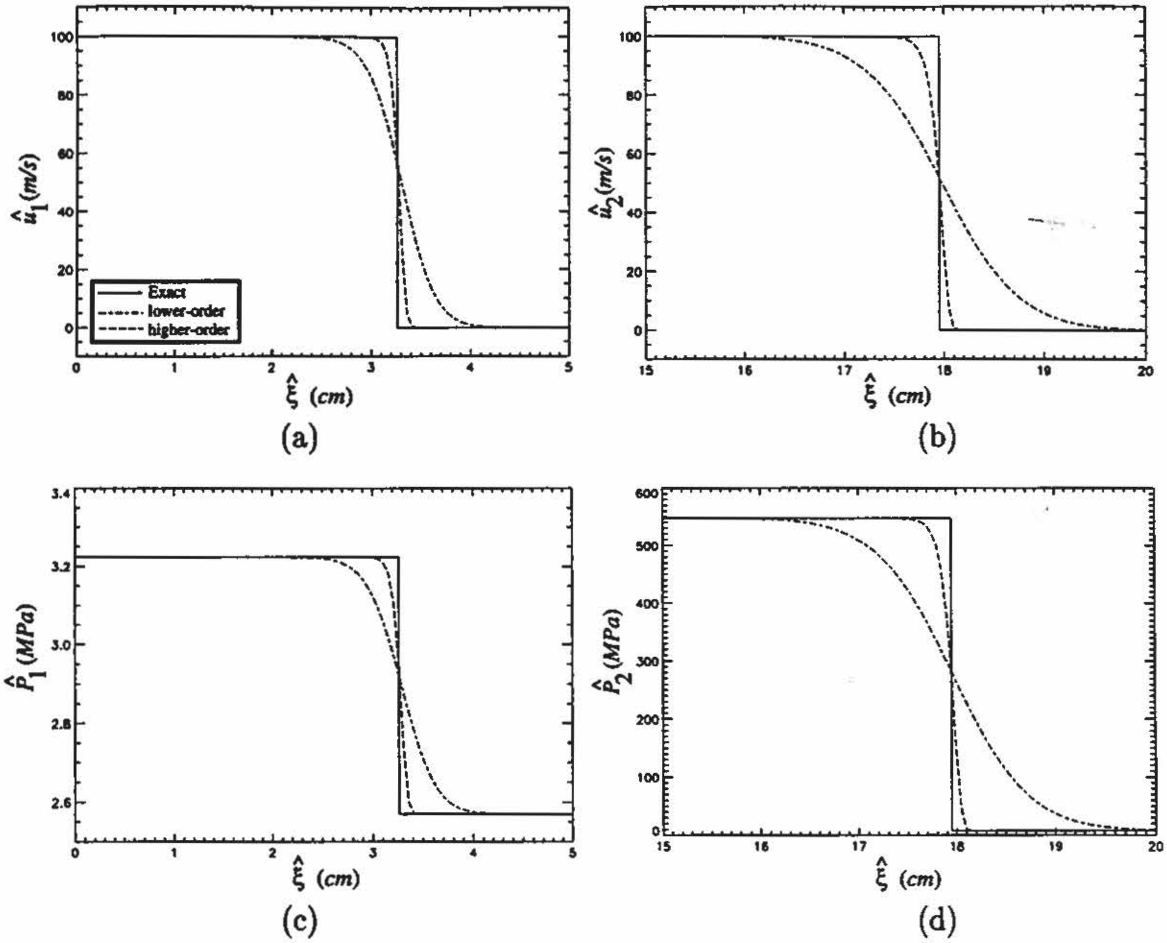

(a) (b)

(c) (d)

Figure 5.5: Comparison of the predicted and exact solutions for the gas and solid shocks: (a,b) gas and solid velocity (measured relative to a fixed laboratory frame); and (c,d) gas and solid pressure.

solution for the pressure and velocity of both the gas and solid are given in Fig. 5.5. Also given in this figure is the numerical prediction obtained using the lower-order numerical flux [Eq. (4.78)]. The jumps predicted by both numerical fluxes agree well with the exact jumps; however, the extra numerical diffusion inherent in the lower-order flux is evident. Though the higher-order flux results in a less diffuse solution, the shocks are still spread over approximately three computational cells. The exact values for the gas and solid shock speeds are 654.34 m/s and 3153.74 m/s, respectively. These values compare well with the numerically predicted values cited above.

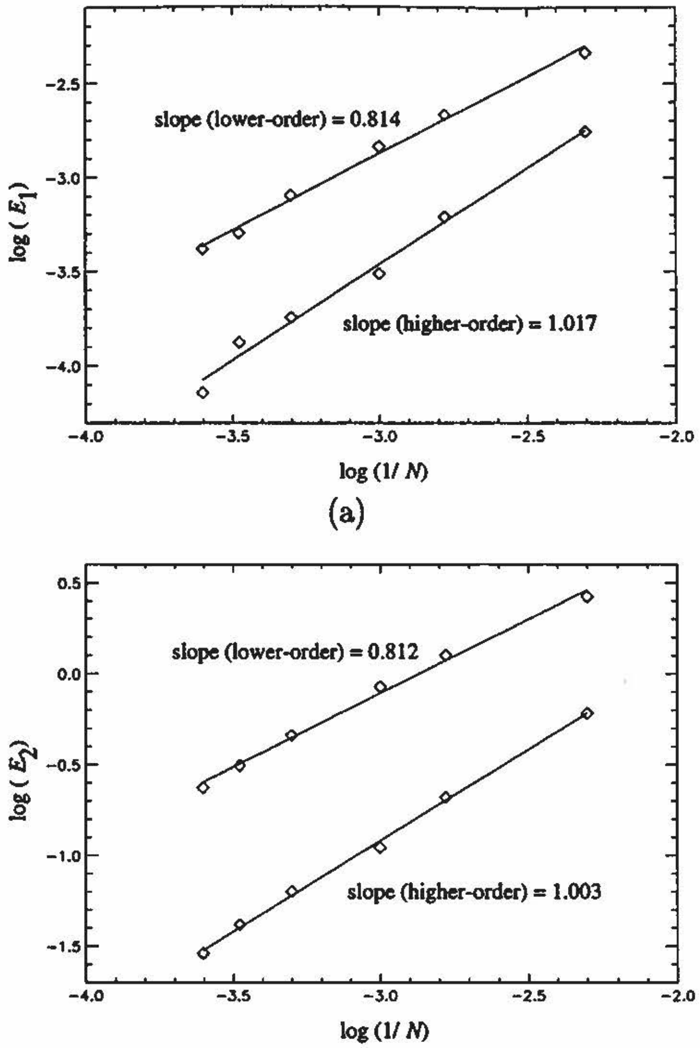

(a)

(b)

Figure 5.6: Numerical convergence data for the inert shock problem: (a) gas; (b) solid.

Convergence data obtained for this test case are plotted in Fig. 5.6. Here, the convergence rates for both the lower-order and higher-order numerical fluxes were determined based on the error defined in Eq. (5.1), where $\hat{P}_1^c = 2.57\ MPa$ and $\hat{P}_2^c = 8.21\ MPa$ are the ambient pressure of the gas and solid, respectively. There exist greater scatter in the data from the linear curve fits than exist for the convergence data obtained for the inert shock tube problem. This increased scatter is likely due to inaccuracies in the placement of the exact solution relative to the numerically predicted solution when computing the error. As such, the exact solution was placed at the location which minimized the computed error. These inaccuracies do not exist for the shock tube simulation since the exact time-dependent solution is known. The convergence rates for the higher-order flux are $p = 1.017$ for the gas, and $p = 1.003$ for the solid. The convergence rates for the lower-order flux are $p = 0.814$ for the gas, and $p = 0.812$ for the solid. A slight discrepancy exists between the convergence rates associated with the higher-order flux for the gas and solid. Though this discrepancy may be attributable to the scatter in the data, it is possible that the flux limiter used in this study gives better results for the gas than for the solid. Optimal accuracy may require the use of a different flux limiter for each phase; this issue is not addressed in this study.

5.3 Inert Compaction Wave Problem

This simulation considers the evolution of an inert compaction wave due to compression of the granular material by a moving piston. Here, the processes of gas and solid convection are coupled with the processes of interphase drag, interphase heat transfer, and material compaction; as such, this problem is an extension of the inert shock problem considered in the previous section.

A compaction wave refers to the propagation of a finite disturbance in volume fraction due to a local mechanical stress imbalance [i.e. $P_2 - P_1 - f \neq 0$ in Eq. (2.52)]. Though it has been experimentally shown that material compaction is a significant component of both DDT and SDT in granular energetic material [14, 15, 97], it is not the intent of this section to give a detailed compaction wave analysis. Rather, results are given which illustrate the evolution of a compaction wave, and a comparison between the numerically predicted compaction wave structure and the steady structure predicted by the analysis of Powers et al. [93] is given. Also, convergence results are given in order to further validate the numerical method. The reader is referred to References [3, 93, 104] for a thorough discussion of inert compaction waves.

Parameter or Ambient Condition	Value	Units
$\hat{b}$	7.60×10^{-4}	m^3/kg
$\hat{R}_1$	8.50×10^{2}	$J/(kg\ K)$
$\hat{c}_{v1}$	2.40×10^{3}	$J/(kg\ K)$
$\hat{c}_{v2}$	1.50×10^{3}	$J/(kg\ K)$
$\hat{\sigma}$	8.98×10^{6}	m^2/s^2
$\hat{q}$	0	J/kg
$\hat{h}$	1.00×10^{7}	$J/(K\ s\ m^{8/3})$
$\hat{\beta}$	1.00×10^{4}	$kg/(s\ m^2)$
$\hat{\mu}_c$	1.00×10^{3}	$kg/(s\ m)$
γ_2	5.00×10^{0}	
$\hat{r}_o$	1.00×10^{-4}	m
$\hat{T}_o$	3.00×10^{2}	K
$\hat{\rho}_{1o}$	1.00×10^{1}	kg/m^3
$\hat{\rho}_{2o}$	1.90×10^{3}	kg/m^3
ϕ_{2o}	7.30×10^{-1}	

TABLE 5.2: PARAMETER VALUES AND AMBIENT CONDITIONS USED FOR THE INERT COMPACTION WAVE PROBLEM

The intragranular stress f and the non-ideal Tait equation of state for the solid used in Reference [93] are adopted for this test case; these relations are given in Appendices I and H, respectively. The virial equation of state given in Appendix G was used for the gas, and the piston velocity was prescribed by Eq. (4.125). The computational domain, which consisted of $N = 600$ nodes, was initialized with the ambient conditions given in TABLE 5.2. Values for the model parameters are also given in this table. The computational run time for this simulation was approximately 45 minutes.

Figure 5.7 shows the numerically predicted history for the gas and solid velocity (measured relative to a fixed laboratory frame), the gas and solid pressure, the solid volume fraction, and the particle number density. Here, $\hat{\xi}$ is position measured relative

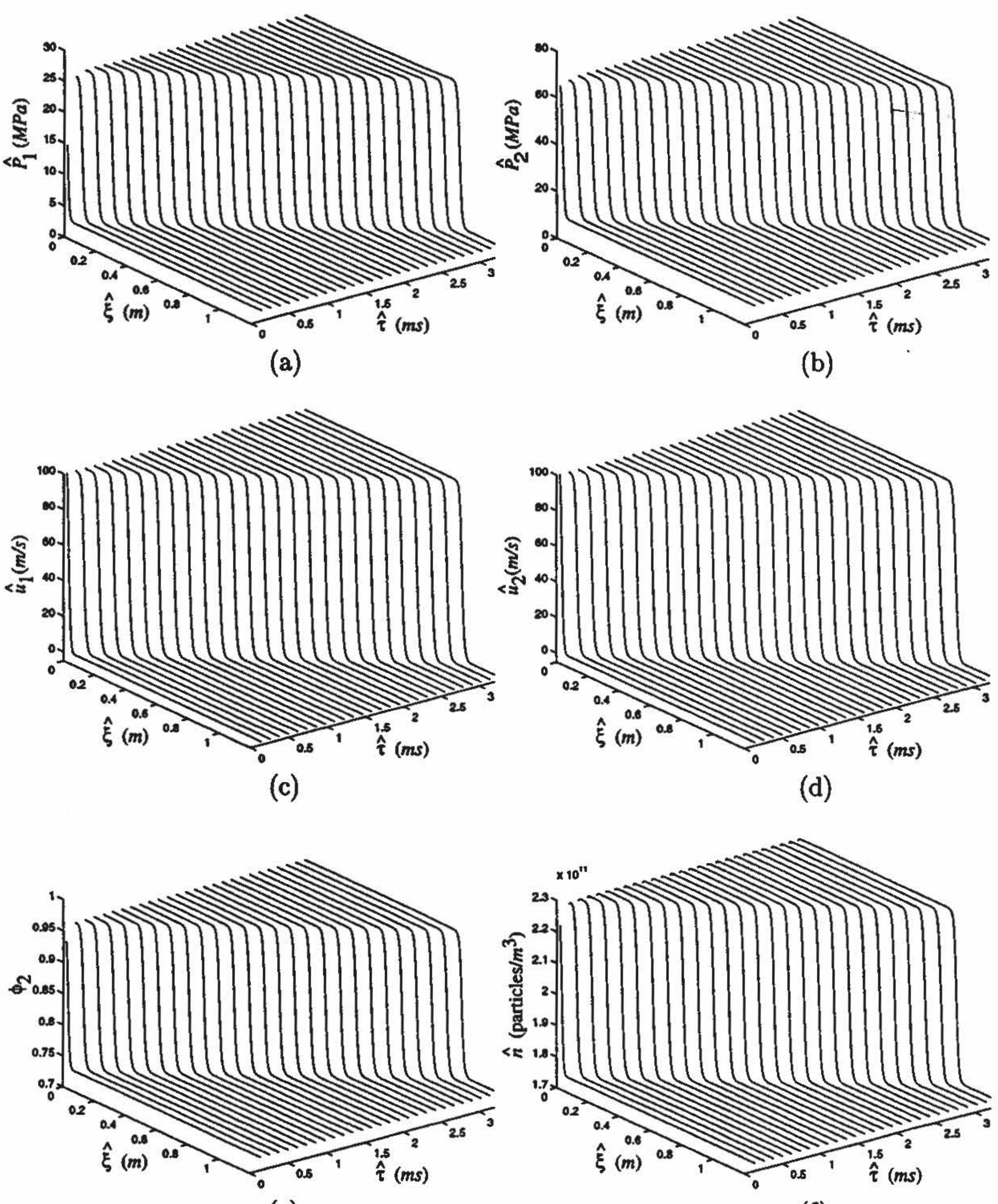

(a) (b)

(c) (d)

(e) (f)

Figure 5.7: Predicted time histories for the inert compaction wave problem: (a,b) gas and solid pressure, (c,d) gas and solid velocity, (e) solid volume fraction, and (f) particle number density.

to the piston surface. A smooth but rapid increase is predicted in all variables in response to the sudden acceleration of the piston. A compaction wave quickly develops and propagates away from the piston with a uniform speed of 418.3 m/s. The predicted time and length required for transition to a fully developed compaction wave are approximately 0.1 ms and 10 cm (measured relative to the piston). The solid volume fraction in the compacted region is predicted to be 0.96, and the solid pressure in the compacted region is predicted to be 67.1 MPa. These values for the compaction wave speed, the final volume fraction, and the final solid pressure agree well with the experimentally determined values reported by Sandusky and Liddiard [104] for the impact of a 100 m/s piston with a bed of porous HMX ($\phi_{2o} = 0.73$). Sandusky and Liddiard observed compaction wave speeds of 432 m/s, final solid volume fractions near 0.94, and final solid pressures near 50 MPa; no values for transition length and time were reported.

Figure 5.8 shows the numerically predicted variation in solid density, velocity, pressure, and volume fraction within the compaction zone at $\hat{\tau} = 3.2$ ms. Also shown in this figure are predictions for the steady wave structure given by the simplified analysis of Powers et al. [93]. In their analysis, Powers et al. ignore gas effects and describe steady compaction wave structure in terms of the solid variables. The flow located between the piston ($\hat{\xi} = 0$ m) and the trailing edge of the compaction wave ($\hat{\xi} = 0.82$ m) is not shown in this figure. The prediction labeled Numerical 1 is the solution shown in Fig. 5.7. The prediction labeled Numerical 2, also shown at $\hat{\tau} = 3.2$ ms, was obtained by ignoring interphase drag and heat transfer, and by ignoring gas effects in Eq. (2.52). As such, a direct comparison can be made between the numerical and analytical predictions for compaction wave structure. Good agreement exists between the Numerical 2 prediction and the analytical prediction. It is noted that a continuous compaction wave structure is predicted, and that interphase drag, interphase heat transfer, and gas effects in Eq. (2.52) increase the final solid pressure,

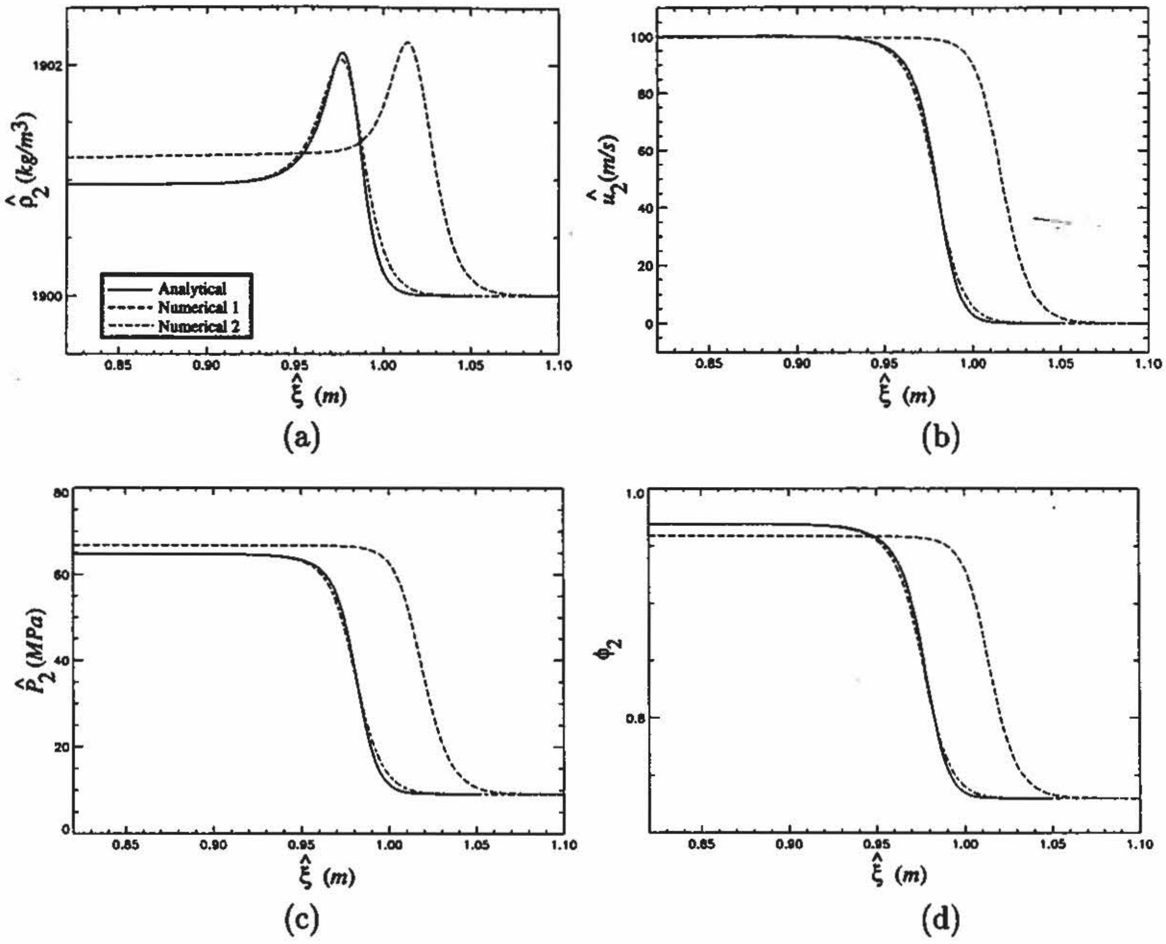

Figure 5.8: Comparison of the predicted and analytical solutions for the inert compaction wave structure: (a) solid density; (b) solid velocity; (c) solid pressure; and (d) solid volume fraction.

and decrease the final solid volume fraction. The results shown here indicate that the gas has little influence on compaction wave structure. The wave speed predicted by the simulation denoted as Numerical 2 is 405.8 m/s; this agrees well with the value of 404.7 m/s predicted by the steady analysis of Powers et al. The compaction wave trajectories for the simulations denoted as Numerical 1 and Numerical 2 are shown in Fig. 5.9.

Convergence data obtained for this test case based on a comparison of the Numerical 2 prediction with the analytical compaction wave structure are plotted in Fig. 5.10. Once again, scatter in the data exist due to inaccuracies in the placement of

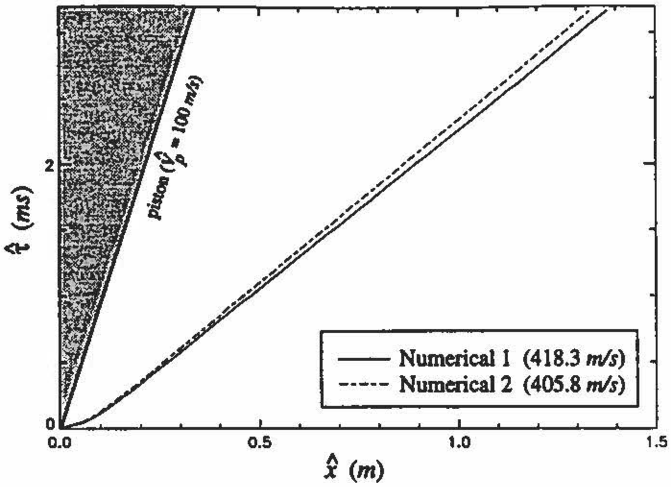

Figure 5.9: Predicted compaction wave trajectories for the inert compaction wave problem.

the analytical solution relative to the numerical solution. Since the compaction wave structure is continuous, this test case provides a good measure for determining the spatial accuracy of the method for a continuous solution. The computed convergence rate is $p = 1.647$. Though this rate is substantially higher than the rates computed for the test cases having discontinuous solutions, it is lower than what would be expected from a truly second-order method. This result is likely due to numerical diffusion introduced by the flux-limiting procedure. It is possible that the convergence rate might improve for more resolved computational grids than used here. However, it is not feasible to investigate this claim since the most resolved case performed as part of this study ($N = 4000$) required nearly 100 hours of CPU time.

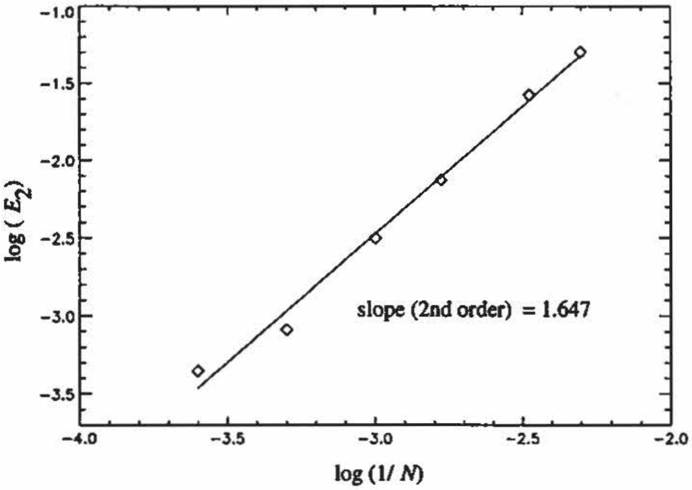

Figure 5.10: Numerical convergence data for the inert compaction wave problem.

6

STEADY ANALYSIS OF TWO-PHASE DETONATION

An analysis of steady two-phase detonation is given in this chapter. In Section 6.1, the steady problem is mathematically posed as an initial-value problem, and the technique used to put the equations into a simplified form suitable for numerical processing is outlined. In Section 6.2, steady two-phase detonation solutions are analyzed and discussed within the framework of classical one-phase detonation theory. To this end, detonation end states of the steady model equations are first analyzed, and then detonation structure is investigated by numerically integrating the steady equations. Two classes of self-propagating detonation structures are identified leading to states predicted by the end state analysis, and existence criteria for each of these classes are determined based on the results of a parametric study. Due to the complexity of the steady equations, the analysis given in this chapter is not comprehensive; however, it does give new results and provides sufficient background for analyzing and discussing detonation solutions predicted by the unsteady analysis given in the following chapter.

6.1 Solution Technique

The first step in seeking a steady wave solution is to assume that such a wave exists; thus, the steady problem does not consider the time-dependent events required for the wave to develop. Here, it is assumed that the wave is propagating to the right at steady speed D, and that the piston is moving with constant speed such that $dv_p/d\tau = 0$ (both D and v_p are measured relative to a fixed laboratory frame). With these assumptions, Eq. (3.7) can be transformed to a reference frame moving with

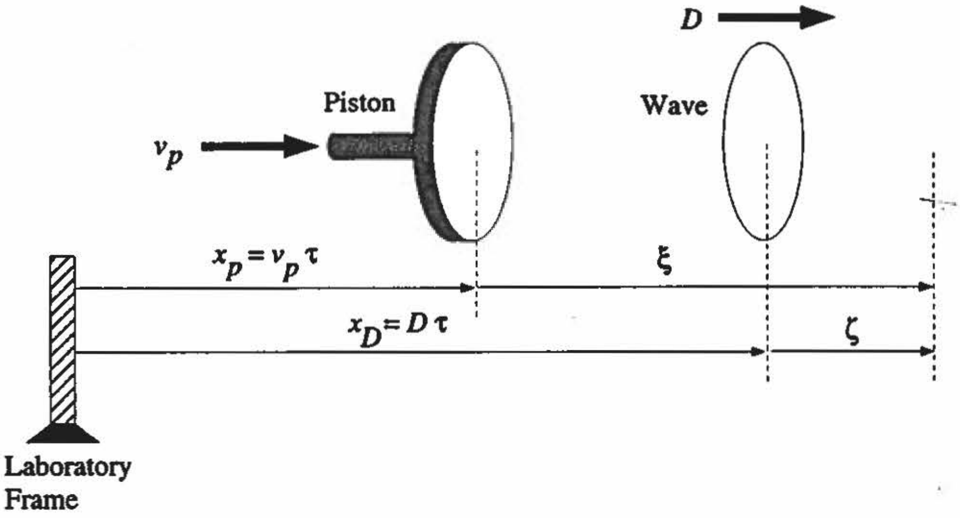

Figure 6.1: Schematic of the steady wave coordinate system.

the wave using the Galilean transformation $\zeta = \xi - (D - v_p)\tau$ and $w_i = v_i - (D - v_p)$ $(i = 1, 2)$, where $D = \hat{D}/\hat{c}_{2o}$, $\zeta = \hat{\zeta}/\hat{r}_o$, and $w_i = \hat{w}_i/\hat{c}_{2o}$ are the ambient freestream solid Mach number, and the non-dimensional position and velocity measured relative to the wave, respectively (see Fig. 6.1). Since Eq. (3.7) is invariant under a Galilean transformation, the model equations valid in the steady wave frame have the same form as Eq. (3.7), with $\partial()/\partial\xi$ and v_i replaced by $\partial()/\partial\zeta$ and w_i, respectively. The steady model equations, obtained by setting $\partial()/\partial\tau = 0$, are then given by the following equations expressed in terms of the wave coordinate ζ:

$$\frac{d}{d\zeta}\left[\rho_1\phi_1 w_1\right] = C_m, \tag{6.1}$$

$$\frac{d}{d\zeta}\left[\rho_1\phi_1 w_1^2 + P_1\phi_1\right] = w_2 C_m + C_d, \tag{6.2}$$

$$\frac{d}{d\zeta}\left[\rho_1\phi_1 w_1\left(e_1 + \frac{w_1^2}{2} + \frac{P_1}{\rho_1}\right)\right] = \left(e_2 + \frac{w_2^2}{2}\right) C_m + w_2 C_d + C_e, \tag{6.3}$$

$$\frac{d}{d\zeta}\left[\rho_2\phi_2 w_2\right] = -\pi_5 C_m, \tag{6.4}$$

$$\frac{d}{d\zeta}\left[\rho_2\phi_2 w_2^2 + P_2\phi_2\right] = -\pi_5 w_2 C_m - \pi_5 C_d, \tag{6.5}$$

$$\frac{d}{d\zeta}\left[\rho_2\phi_2 w_2\left(e_2 + \frac{w_2^2}{2} + \frac{P_2}{\rho_2}\right)\right] = -\pi_5\left(e_2 + \frac{w_2^2}{2}\right) - \pi_5 w_2 C_d - \pi_5 C_e, \tag{6.6}$$

$$\frac{d}{d\zeta}\left[\rho_2 w_2 \phi_2^2\right] = \pi_7 \rho_2 \phi_1 \phi_2^2 \left[P_2 - \pi_5 P_1 - f(\phi_2)\right] - 2\pi_5 \phi_2 C_m, \quad (6.7)$$

$$\frac{d}{d\zeta}\left[w_2 n\right] = 0, \quad (6.8)$$

$$\frac{d}{d\zeta}\left[\rho_2 \phi_2 w_2 I\right] = \rho_2 \phi_2 C_I - \pi_5 I C_m. \quad (6.9)$$

Here, it is understood that C_d is expressed in terms of the velocities w_i. Freestream conditions for these equations specified at the location $\zeta = 0$ are

$$\rho_1(0) = 1, \qquad \rho_2(0) = 1, \qquad w_1(0) = -D, \qquad w_2(0) = -D,$$

$$T_1(0) = \pi_6 T_o, \qquad T_2(0) = T_o, \qquad \phi_2(0) = \phi_{2o}, \qquad r(0) = 1, \qquad I(0) = 0, \quad (6.10)$$

where $T_o = \hat{c}_{v2o}\hat{T}_o/\hat{c}_{2o}^2$, and $\hat{T}_o = \hat{T}_{1o} = \hat{T}_{2o}$ is the dimensional ambient temperature of the mixture. When these initial conditions are substituted into Eqs. (6.1-6.9), it is observed that the inert freestream flow is an equilibrium state since all forcing terms vanish [as discussed in Appendix I, the quantity $P_2 - \pi_5 P_1 - f$ in Eq. (6.7) vanishes for the ambient state]. For this analysis, the virial equation of state given in Appendix G is used for the gas, and the non-ideal Tait equation of state given in Appendix H is used for the solid. The virial state relation for the gas was chosen for its simplicity. Its use enables one to predict certain results commensurate with experiments (discussed in the following section) over a limited range of conditions. More commonly used product state relations which are valid over a wider range of detonation conditions include the JWL (Jones-Wilkins-Lee) equation of state [71] and the BKW equation of state [76]. The expression for the intragranular stress f is given in Appendix I.

Using the constitutive relations given by Eqs. (2.55-2.61), it is possible to reduce Eqs. (6.1-6.9) to a coupled system of five ordinary differential equations for the solid variables ρ_2, ϕ_2, w_2, P_2, and the ignition variable I; these variables will be referred to as primary variables. All other variables are algebraically expressed in terms of these five primary variables. Alternatively, Eqs. (6.1-6.9) can be reduced to a system of five ordinary differential equations for the gas variables ρ_1, ϕ_1, w_1, P_1, and the ignition variable I. The preferred choice of primary variables is largely dependent upon the specific problem being considered. The solid variables were used as primary variables for most problems considered in this study; however, for some problems involving sonic singularities in the gas it was necessary to solve the steady problem posed in terms of the gas variables. Only the technique for obtaining the reduced system of ordinary differential equations for the solid primary variables follows. A similar reduction technique is used to obtain the reduced system of ordinary differential equations for the gas variables.

First, Eq. (2.60) is used in Eq. (6.8) to replace n in favor of r and ϕ_2. The resulting homogeneous differential equation is directly integrated, and initial conditions applied, to give an algebraic expression for r in terms of ϕ_2 and w_2:

$$r = \sqrt[3]{-\frac{\phi_2 w_2}{\phi_{2o} D}}. \tag{6.11}$$

Next, Eq. (6.1) is multiplied by π_5, and the resulting expression is added to Eq. (6.4) to obtain a homogeneous differential equation for the mixture mass. Similarly, Eqs. (6.2) and (6.5), and Eqs. (6.3) and (6.6) are used to obtain homogeneous differential equations for the mixture momentum and energy, respectively. These equations are then directly integrated, and initial conditions applied, to give algebraic expressions relating the gas and solid variables:

$$\pi_5 \rho_1 \phi_1 w_1 + \rho_2 \phi_2 w_2 = -\pi_5 \phi_{1o} D - \phi_{2o} D, \tag{6.12}$$

$$\pi_5 \left(\rho_1 \phi_1 w_1^2 + P_1 \phi_1\right) + \rho_2 \phi_2 w_2^2 + P_2 \phi_2 = \pi_5 \phi_{1o} \left(D^2 + P_{1o}\right) + \phi_{2o} \left(D^2 + P_{2o}\right), \tag{6.13}$$

$$\begin{aligned} &\pi_5 \rho_1 \phi_1 w_1 \left(e_1 + \frac{w_1^2}{2} + \frac{P_1}{\rho_1}\right) + \rho_2 \phi_2 w_2 \left(e_2 + \frac{w_2^2}{2} + \frac{P_2}{\rho_2}\right) \\ &\quad = -\pi_5 \phi_{1o} D \left(e_{1o} + \frac{D^2}{2} + P_{1o}\right) - \phi_{2o} D \left(e_{2o} + \frac{D^2}{2} + P_{2o}\right). \end{aligned} \tag{6.14}$$

Here, $P_{1o} = \dfrac{\hat{P}_{1o}}{\hat{\rho}_{1o} \hat{c}_{2o}^2}$, $P_{2o} = \dfrac{\hat{P}_{2o}}{\hat{\rho}_{2o} \hat{c}_{2o}^2}$, $e_{1o} = \dfrac{\hat{e}_{1o}}{\hat{c}_{2o}^2}$, and $e_{2o} = \dfrac{\hat{e}_{2o}}{\hat{c}_{2o}^2}$ are the non-dimensional ambient pressure and internal energy of the gas and solid, respectively. Using the relations $\phi_1 = 1 - \phi_2$, $e_1 = e_1(\rho_1, P_1)$, and $e_2 = e_2(\rho_2, P_2)$, Eqs. (6.12-6.14) can be solved for the gas variables ρ_1, w_1, and P_1 in terms of the solid primary variables. The functional form of the solution is given by the following (the reader is referred to Reference [95] for details concerning this solution):

$$A_1\rho_1^3 + A_2\rho_1^2 + A_3\rho_1 + A_4 = 0, \tag{6.15}$$

$$w_1 = w_1\left(\rho_2, \phi_2, w_2, P_2; \rho_1\right), \tag{6.16}$$

$$P_1 = P_1\left(\rho_2, \phi_2, w_2, P_2; \rho_1\right), \tag{6.17}$$

where

$$A_1 = A_1\left(\rho_2, \phi_2, w_2, P_2\right), \qquad A_2 = A_2\left(\rho_2, \phi_2, w_2, P_2\right),$$

$$A_3 = A_3\left(\rho_2, \phi_2, w_2, P_2\right), \qquad A_4 = A_4\left(\rho_2, \phi_2, w_2, P_2\right).$$

The cubic expression for ρ_1 [Eq. (6.15)] is a consequence of the gas virial equation of state. This expression has three roots: one root corresponds to a shocked gas, one root corresponds to an unshocked gas, and one root has a negative value and is thus non-physical. The presence of a third non-physical root is due to the inclusion of non-ideal gas effects ($A_1 \equiv 0$ for an ideal gas). With ρ_1 known, w_1 and P_1 can be computed from the relations denoted by Eqs. (6.16) and (6.17). Here, both w_1 and P_1 depend upon the root chosen for ρ_1, i.e. whether the gas is shocked or unshocked.

The remaining differential equations [Eqs. (6.4-6.7), and (6.9)] are expressed in non-conservative form and solved for the derivatives of the primary variables. Since the particle radius and all gas variables are known functions of the primary variables, the reduced autonomous system of ordinary differential equations can be expressed in the standard form

$$\frac{d\mathbf{y}_2}{d\zeta} = \mathbf{h}_2(\mathbf{y}_2), \tag{6.18}$$

where $\mathbf{y}_2 = [\rho_2,\ \phi_2,\ w_2,\ P_2,\ I]^T$ is the dependent vector of solid primary variables, and $\mathbf{h}_2$ is a vector-valued function of $\mathbf{y}_2$. Given suitable initial conditions at the detonation front [i.e., $\mathbf{y}_2(\zeta = 0)$], the initial-value problem can be numerically solved to predict two-phase detonation structure.

If the gas variables are used as primary variables, then Eqs. (6.12-6.14) are solved for ρ_2, w_2, and P_2 in terms of the gas variables, and a reduced autonomous system of ordinary differential equations having the form

$$\frac{d\mathbf{y}_1}{d\zeta} = \mathbf{h}_1(\mathbf{y}_1), \tag{6.19}$$

is obtained. Here, $\mathbf{y}_1 = [\rho_1,\ \phi_1,\ w_1,\ P_1,\ I]^T$ is the dependent vector of gas primary variables, and $\mathbf{h}_1$ is a vector-valued function of $\mathbf{y}_1$.

Conditions at the detonation front are obtained from the two-phase Rankine-Hugoniot relations given by Eqs. (3.49-3.58). Since a detonation wave propagates supersonically with respect to the ambient gas and solid, a shock in either the gas or solid, or in both phases, exists at the front of the wave. Given the ambient state of the mixture [Eq. (6.10)], the Rankine-Hugoniot relations can be used to obtain conditions immediately behind the shock located at $\zeta = 0$ (see Fig. 6.2). If the ambient mixture initially contains no discontinuities in volume fraction, then the Rankine-Hugoniot relations given by Eqs. (3.59-3.68) are used to determine the shocked conditions. Given the shocked conditions, Eq. (6.18) is then integrated on $\zeta \in [0, -\infty)$ to predict detonation structure.

Lastly, it is noted that certain components of $\mathbf{h}_2$ have a $[r(w_2^2 - c_2^2)]^{-1}$ dependency and are thus singular at $r = 0$ or $w_2^2 = c_2^2$. Here, the complete combustion singularity ($r = 0$) is a consequence of the forms chosen for the phase interaction terms; this singularity is present in most two-phase combustion models [5, 23]. The sonic singularity, which is different from the sonic singularity associated with a parabolic degeneracy of the model equations as discussed in Chapter 3, arises when the solid velocity equals the local solid sound speed. This singularity is also present in the steady equations for one-phase systems [108]. Also, it is apparent when one solves the steady problem in terms of the gas variables that certain components of $\mathbf{h}_1$ have a $[r(w_1^2 - c_1^2)]^{-1}$ de-

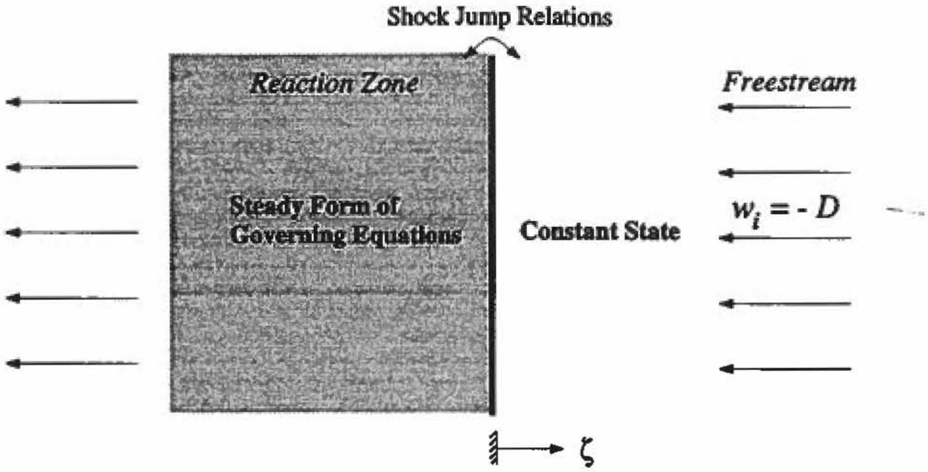

Figure 6.2: Illustration of the initial-value problem for the steady detonation structure analysis.

pendency and are thus singular when $w_1^2 = c_1^2$. For the steady problem posed in terms of the solid variables, Eqs. (6.15) predicts complex, non-physical values for the gas density after the gas velocity becomes locally sonic. The role of these singularities in determining existence criteria for steady two-phase detonations has previously been analyzed in Reference [95], and is further analyzed in the following section.

Difficulties associated with the numerical integration of Eq. (6.18) near $r = 0$ or $w_2^2 = c_2^2$ are eliminated by transforming the independent variable ζ to a new independent variable z defined by the following:

$$\frac{d\zeta}{dz} = r\left(w_2^2 - c_2^2\right). \tag{6.20}$$

The initial condition for this additional differential equation is $\zeta(0) = 0$. This equation is integrated for $z > 0$ in the case of a shocked solid ($w_2^2 < c_2^2$), and for $z < 0$ in the case of an unshocked solid ($w_2^2 > c_2^2$). Using this definition, Eq. (6.18) can be expressed in terms of z by direct application of the chain rule:

$$\frac{d\mathbf{y}_2}{dz} = r\left(w_2^2 - c_2^2\right)\mathbf{h}_2(\mathbf{y}_2). \tag{6.21}$$

Similarly, if the steady problem is posed in terms of $\mathbf{y}_1$, then it is necessary to solve the following equations in order to eliminate numerical difficulties near $r = 0$ or $w_1^2 = c_1^2$:

$$\frac{d\zeta}{dz} = r\left(w_1^2 - c_1^2\right), \tag{6.22}$$

$$\frac{d\mathbf{y}_1}{dz} = r\left(w_1^2 - c_1^2\right)\mathbf{h}_1(\mathbf{y}_1). \tag{6.23}$$

6.2 Steady Solutions

The steady problem requires the solution of an autonomous nonlinear system of six coupled ordinary differential equations given by Eqs. (6.20) and (6.21) [or Eqs. (6.22) and (6.23)], subject to initial conditions at the detonation front. Much information can be obtained about the solutions using a geometrical analysis based on nonlinear dynamical systems theory [73, 124]. Such an analysis identifies detonation end states and determines their structural stability. Though a detailed geometrical analysis is beyond the scope of this study, nonlinear dynamical systems theory does provide a proper framework for discussing and analyzing solutions of Eqs. (6.20) and (6.21).

We first analyze detonation end states in Subsection 6.2.1, and then consider detonation structure in Subsections 6.2.2 and 6.2.3.

6.2.1 Detonation End States

An equilibrium end state $\mathbf{y}_2^\circ$ of Eqs. (6.20) and (6.21) is reached when the forcing terms in these equations vanish. With $\mathbf{y}_2^\circ$ known, the gas variables ρ_1, w_1, and P_1 at this state are given by Eqs. (6.15- 6.17). The structural stability of the end state is determined by analyzing the linear system of ordinary differential equations obtained by linearizing Eqs. (6.20) and (6.21) about this end state. Since a rigorous structural stability analysis is not feasible due to the complexity of the steady equations, equilibrium states $\mathbf{y}_2^\circ$ and their structural stability are determined here by numerically solving the full initial-value problem.

Of special importance in this study is the complete combustion end state $r = 0$ (thus, $\phi_2 = 0$ and $\phi_1 = 1$). For this case, the forcing term in Eq. (6.20) vanishes, and $\mathbf{y}_2^o$ is determined by equating the forcing term in Eq. (6.21) to zero and solving the resulting nonlinear algebraic problem. Though this problem is difficult to solve, a simple analysis can be performed to determine the complete combustion end states for the gas. This is possible because ϕ_2 vanishes at complete combustion; ~~thus~~, the gas end state is independent of the solid end state. For $\phi_2 = 0$ ($\phi_1 = 1$), inspection of Eqs. (6.12-6.14) shows that the gas quantities are dependent only upon the ambient conditions (quantities labeled with subscript "o") and the steady wave speed D. As such, these equations can be solved for the gas quantities at the complete combustion state.

To this end, we set $\phi_2 = 0$ and $\phi_1 = 1$ in Eqs. (6.12-6.14), use the resulting expression from Eq. (6.12) to eliminate w_1 in Eqs. (6.13) and (6.14) in favor of ρ_1, and rearrange terms to obtain

$$P_1 - P_a = -\left(\rho_a D\right)^2 \left(\frac{1}{\rho_1} - \frac{1}{\rho_a}\right), \tag{6.24}$$

$$e_1 - e_a = -\frac{1}{2}\left(\frac{1}{\rho_1} - \frac{1}{\rho_a}\right)\left(P_1 + P_a\right), \tag{6.25}$$

where

$$\rho_a \equiv \phi_{1o} + \frac{1}{\pi_5}\phi_{2o}, \qquad P_a \equiv \phi_{1o}P_{1o} + \frac{1}{\pi_5}\phi_{2o}P_{2o}, \qquad e_a \equiv \frac{\phi_{1o}e_{1o} + \frac{1}{\pi_5}\phi_{2o}e_{2o}}{\phi_{1o} + \frac{1}{\pi_5}\phi_{2o}}.$$

Here, ρ_a, P_a, and e_a are the non-dimensional ambient density, pressure, and internal energy of the mixture. Equations (6.24) and (6.25) are the two-phase Rayleigh line and Hugoniot relation for the complete combustion state, respectively. Given the expression for $e_1(\rho_1, P_1)$, Eqs. (6.24) and (6.25) can be combined to form a cubic expression for ρ_1 which is simply Eq. (6.15) evaluated for $\phi_2 = 0$ ($\phi_1 = 1$). Depending upon the ambient conditions and the wave speed D, this cubic expression may have 1) a single real root and a pair of complex conjugate roots, 2) two equal real roots and a third distinct real root, or 3) three distinct real roots. As discussed previously, one of the real roots for all three cases is the non-physical result $\rho_1 < 0$; therefore, case 1) predicts physically meaningless end states. Physically meaningful end states associated with the remaining two cases are best analyzed by plotting Eqs. (6.24) and (6.25) in the $(1/\rho_1)$-P_1 plane.

Equation (6.24) is the equation of a line in the $(1/\rho_1)$-P_1 plane which, for fixed ambient conditions, has a negative slope which is proportional to D^2. Equation (6.25) describes a nonlinear curve in this plane which is independent of D. Dimensional plots of these equations generated using parameters and ambient conditions representative of granular HMX (TABLE 6.1) are shown in Figure 6.3. In this figure, the Rayleigh lines for three different waves speeds $\hat{D}$ are shown. Equilibrium end states are given by the points of intersection of the Rayleigh line and the Hugoniot curve. For waves speeds $\hat{D} < \hat{D}_{CJ}$, the corresponding Rayleigh lines (not shown in this figure) do not intersect the Hugoniot curve and non-physical end states are predicted; this scenario corresponds to case 1) identified in the previous paragraph. For $\hat{D} = \hat{D}_{CJ}$, a single physically meaningful end state is predicted corresponding to case 2) identified above. Thus, analogous to steady one-phase detonation theory [34], there is predicted a minimum wave speed required for a steady two-phase detonation to exists; this minimum wave speed is referred to as the *Chapman-Jouguet* wave speed, $\hat{D}_{CJ}$, and the resulting detonation wave is referred to as a *Chapman-Jouguet* (CJ) detonation. For $\hat{D} > \hat{D}_{CJ}$, two physically meaningful end states are predicted corresponding to case 3) identified above. The detonation wave associated with the end state having the larger value of ρ_1 is referred to as a *strong* detonation, and the other is referred to as a *weak* detonation. Also, there exist other solutions of Eqs. (6.24) and (6.25) for wave speeds much smaller than those considered here. These solutions, which are not relevant to this study, are associated with steady two-phase deflagration waves.

An analysis of the complete combustion end states gives that the Mach number of the gas relative to the steady detonation front is locally unity ($M_1^2 = 1$) for the CJ end state, is less than unity ($M_1^2 < 1$) for the strong end state, and is greater than

Parameter or Ambient Condition	Value	Units	Reference
$\hat{b}$	7.60×10^{-4}	m^3/kg	
$\hat{R}_1$	8.50×10^{2}	$J/(kg\ K)$	[95]
$\hat{c}_{v1o}$	2.40×10^{3}	$J/(kg\ K)$	[5, 95]
$\hat{c}_{v2o}$	1.50×10^{3}	$J/(kg\ K)$	[5, 23, 95]
$\hat{\sigma}$	8.98×10^{6}	m^2/s^2	[93, 95]
$\hat{q}$	5.84×10^{6}	J/kg	[23, 95]
$\hat{k}_I$	1.00×10^{6}	s^{-1}	
$\hat{T}_I$	2.69×10^{3}	K	
I_{ig}	5.00×10^{-1}		
$\hat{a}$	2.90×10^{-9}	$m/(Pa\ s)$	[23, 95]
$\hat{h}$	1.00×10^{7}	$J/(K\ s\ m^{8/3})$	[95]
$\hat{\beta}$	1.00×10^{4}	$kg/(s\ m^2)$	[95]
$\hat{\mu}_c$	1.00×10^{6}	$kg/(s\ m)$	[95]
m	1.00×10^{0}		[23, 95]
γ_2	5.00×10^{0}		[93, 95]
$\hat{r}_o$	1.00×10^{-4}	m	[8, 23, 95]
$\hat{T}_o$	3.00×10^{2}	K	
$\hat{\rho}_{1o}$	1.00×10^{1}	kg/m^3	[95]
$\hat{\rho}_{2o}$	1.71×10^{3}	kg/m^3	[111]
ϕ_{2o}	7.00×10^{-1}		[111]

TABLE 6.1: PARAMETER VALUES AND AMBIENT CONDITIONS USED TO COMPUTE THE STEADY *SHOCKED GAS-UNSHOCKED SOLID CJ* DETONATION STRUCTURE

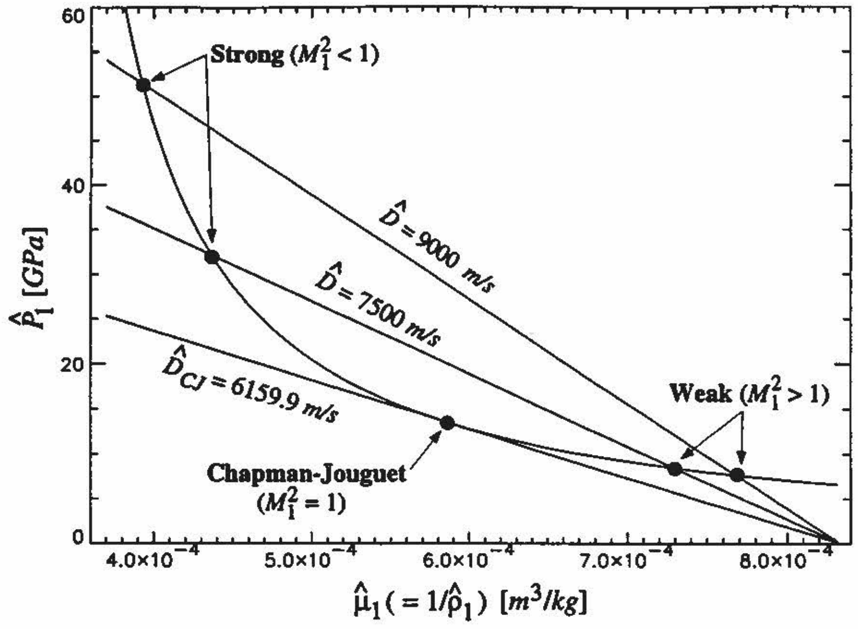

Figure 6.3: Two-phase Rayleigh lines and Hugoniot curve.

unity ($M_1^2 > 1$) for the weak end state. The CJ detonation is commonly thought to be the unique steady solution for a self-propagating detonation since it does not require external energy input, such as provided by a moving piston, to sustain propagation of the wave. Additionally, since $M_1^2 = 1$ at the CJ end state, the detonation is not susceptible to degradation by rarefaction waves originating from behind the wave. Weak waves, having $M_1^2 > 1$ at their end state, are also not susceptible to rarefactions from the rear, and do not require piston support for their propagation; thus, they too are self-propagating detonations. However, strong detonations, having $M_1^2 < 1$ at their end state, are susceptible to rarefactions from the rear, and do require piston support for their propagation. As previously discussed, if a moving piston providing support for a strong detonation is suddenly stopped, a rarefaction will be produced which will eventually overtake the detonation thereby reducing it to either a CJ or weak detonation.

The ideas discussed in the preceding two paragraphs are further illustrated in Fig. 6.4 which gives steady detonation wave speed as a function of piston velocity. For

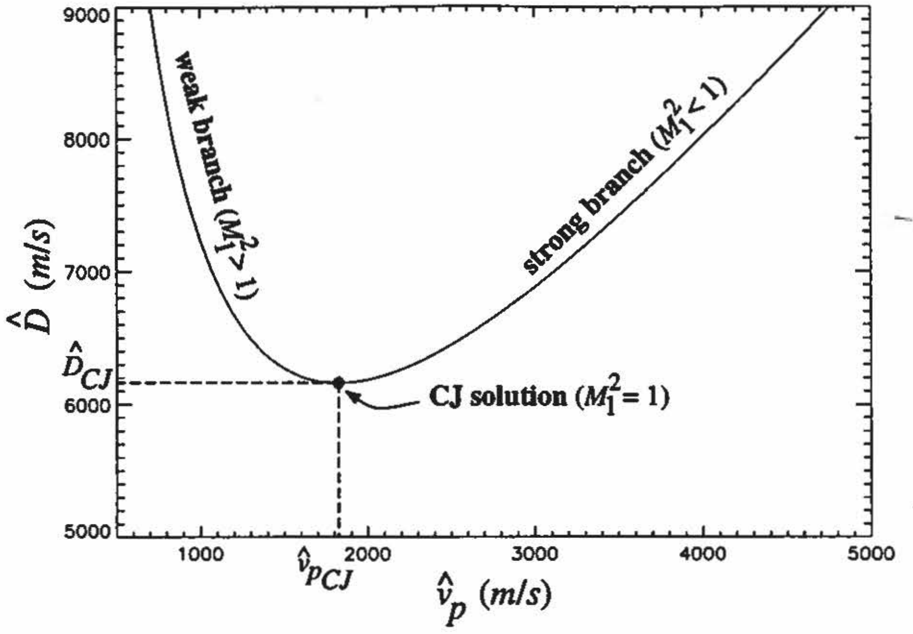

Figure 6.4: Steady detonation wave speed vs. piston velocity.

fixed wave speed $\hat{D}$, the piston velocity is defined as the gas velocity at the complete combustion end state measured relative to a laboratory frame, $\hat{v}_p = \hat{w}_1 + \hat{D}$. As such, the gas flow between the piston and the end of the reaction zone is time-independent. Two branches are identified on the curve in this figure: a weak branch and a strong branch. The weak branch is associated with weak detonation end states, and the strong branch is associated with strong detonation end states; these two branches are joined at the CJ end state. A continuum of strong detonation end states are predicted for piston velocities in excess of $\hat{v}_{p_{CJ}}$, and a continuum of weak detonation end states are predicted for piston velocities less than $\hat{v}_{p_{CJ}}$. For the scenario depicted here, the CJ end state is obtained only for a piston velocity of $\hat{v}_{p_{CJ}}$.

In addition to the complete combustion end states, there exist other singular points of Eqs. (6.20) and (6.21). First, there exist end states $\mathbf{y}_2^\circ$ such that $\mathbf{h}_2(\mathbf{y}_2^\circ) = [0,\ 0,\ 0,\ 0,\ 0]^T$, but $r(w_2^2 - c_2^2) \neq 0$. These end states, which were not predicted in this study, are equilibrium points for Eq. (6.18) associated with incomplete combustion. Second, there exist states $\mathbf{y}_2^\circ$ such that $r(w_2^2 - c_2^2)\mathbf{h}_2(\mathbf{y}_2^\circ) \neq [0,\ 0,\ 0,\ 0,\ 0]^T$, but

$r(w_2^2 - c_2^2) = 0$. These singularities are non-equilibrium points having non-physical solutions since the spatial derivatives in Eq. (6.18) are undefined at these points. Similar singularities also exist for the gas. A thorough discussion of singular points for steady two-phase models is given by Bilicki et al. [18]

Though the end state analysis identifies physically meaningful CJ, strong, and weak detonation end states, one must consider detonation structure in order to determine whether a path exists in phase space connecting the initial conditions at the detonation front to these end states. The accessibility of these detonation end states is dependent upon both their structural stability and the initial conditions applied at the detonation front. In general, the detonation structure may be relatively simple or very complex. Regardless of the structure, if a steady wave exists for which all of the solid is consumed by combustion, then the structure must terminate at one of these three end states.

In the following subsections, we focus on self-propagating detonations identified by a steady structure analysis which terminate at states predicted by the equilibrium end state analysis. In particular, we identify 1) CJ waves having a single lead shock in the gas and an unshocked solid, and 2) weak waves having a single lead shock in the gas and an unshocked solid. The first class of waves have previously been predicted by the steady analysis of Powers et al. [95]; the second class of waves has not been previously predicted. Results of a parametric study are given which identify regions of parameter space associated with both classes of detonation, and regions for which neither of these classes exists. Both the analysis given in Reference [95] and the present analysis did not identify steady detonation structures having a shocked solid.

6.2.2 Chapman-Jouguet Detonation Structure

In this subsection, we show the structure of a steady CJ detonation having a single lead shock in the gas and an unshocked solid, and give existence criteria for this class of detonations.

Values for the ambient conditions and model parameters used to compute the CJ detonation structure are given in TABLE 6.1; when available, references for these values are also provided. Here, the values for $\hat{\rho}_{2o}$ and ϕ_{2o} were chosen such that the ambient mixture density ($\hat{\rho}_a = 1200\ kg/m^3$) and solid volume fraction match those of the DDT experiment [80] for granular HMX as reported by Stewart et al. [111]. Values for the gas constant, $\hat{R}_1$, and the virial coefficient, $\hat{b}$, were chosen such that 1) predicted steady CJ detonation pressures and wave speeds reasonably agree with predictions from the thermochemistry code TIGER [27] as reported by Butler and Krier [23], and 2) the predicted steady CJ detonation wave speed closely matches the experimental value reported in Reference [111]. Values for the solid equation of state parameters, $\hat{\sigma}$ and γ_2, used by Powers et al. [92, 93] are adopted here. These values were chosen by Powers et al. such that solid shock and compaction wave predictions match solid shock [78] and compaction wave data [105]. Values for the ignition parameters, $\hat{k}_I$, $\hat{T}_I$, and I_{ig}, were chosen such that 1) the time and length required for DDT given in Chapter 7 match the values reported in Reference [111] for the impact of a 100 m/s piston, and 2) the predicted distance required for ignition behind the lead shock of steady detonation structures is much smaller than the reaction zone length. Values for the drag parameter, $\hat{\beta}$, the heat transfer parameter, $\hat{h}$, and the compaction viscosity, $\hat{\mu}_c$, were largely chosen so that a steady two-phase CJ detonation structure could be predicted. The high value for $\hat{\mu}_c$ used here was also used by Powers et al. [95] to predict CJ detonation structures in the absence of theory for weak detonations. No reliable experimental data exist for determining values for these parameters under detonation conditions; however, the values for $\hat{\beta}$ and $\hat{h}$ used here roughly match the values used in empirical drag and heat transfer relations valid under less extreme conditions [91, 95].

For the structure analysis, Eqs. (6.20) and (6.21) [and Eqs. (6.22) and (6.23)]

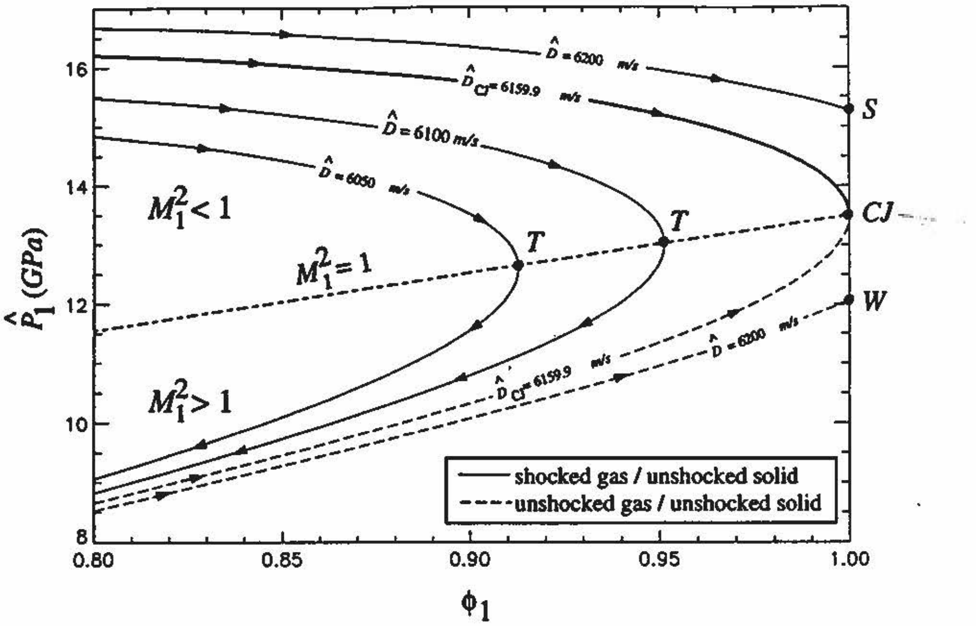

Figure 6.5: $\hat{P}_1$-ϕ_1 phase plane for the steady *shocked gas-unshocked solid* CJ detonation structure analysis.

were numerically integrated using an implicit stiff ordinary differential equation solver contained in the software package LSODE. The results of this analysis are summarized in the ϕ_1-$\hat{P}_1$ phase plane shown in Fig. 6.5. For clarity, only trajectories in the neighborhood of the complete combustion state ($\phi_1 = 1$) are given. Here, each trajectory is associated with a different steady wave speed $\hat{D}$, and is parameterized by position $\hat{\zeta}$. The upper and lower regions of this plane correspond to subsonic and supersonic gas flow, respectively; these two regions are separated by the sonic curve $M_1 = 1$. Since the gas is shocked, all trajectories initially lie in the subsonic region of the plane.

A continuum of trajectories are predicted for $\hat{D} < \hat{D}_{CJ} = 6159.9\ m/s$ which do not reach the complete combustion state ($\phi_1 = 1$); rather, they intersect the sonic curve at the points labeled T (for turning point), reverse direction, and proceed into the supersonic region of the plane. The points T are non-equilibrium points at which $r(w_1^2 - c_1^2) = 0$ and $r(w_1^2 - c_1^2)\mathbf{h}_1(\mathbf{y}_1) \neq [0,\ 0,\ 0,\ 0, 0]^T$ in Eqs. (6.22) and (6.23), respectively. Consequently, the spatial derivative of the gas variables is undefined at these points resulting in non-physical solutions. Bilicki et al. [18] refer to such points as "turning points" because the solutions become double-valued functions of position as the trajectories progress into the supersonic region of the plane. As $\hat{D}$ approaches $\hat{D}_{CJ}$, the turning point T approaches the complete combustion state CJ. For a unique value of the wave speed $\hat{D}_{CJ}$, the solution trajectory terminates at the complete combustion state CJ identified by the equilibrium end state analysis. At this point, $r(w_1^2 - c_1^2) = 0$ and $r(w_1^2 - c_1^2)\mathbf{h}_1(\mathbf{y}_1) = [0,\ 0,\ 0,\ 0,\ 0]^T$. A continuum of solution trajectories are predicted for $\hat{D} > \hat{D}_{CJ}$ which remain in the subsonic region of the plane and terminate at complete combustion states S; these waves represent strong detonations. For completeness, solution trajectories associated with *unshocked gas-unshocked solid* structures leading to the states CJ and W are also shown in this figure. Here, W denotes a weak detonation end state. These structures are typically dismissed as non-physical since, in the absence of a lead shock, there is no clear mechanism for combustion initiation. As such, it was necessary to assume that $I_{ig} \rightarrow 0$ in order to predict these unshocked structures.

Figure 6.6 shows the spatial structure of the *shocked gas-unshocked solid* CJ detonation associated with the trajectory leading to state CJ in Fig. 6.5. Here, the detonation is propagating to the right at speed $\hat{D}_{CJ} = 6159.9\ m/s$, and the gas shock is located at $\hat{\xi} = 0\ mm$. Combustion is quickly initiated as the solid particles cross the shock. As seen in Figs. 6.6(a,c), the gas pressure and Mach number squared change discontinuously from their ambient values of 2.57 MPa and 108.24 to 0.3196 GPa and 0.138 at the shock, respectively. The gas pressure subsequently increases to 13.48 GPa at complete reaction, and the gas Mach number increases to unity at complete reaction. The predicted increase in gas pressure within the reaction zone contrasts one-phase detonation theory which predicts a decrease in pressure due to exothermic heat release [34]. As seen in Figs. 6.6(b,d), the solid pressure and Mach number are continuous throughout the wave, with the solid pressure increasing from

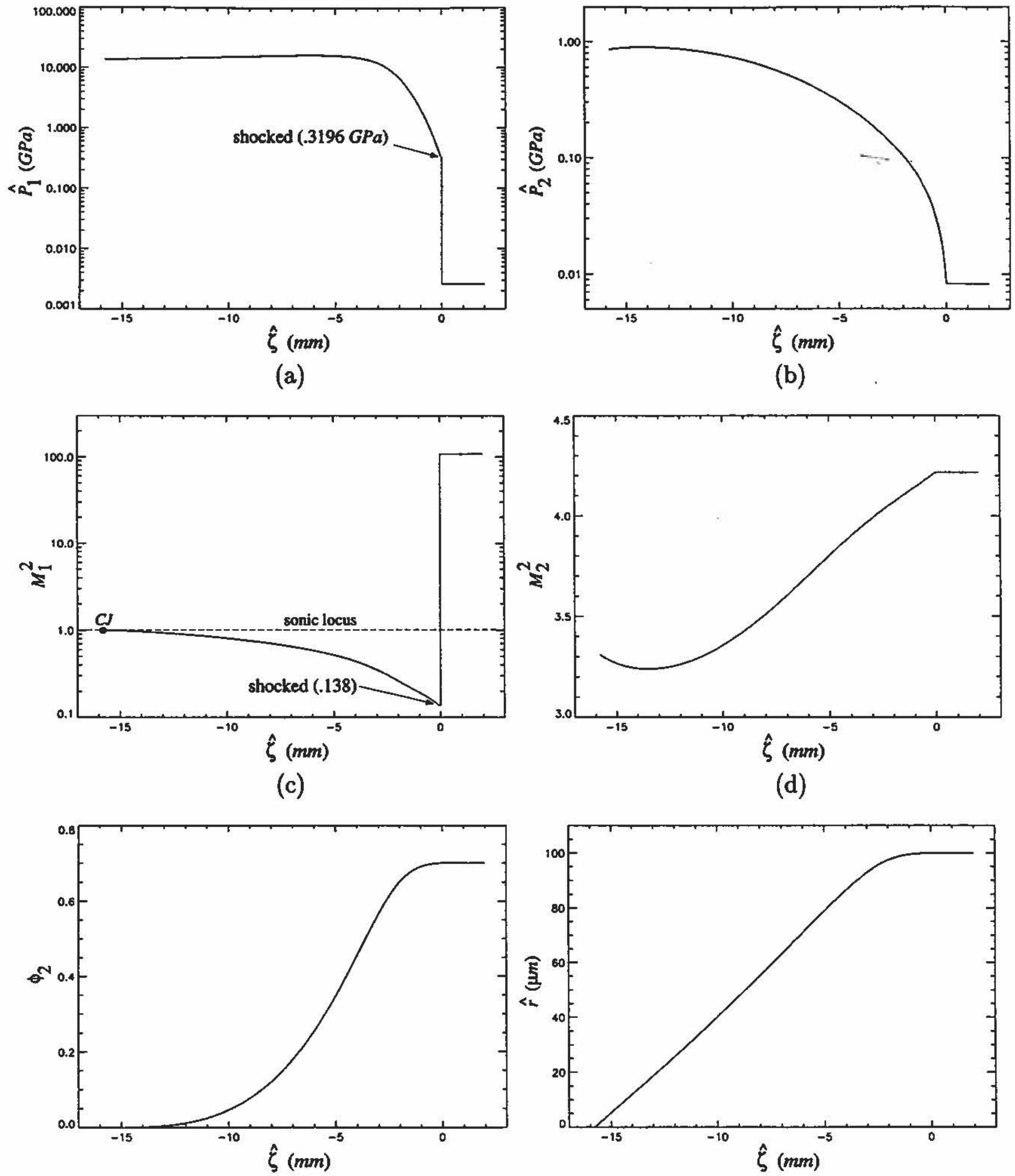

(a) (b)

(c) (d)

(e) (f)

Figure 6.6: *Shocked gas-unshocked solid CJ* detonation structure: (a,b) gas and solid pressure; (c,d) gas and solid Mach number squared (relative to the wave frame); (e) solid volume fraction; and (f) particle radius.

its ambient value of 8.21 MPa to 0.856 GPa at complete reaction, and the solid Mach number squared decreasing from its ambient value of 4.22 to 3.31 at complete reaction. The solid flow remains supersonic throughout the wave. As shown in Figs. 6.6(e,f), a continuous variation in both solid volume fraction and particle radius is predicted. These quantities decrease from their respective ambient values of 0.7 and 100 μm to zero at complete reaction. The predicted reaction zone length is approximately 15.8 mm.

The distance behind the gas shock required for ignition, $\hat{l}_{ig}$, is easily estimated from the dimensional form of Eq. (B.10):

$$\frac{dI}{d\hat{\tau}} = \hat{k}_I\,(1-I)\left[\frac{\hat{P}_1\phi_1 + \hat{P}_2\phi_2 - \hat{P}_{1o}\phi_{1o} - \hat{P}_{2o}\phi_{2o}}{\hat{P}_{1o}\phi_{1o} + \hat{P}_{2o}\phi_{2o}}\right]^2 \exp\left[-\frac{\hat{T}_I}{\hat{T}_1\phi_1 + \hat{T}_2\phi_2}\right]. \qquad (6.26)$$

This equation, which is the characteristic equation for the ignition variable, is valid along solid particle paths defined by $\frac{d\hat{\xi}}{d\hat{\tau}} = \hat{v}_2$. Here, we assume that the gas and solid thermodynamic variables and volume fraction change more slowly than the ignition variable. As such, we assume these quantities to be constant, directly integrate Eq. (6.26), apply the initial condition $I(\hat{\tau} = 0) = 0$, and solve for $\hat{\tau}$ to obtain

$$\hat{\tau} = -\hat{\tau}_c \ln\left[1 - I\right], \qquad (6.27)$$

where

$$\hat{\tau}_c = \left\{\hat{k}_I\left[\frac{\hat{P}_1\phi_1 + \hat{P}_2\phi_2 - \hat{P}_{1o}\phi_{1o} - \hat{P}_{2o}\phi_{2o}}{\hat{P}_{1o}\phi_{1o} + \hat{P}_{2o}\phi_{2o}}\right]^2 \exp\left[-\frac{\hat{T}_I}{\hat{T}_1\phi_1 + \hat{T}_2\phi_2}\right]\right\}^{-1}.$$

Thus, $\hat{\tau}_c$ is inversely proportional to the ignition rate parameter $\hat{k}_I$. Since the gas is shocked and the solid is unshocked for the CJ detonation structure shown in Fig. 6.6, we choose the shocked gas pressure (0.3196 GPa) and temperature (5908 K), the ambient solid pressure (8.208 MPa) and temperature (300 K), and the ambient gas and solid volume fraction (0.3 and 0.7, respectively) as characteristic values. Using these values, and the values for $\hat{k}_I$, $\hat{T}_I$, and $I = I_{ig}$ given in TABLE 6.1, in Eq. 6.27 gives an estimate for the ignition time, $\hat{\tau}_{ig}$; the estimated ignition time is

0.014 μs. Using $\hat{D}_{CJ} = 6159.9\ m/s$ as a characteristic velocity for the unshocked solid particles, the ignition length is given by $\hat{l}_{ig} = \hat{D}_{CJ}\hat{\tau}_{ig}$; the estimated ignition length is $\sim$ 0.083 mm. Consequently, the ignition length is much smaller than the predicted reaction zone length. This result is confirmed by the numerical computations for steady detonation structure.

The existence of steady *shocked gas-unshocked solid CJ* detonations such as the one illustrated in Fig. 6.6 is dependent upon many factors including the relaxation rates associated with interphase drag ($\hat{\beta}$), interphase heat transfer ($\hat{h}$), and material compaction ($\hat{\mu}_c$). Values for the parameters $\hat{\beta}$, $\hat{h}$, and $\hat{\mu}_c$ under detonation conditions are among the most difficult to ascertain from experiments. Here, we determine existence criteria for this class of detonations based on the rates of these relaxation processes. To this end, we use the model parameters and ambient conditions given in TABLE 6.1 as a baseline, independently vary the parameters $\hat{\beta}$, $\hat{h}$, and $\hat{\mu}_c$ (while holding the burn rate parameters $\hat{a}$ and m fixed), and numerically integrate the model equations to predict regions in $\hat{\beta}$-$\hat{h}$-$\hat{\mu}_c$ space for which these detonation structures exist. Depending upon the values for these parameters, the length scales associated with these processes change relative to the reaction zone length. As such, this analysis demonstrates the importance of these length scales in determining detonation wave structure. The range of parameter values examined here is large; as such, not all values are physically relevant. Nonetheless, uncertainties associated with the rates of these processes under detonation conditions suggests that one consider a range of possible values. Since both the ambient conditions and equation of state parameters are held fixed for this study, the CJ wave speed, which is independent of $\hat{\beta}$, $\hat{h}$, and $\hat{\mu}_c$, is 6159.9 m/s for all cases considered.

Results of the parametric study are summarized in Fig. 6.7. Three distinct regions are identified: 1) regions in which *shocked gas-unshocked solid CJ* structures are predicted; 2) regions in which no *shocked gas-unshocked solid CJ* structures are

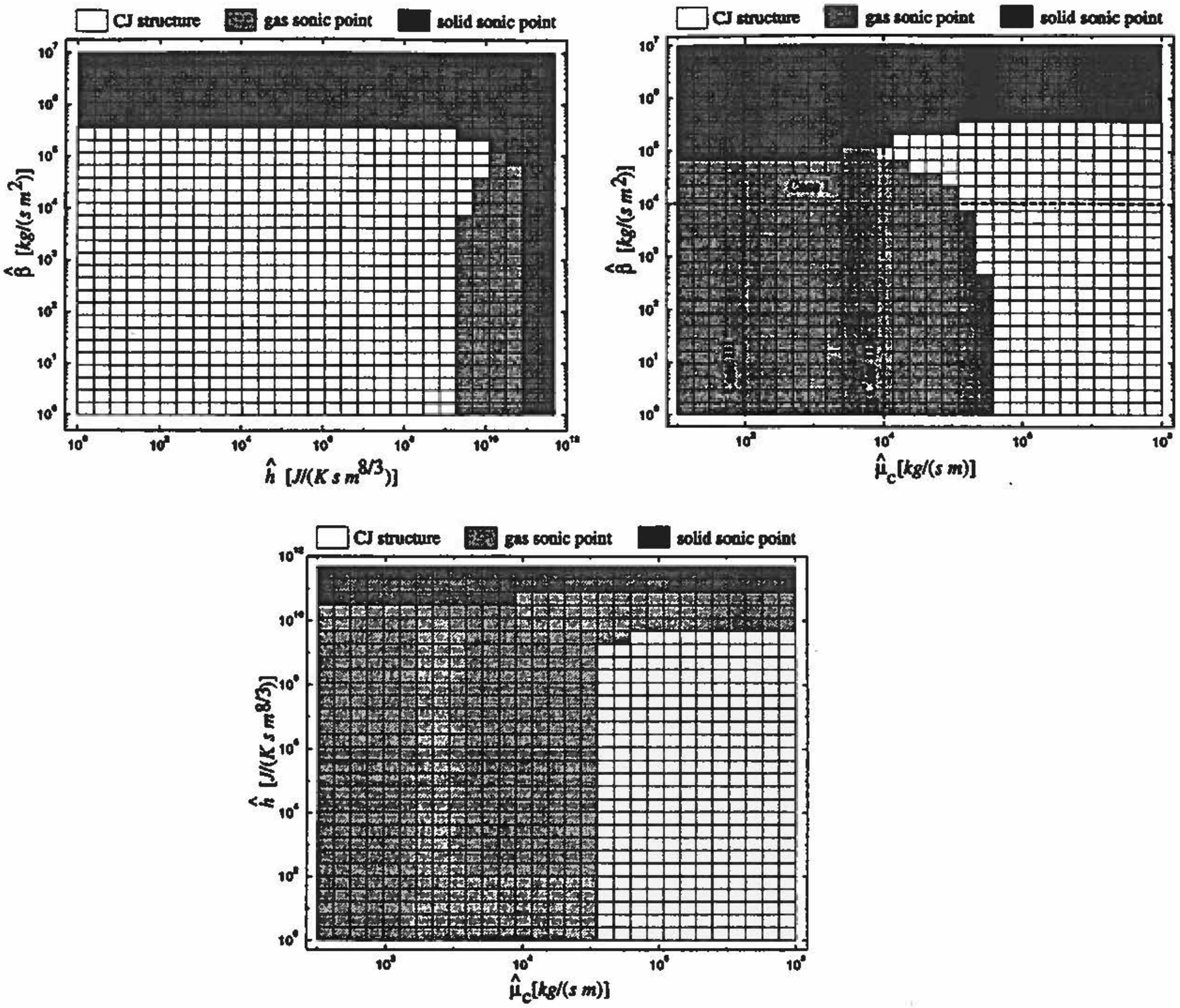

Figure 6.7: Existence criteria for a *shocked gas-unshocked solid CJ* detonation ($\hat{\rho}_a = 1200\ kg/m^3$).

predicted as a gas sonic point is reached within the reaction zone; and 3) regions in which no *shocked gas-unshocked solid CJ* structures are predicted as a solid sonic point is reached within the reaction zone. At the gas sonic points, the forcing terms in Eqs. (6.22) and (6.23) locally vanish; this has physical implications to be discussed in the following section. At the solid sonic points, the forcing term in Eq. (6.20) locally vanishes, while the forcing term in Eq. (6.21) does not; consequently, these solutions must be immediately rejected as non-physical since the solid variables become double-valued functions of position as the integration is continued beyond these points.

The results shown in Fig. 6.7 indicate that steady *shocked gas-unshocked solid CJ* structures do not exist for high interphase drag, high interphase heat transfer, or high material compaction rates. For high drag and heat transfer rates [i.e., approximately $\hat{\beta} > 4 \times 10^5\ kg/(s\ m^2)$ and $\hat{h} > 1 \times 10^{11}\ J/(K\ s\ m^{8/3})$], the solid flow becomes choked within the reaction zone as a sonic point is reached in the solid. This scenario is analogous to one-phase flow through a duct with friction and heat addition [108]. The gas, having a higher velocity and temperature than the solid, exerts a positive drag force on the solid particles, and transfers thermal energy to the unshocked solid flow. If the rates of interphase drag and heat transfer exceed the combustion rate, then the solid flow will be driven to a sonic point within the reaction zone; otherwise, the solid flow remains supersonic throughout the reaction zone. For low interphase drag and heat transfer rates [i.e., approximately $\hat{\beta} < 4 \times 10^5\ kg/(s\ m^2)$ and $\hat{h} < 1 \times 10^{11}\ J/(K\ s\ m^{8/3})$], and high material compaction rates [i.e., approximately $\hat{\mu}_c < 4 \times 10^5\ kg/(s\ m)$], the gas flow becomes choked within the reaction zone as a sonic point is reached in the gas.

Though the combustion rate parameters $\hat{a}$ and m were held fixed for this parameter study, it is likely that similar results would be obtained by fixing either $\hat{\beta}$, $\hat{h}_c$, or $\hat{\mu}_c$, and allowing $\hat{a}$ and m to vary, as it is the relative rates which are of importance. Here, we seek simple expressions for the reaction time, $\hat{\tau}_{rxn}$, and reaction zone length, $\hat{l}_{rxn}$, in terms of the combustion rate parameters $\hat{a}$ and m. It is easily shown from the dimensional form of the characteristic equation for the compaction mode [Eq. (B.8)] that $\hat{\tau}_{rxn}$ is inversely proportional to the combustion rate. To this end, we assume that $\hat{\mu}_c$ is large so that material compaction may be ignored. As such, the dimensional form of Eq. (B.8) reduces to

$$\frac{d\phi_2}{d\hat{\tau}} = -\left(\frac{3}{\hat{r}}\right)\phi_2 \hat{a} \hat{P}_1^m. \tag{6.28}$$

This equation is valid along solid particle paths defined by $\frac{d\hat{\xi}}{d\hat{\tau}} = \hat{v}_2$. Next, we use Eq. (2.15) to replace $\hat{r}$ in Eq. (6.28) in favor of ϕ_2 and $\hat{n}$, and assume that both $\hat{n}$ and $\hat{P}_1$ are constant throughout much of the reaction zone. Steady predictions have shown this to be a reasonable assumption outside of a relatively small region near the lead shock where the gas pressure changes by several orders of magnitude. Consequently, we choose the characteristic values $\hat{n} = \hat{n}_o$ and $\hat{P}_1 = \hat{P}_{1CJ}$, integrate the resulting ordinary differential equation, apply the initial condition $\phi_2(\hat{\tau} = 0) = \phi_{2o}$, and solve for $\hat{\tau}$ to obtain

$$\hat{\tau} = \frac{\hat{r}_o}{\hat{a}\hat{P}_{1CJ}^m}\left[1 - \left(\frac{\phi_2}{\phi_{2o}}\right)^{1/3}\right].$$

In this expression we have replaced $\hat{n}_o$ in favor of ϕ_{2o} and $\hat{r}_o$ using Eq. (2.15). Setting $\phi_2 = 0$ in this expression gives an estimate for $\hat{\tau}_{rxn}$:

$$\hat{\tau}_{rxn} = \frac{\hat{r}_o}{\hat{a}\hat{P}_{1CJ}^m}. \tag{6.29}$$

Thus, the reaction time is directly proportional to the ambient particle radius, and inversely proportional to the combustion rate. Using the values for $\hat{a}$, m, and $\hat{r}_o$ given in TABLE 6.1, and the value $\hat{P}_{1CJ} = 13.5\ GPa$, then $\hat{\tau}_{rxn} = 2.55\ \mu s$. Based on this reaction time, an estimate for the reaction zone length is $\hat{l}_{rxn} = \hat{D}_{CJ}\hat{\tau}$, where $\hat{D}_{CJ}$ is a characteristic velocity for the unshocked solid particles. The estimated reaction zone length is 15.73 mm, which agrees well with the predicted value for the CJ detonation shown in Fig. 6.6. As the combustion rate increases, $\hat{l}_{rxn}$ decreases and, for fixed interphase drag and heat transfer parameters, the length scales associated with these processes greatly exceed the reaction zone length; consequently, these relaxation processes become inconsequential. There likely exists a critical combustion rate for which the solid flow first becomes choked within the reaction zone. For combustion rates in excess of this value the solid flow will remain supersonic throughout the reaction zone.

Lastly, it was shown by Powers et al. [95] that CJ structures having a lead

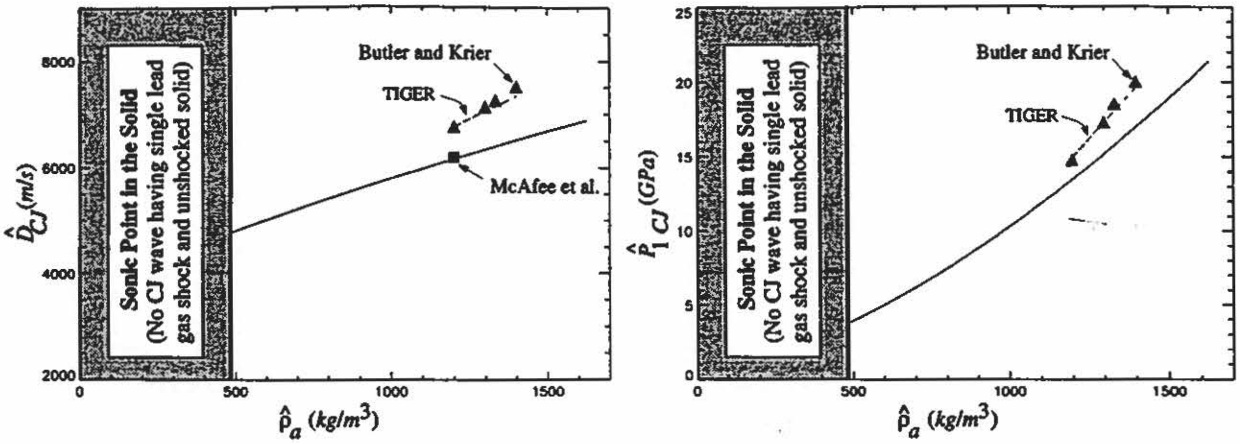

(a)

(b)

Figure 6.8: Variation in (a) CJ wave speed and (b) CJ gas pressure with ambient mixture density.

shock in the gas and an unshocked solid do not exist for ambient mixture densities ($\hat{\rho}_a \equiv \hat{\rho}_{1o}\phi_{1o} + \hat{\rho}_{2o}\phi_{2o}$) below a minimum critical value. Here, we vary the ambient mixture density by holding $\hat{\rho}_{1o}$ and $\hat{\rho}_{2o}$ fixed and allowing ϕ_{2o} (and thus ϕ_{1o}) to vary. Once again, we use the model parameters and ambient conditions given in TABLE 6.1 as a baseline, and integrate the steady equations to predict the minimum critical value of $\hat{\rho}_a$ for which a *shocked gas-unshocked solid* CJ detonation exists. The result is shown in Fig. 6.8. No *shocked gas-unshocked solid* CJ detonation structures are predicted for $\hat{\rho}_a < 486\ kg/m^3$ since a solid sonic point is reached within the reaction zone. At these points, the spatial derivative of the solid variables is undefined. This result is physically significant in that the ambient mixture density can be directly controlled in experiments, and provides a measure of the extent of material damage in cast explosives. In contrast, the existence results obtained for variable $\hat{\beta}$-$\hat{h}$-$\hat{\mu}_c$ are less dependent on the properties of the ambient material, and more dependent on the local conditions of the evolving flow.

Figure 6.8(a) shows the predicted variation in $\hat{D}_{CJ}$ with $\hat{\rho}_a$. Also shown in this figure are numerical predictions given by the unsteady analysis of Butler and Krier [23], numerical predictions given by the thermochemistry code TIGER [27] (as reported by

Butler and Krier), and the experimental value determined by McAfee et al. [80] (as reported by Stewart et al. [111]). Experiments with compressed solid high-explosives have shown $\hat{D}_{CJ}$ to be an increasing function of $\hat{\rho}_a$ [77]. The model predictions exhibit this variation, and also reasonably agree with the referenced results. The predicted variation in $\hat{P}_{1CJ}$ with $\hat{\rho}_a$ is shown in Fig. 6.8(b). Here, an approximately parabolic relationship is predicted which is representative of experimentally observed trends for solid high-explosives [55]. Also shown in this figure are the numerical predictions reported in Reference [23]. Once again, fair agreement exists between the current model predictions and the referenced predictions.

The result of Fig. 6.8 can be explained as follows. As $\hat{\rho}_a$ decreases, $\hat{P}_{1CJ}$ decreases; consequently, the reaction time and reaction zone length, based on Eq. (6.29), increase. As the reaction zone length increases with decreasing $\hat{\rho}_a$, the length scales associated with interphase drag and heat transfer eventually become the same order as the reaction zone length, and the drag and heat transfer rates become sufficient to choke the solid within the reaction zone.

In summary, large regions are predicted in $\hat{\beta}$-$\hat{h}$-$\hat{\mu}_c$ parameter space for which no CJ detonation structures having a single lead shock in the gas and an unshocked solid exist. Furthermore, these structures do not exist for ambient mixture densities below a minimum critical value. As shown in the following subsection, steady weak detonation structures having a single lead shock in the gas and unshocked solid are predicted for parameter values located in regions where a gas sonic point is reached within the reaction zone. The steady analysis performed in this study was unable to identify steady detonation structures for parameter values located in regions where a solid sonic point is reached within the reaction zone. This is not to imply that steady detonations do not exist for these parameter values; rather, the steady analysis became very complicated due to sonic singularities in both the gas and solid, and the results of the analysis were essentially inconclusive. As such, two possibilities remain for parameter values in these regions: 1) the solutions are time-dependent and, thus, no steady structures exist, or 2) more complicated steady structures exist than considered here, possibly having multiple shocks. It is difficult to predict multiple shock structures using a strictly steady-state analysis since both the number and relative locations of the shocks are not known *a priori*. As such, an unsteady analysis can facilitate a steady analysis of more complicated two-phase detonation structures. This issue is addressed in Chapter 7.

6.2.3 Weak Detonation Structure

In this subsection, we demonstrate the existence of weak detonation structures having a single lead shock in the gas and and unshocked solid, and give an example of such a structure. To this end, we choose $\hat{\mu}_c = 1 \times 10^2 \; kg/(s \; m)$, and use the values given in TABLE 6.1 for all remaining model parameters and the ambient conditions. This value of $\hat{\mu}_c$ was used in the unsteady DDT numerical simulations reported by Son et al. [109, 110], Kober et al. [59], and Stewart et al. [111]. Also, the numerical simulations of Baer et al. [5] used values of $\hat{\mu}_c$ close to this value. For the present model, it is seen from Fig. 6.7 that this value of $\hat{\mu}_c$ results in a gas sonic point being reached within the reaction zone for the *shocked gas-unshocked solid CJ* detonation structure.

Results of the weak detonation structure analysis are summarized in the ϕ_1-$\hat{P}_1$ phase plane shown in Fig. 6.9. For clarity, only trajectories in the neighborhood of the complete combustion state ($\phi_1 = 1$) are given. Once again, each trajectory is associated with a different steady wave speed $\hat{D}$, and is parameterized by position $\hat{\zeta}$. All solution trajectories shown in this figure originate from a shocked gas state which is dependent upon the wave speed $\hat{D}$.

A continuum of trajectories are predicted for $\hat{D} < \hat{D}_W = 6169.366 \; m/s$ which do not reach the complete combustion state, but reach a turning point T at which the spatial derivative of the gas variables is undefined. As such, non-physical solutions

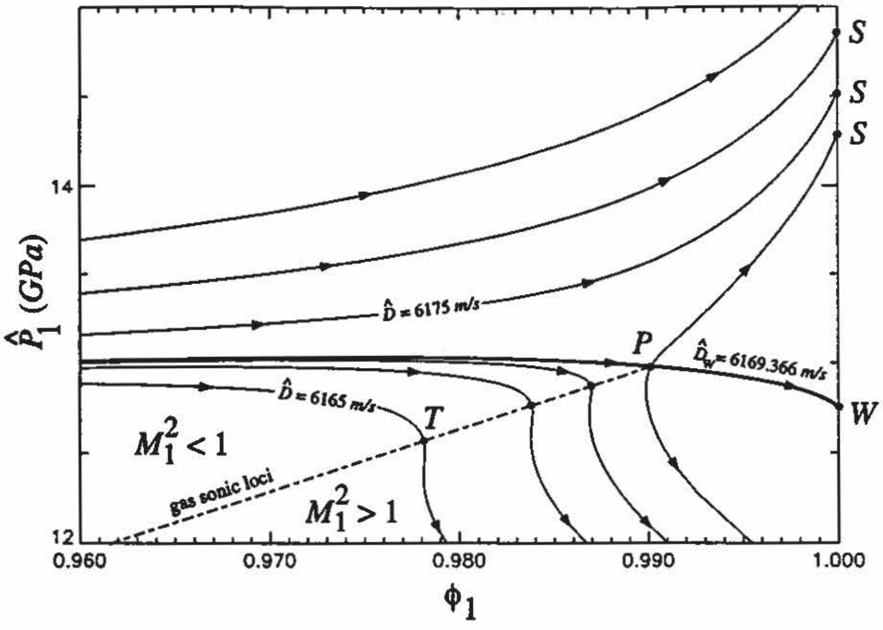

Figure 6.9: $\hat{P}_1$-ϕ_1 phase plane for the *shocked gas-unshocked solid* weak detonation structure analysis.

are predicted. For $\hat{D} = \hat{D}_W > \hat{D}_{CJ}$, the solution trajectory is a manifold of the saddle point P (for pathological). At P, both the quantity $r(w_1^2 - c_1^2)$ and the components of $r(w_1^2 - c_1^2)\mathbf{h}_1(\mathbf{y}_1)$ simultaneously vanish; consequently, it is possible to continue the integration from P to either the strong end state S or the weak end state W. For $\hat{D} > \hat{D}_W$, a continuum of strong detonation trajectories are predicted which terminate at complete combustion states S. Similar phase space topologies have been documented by Fickett and Davis [34] for steady one-phase weak detonations, and by Powers and Gonthier [96] for steady one-phase weak underdriven oblique detonations. Since a unique value for the wave speed is required to traverse the saddle point, weak detonations are often referred to as eigenvalue detonations.

Figure 6.10 shows the structure for the *shocked gas-unshocked solid* weak detonation associated with the trajectory leading to state W in Fig. 6.9. Here, the detonation is propagating to the right at speed $\hat{D}_W = 6169.366\ m/s$, and the gas shock is located at $\hat{\xi} = 0\ mm$. Once again, combustion initiation occurs almost immediately upon crossing the shock. It is seen in Figs. 6.10(a,c) that the gas pressure and Mach num-

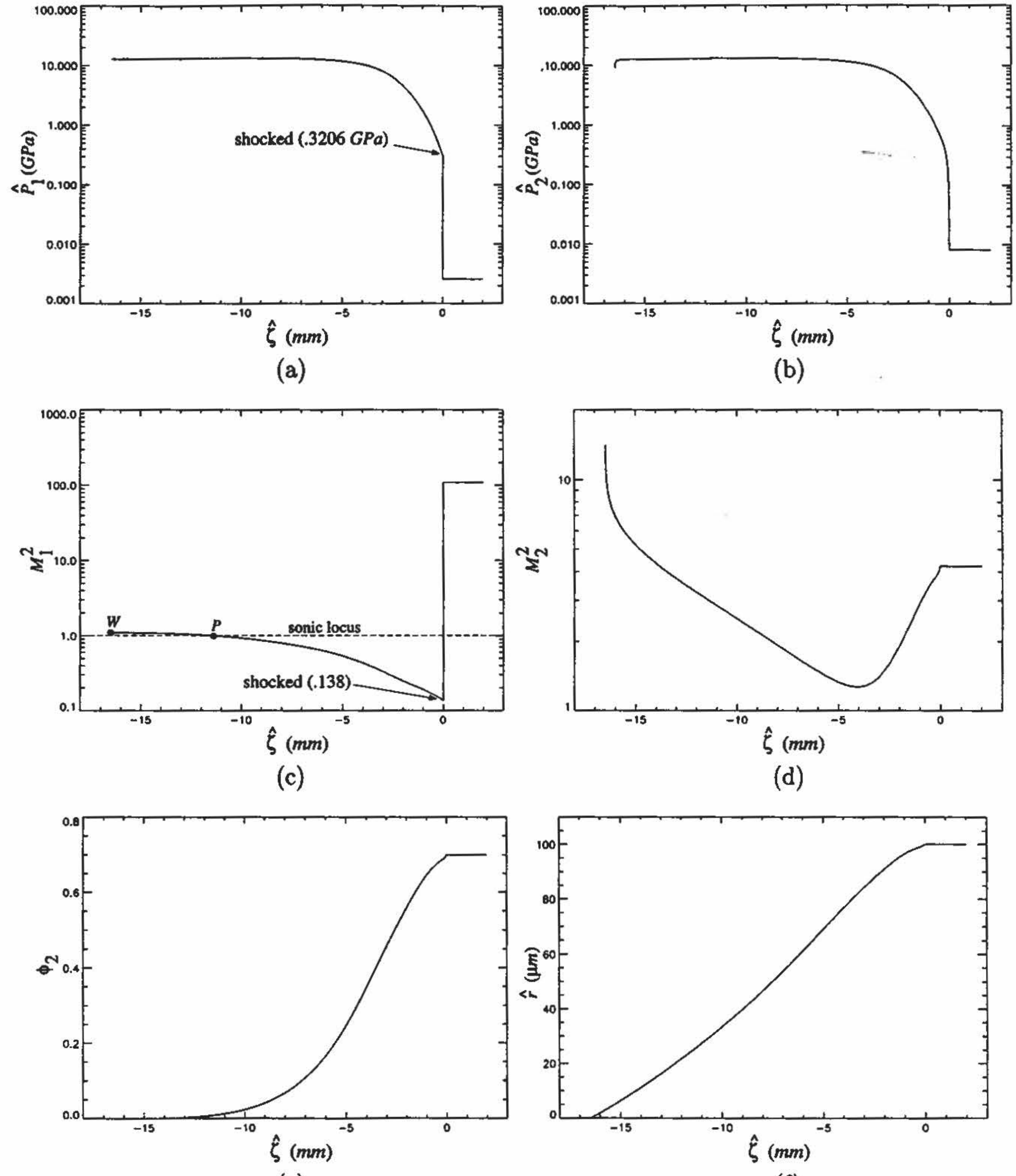

(a) (b)

(c) (d)

(e) (f)

Figure 6.10: *Shocked gas-unshocked solid* weak detonation structure: (a,b) gas and solid pressure; (c,d) gas and solid Mach number squared (relative to the wave frame); (e) solid volume fraction; and (f) particle radius.

Parameter	Case I	Case II	Case III	Units
$\hat{\beta}$	1×10^4	variable	variable	$kg/(s\ m^2)$
$\hat{h}$	1×10^7	1×10^7	1×10^7	$J/(K\ s\ m^{8/3})$
$\hat{\mu}_c$	variable	1×10^4	1×10^2	$kg/(s\ m)$

TABLE 6.2: CASES USED TO ILLUSTRATE BIFURCATIONS IN STEADY DETONATION STRUCTURE

ber squared change discontinuously from their ambient values of 2.57 MPa and 108.57 to 0.3206 GPa and 0.138 at the shock, respectively. Subsequently, the gas pressure increases to 12.75 GPa at complete reaction, and the gas Mach number squared increases to unity at $\zeta = -11.343\ mm$, and further increases to 1.094 at complete reaction. Due to the gas sonic point within the reaction zone, only gas acoustic waves generated in the region $-11.343 < \hat{\zeta} < 0\ mm$ influence the lead shock. It is seen in Figs. 6.10(b,d) that a continuous change in solid pressure and Mach number is predicted as the solid is unshocked. The solid pressure increases from its ambient value of 8.21 MPa to 8.896 GPa at complete reaction. The solid Mach number squared decreases from its ambient value of 4.23 to 1.266 at $\hat{\zeta} = -4.02\ mm$, and then increases to 13.261 at complete reaction. Also, it is seen in Figs. 6.10(e,f) that a continuous variation in both solid volume fraction and particle radius is predicted. The predicted reaction zone length is 16.46 mm.

Shown in Fig. 6.11 is the predicted variation in steady detonation wave speed for the three cases identified in TABLE 6.2. These three cases, which correspond to the dashed lines identified in the $\hat{\beta}$-$\hat{h}$-$\hat{\mu}_c$ parameter space of Fig. 6.7, illustrate bifurcations in the predicted steady detonation structure. For Case I, the parameters $\hat{\beta}$ and $\hat{h}$ are fixed, and $\hat{\mu}_c$ is varied over the range $1 \times 10^1 \leq \hat{\mu}_c \leq 1 \times 10^8\ kg/(s\ m)$. For Cases II and III, the parameters $\hat{h}$ and $\hat{\mu}_c$ are fixed, and $\hat{\beta}$ is varied over the range $1 \times 10^1 \leq \hat{\beta} \leq 1 \times 10^7\ kg/(s\ m^2)$. A different value for $\hat{\mu}_c$ is used in Cases II and

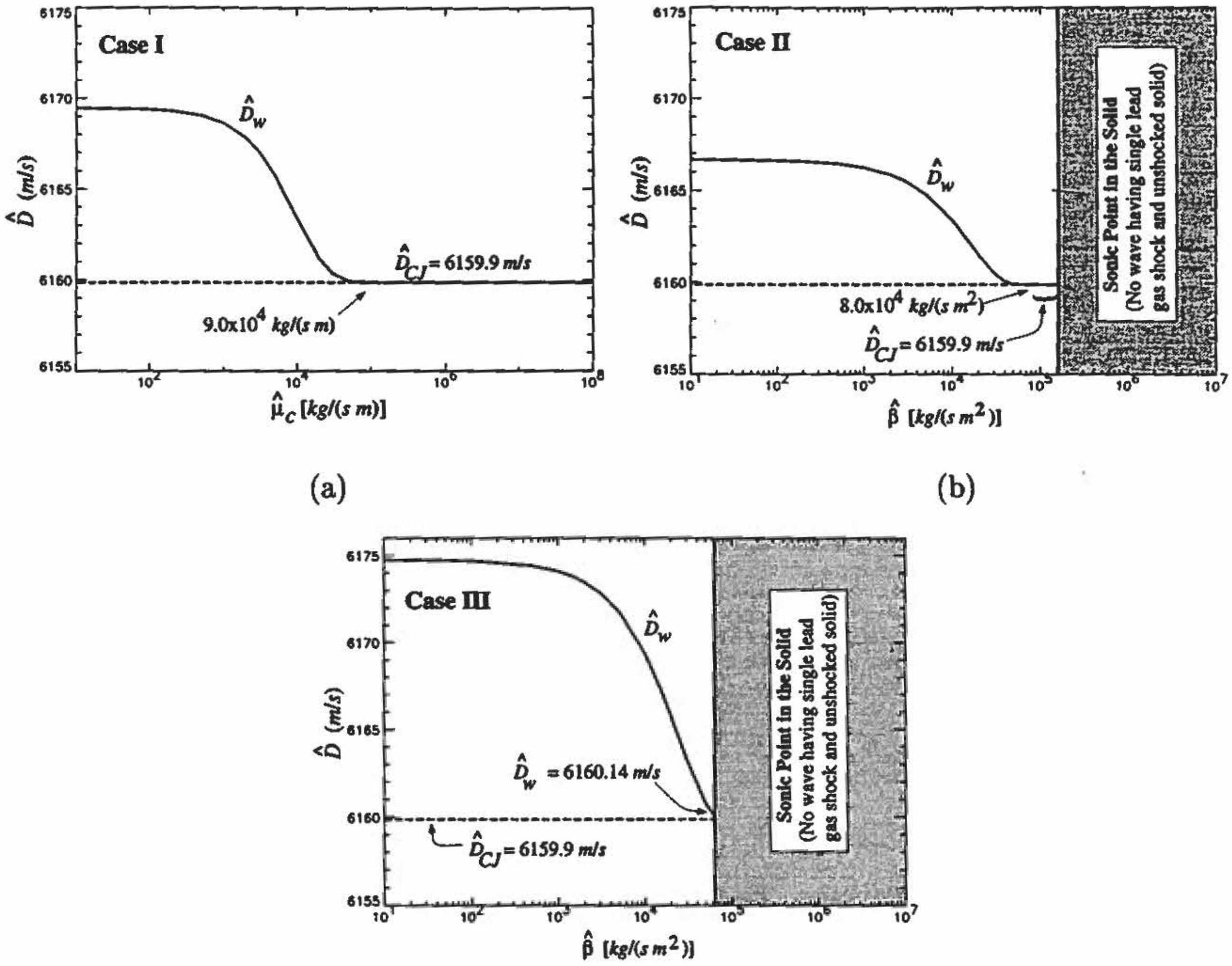

(a) (b)

(c)

Figure 6.11: Bifurcation diagrams for the three cases identified in TABLE 6.2.

III to illustrate a difference in the steady solution near the boundary where a solid sonic point is first predicted. The value $\hat{h} = 1 \times 10^7\ J/(K\ s\ m^{8/3})$ was used for all three cases. Values for the ambient conditions and the remaining model parameters are given in TABLE 6.1.

For Case I, Fig. 6.11(a) shows that a continuum of weak detonation structures having speed $\hat{D}_W$ are predicted for $\hat{\mu}_c \leq 9 \times 10^4\ kg/(s\ m)$. For $\hat{\mu}_c < 1 \times 10^3\ kg/(s\ m)$, $\hat{D}_W$ is insensitive to changes in $\hat{\mu}_c$, and is approximately equal to 6169.37 m/s. As $\hat{\mu}_c$ increases, $\hat{D}_W$ continuously approaches $\hat{D}_{CJ}$. The *shocked gas-unshocked solid* weak detonation structure undergoes a bifurcation to a *shocked gas-unshocked solid*

CJ detonation structure for approximately $\hat{\mu}_c = 9 \times 10^4\ kg/(s\ m)$. A continuum of *shocked gas-unshocked solid* CJ structures are predicted as the value of $\hat{\mu}_c$ is further increased.

For Case II, Fig. 6.11(b) shows that a continuum of weak detonation structures are predicted for $\hat{\beta} < 8 \times 10^4\ kg/(s\ m^2)$. Here, $\hat{D}_W$ is insensitive to changes in $\hat{\beta}$ for $\hat{\beta} < 1 \times 10^3\ kg/(s\ m^2)$, and is approximately equal to 6166.64 m/s. There exists a bifurcation from weak structures to CJ structures as $\hat{\beta}$ increases. A CJ structure is first predicted for approximately $\hat{\beta} = 8 \times 10^4\ kg/(s\ m^2)$. A continuum of CJ structures are predicted for $8 \times 10^4 \leq \hat{\beta} \leq 1.3 \times 10^5\ kg/(s\ m^2)$. For $\hat{\beta} > 1.3 \times 10^5\ kg/(s\ m^2)$, no steady *shocked gas-unshocked solid* detonation structures are predicted since a solid sonic point is reached within the reaction zone.

For Case III, Fig. 6.11(c) shows that a continuum of weak structures are predicted for $\hat{\beta} < 6.16 \times 10^4\ kg/(s\ m^2)$. Once again, $\hat{D}_W$ is insensitive to changes in $\hat{\beta}$ for $\hat{\beta} < 1 \times 10^3\ kg/(s\ m^2)$, and is approximately equal to 6174.75 m/s. For increasing $\hat{\beta}$, $\hat{D}_W$ approaches but does not reach $\hat{D}_{CJ}$ since a solid sonic condition is predicted within the reaction zone for $\hat{\beta} > 6.16 \times 10^4\ kg/(s\ m^2)$. For this case, the minimum steady wave speed for a *shocked gas-unshocked solid* detonation is $\hat{D}_W = 6160.14\ m/s$.

7

UNSTEADY ANALYSIS OF TWO-PHASE DETONATION

In this chapter, we give an unsteady analysis of the piston-initiated DDT problem. The goals of this analysis are three-fold: 1) to demonstrate the existence of DDT events which give rise to the steady detonation structures predicted in the previous chapter; 2) to investigate the evolution of detonation for parameter values and ambient conditions for which no steady *shocked gas-unshocked solid* detonations were predicted; and 3) to investigate the influence of material compaction, interphase drag, and ambient solid volume fraction on DDT and detonation wave structure. Throughout, emphasis is placed on comparing detonation structures predicted by the unsteady analysis with results of the steady analysis.

We focus on Cases I and II identified in TABLE 6.2, and fix all remaining model parameters and the ambient conditions at the values listed in TABLE 6.1. Case I is considered in Section 7.1, where we show the existence of DDT events which give rise to the CJ and weak detonation structures shown in Figs. 6.6 and 6.10, respectively, and investigate the influence of compaction viscosity, $\hat{\mu}_c$, on both DDT and detonation wave structure. Case II is considered in Section 7.2.1, where we investigate the evolution of detonation for values of the drag parameter, $\hat{\beta}$, greater than the maximum value for which steady *shocked gas-unshocked solid* CJ structures were predicted. Here, it is demonstrated that CJ structures having a single shock in both the gas and solid evolve, as do CJ structures having only a single lead shock in the solid. Also, the influence of $\hat{\beta}$ on DDT is investigated. Lastly, in Section 7.3 we show that CJ structures having a single shock in both the gas and solid also evolve for ambient mixture densities less than the minimum value for which steady *shocked gas-*

unshocked solid CJ structures were predicted. As mentioned in the previous chapter, this is a physically interesting case as the ambient mixture density of the material is known *a priori*, and is a direct measure of the extent of material damage in cast explosives or propellants. The piston velocity prescribed by Eq. 4.125 was used for all simulations performed in this analysis.

7.1 Effect of Material Compaction

For Case I shown in Fig. 6.11(a), the steady analysis predicts a continuum of *shocked gas-unshocked solid* weak detonation structures for $\hat{\mu}_c \leq 9 \times 10^4\ kg/(s\ m)$, and a continuum of *shocked gas-unshocked solid CJ* detonation structures for $\hat{\mu}_c$ greater than this value. In this section, we first give DDT results for $\hat{\mu}_c = 1 \times 10^2\ kg/(s\ m)$ which demonstrate the evolution of a *shocked gas-unshocked solid* weak detonation structure, and then give DDT results for $\hat{\mu}_c = 1 \times 10^6\ kg/(s\ m)$ which demonstrate the evolution of a *shocked gas-unshocked solid CJ* detonation structure. This section is concluded by summarizing DDT results and detonation structures predicted for several values of $\hat{\mu}_c$ within the range $1 \times 10^2 \leq \hat{\mu}_c\ kg/(s\ m) \leq 1 \times 10^7\ kg/(s\ m)$. The computational domain used for these unsteady numerical simulations was defined for $0 \leq \hat{\xi} \leq 50\ cm$, and consisted of $N = 1500$ uniformly spaced nodes. The average CPU time for a single simulation was approximately five hours.

7.1.1 Evolution of a Weak Detonation

Shown in Fig. 7.1 are the predicted velocity (measured relative to the laboratory frame), pressure, and temperature history of the gas for $\hat{\mu}_c = 1 \times 10^2\ kg/(s\ m)$. Also shown in this figure are the spatial profiles at $\hat{\tau} = 210\ \mu s$. The predicted solid velocity, pressure, and temperature history are shown in Fig. 7.2. Each of the curves for the solid variables is plotted up to the point of complete combustion ($\phi_{2\epsilon} = 1 \times 10^{-5}$). In these figures, $\hat{\xi}$ is position measured relative to the piston surface.

The moving piston transmits energy to the ambient granular material through forward propagating gas and solid acoustic waves. As discussed in Chapter 2, the non-dimensional model parameter $\pi_7 = \frac{\hat{\rho}_{2o}\hat{c}_{2o}\hat{r}_o}{\hat{\mu}_c}$ is the ratio of the characteristic time associated with the propagation of solid acoustic waves in the ambient solid to the characteristic time associated with compaction of the ambient material. For this simulation, $\pi_7 = 5.13$; thus, compaction occurs on a faster time scale than does the propagation of solid acoustic waves. As such, a solid shock does not form in response to the accelerating piston due to the rapid relaxation in solid pressure associated with material compaction (i.e., $\hat{P}_2 \rightarrow \hat{P}_1 + \hat{f}$). Rather, a dispersed compaction wave quickly forms which propagates away from the piston at constant speed. The predicted compaction wave speed relative to the fixed laboratory frame is 401.98 m/s, which is well below the ambient solid sound speed (3000 m/s). The predicted compaction zone thickness is approximately 5.0 mm. A continuous variation in all variables is predicted within the compaction zone. The gas pressure and temperature increase from their ambient values of 2.57 MPa and 300 K to approximately 19.81 MPa and 330.25 K, and the solid pressure and temperature increase from their ambient values of 8.21 MPa and 300 K to approximately 55.59 MPa and 304.53 K within the compaction zone, respectively. The gas and solid velocity increase from 0 m/s to 100 m/s, as required by the zero mass flux boundary condition at the piston surface. The predicted solid volume fraction in the compacted region is approximately 0.94. The gas and solid states in the compacted region are not constant, but deviate slightly due to thermal non-equilibrium between the phases. However, since the temperature difference between the gas and solid is small, the rate of thermal energy transfer is accordingly small.

As time advances, the width of the compacted region increases as the compaction wave propagates away from the piston. Combustion initiation is predicted to occur at the piston surface after an induction period of approximately 135 μs. Induction

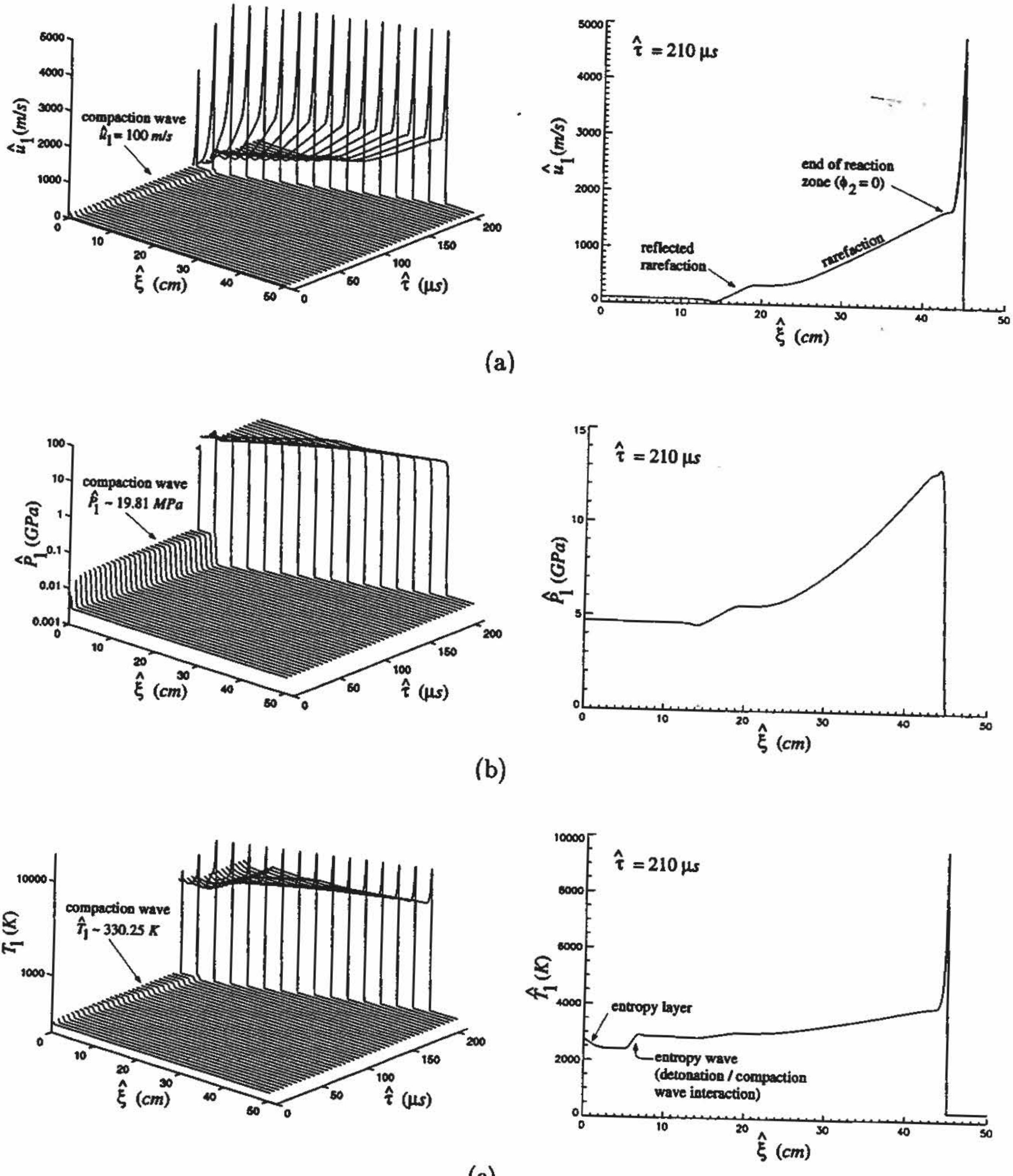

Figure 7.1: Predicted time histories for the *shocked gas-unshocked solid* weak detonation simulation: (a) gas velocity, (b) gas pressure, and (c) gas temperature.

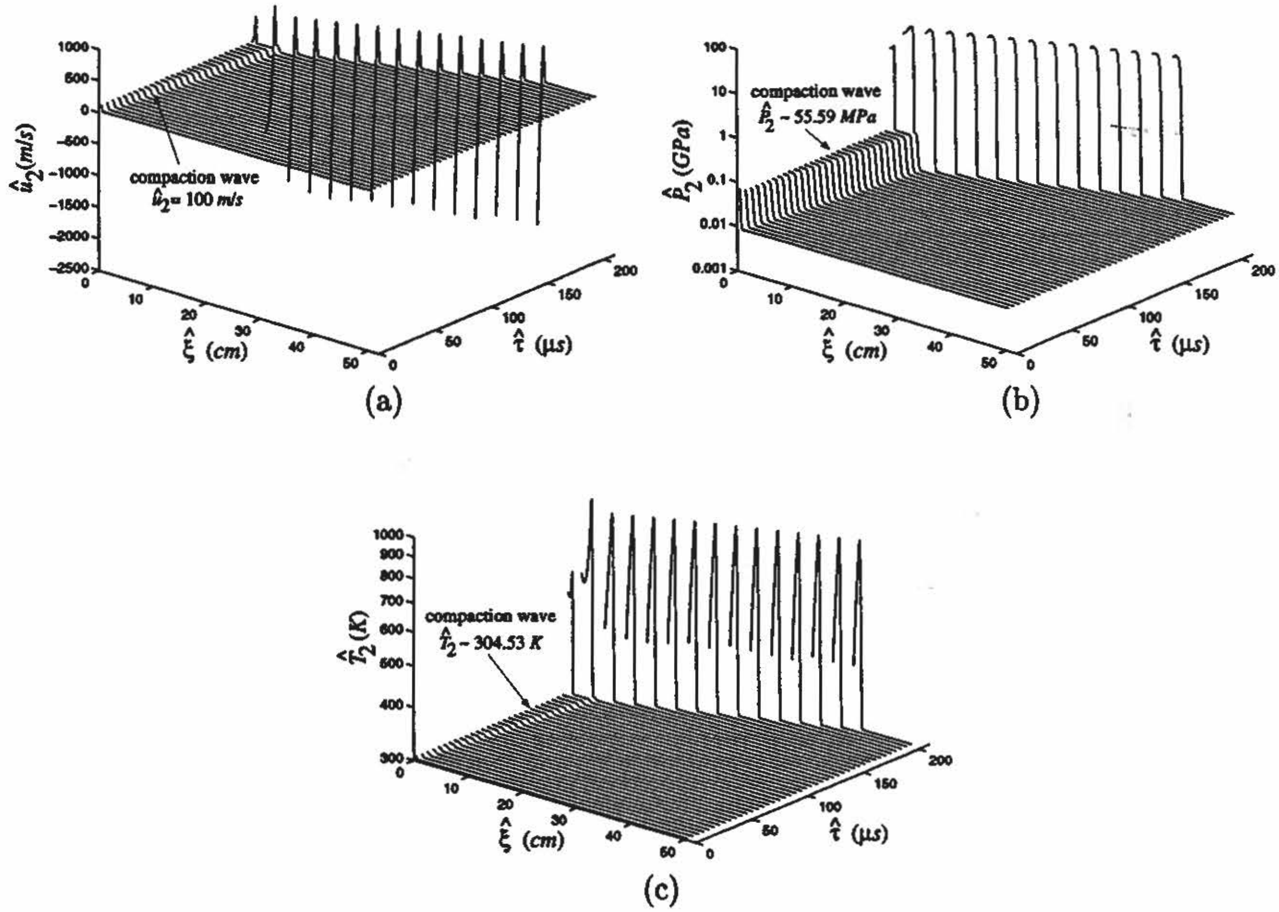

Figure 7.2: Predicted time histories for the *shocked gas-unshocked solid* weak detonation simulation: (a) solid velocity, (b) solid pressure, and (c) solid temperature.

periods prior to the onset of sustained combustion are characteristic of piston-initiated DDT in granular high-explosives [8, 80, 81]. It is widely accepted that during the induction period, weakly exothermic chemical reactions take place due to localized heating of the explosive material as it is compacted. As previously discussed, possible heating mechanisms include adiabatic shear localization within explosive particles, friction between explosive particles, and adiabatic compression of the gas contained within the interstices of explosive particles. As progressively more energy is liberated due to combustion, the reaction rate increases resulting in a self-accelerating process. Since chemical reaction is local in nature, the compacted explosive nearest the piston surface incubates the longest and, consequently, is first to undergo sustained combustion. The onset of sustained combustion marks the end of the induction period. In this study, the induction period is modeled using the evolution equation for the ignition variable I [Eq. (2.9)]. Within the context of this model, the higher-temperature gas in the compacted region transfers an increasing amount of thermal energy to the solid as time advances due heat transfer. As such, both the solid pressure and temperature increase, resulting in a net increase in the growth rate of I. At the time of combustion initiation, defined as the time at which $I = I_{ig} = 0.5$, the thermal energy acquired by the solid is assumed sufficient to initiate full-scale combustion.

An estimate for the induction time can be obtained from Eq. (6.27). To this end, we choose as characteristic values the gas pressure (19.81 MPa) and temperature (330.25 K), the solid pressure (55.59 MPa) and temperature (304.53 K), and the gas and solid volume fraction (0.06 and 0.94, respectively) in the compacted region. Substituting these values into Eq. (6.27) gives an estimated ignition time of 162 μs. This value reasonably agrees with the numerically predicted value of 135 μs.

As seen in Figs. 7.1 and 7.2, a rapid increase in the velocity, pressure, and temperature of both the gas and solid is predicted following the onset of combustion. Transition to detonation is predicted to occur almost immediately. The detonation continuously accelerates and strengthens as it propagates through the compacted material. The solid is first completely consumed at the piston surface approximately 140 μs after piston impact; consequently, the solid is not directly affected by the moving piston for $\hat{\tau} \geq 140$ μs. The accelerating detonation overtakes the compaction wave approximately 145 μs after piston impact. Since the gas and solid pressure, gas and solid temperature, and solid volume fraction continuously decrease immediately in front of the detonation as it traverses the compaction zone structure, both a left-propagating rarefaction and a right-propagating entropy wave are produced by the interaction. For this case, the entropy wave has a continuous structure (i.e., it is not

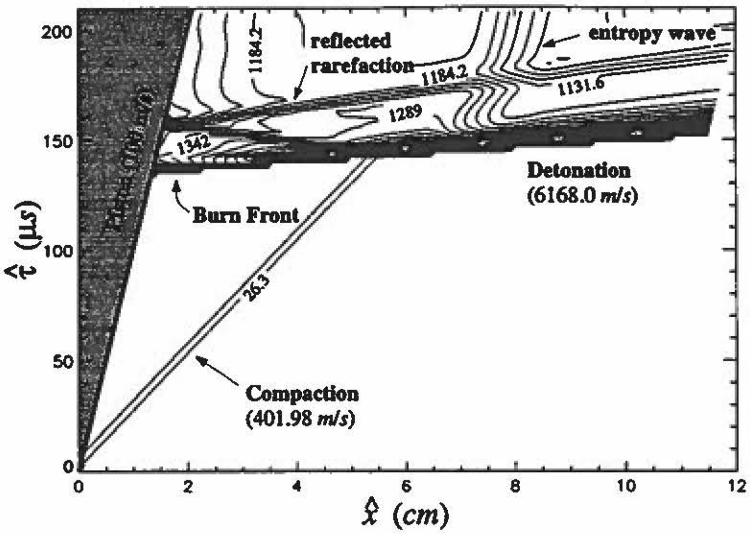

Figure 7.3: Predicted gas density (kg/m^3) contours for the *shocked gas-unshocked solid* weak detonation simulation.

a contact discontinuity). These waves are evident in Fig. 7.3 which gives gas density contours projected in the $\hat{x}$-$\hat{\tau}$ plane. Subsequently, the left-propagating rarefaction reflects off the piston surface, the entropy wave continues to propagate slowly to the right, and the accelerating detonation relaxes to a steady weak detonation propagating at speed 6168 m/s. Following the detonation is a right-propagating rarefaction which reduces the gas velocity at the end of the reaction zone to that of the piston (100 m/s). The rarefactions are indicated in the spatial profiles for the gas velocity and pressure at $\hat{\tau} = 210$ μs [Figs. 7.1(a,b)], and the entropy wave is indicated in the spatial profile for the gas temperature at $\hat{\tau} = 210$ μs [Fig. 7.1(c)]. Since the gas velocity (measured relative to the piston) is zero through the entropy wave at $\hat{\tau} = 210$ μs, and since thermal diffusion is absent from the model, the wave does not move relative to the piston, nor does its amplitude decrease as time advances.

Also indicated in the gas temperature profile of Fig. 7.1(c) is an entropy layer immediately next to the piston surface which is generated during the transition process. Menikoff [82, 83] and Menikoff and Lackner [85] have shown that shock-capturing methods predict a spurious entropy layer when a shock interacts with a solid boundary, and have proposed a production mechanism for this anomalous structure which is a direct consequence of the artificial width of the numerically predicted shock. For hyperbolic equations, the time interval associated with the shock-boundary interaction is zero since the shock is a discontinuity. However, numerical shocks, having an artificial width due to numerical diffusion, interact with the boundary over a finite time interval. Since entropy production occurs only during the interaction period, the predicted width of the spurious entropy layer is close to the artificial shock width. Though not reported in this dissertation, spurious entropy layers were numerically predicted near the piston surface when the piston was impulsively set into constant velocity motion. Glaister [37] has also predicted spurious entropy layers for similar types of problems. Since the piston was continuously accelerated from rest to a constant velocity for the simulations reported in this thesis, the effects of the entropy production mechanism may be minimal. Furthermore, the width of the entropy layer predicted here is much larger than the length of three computational cells, the typical length needed to numerically capture shocks. Nevertheless, it is difficult to conclusively determine if this entropy layer is physical, or if it is a numerical artifact of the shock-capturing method.

The predicted solid volume fraction history is shown in Fig. 7.4. Here, the inert compaction wave is seen propagating away from the piston for early time. Across this wave, the ambient mixture is compacted from a solid volume fraction of 0.70 to 0.94. Following combustion initiation at the piston surface at $\hat{\tau} = 135\ \mu s$, combustion consumes the solid as the resulting detonation propagates through the compacted material. As seen in this figure, the detonation is about to overtake the compaction wave at $\hat{\tau} = 141.95\ \mu s$. Soon afterwards, the steady detonation forms. The solid volume fraction continuously decreases from 0.70 to $\phi_{2\epsilon} = 1 \times 10^{-5}$ through the steady detonation structure.

The numerically predicted compaction wave and burn front trajectories in the $\hat{x}$-$\hat{\tau}$

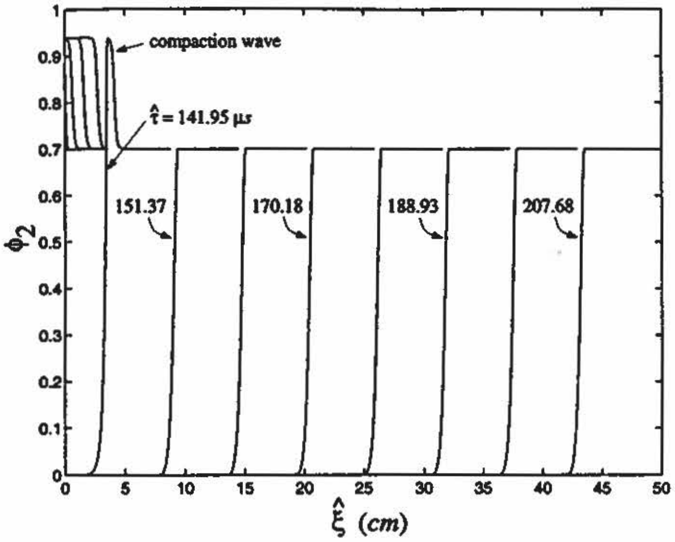

Figure 7.4: Numerically predicted solid volume fraction history for the *shocked gas-unshocked solid* weak detonation simulation.

plane are shown in Fig. 7.5. Also shown in this figure are the compaction wave and burn front trajectories observed experimentally by McAfee et al. [80] (as reported by Stewart et al. [111]). In their experiment, McAfee et al. impacted a bed of granular HMX with an explosively driven piston. The granular material, which was confined by a thick-walled steel tube, was prepared such that $\phi_{2_o} \cong 0.70$ and $\hat{\rho}_a \cong 1200\ kg/m^3$. The size of the HMX granules ranged from 10-100 μm, and the impact velocity of the piston was approximately 100 m/s. These values are representative of the ones used in this study.

As seen in Fig. 7.5, good agreement exists between the numerically predicted and experimentally observed compaction and detonation wave trajectories. Though the experiment indicates that combustion is first initiated at the piston surface, as is predicted by the model, it is observed to occur much sooner ($\hat{\tau} \sim 88\ \mu s$) than predicted by the model. The experiment indicates that a low speed ($\sim 400\ m/s$) combustion wave propagates away from the piston following combustion initiation, and that an inert solid plug is formed slightly ahead of the combustion front, approximately 120 μs from the time of piston impact. As the plug accelerates and grows in size, a shock

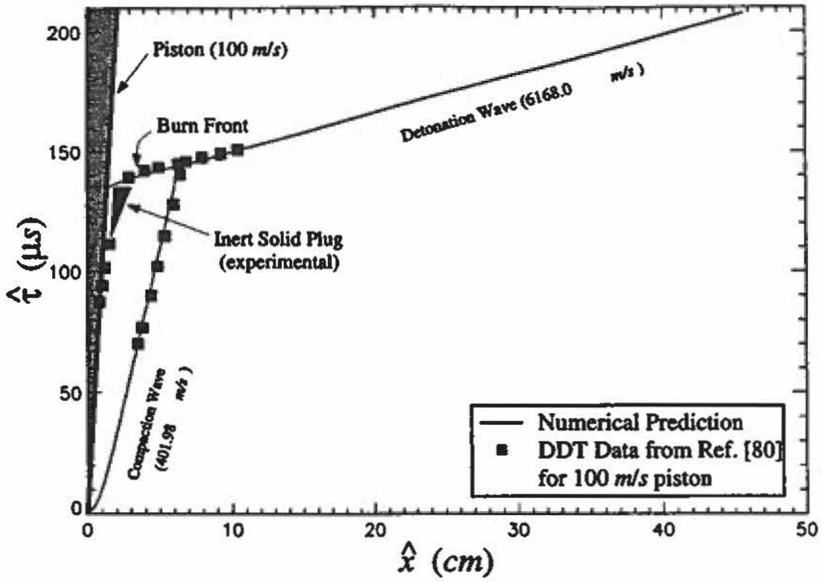

Figure 7.5: Comparison of the predicted compaction wave and burn front trajectories for the *shocked gas-unshocked solid* weak detonation simulation with the experimental wave trajectories identified by McAfee et al. [80].

is formed immediately ahead of the plug which ignites the material resulting in the formation of a second combustion wave. This second wave then quickly undergoes a transition to detonation. This sequence of events, including inert plug formation, has also been recently observed by Luebcke et al. [75] during DDT in granular PETN. Though the model does not predict the slow speed combustion wave, nor the formation of an inert solid plug, it does reasonably predict 1) the compaction wave speed, 2) the compaction wave thickness, 3) the solid volume fraction behind the lead compaction wave, 4) the time and distance associated with transition to detonation, and 5) the detonation wave speed. Here, the time and distance for transition to detonation are defined by the point in the $\hat{\xi}$-$\hat{\tau}$ plane where the detonation speed, as measured by the slope of the burn front, approximately equals the steady detonation speed. A comparison of the numerically predicted and experimentally observed values for these quantities is given in TABLE 7.1.

Lastly, a comparison of the numerically predicted detonation structure with the *shocked gas-unshocked solid* weak detonation structure predicted by the steady anal-

Quantity	Experiment	Model
compaction wave speed	400 m/s	401.98 m/s
compaction wave thickness	2 mm	5 mm
solid volume fraction behind the lead compaction wave	0.90	0.94
time to detonation	142 μs	138 μs
distance to detonation measured relative to the piston	25 mm	10 mm
detonation wave speed	6200 m/s	6169.4 m/s

TABLE 7.1: COMPARISON OF NUMERICALLY PREDICTED QUANTITIES WITH THE RESULTS OF THE DDT EXPERIMENT GIVEN IN REFERENCE [80]

ysis is given in Fig. 7.6. This figure shows the variation in density, velocity, pressure, temperature, and Mach number squared (measured relative to the wave) of the gas and solid, and in the solid volume fraction and particle radius within the reaction zone. The flow located between the piston surface ($\hat{\xi} = 0\ cm$) and the end of the reaction zone ($\hat{\xi} = 43.4\ cm$) is not shown in this figure. Good agreement exists between the predicted solutions. As such, it is clear that a *shocked gas-unshocked solid* weak detonation structure has evolved. The numerical method is able to capture the gas shock with approximately three computational cells without the generation of spurious oscillations. Though not very evident here, the numerical method has difficulty accurately predicting the variation in solid quantities near the end of the reaction zone; this difficulty is slightly noticeable in the numerically predicted solid density profile. Reasons for this difficulty are unclear, but it is likely a consequence of the burn termination technique used in this study.

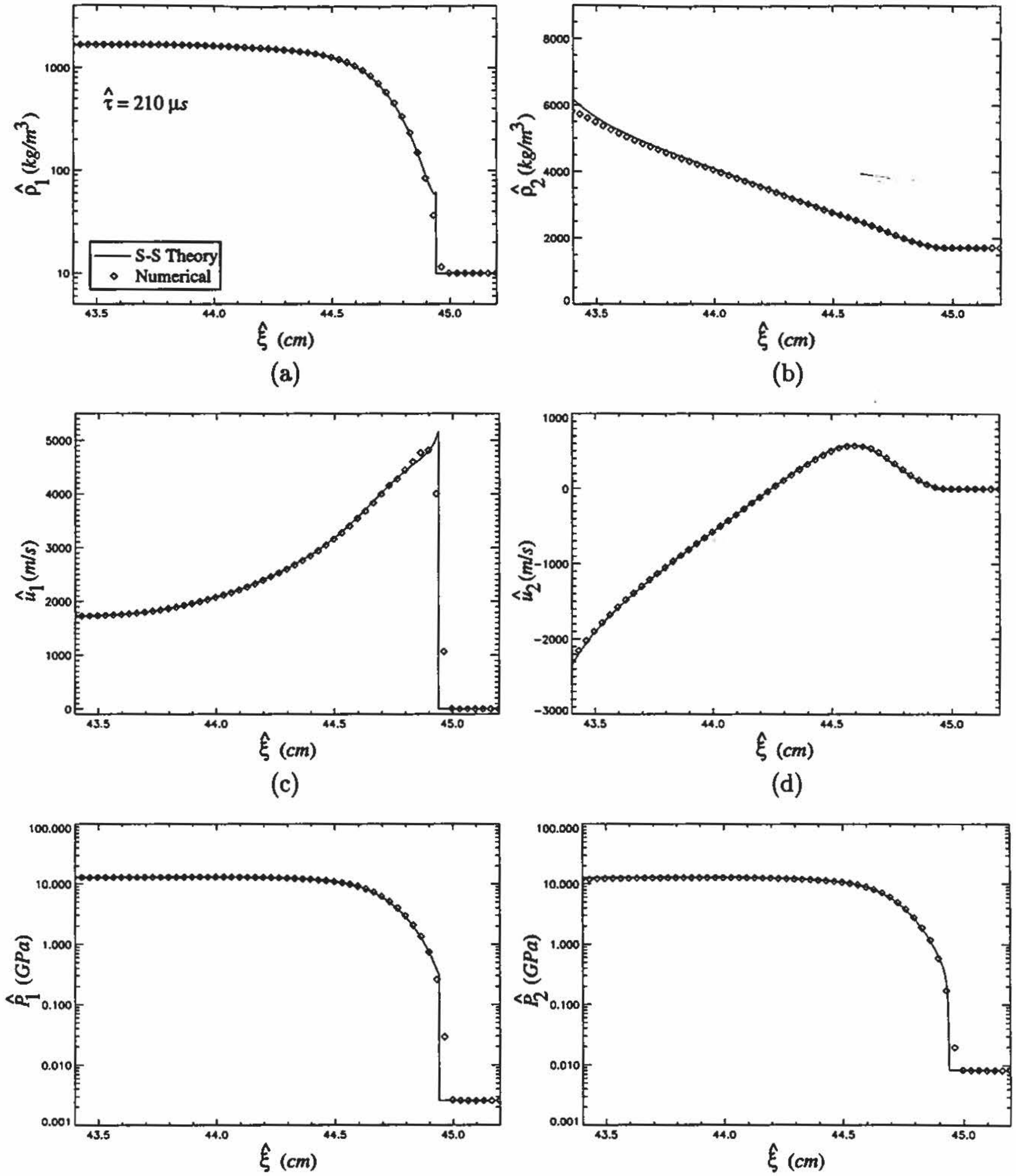

(a) (b)

(c) (d)

(e) (f)

Figure 7.6: Comparison of the *shocked gas-unshocked solid* weak detonation structures predicted by the steady and unsteady detonation analyses: (a,b) gas and solid density; (c,d) gas and solid velocity; (e,f) gas and solid pressure; (g,h) gas and solid temperature; (i,j) gas and solid Mach number squared (relative to the wave); (k) solid volume fraction; and (l) particle radius.

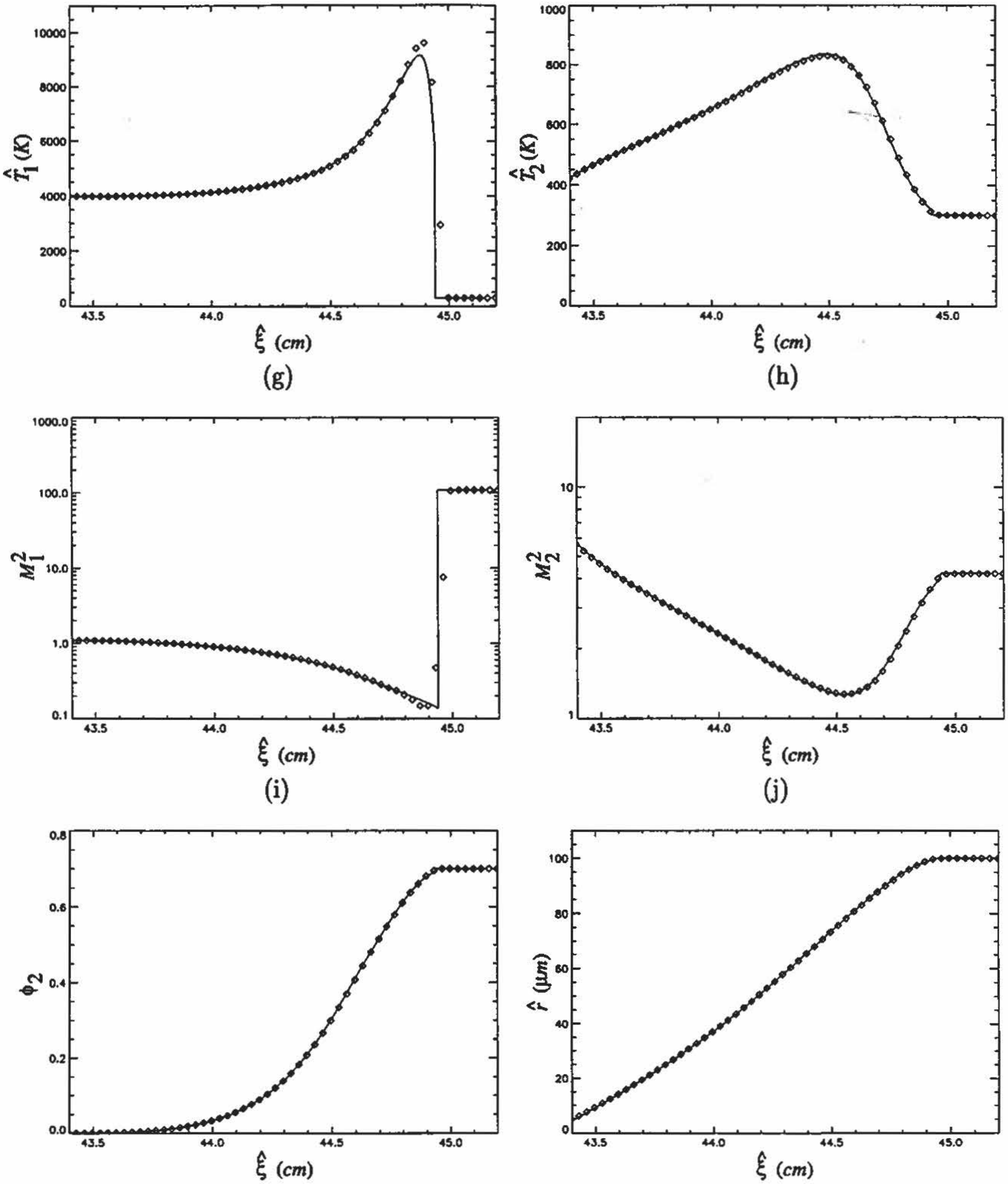

(g) (h)

(i) (j)

(k) (l)

Figure 7.6 (Continued)

7.1.2 Evolution of a Chapman-Jouguet Detonation

Shown in Fig. 7.7 are the predicted velocity, pressure, and temperature history of the gas for $\hat{\mu}_c = 1 \times 10^6\ kg/(s\ m)$. Also shown in this figure are the spatial profiles for these quantities at $\hat{\tau} = 89\ \mu s$. The predicted solid velocity, pressure, and temperature history are shown in Fig. 7.8. Once again, each of the curves for the solid variables is only plotted up to the point of complete combustion.

For this simulation, $\pi_7 = 5.13 \times 10^{-4}$; consequently, the time scale associated with compaction of the ambient material is much larger than the time scale associated with the propagation of solid acoustic waves through the ambient solid. Since the relaxation in solid pressure due to material compaction is insignificant during the short time interval required for the piston to accelerate to its maximum constant velocity ($2\ \mu s$), forward propagating gas and solid acoustic waves generated by the moving piston rapidly coalesce to form shocks. The gas shock, which evolves almost immediately following the initial movement of the piston, is not evident in the history profiles of Fig. 7.7. However, the faster propagating solid shock is evident in the history profiles of Fig. 7.8. Here, the solid velocity, pressure, and temperature for $\hat{\tau} < 10\ \mu s$ are close to the shocked solid velocity ($100\ m/s$), pressure ($.548\ GPa$), and temperature ($341.38\ K$) associated with a $100\ m/s$ piston.

Combustion is initiated at the piston surface after a short induction period of approximately $3\ \mu s$. An estimate for the induction time can be obtained from Eq. (6.27). To this end, we choose as characteristic values the shocked gas and solid pressure ($3.22\ MPa$ and $0.548\ GPa$, respectively), and the shocked gas and solid temperature ($318.44\ K$ and $341.38\ K$, respectively) associated with a $100\ m/s$ piston, and the ambient gas and solid volume fraction (0.30 and 0.70, respectively). The estimated ignition time is $0.94\ \mu s$; thus, ignition rapidly occurs due to compression of the material. The shocked gas pressure, gas temperature, and solid temperature produce a relatively small increase in the growth rate of the ignition variable I. The high

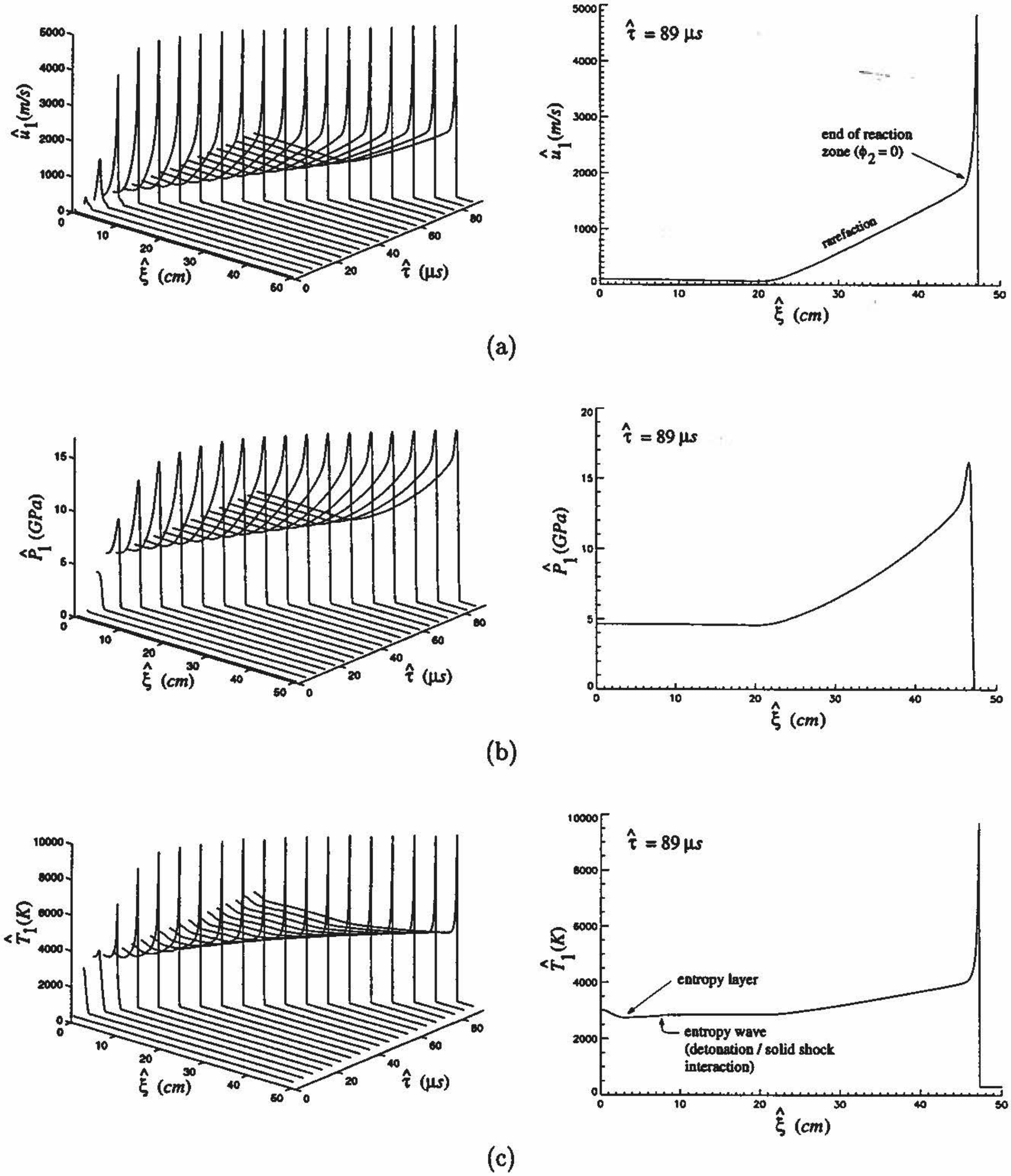

Figure 7.7: Predicted time histories for the *shocked gas-unshocked solid CJ* detonation simulation: (a) gas velocity, (b) gas pressure, and (c) gas temperature.

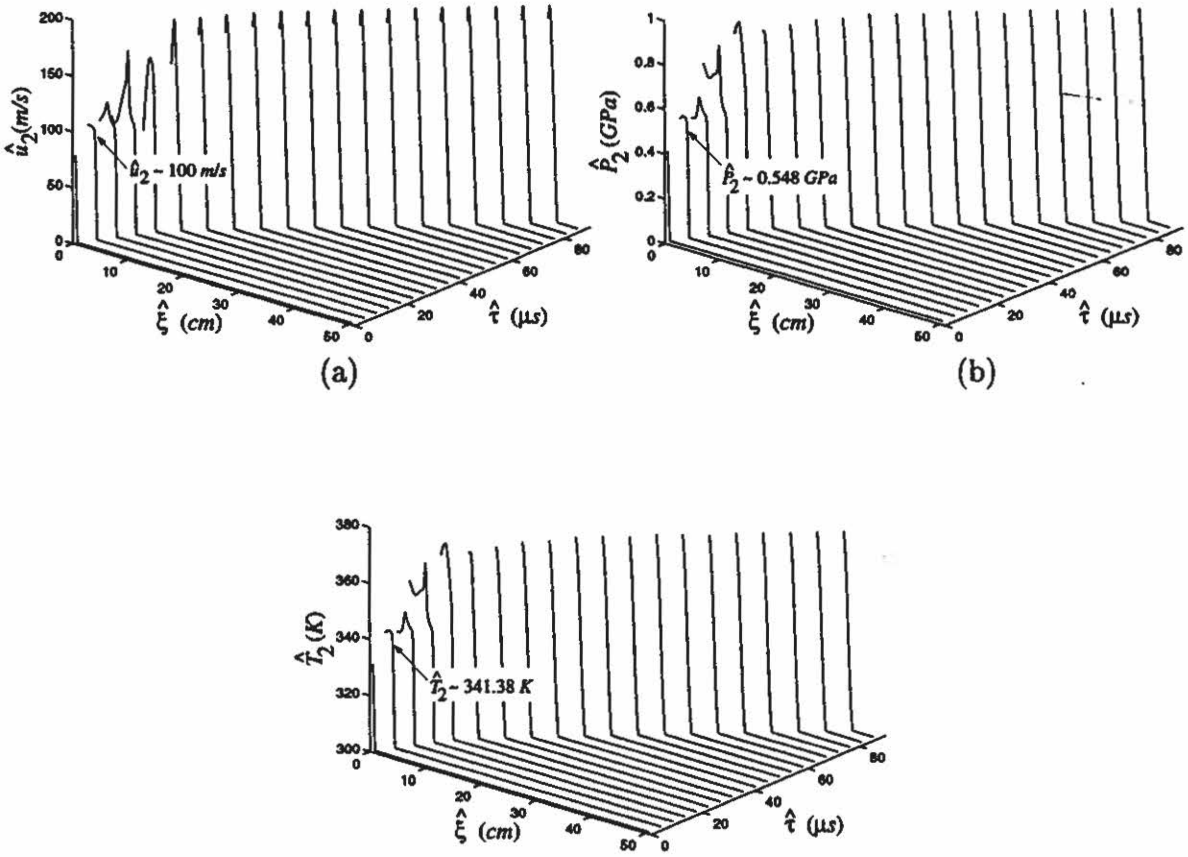

(a)

(b)

(c)

Figure 7.8: Predicted time histories for the *shocked gas-unshocked solid* CJ detonation simulation: (a) solid velocity, (b) solid pressure, and (c) solid temperature.

shocked solid pressure is primarily responsible for the rapid increase in the growth rate of I resulting in ignition.

Following ignition, the gas velocity, pressure, and temperature rapidly increase as the combustion wave strengthens and undergoes transition to detonation. Smaller increases in the solid velocity, pressure, and temperature are predicted during the transition process. The solid is completely consumed at the piston surface approximately 16 μs after piston impact. The solid shock, propagating at speed 3116.4 m/s, is overtaken by the strengthening detonation 20.12 μs after piston impact. Small amplitude rarefaction and entropy waves are generated in the gas as the detonation overtakes the solid shock. The rarefaction is not noticeable in the spatial profiles for the gas velocity, pressure, and temperature at $\hat{\tau} = 89\ \mu s$ [Fig. 7.7], and the entropy wave is barely noticeable in the spatial profile for the gas temperature. Once again, an entropy layer is generated immediately next to the piston during the transition process as indicated in the gas temperature profile. Subsequently, the strengthening detonation relaxes to a steady CJ detonation propagating at speed 6154.6 m/s. Following the steady detonation is a right-propagating rarefaction, which is indicated in Fig. 7.7(a).

The solid volume fraction history is shown in Fig. 7.9. No compacted region is predicted in response to the moving piston, and the solid volume fraction monotonically decreases from its ambient value to zero through the detonation wave structure. The predicted trajectories for both the inert solid shock and the burn front are shown in Fig. 7.10. The predicted time and length required for transition to detonation are approximately 21 μs and 60 mm, respectively.

A comparison of the numerically predicted detonation structure with the *shocked gas-unshocked solid* CJ structure given by the steady analysis is shown in Fig. 7.11. Good agreement exists between the solutions.

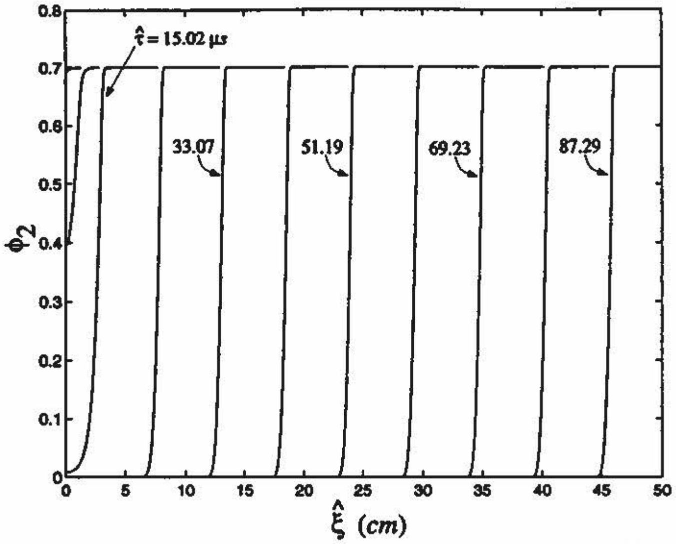

Figure 7.9: Predicted solid volume fraction history for the *shocked gas-unshocked solid* CJ detonation simulation.

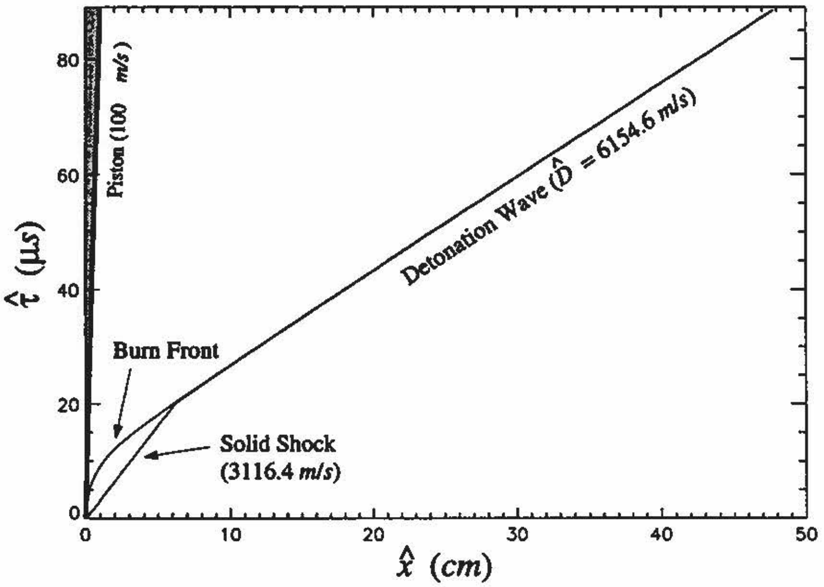

Figure 7.10: Predicted solid shock and burn front trajectories for the *shocked gas-unshocked solid* CJ detonation simulation.

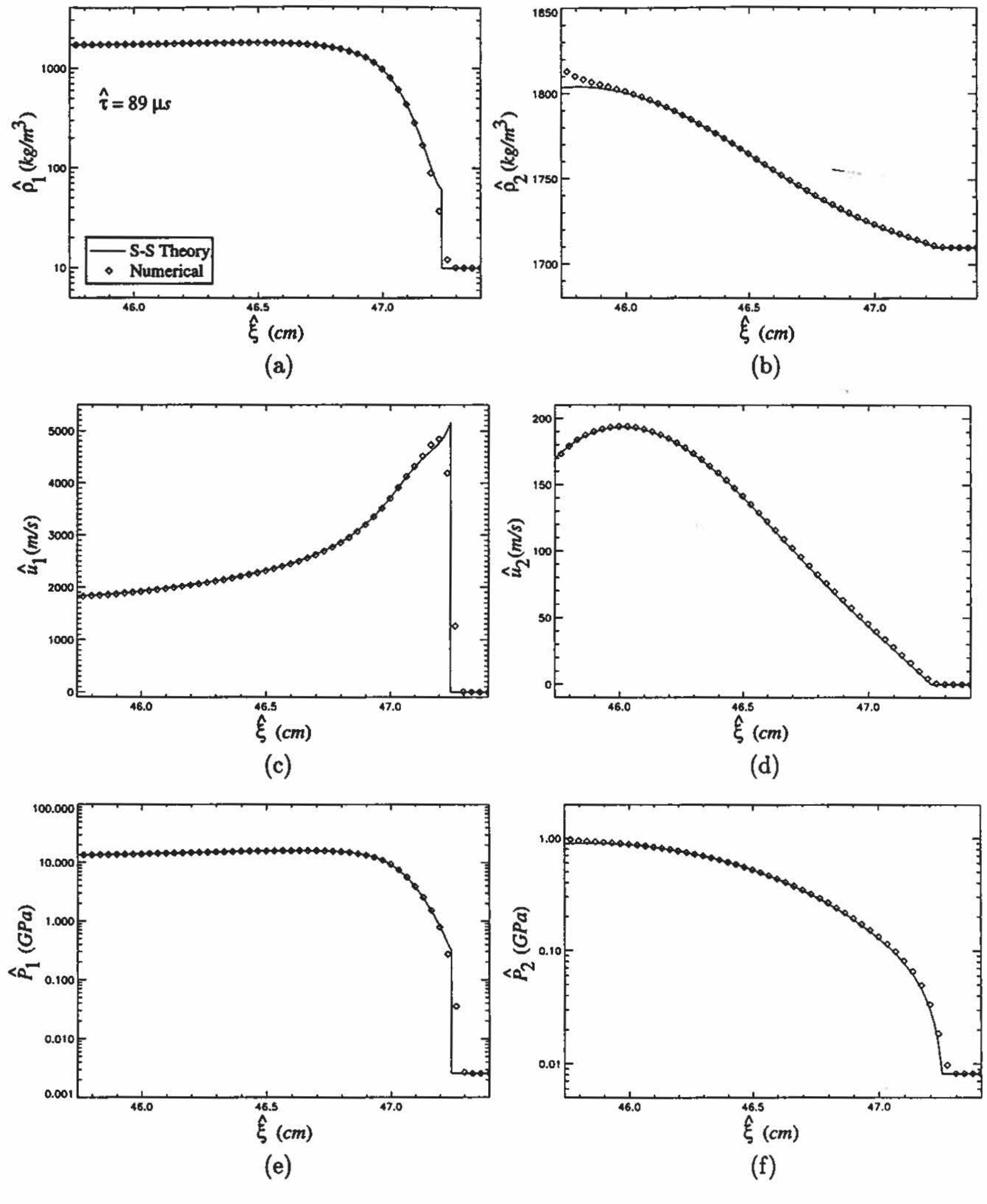

(a) (b)

(c) (d)

(e) (f)

Figure 7.11: Comparison of the *shocked gas-unshocked solid CJ* detonation structures predicted by the steady and unsteady detonation analyses: (a,b) gas and solid density; (c,d) gas and solid velocity; (e,f) gas and solid pressure; (g,h) gas and solid temperature; (i,j) gas and solid Mach number squared (relative to the wave); (k) solid volume fraction; and (l) particle radius.

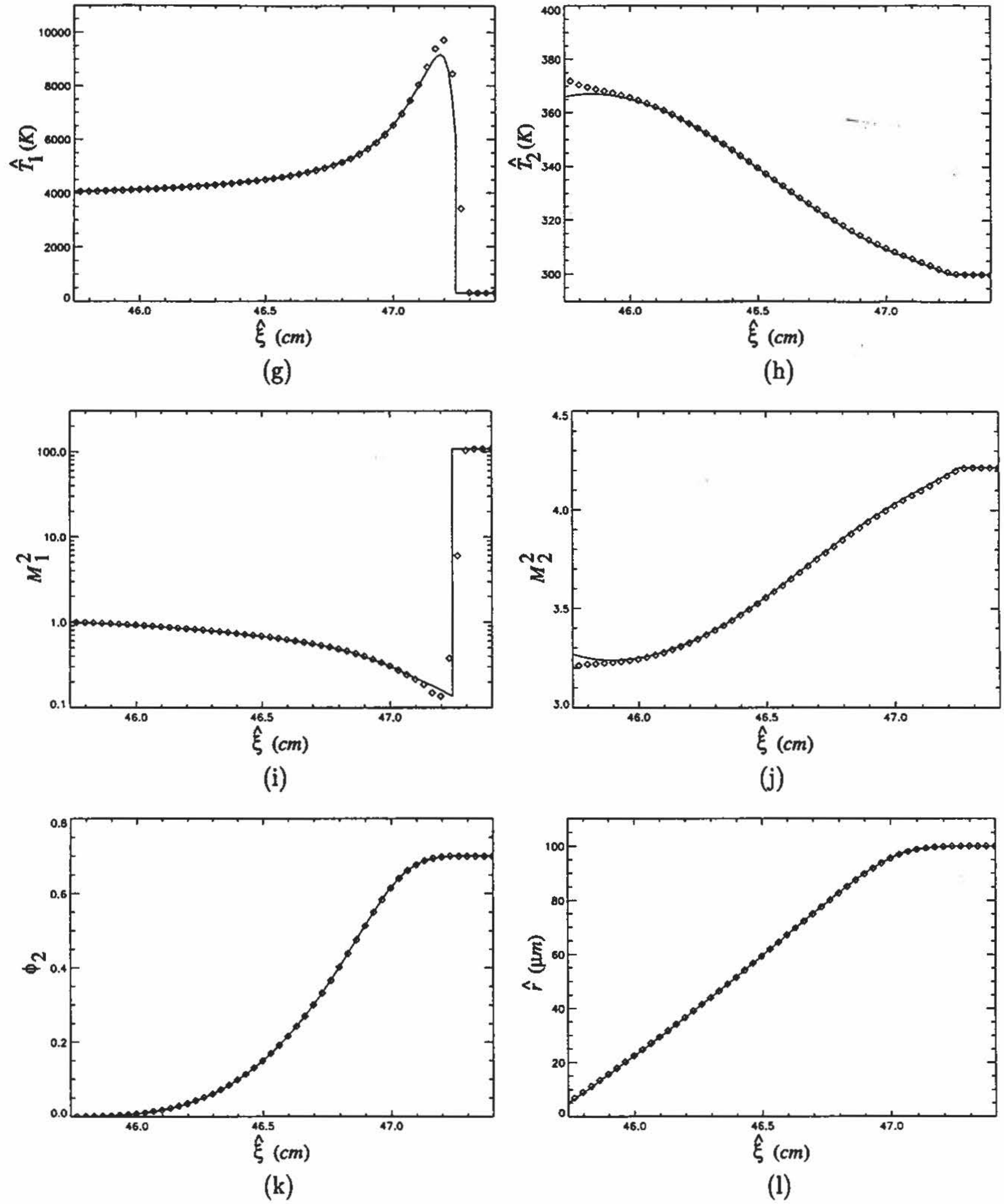

(g) (h)

(i) (j)

(k) (l)

Figure 7.11 (Continued)

7.1.3 Summary of Results for Increasing Compaction Viscosity

The relaxation time associated with changes in solid volume fraction due to the non-equilibrium stress condition $\hat{P}_2 - \hat{P}_1 - f(\phi_2) \neq 0$ is inversely proportional to $\hat{\mu}_c$. This is easily seen from the dimensional form of the characteristic equation for the compaction mode, repeated here for convenience:

$$\frac{d\phi_2}{d\hat{\tau}} = \frac{\phi_1\phi_2}{\hat{\mu}_c}\left[\hat{P}_2 - \hat{P}_1 - f(\phi_2)\right] - \left(\frac{3}{\hat{r}}\right)\phi_2\hat{a}\hat{P}_1^m. \tag{7.1}$$

This equation is valid along solid particle paths defined by $\frac{d\hat{\xi}}{d\hat{\tau}} = \hat{v}_2$. The first term on the right hand side of this equation accounts for changes in solid volume fraction due to material compaction, and the second term accounts for changes due to combustion.

Figure 7.12 gives the variation in gas and solid pressure, and gas and solid Mach number squared (measured relative to the wave) within the reaction zone as predicted by both the steady and unsteady analysis for increasing values of $\hat{\mu}_c$. In these plots, position is given by the steady wave coordinate, ζ. Each detonation structure consists of a shocked gas and an unshocked solid. Weak detonation structures are predicted for $\hat{\mu}_c = 1 \times 10^2$, 1×10^3, and 1×10^4 $kg/(s\ m)$, and CJ detonation structures are predicted for $\hat{\mu}_c = 1 \times 10^5$, 1×10^6, and 1×10^7 $kg/(s\ m)$. Due to the gas shock, $\hat{P}_2 - \hat{P}_1 - f(\phi_2) \neq 0$ immediately behind the shock; the subsequent relaxation in ϕ_2 is governed by Eq. 7.1. As seen in the pressure plot, the gas and solid pressures rapidly equilibrate for $\hat{\mu}_c = 1 \times 10^2$ (actually, a small pressure difference is predicted throughout much of the reaction zone, particularly near the shock). For this value of $\hat{\mu}_c$, the gas sonic point is located within the reaction zone at $\hat{\zeta} = -11.31$ mm; the location of this point is identified in the Mach number plot. As $\hat{\mu}_c$ increases, the relaxation rate associated with material compaction decreases, larger gas and solid pressure differences are predicted, and the location of the gas sonic point approaches the complete combustion end state. The gas sonic point is located at the end of the reaction zone for the CJ structures. Results of the unsteady analysis indicate that

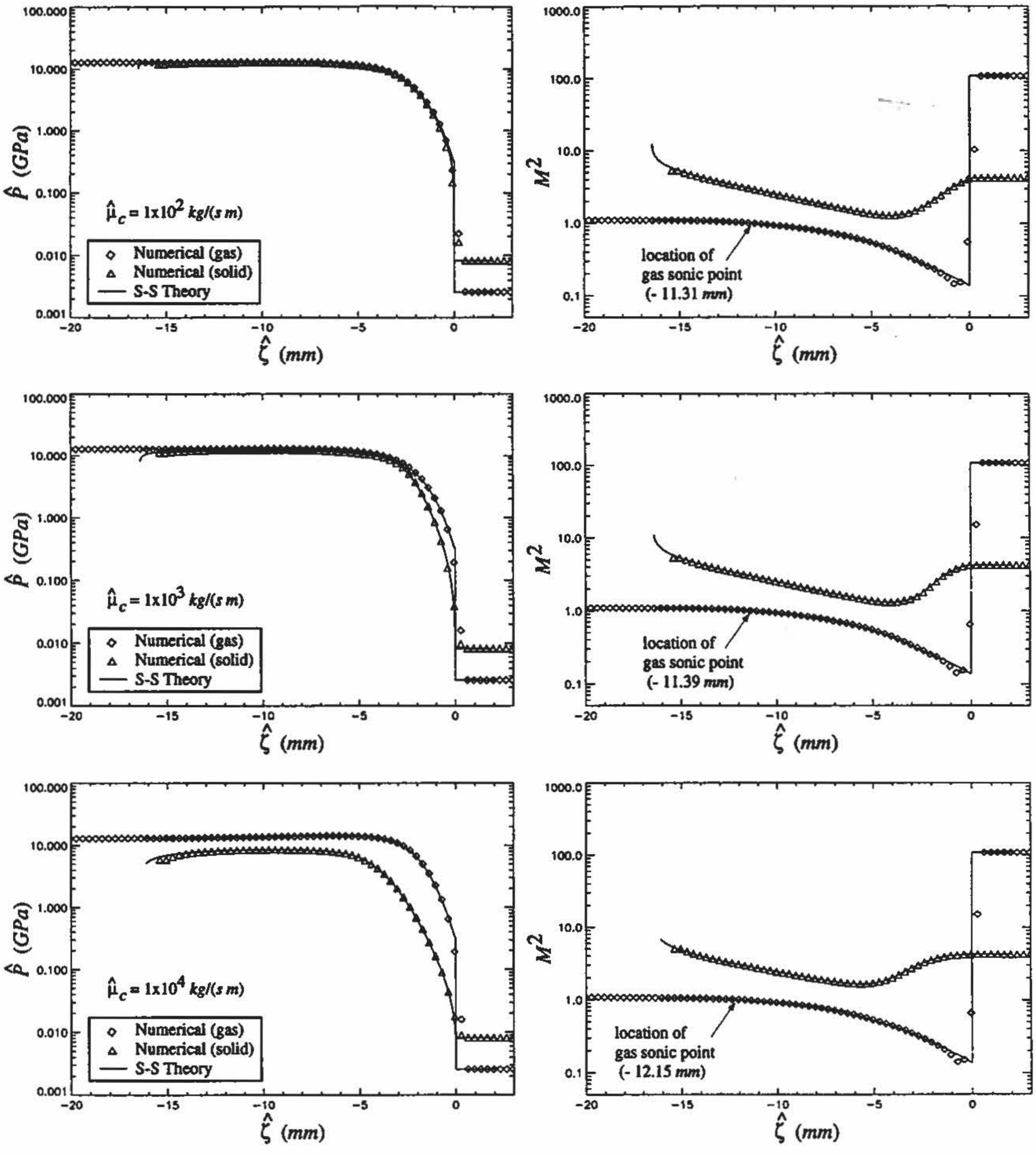

Figure 7.12: Summary of predicted *shocked gas-unshocked solid* detonation structures for increasing values of compaction viscosity.

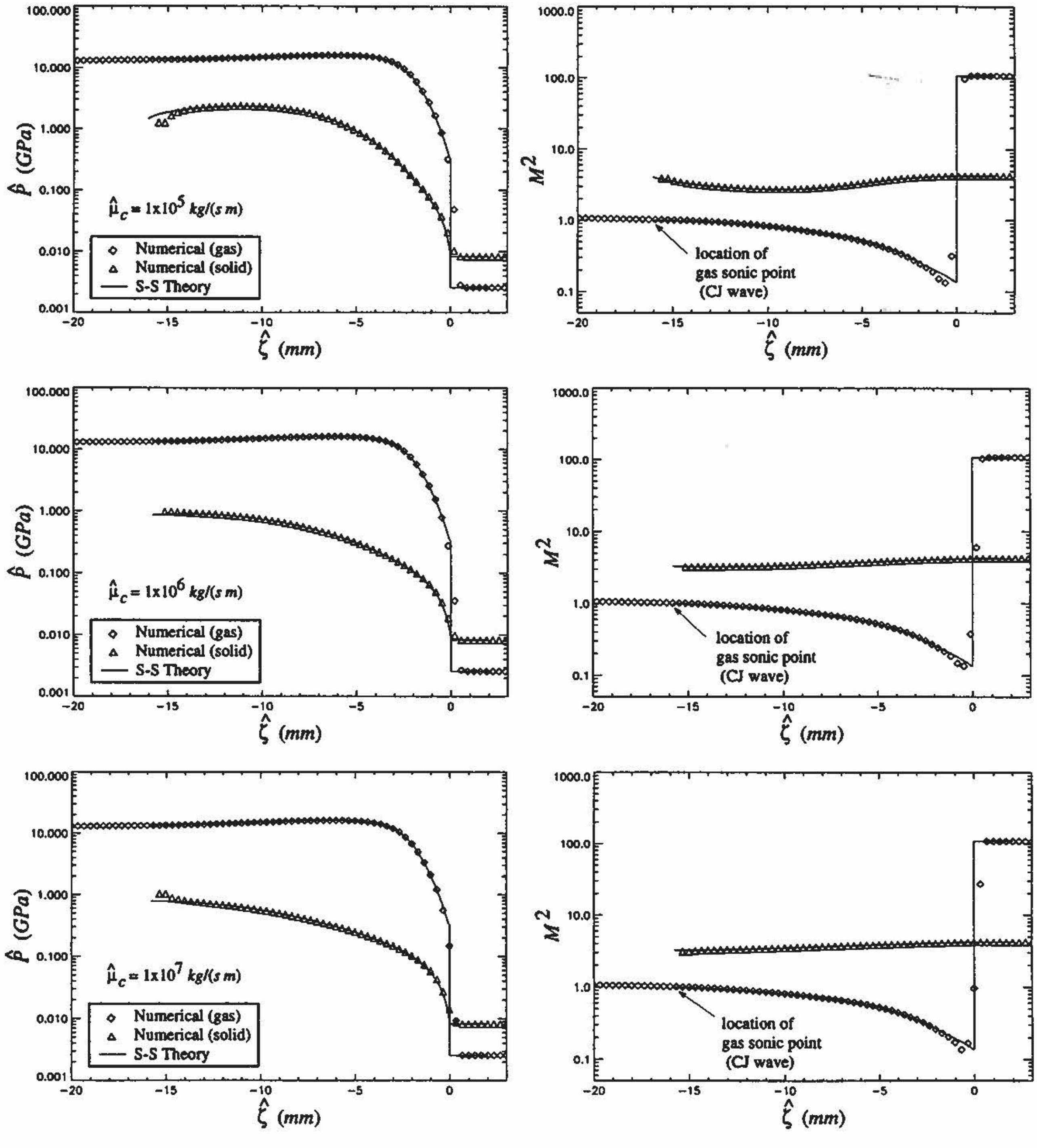

Figure 7.12 (Continued)

the bifurcation from weak to CJ structures occurs near $\hat{\mu}_c = 9 \times 10^4\ kg/(s\ m)$, in agreement with the result predicted by the steady analysis for Case I.

The length scale associated with the equilibration $\hat{P}_2 \rightarrow \hat{P}_1 + \hat{f}(\phi_2)$ near the shock for $\hat{\mu}_c = 1 \times 10^2\ kg/(s\ m)$, as seen in Fig. 7.12, is smaller than the length of the artificial shock structure predicted by the numerical method, and is substantially smaller than the reaction zone length. Accurate numerical predictions are dependent upon the properties of the numerical method, and require that physical length scales be much larger than artificial length scales associated with numerical diffusion and dispersion. As such, the physics governing the formation of this relaxation layer is masked by numerical diffusion and not accurately predicted. Though the error shown in Fig. 7.12 does not appear severe when compared to the steady solution, the magnitude of the error will increase for smaller values of $\hat{\mu}_c$. Furthermore, since the length of this relaxation layer is much smaller than the reaction zone length, it becomes computationally impractical to resolve this layer, which would require a prohibitively large number of grid points within the reaction zone.

Figure 7.13 gives the predicted variation in the compaction and combustion rates, identified by the forcing terms in Eq. (7.1), along solid particle paths within the reaction zone for the structures shown in Fig. 7.12. The results shown here are predicted by the steady analysis. In these figures, both rates are zero ahead of the shock since the freestream flow is an equilibrium state. For $\hat{\mu}_c = 1 \times 10^2\ kg/(s\ m)$, the compaction rate rapidly decreases as the solid particles cross the gas shock. Here, the high pressure gas contained within the interstices of the solid particles push the solid particles apart, thereby locally decreasing the solid volume fraction. Combustion, which also locally decreases the solid volume fraction, is insignificant during this short time interval. Subsequently, the combustion rate accelerates, and eventually dominates the compaction rate. Both rates vanish at the complete combustion end state. For larger values of $\hat{\mu}_c$, the compaction rate becomes less significant as compared to the combustion rate. In fact, the compaction rate is inconsequential for approximately $\hat{\mu}_c > 1 \times 10^5 \ kg/(s \ m)$.

The complete combustion gas end states predicted by both the steady and unsteady analysis for the different values of $\hat{\mu}_c$ considered here are listed in TABLE 7.2. Overall, the predictions agree well. However, wave speeds predicted by the unsteady analysis are consistently lower than those predicted by the steady analysis, although the discrepancy is less than 0.1 per-cent. The discrepancy may be due in part to the burn termination technique used in the unsteady analysis to avoid singularities associated with the complete combustion state. Since the solid particles are not completely consumed, a small amount of energy is retained by the solid near the end of the reaction zone which would otherwise be transferred to the gas and used to support the detonation (for CJ detonations). Other possible reasons for the discrepancy include uncertainties when computing the wave speeds, and insufficient grid resolution. Also, it is possible that the unsteady numerical solutions were slightly under-developed, and that better agreement might be obtained by allowing the solutions to evolve for longer time periods.

The predicted variation in time to detonation, $\hat{\tau}_{DDT}$, and distance to detonation, $\hat{\xi}_{DDT}$, with $\hat{\mu}_c$ are shown in Fig. 7.14. Here, distance to detonation is measured relative to the piston surface. For small values of $\hat{\mu}_c$ [i.e., $\hat{\mu}_c < 1 \times 10^3 \ kg/(s \ m)$], material compaction dominates non-linear acoustic effects associated with gas and solid convection. As such, gas and solid shocks do not form; rather compaction waves are generated which propagate away from the piston at speeds below the ambient solid sound speed (3000 m/s). The solid pressure in the compacted region ($\sim 50 \ MPa$) is considerably lower than the corresponding shocked solid pressure resulting from the impact of a 100 m/s piston (547.5 MPa), and the ignition time is delayed; consequently, $\hat{\tau}_{DDT}$ is large. Once combustion is initiated, transition to detonation rapidly occurs in the compacted material where the mixture density is high ($\sim 1612 \ kg/m^3$);

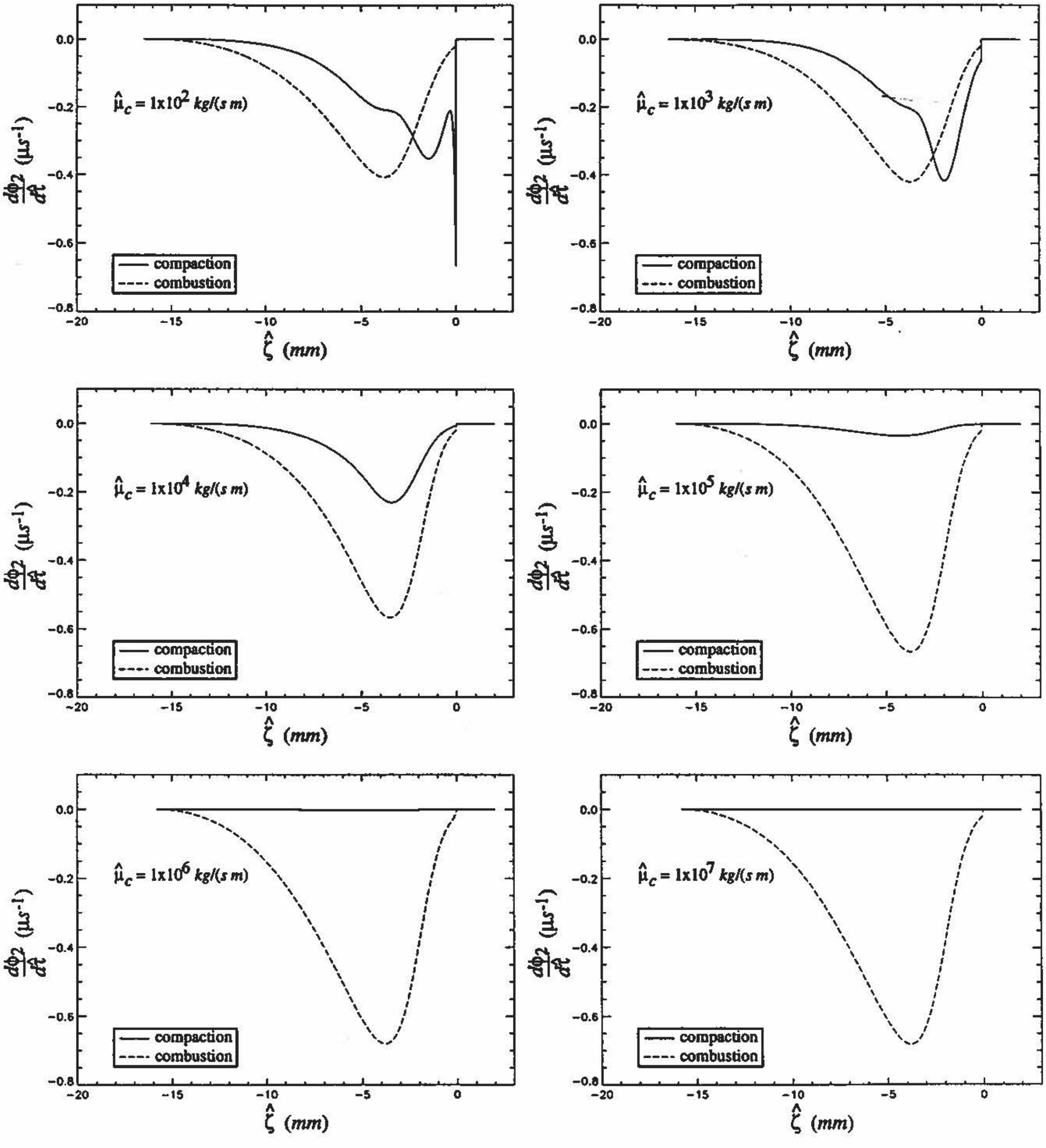

Figure 7.13: Predicted variation in the compaction and combustion rates within the reaction zone for increasing values of compaction viscosity.

$\hat{\mu}_c$ [$kg/(s\ m)$]	*Unsteady Analysis*					*Steady Analysis*				
	$\hat{\rho}_1$ final (kg/m^3)	$\hat{u}_1$ final (m/s)	$\hat{P}_1$ final (GPa)	M_1^2 final	$\hat{D}$ (m/s)	$\hat{\rho}_1$ final (kg/m^3)	$\hat{u}_1$ final (m/s)	$\hat{P}_1$ final (GPa)	M_1^2 final	$\hat{D}$ (m/s)
1×10^2	1665	1723	12.8	1.09	6168.0	1664	1721	12.8	1.09	6169.4
1×10^3	1667	1727	12.8	1.09	6166.1	1666	1726	12.8	1.09	6168.1
1×10^4	1680	1761	13.0	1.06	6162.1	1680	1761	13.0	1.06	6163.4
1×10^5	1702	1820	13.5	1.00	6157.2	1704	1822	13.5	1.00	6159.9
1×10^6	1704	1821	13.5	1.00	6154.6	1704	1822	13.5	1.00	6159.9
1×10^7	1704	1823	13.5	1.00	6154.2	1704	1822	13.5	1.00	6159.9

TABLE 7.2: COMPARISON OF THE PREDICTED GAS END STATES FOR CASE I IDENTIFIED IN TABLE 6.2 WITH THE VALUES GIVEN BY THE STEADY DETONATION ANALYSIS

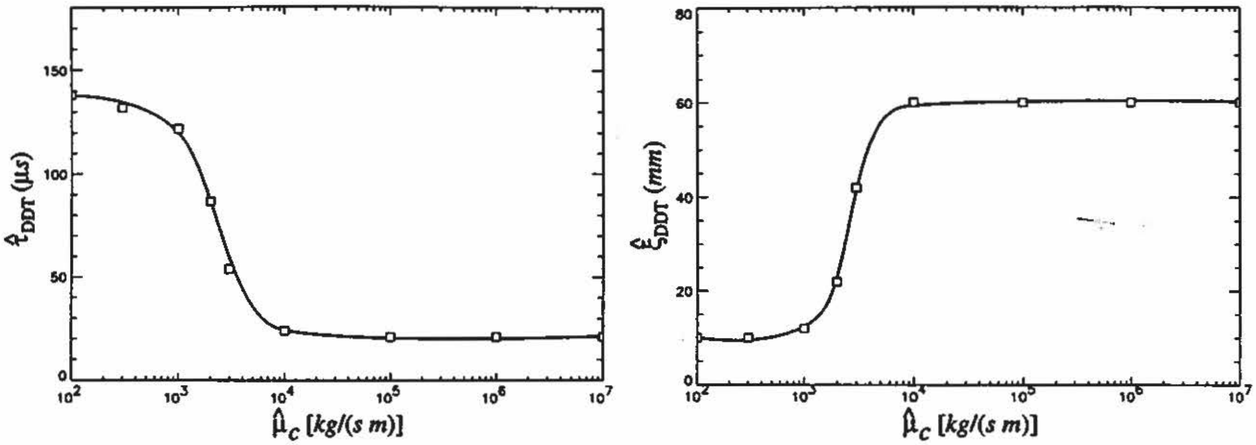

Figure 7.14: Predicted time and distance to detonation for Case I identified in Table 6.2.

consequently, $\hat{\xi}_{DDT}$ is small. This result is consistent with both experiments [15] and numerical modeling results [23] of DDT in granular high-explosives which show that transition length decreases with increasing ambient mixture density. The opposite trends are predicted for large values of $\hat{\mu}_c$ [i.e., $\hat{\mu}_c > 1 \times 10^4\ kg/(s\ m)$]. Here, non-linear acoustic effects dominate material compaction, and gas and solid shocks quickly form. Little compaction takes place. The shocked solid pressure is sufficient to rapidly initiate combustion; consequently, $\hat{\tau}_{DDT}$ is small. Also, $\hat{\xi}_{DDT}$ is large as the mixture density in the shocked region is relatively low ($\sim 1240\ kg/m^3$). For intermediate values of $\hat{\mu}_c$ [i.e., $1 \times 10^3\ kg/(s\ m) \leq \hat{\mu}_c \leq 1 \times 10^4\ kg/(s\ m)$], both material compaction and convection are important, and $\hat{\tau}_{DDT}$ and $\hat{\xi}_{DDT}$ are sensitive to small changes in $\hat{\mu}_c$.

7.2 Effect of Interphase Drag

For Case II shown in Fig. 6.11(b), the steady analysis predicts a continuum of *shocked gas-unshocked solid* weak detonation structures for $\hat{\beta} < 8 \times 10^4\ kg/(s\ m^2)$, and a continuum of *shocked gas-unshocked solid* CJ detonation structures for $8 \times 10^4 \leq \hat{\beta} \leq 1.3 \times 10^5\ kg/(s\ m^2)$. No steady *shocked gas-unshocked solid* detonation structures were predicted for $\hat{\beta} > 1.3 \times 10^5\ kg/(s\ m^2)$ as a solid sonic point was reached within the reaction zone. In this section, we first give DDT results for $\hat{\beta} = 1.1 \times 10^6\ kg/(s\ m^2)$ which illustrate the evolution of a CJ detonation structure having a lead shock in the solid, followed by a shock in the gas, and then summarize the DDT results and detonation structures predicted for several values of $\hat{\beta}$ within the range $1 \times 10^5 \leq \hat{\beta} \leq 1 \times 10^9\ kg/(s\ m^2)$. The computational domain used for the unsteady numerical simulations was defined for $0 \leq \hat{\xi} \leq 50\ cm$, and consisted of $N = 3000$ uniformly spaced nodes. The CPU time for these simulations ranged from approximately 15 to 120 hours.

7.2.1 Evolution of a Two-Shock Chapman-Jouguet Detonation

Shown in Fig. 7.15 are the predicted velocity, pressure, and temperature history of the gas for $\hat{\beta} = 1.1 \times 10^6\ kg/(s\ m^2)$. The spatial profiles for these quantities at $\hat{\tau} = 90\ \mu s$ are also shown in this figure. The predicted solid velocity, pressure, and temperature history are shown in Fig. 7.16.

The histories for the gas and solid quantities are qualitatively similar to those predicted and discussed in the previous section. Initially, a compaction wave propagating at speed 2983.7 m/s is predicted to evolve in response to the moving piston. Combustion is initiated at the piston surface at $\hat{\tau} \sim 4\ \mu s$, and the resulting combustion wave strengthens and undergoes a transition to detonation at approximately $\hat{\tau} = 26\ \mu s$. Subsequently, the accelerating detonation overtakes the compaction wave, and relaxes to a steady two-shock CJ detonation propagating at speed 6158.6 m/s.

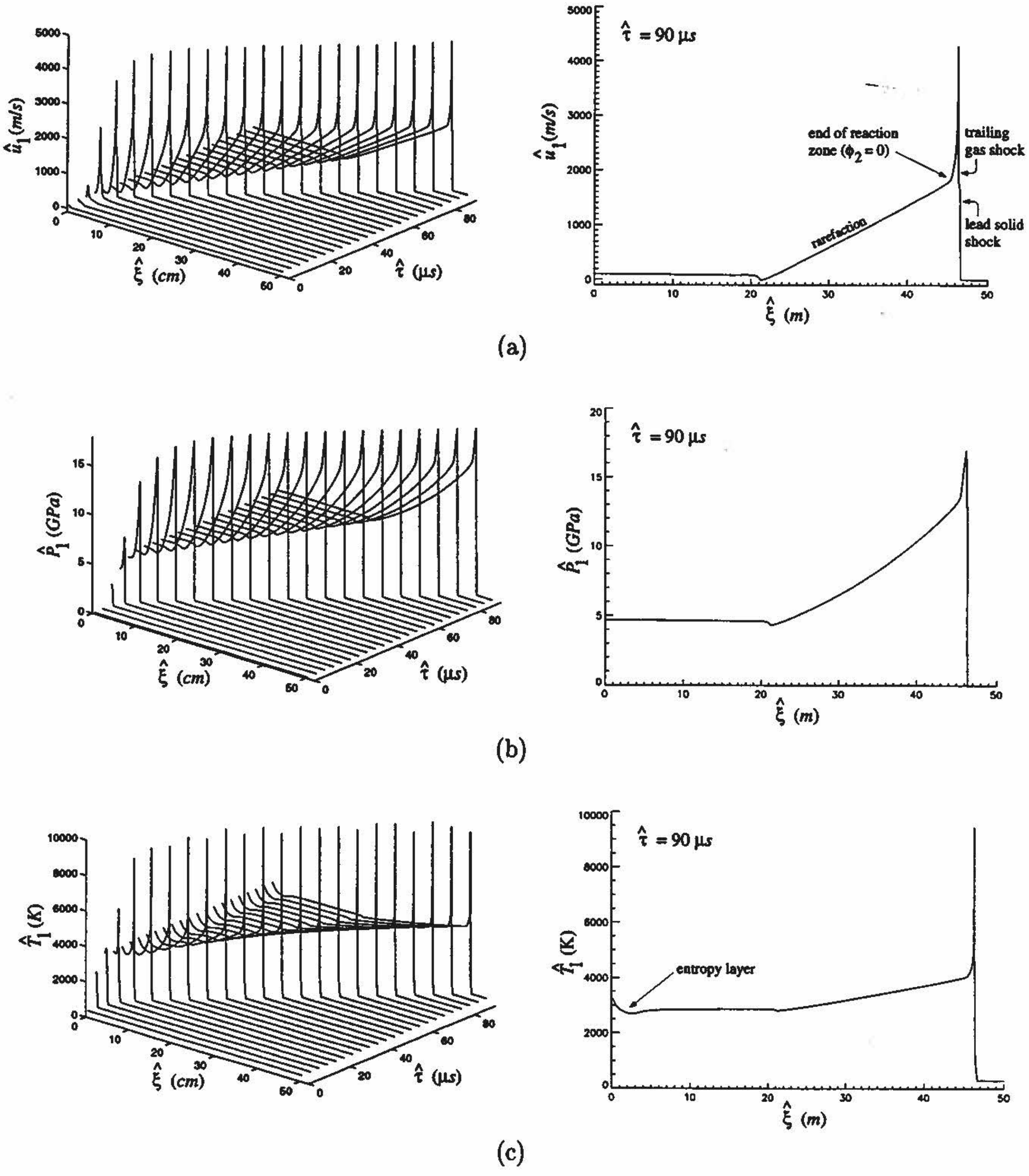

Figure 7.15: Predicted time histories for the *shocked gas-shocked solid CJ* detonation simulation: (a) gas velocity, (b) gas pressure, and (c) gas temperature.

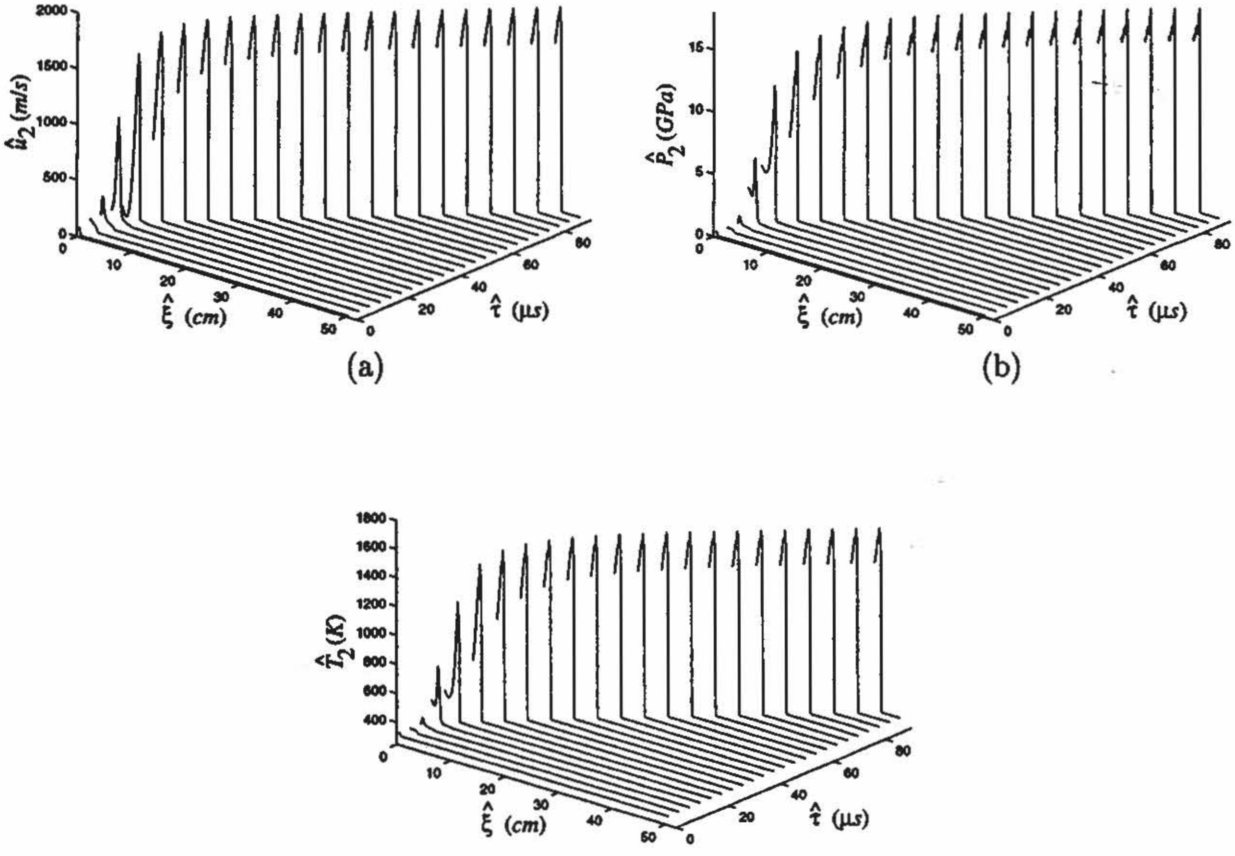

(a) (b)

(c)

Figure 7.16: Predicted time histories for the *shocked gas-shocked solid CJ* detonation simulation: (a) solid velocity, (b) solid pressure, and (c) solid temperature.

The two-shock structure of the detonation wave is barely noticeable in the spatial profile for the gas velocity at $\hat{\tau} = 90\ \mu s$ [Fig. 7.15(a)].

The solid volume fraction history is shown in Fig. 7.17. Here, the effect of the two-shock detonation structure is evident, as these spatial profiles appear different from those predicted in the previous section. Following the onset of combustion, a compacted region having $\phi_2 > 0.70$ is seen to develop immediately ahead of the combustion front. The solid shock is located at the front of the compacted region, and the gas shock is located at the point where ϕ_2 is a maximum. This compacted region results from the coupling between exothermic energy release by combustion

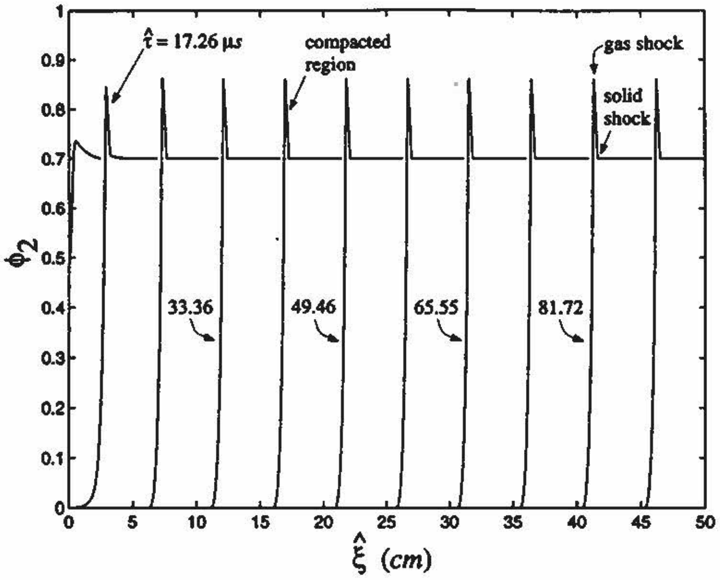

Figure 7.17: Predicted solid volume fraction history for the *shocked gas-shocked solid CJ* detonation simulation.

and large interphase drag. The drag force exerted by the high velocity gas on the lower velocity solid is sufficient to choke the solid within the reaction zone resulting in the formation of a solid shock. Though combustion is initiated by the solid shock, significant combustion only occurs behind the gas shock where the gas pressure is high. The compacted region steepens as the combustion wave accelerates and undergoes transition to steady detonation, and subsequently continues to propagate with the detonation. No change in the spatial profiles is seen for approximately $\hat{\tau} > 30$ μs. Solid volume fraction histories similar to the one shown here have been predicted by Baer and Nunziato [5] and Baer et al. [7] for the DDT of granular high-explosives, though only a vague description of the resulting detonation structure was given.

The predicted compaction wave and burn front trajectories are shown in Fig. 7.18. Also indicated in this figure is the distance between the compaction front and the burn front, $\Delta\hat{x}_s$. Here, the burn front is assumed to be located at the gas shock since this location marks the onset of significant combustion. The predicted time and length required for transition to detonation are approximately 25.8 μs and

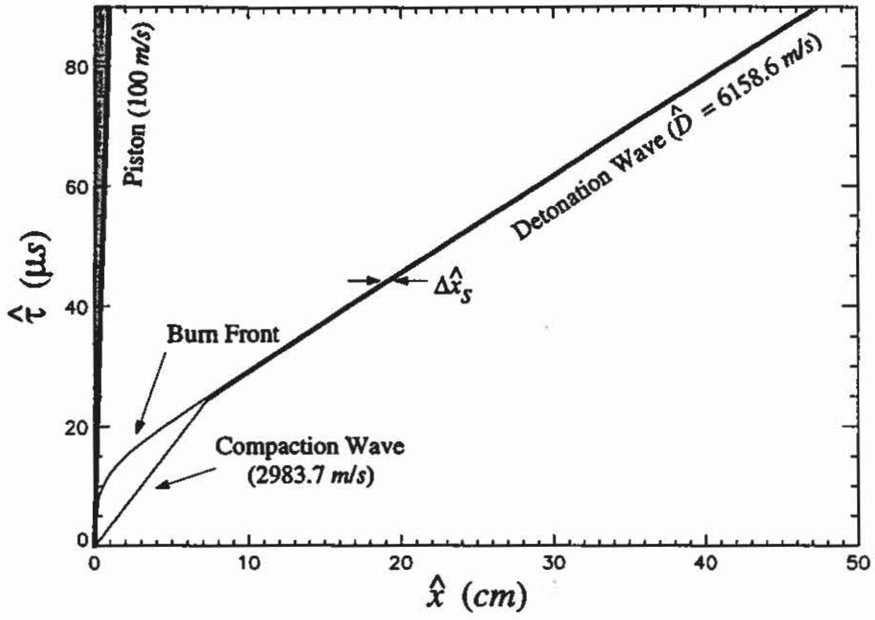

Figure 7.18: Predicted compaction wave and burn front trajectories for the *shocked gas-shocked solid CJ* detonation simulation.

71 *mm*, respectively. The predicted variation in $\Delta\hat{x}_s$ with time is shown in Fig. 7.19. As seen in this figure, the compaction front propagates faster than the burn front for approximately $\hat{\tau} < 12.5$ μs. For $12.5 \leq \hat{\tau} \leq 24.0$ μs, the distance between the compaction and burn front narrows as the combustion wave strengthens and accelerates. At approximately $\hat{\tau} = 24$ μs, $\Delta\hat{x}_s$ has nearly reached its equilibrium value of 3.33 *mm* associated with steady detonation. The small "wiggles" in this curve are due to the technique used in the numerical algorithm for determining the location of the fronts, and are equal in length to one computational cell (0.17 *mm*). As such, they should not be construed as resulting from a dynamical or numerical instability.

The numerically predicted detonation wave structure is shown in Fig. 7.20. The location of the gas and solid shocks, which are smeared over approximately three computational cells due to numerical diffusion, are evident in these plots. Across the solid shock, an abrupt change in all solid quantities is predicted, as is an abrupt decrease in particle radius. A continuous variation in the gas quantities, and the solid

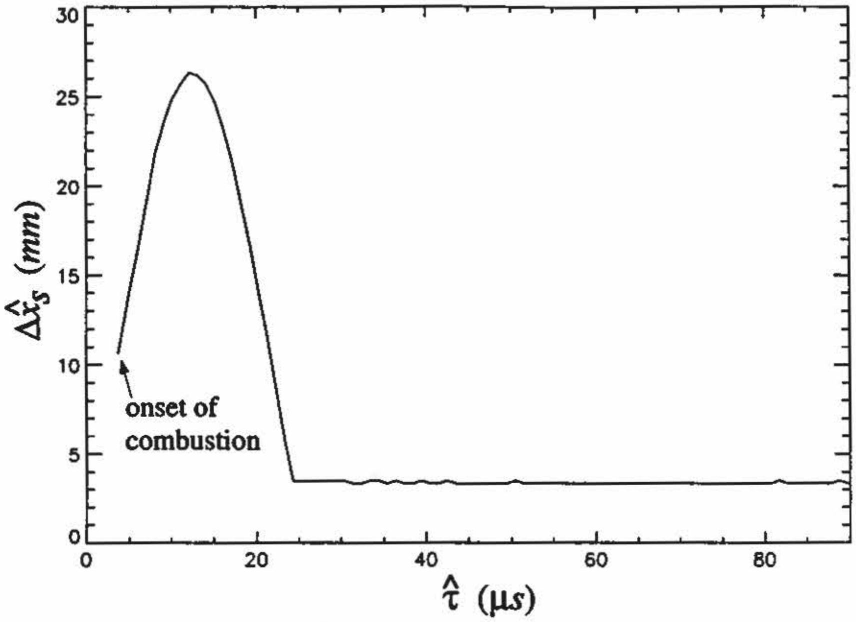

Figure 7.19: Predicted history for the distance between the lead solid shock and the trailing gas shock for the *shocked gas-shocked solid CJ* detonation simulation.

volume fraction, is predicted across the solid shock. The rapid change in gas velocity through the solid shock seen in Fig. 7.20(c) is due to the large value of $\hat{\beta}$ used in this simulation; consequently, the gas and solid velocities rapidly equilibrate through the solid shock. All quantities vary continuously throughout the compaction region located between the solid and gas shocks. An abrupt change in the gas quantities is predicted across the gas shock, while the solid quantities, solid volume fraction, and particle radius remain continuous. Significant combustion occurs behind the gas shock, reducing both the solid volume fraction and particle radius to near zero as the solid is consumed. All quantities vary continuously throughout the region located between the gas shock and the end of the reaction zone.

As seen in Fig. 7.20(i), the gas Mach number measured relative to the wave is locally unity at the end of the reaction zone. Furthermore, the numerically predicted gas density (1704 kg/m^3), velocity (1822 m/s), and pressure (13.5 GPa) at the complete combustion state exactly match the CJ values for the gas predicted by the steady equilibrium end state analysis. The numerically predicted detonation wave speed (6158.6 m/s) also agrees well with the CJ wave speed (6159.9 m/s) predicted by the end state analysis. Consequently, this wave is an example of a *shocked gas-shocked solid* CJ detonation structure.

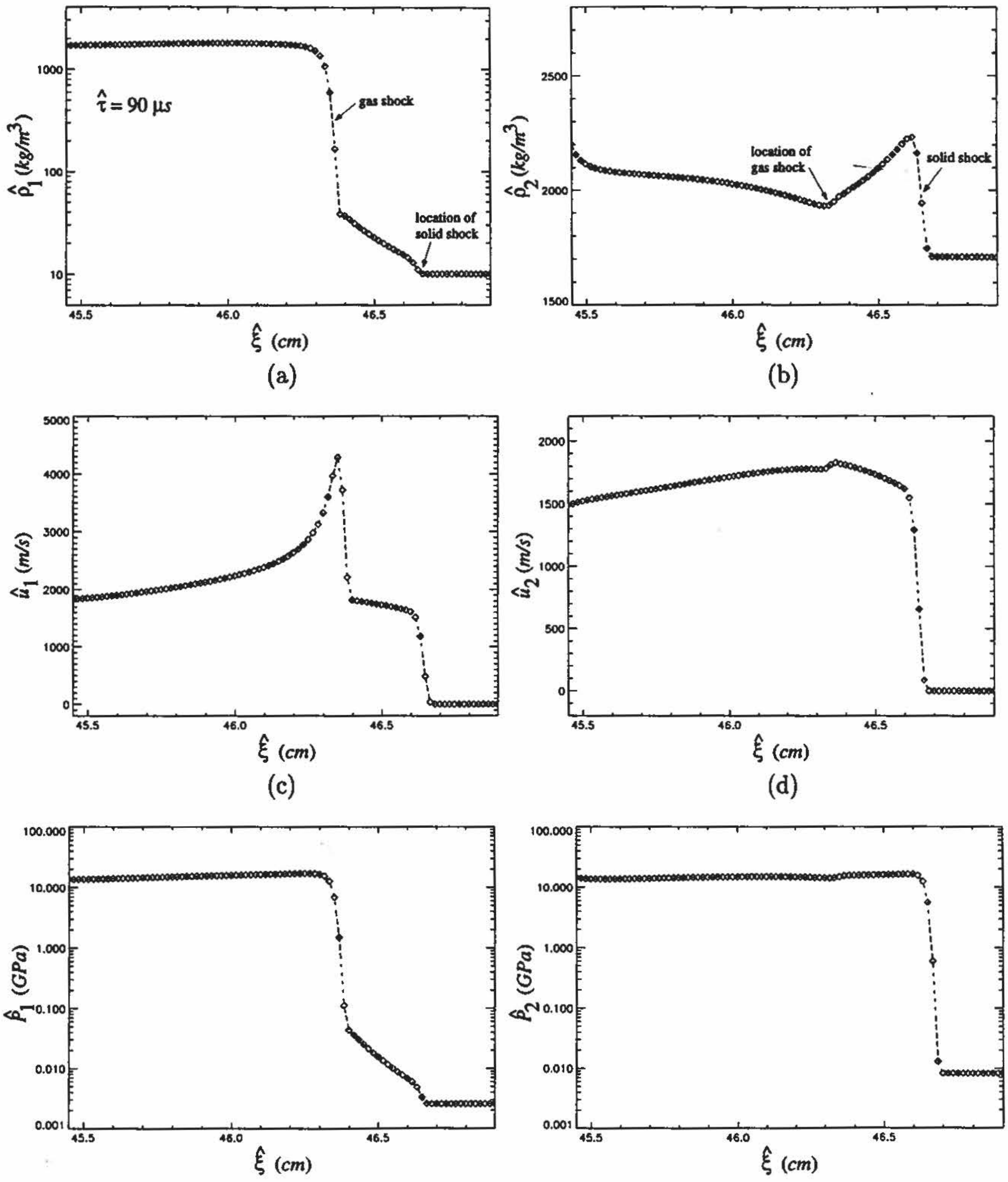

Figure 7.20: Predicted *shocked gas-shocked solid CJ* detonation structure: (a,b) gas and solid density; (c,d) gas and solid velocity; (e,f) gas and solid pressure; (g,h) gas and solid temperature; (i,j) gas and solid Mach number squared (relative to the wave); (k) solid volume fraction; and (l) particle radius.

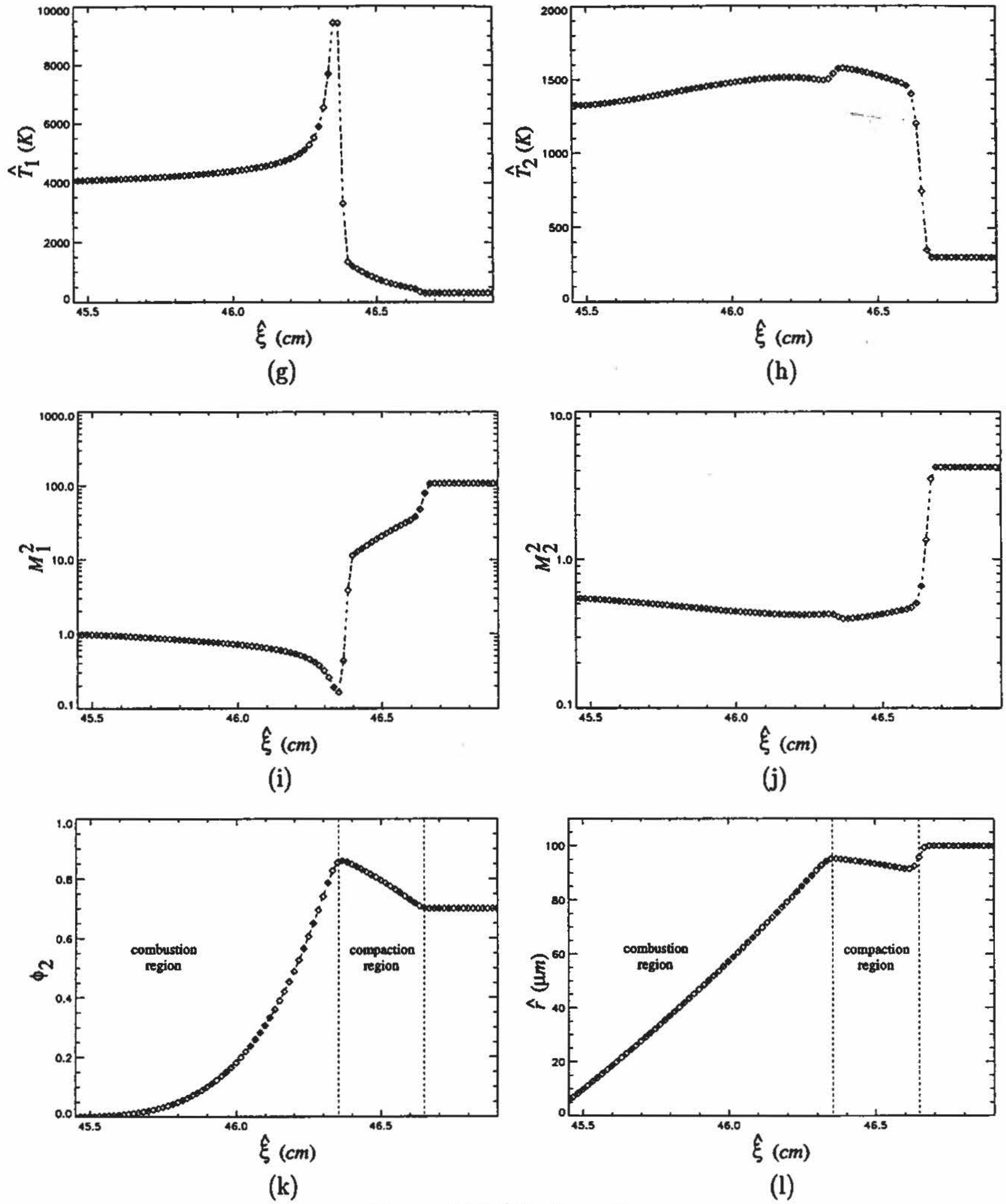

(g) (h)

(i) (j)

(k) (l)

Figure 7.23 (Continued)

7.2.2 Summary of Results for Increasing Drag Coefficient

The drag relaxation time associated with changes in gas and solid velocity due to the non-equilibrium kinematic condition $\hat{v}_2 - \hat{v}_1 \neq 0$ is directly proportional to $\hat{\beta}$. Here, we summarize detonation structures predicted by the unsteady numerical analysis for several values of $\hat{\beta}$ associated with Case II identified in Table 6.2. In particular, we consider values $\hat{\beta} \geq 1 \times 10^5\ kg/(s\ m^2)$, and focus on the evolution of detonation structure for cases in which the steady structure analysis proved inconclusive. For $\hat{\beta} < 1 \times 10^5\ kg/(s\ m^2)$, both the steady and unsteady analysis predict weak and CJ detonation structures similar to those discussed in the previous section. An example of such a weak detonation structure is given in Fig. 7.12 for $\hat{\beta} = 1 \times 10^4\ kg/(s\ m^2)$ $[\hat{\mu}_c = 1 \times 10^4\ kg/(s\ m)]$.

Shown in Fig. 7.21 is the predicted variation in gas and solid velocity, and gas and solid Mach number squared (measured relative to the wave) within the reaction zone for increasing values of $\hat{\beta}$. As shown later in this section, each of these structures is a CJ detonation. In particular, the structure predicted for $\hat{\beta} = 1 \times 10^5\ kg/(s\ m^2)$ is a *shocked gas-unshocked solid* CJ detonation. A comparison of this structure with the structure predicted by the steady analysis for this same value of $\hat{\beta}$ is given in the figure. Good agreement exists between the predicted solutions. As a consequence of the relatively small value for $\hat{\beta}$ used here, a difference of at least 2000 m/s is predicted between the gas and solid velocity at each point within the reaction zone. Though the solid is nearly choked ($M_2^2 = 1.09$) at $\hat{\zeta} = -3.2\ mm$, the solid flow remains entirely supersonic throughout the reaction zone.

For $\hat{\beta} = 2 \times 10^5\ kg/(s\ m^2)$, the unsteady analysis predicts the evolution of a two-shock CJ detonation structure having a lead shock in the gas, followed by a weak shock in the solid. This result is consistent with the steady analysis in that no unshocked solid structures were predicted for approximately $\hat{\beta} > 1.3 \times 10^5\ kg/(s\ m^2)$ as the solid becomes choked within the reaction zone. Here, the trailing solid shock is located at $\hat{\zeta} = -1.75\ mm$, slightly ahead of the point $\hat{\zeta} = -2.6\ mm$ where the steady analysis predicts that the solid first becomes choked for $\hat{\beta} = 1.3 \times 10^5\ kg/(s\ m^2)$. The unsteady analysis predicts a similar structure for $\hat{\beta} = 3 \times 10^5\ kg/(s\ m^2)$, with the exception that the solid shock is stronger, and is located closer to the lead gas shock. The solid shock is strengthened due to the higher rate of conversion of gas kinetic energy into solid energy. As such, the difference in the gas and solid velocities is seen to decrease with increasing $\hat{\beta}$.

For $\hat{\beta} = 4 \times 10^5\ kg/(s\ m^2)$, the location of the solid shock is coincident with the lead gas shock, and the solid flow is subsonic throughout the reaction zone. This result suggests that there exists a unique value of $\hat{\beta}$, close to the value used in this simulation, for which a steady CJ detonation structure evolves having a single gas-solid compound shock. As discussed in Chapter 3, such compound discontinuities are admitted by the two-phase Rankine-Hugoniot relations, Eqs. (3.59-3.67), and satisfy the two-phase entropy criterion given by Eq. (3.68).

As $\hat{\beta}$ is further increased, CJ detonation structures having a lead solid shock are predicted. For $\hat{\beta} = 6 \times 10^5$, 1.1×10^6, and $1 \times 10^7\ kg/(s\ m^2)$, the solid shock is followed by a gas shock located within the reaction zone which is seen to weaken and move further behind the solid shock with increasing $\hat{\beta}$. The gas shock weakens due to the increasing drag relaxation rate immediately behind the gas shock, causing the gas velocity to rapidly decrease in response to the lower velocity solid. For $\hat{\beta} = 1 \times 10^8$ and $1 \times 10^9\ kg/(s\ m^2)$, the gas flow smoothly transitions from supersonic to subsonic flow near the point $\hat{\zeta} = -5.5\ mm$, and the solid flow is entirely subsonic throughout the reaction zone. In fact, little difference is seen here between the two solutions, both of which are examples of *unshocked gas-shocked solid* CJ detonation structures. As seen in the velocity plots of the lead shocked solid structures, the unshocked gas velocity rapidly equilibrates with the shocked solid velocity due to the large values of $\hat{\beta}$. Once again, the length scale associated with this relaxation process is on the order of the artificial shock width; consequently, the physics governing this process is masked by numerical diffusion and not accurately predicted. The error associated with these inaccuracies is difficult to assess in the absence of steady-state solutions. Though numerical simulations were not performed for $\hat{\beta} > 1 \times 10^9\ kg/(s\ m^2)$ due to computational time requirements [the simulation for $\hat{\beta} = 1 \times 10^9\ kg/(s\ m^2)$ required approximately 120 hours of CPU time], it is reasonable to expect, based on the results given here, that a continuum of *unshocked gas-shocked solid CJ* detonation structures exist for values of $\hat{\beta} > 1 \times 10^9\ kg/(s\ m^2)$.

A physical estimate for $\hat{\beta}$ can be obtained using an empirical drag coefficient relation for the flow of gas around a solid sphere, C_D [122]:

$$C_D = \frac{24}{Re} + \frac{6}{1+\sqrt{Re}} + 0.4, \qquad 0 < Re \leq 2 \times 10^5, \tag{7.2}$$

where Re is the Reynolds number based on the diameter of the sphere. We choose the following characteristic values which are representative of the conditions immediately behind the shock of *shocked gas-unshocked solid* detonation structures predicted in this study: $\hat{\rho}_1 = 60\ kg/m^3$, $|\hat{u}_2 - \hat{u}_1| = 4000\ m/s$, $\hat{r} = 100\ \mu s$. We choose a gas viscosity of $9 \times 10^{-5}\ kg/(s\ m)$ which is representative of heated air ($\hat{T}_1 > 2500°\ K$). Based on these values, we obtain $Re = 5.3 \times 10^5$ and $C_D = 0.4082$. Though this value of Re is slightly outside the range of validity of Eq. (7.2), we use this relation to obtain a first-order estimate for the drag force exerted by the gas on a single particle, which is computed to be 24.6 N. Assuming $\hat{n} = 1.67 \times 10^{11}$ particles/m^3, which is a representative value predicted in this study, and neglecting interactions between particles, the drag force per unit volume for a system of particles is computed to be $4.11 \times 10^{12}\ N/m^3$. Thus, from Eq. (2.2) we have that

$$\hat{\beta}\frac{\phi_1\phi_2}{\hat{r}}\,|\hat{u}_2 - \hat{u}_1| \sim 4.11 \times 10^{12}\ N/m^3.$$

Choosing $\phi_1 = 0.3$ (thus $\phi_2 = 0.7$), the estimate $\hat{\beta} = 4.89 \times 10^5\ kg/(s\ m^2)$ is obtained. Similar estimates for $\hat{\beta}$ are obtained based on the the scaling analysis given by Meni-

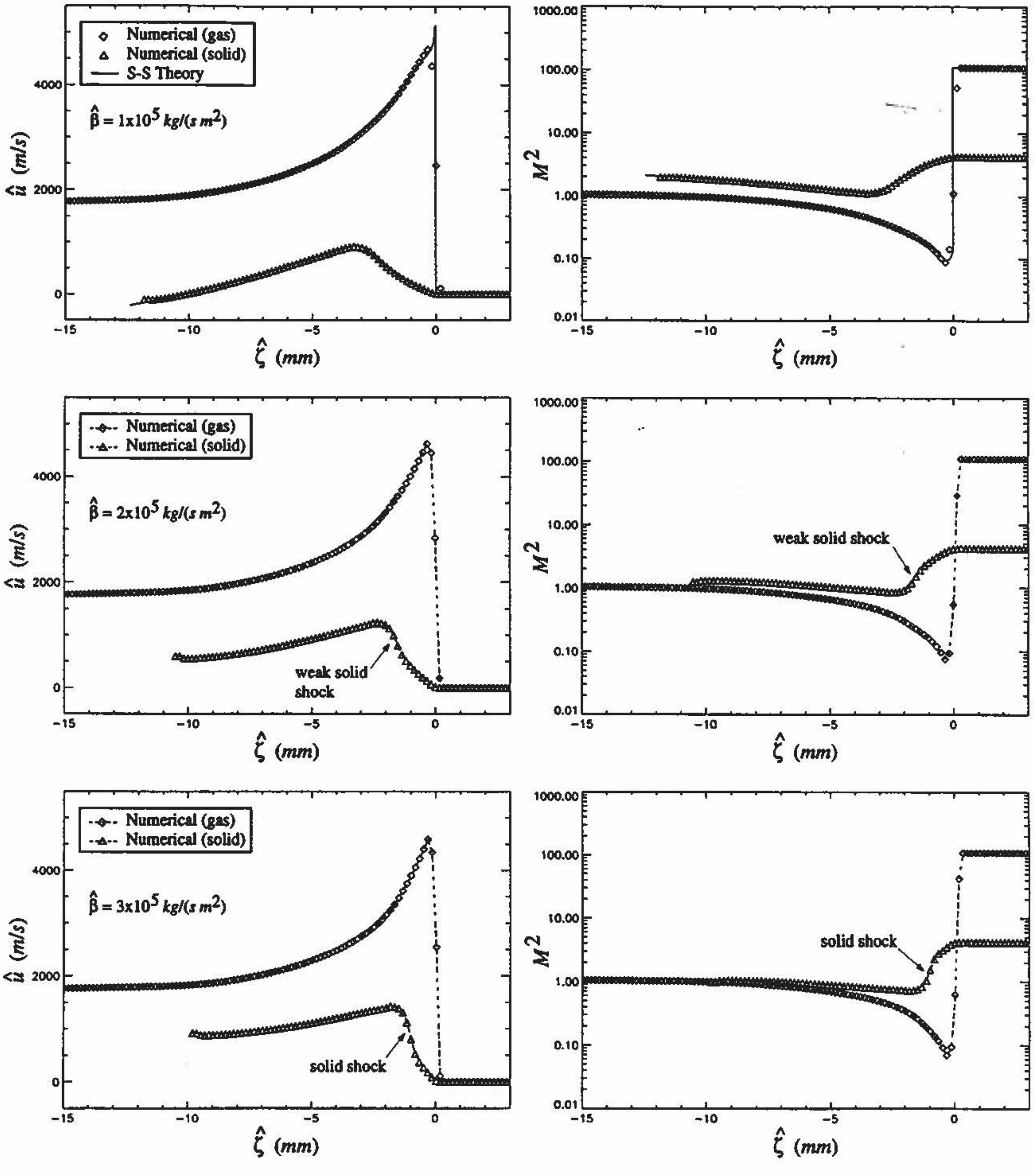

Figure 7.21: Summary of predicted detonation structures for increasing values of the drag coefficient.

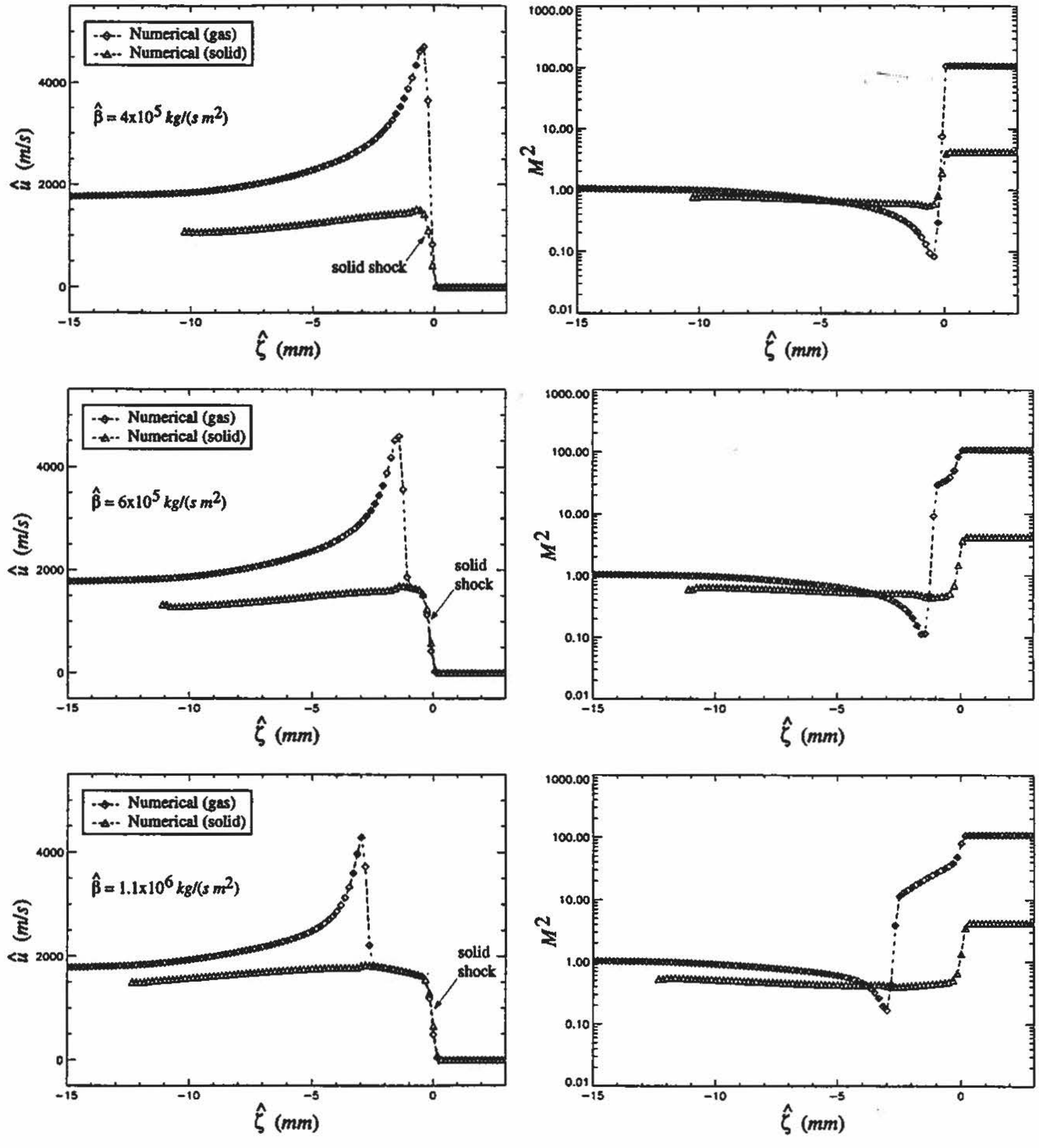

Figure 7.21 (Continued)

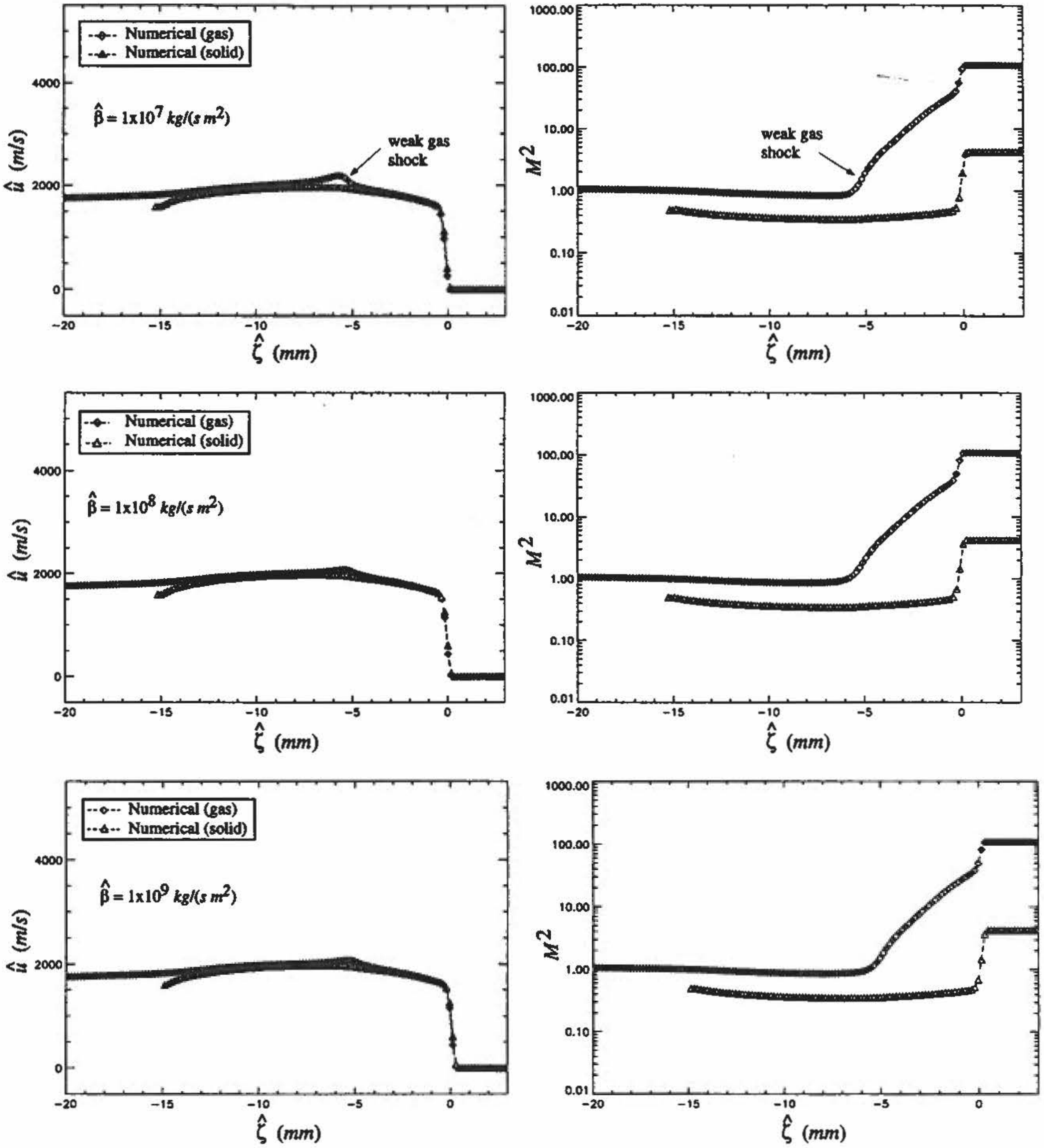

Figure 7.21 (Continued)

koff et al. [84], while slightly larger estimates are obtained based on the empirical drag relation used by Baer and Nunziato [5]. For this value of $\hat{\beta}$, the detonation structures having a shock in both the gas and solid are predicted to evolve.

Figure 7.22 gives the predicted variation in the compaction and combustion rates, identified in Eq. (7.1), along solid particle paths within the reaction zone of the detonation structures shown in Fig. 7.21. The combustion rate is strictly negative and thus only locally decreases the solid volume fraction within the reaction zone. For CJ detonation structures having a lead gas shock, i.e. for $\hat{\beta} = 1 \times 10^5$, 2×10^5, and 3×10^5 $kg/(s\ m^2)$, the compaction rate is negative since the sum of the gas pressure and the intragranular stress is everywhere greater than the solid pressure. For these cases, the high gas pressure within the interstices of the solid particles pushes the particles apart, thereby locally decreasing the solid volume fraction. For $\hat{\beta} \geq 4 \times 10^5$ $kg/(s\ m^2)$, the strength of the solid shock is sufficient to produce a compacted region having $\phi_2 > 0.70$ at the front of the detonation structure. In this region, the solid pressure exceeds the sum of the gas pressure and the intragranular stress, and the bed of solid particles is compacted. The size of the compacted region is seen to increase with $\hat{\beta}$. Though combustion is initiated by the lead solid shock, the combustion rate is small throughout much of the compacted region. The compaction rate vanishes quickly as the gas and solid pressure nearly equilibrate in the region behind the gas shock. Based on these results, it is concluded that the existence of a compacted region within the reaction zone is directly associated with the presence of a lead solid shock.

The numerically predicted results for detonation structure obtained for the different values of $\hat{\beta}$ are summarized in TABLE 7.3. The predicted values for $\hat{\rho}_1$ final, $\hat{u}_1$ final, $\hat{P}_1$ final, M_1^2 final, and $\hat{D}$ for all values of $\hat{\beta}$ agree well with the values predicted by the steady equilibrium end state analysis for the CJ state. This indicates that the predicted waves are CJ detonations. The predicted minimum value for M_1^2 within

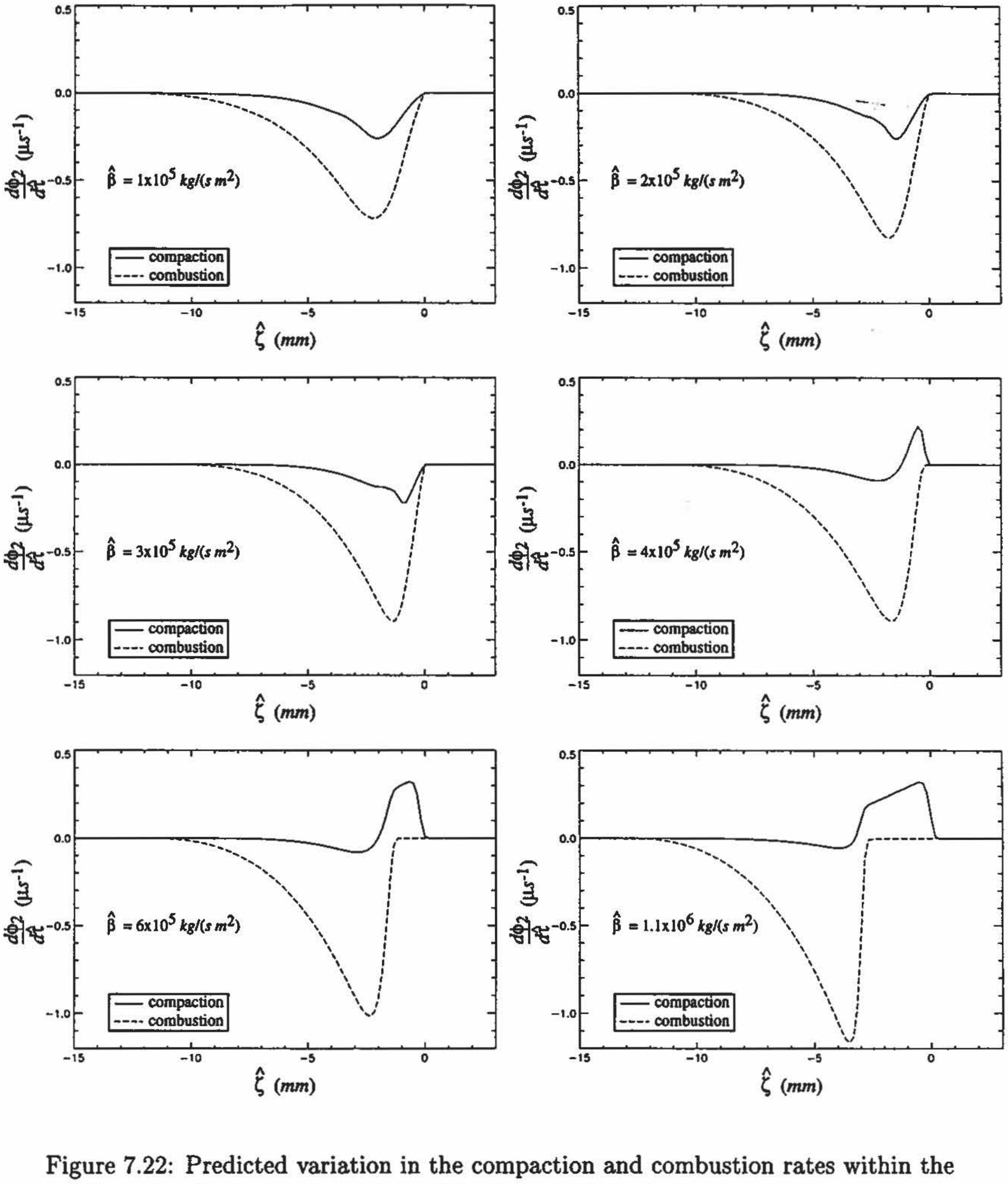

Figure 7.22: Predicted variation in the compaction and combustion rates within the reaction zone for increasing values of the drag coefficient.

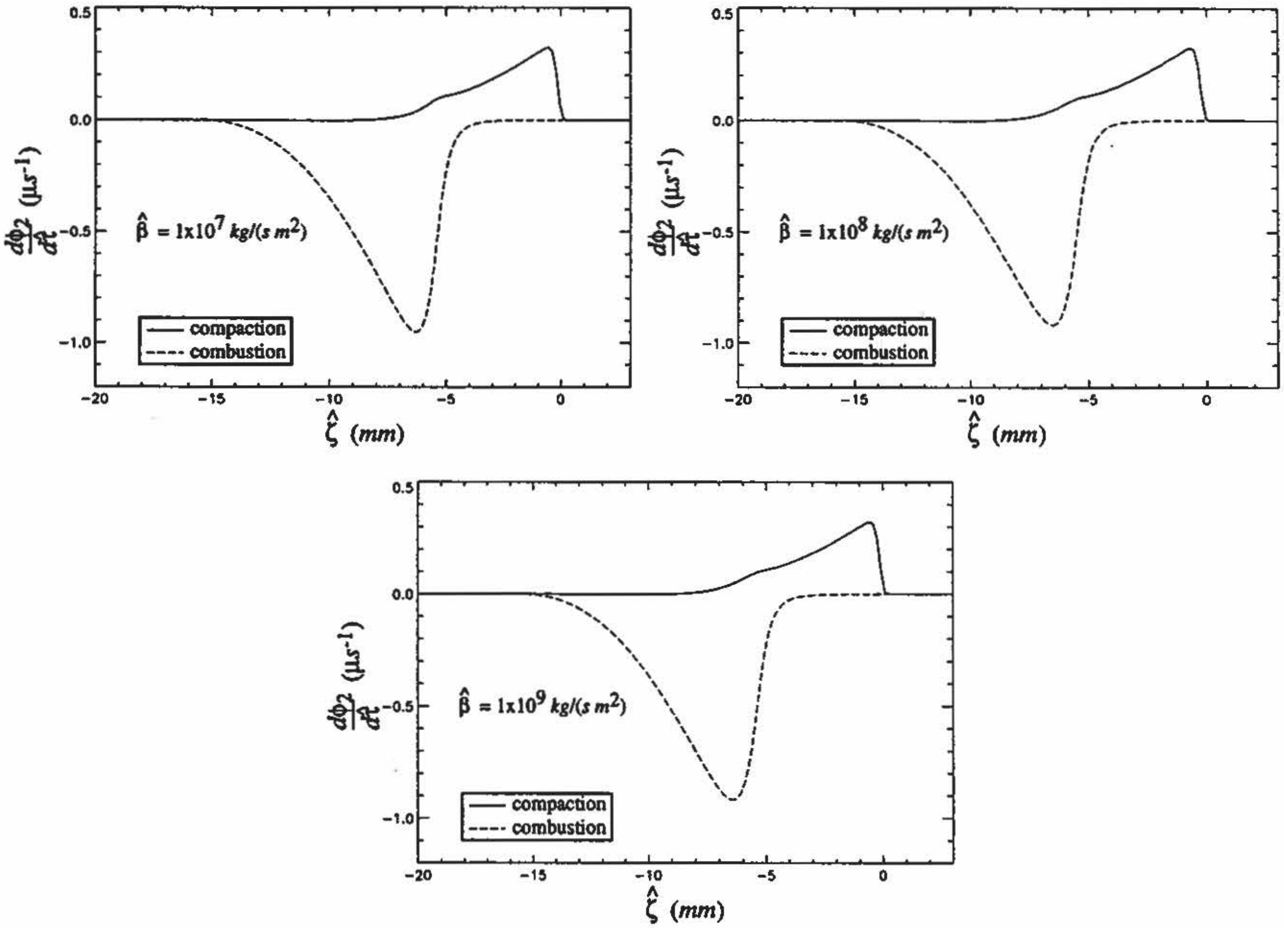

Figure 7.22 (Continued)

$\hat{\beta}$ $[kg/(s\ m^2)]$	$\hat{\rho}_1$ final (kg/m^3)	$\hat{u}_1$ final (m/s)	$\hat{P}_1$ final (GPa)	M_1^2 final	M_1^2 minimum	$\hat{D}$ (m/s)	$\Delta\hat{x}_s$ (mm) (mm)
1.0×10^5	1704	1822	13.5	1.00	0.086	6158.6	no solid shock
2.0×10^5	1704	1821	13.5	1.00	0.075	6157.8	−1.75
3.0×10^5	1705	1823	13.5	1.00	0.069	6157.8	−1.24
4.0×10^5	1704	1822	13.5	1.00	0.083	6157.7	0.00
6.0×10^5	1704	1822	13.5	1.00	0.112	6157.3	1.65
1.1×10^6	1704	1822	13.5	1.00	0.165	6158.6	3.33
1.0×10^7	1704	1821	13.5	1.00	0.829	6157.2	5.65
1.0×10^8	1704	1821	13.5	1.00	0.858	6159.1	no gas shock
1.0×10^9	1704	1822	13.5	1.00	0.859	6159.1	no gas shock
CJ state	1704	1822	13.5	1.00	—	6159.9	—

TABLE 7.3: PREDICTED GAS END STATES FOR CASE II IDENTIFIED IN TABLE 6.2.

the reaction zone decreases with $\hat{\beta}$ for $1 \times 10^5 \leq \hat{\beta} \leq 3 \times 10^5$ $kg/(s\ m^2)$, and increases with $\hat{\beta}$ for $\hat{\beta} > 3 \times 10^5$ $kg/(s\ m)$. Since the predicted wave speed is nearly constant ($\sim \hat{D}_{CJ} = 6159.9$ m/s), the shocked value for M_1^2 is nearly constant for detonation structures having a lead gas shock. Consequently, the decrease in the minimum value for M_1^2 is due to the drag relaxation process immediately following the gas shock. This conclusion is substantiated by the steady analysis which predicts a thin relaxation layer immediately behind the gas shock of *shocked gas-unshocked solid* CJ detonation structures which further decreases M_1^2 from its shocked value. Furthermore, this minimum value is predicted to decrease with increasing $\hat{\beta}$ (for $\hat{\beta}$ less than the maximum value associated with *shocked gas-unshocked solid* CJ detonation structures). For larger values of $\hat{\beta}$, a lead solid shock is predicted, and the minimum value for M_1^2 increases with $\hat{\beta}$ as the trailing gas shock weakens. Also summarized in Table 7.3 is the predicted distance between the lead solid shock and the trailing gas shock, $\Delta\hat{x}_s$, for two-shock detonation structures.

Based on these results, the steady model equations were numerically integrated in an attempt to predict the two-shock CJ detonation structure for $\hat{\beta} = 1.1 \times 10^6$ $kg/(s\ m^2)$, and the *unshocked gas-shocked solid* CJ detonation structure for $\hat{\beta} = 1 \times 10^9$ $kg/(s\ m^2)$. The results are compared to the detonation structures predicted by the unsteady analysis in Figs. 7.23 and 7.24, respectively. Here, no complete structures were predicted by the steady analysis due to difficulties encountered near gas sonic points. This does not indicate that no such steady structures exist; rather, the results of the steady structure analysis are inconclusive.

For the incomplete steady result shown in Fig. 7.23, the wave speed was fixed at $\hat{D}_{CJ} = 6159.9$ m/s, and the distance between the lead solid shock and the trailing gas shock, $\Delta\hat{x}_s$, was adjusted in order to minimize the value of ϕ_2 at the location of the gas sonic point. In other words, $\Delta\hat{x}_s$ was adjusted in order to get as close as possible to the complete combustion state ($\phi_2 = 0$) before reaching a gas sonic

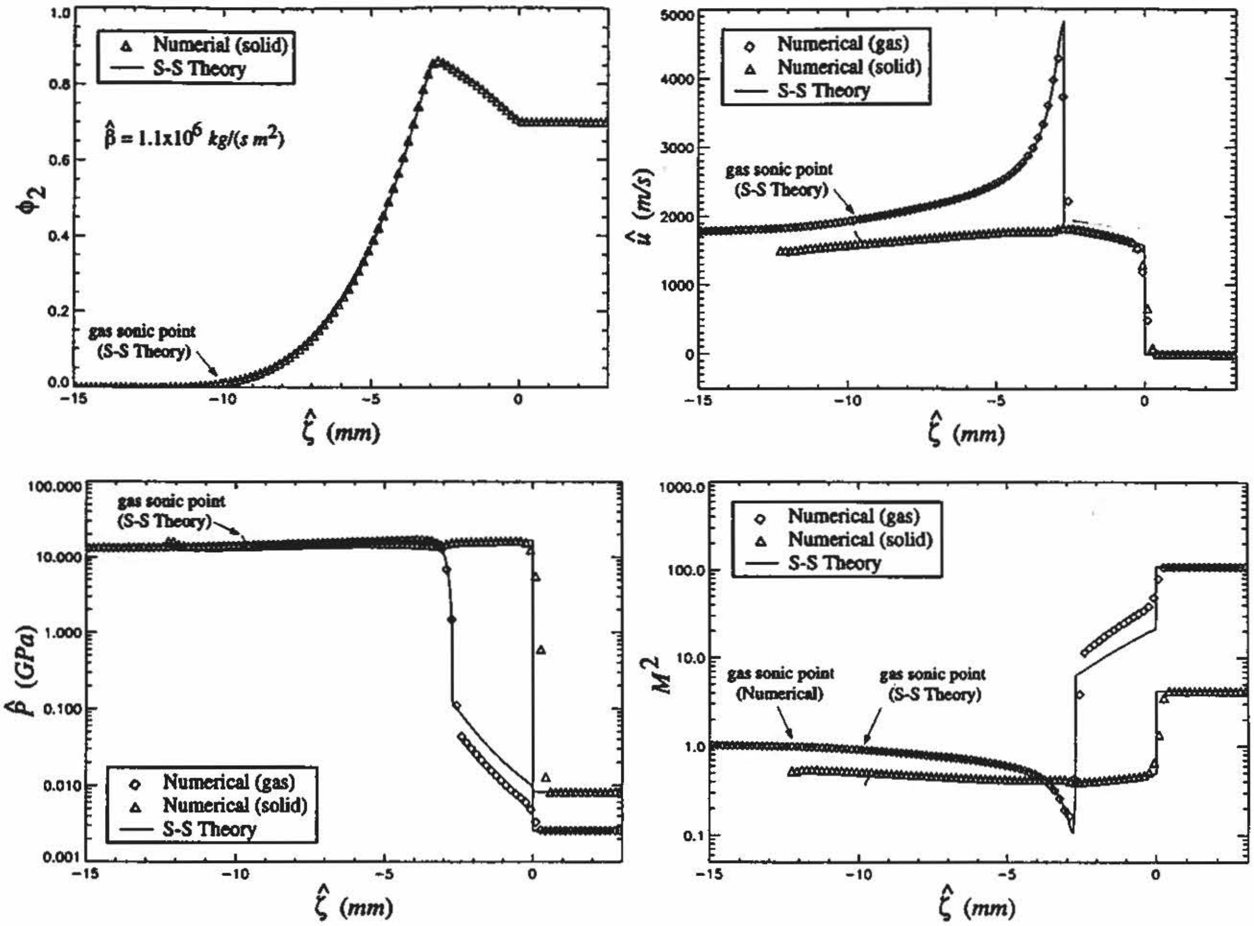

Figure 7.23: Comparison of the numerically predicted *shocked gas-unshocked solid CJ* detonation structure with an incomplete structure predicted by the steady analysis for $\hat{\beta} = 1.1 \times 10^6\ kg/(s\ m^2)$.

point. A minimum value of $\phi_2 = 0.08$ was predicted. The predicted minimum value proved to be very sensitive to $\Delta\hat{x}_s$. In fact, substantial decreases in ϕ_2 were still being predicted for values of $\Delta\hat{x}_s$ differing only by $1 \times 10^{-16}\ m$, the level of machine precision. As seen in this figure, with the exception of the region located immediately behind the lead solid shock, good agreement exists between the structure predicted by the unsteady analysis and the incomplete structure predicted by the steady analysis. Though it appears that the steady analysis predicts a discontinuous jump in gas velocity, pressure, and Mach number at the lead solid shock, careful examination of the data indicates a fully resolved drag relaxation layer. Since the width of this layer

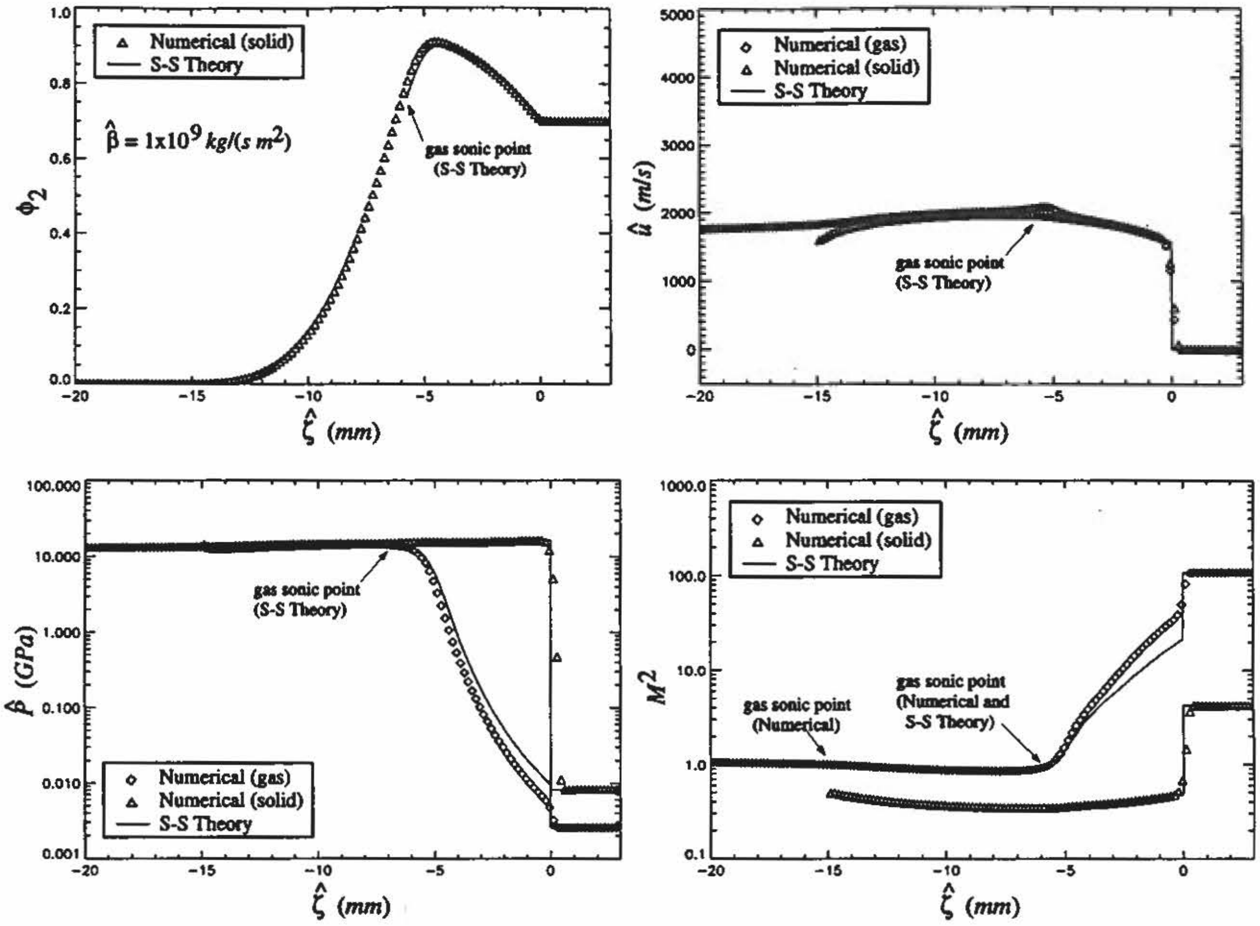

Figure 7.24: Comparison of the numerically predicted *unshocked gas-shocked solid CJ* detonation structure with an incomplete structure predicted by the steady analysis for $\hat{\beta} = 1 \times 10^9\ kg/(s\ m^2)$.

is much smaller than the artificial shock width, the numerical method is unable to accurately resolve this layer; the error is evident. It was determined numerically that the gas sonic point predicted by the steady analysis is not a saddle point, but is a non-equilibrium turning point since $r(w_1^2 - c_1^2) = 0$ and $r(w_1^2 - c_1^2)\mathbf{h}_1(\mathbf{y}_1) \neq [0,\ 0,\ 0,\ 0,\ 0]^T$ in Eqs. (6.22) and (6.23), respectively. Consequently, it is not possible to obtain a physically meaningful solution by integrating the steady equations through this point.

For the incomplete steady result shown in Fig. 7.24, the wave speed was fixed at $\hat{D}_{CJ} = 6159\ m/s$, and the steady equations were numerically integrated for an unshocked gas and a shocked solid. A gas sonic point was predicted within the reaction zone, which was numerically determined to be a saddle point since $r(w_1^2 - c_1^2) = 0$ and $r(w_1^2 - c_1^2)\mathbf{h}_1(\mathbf{y}_1) = [0,\ 0,\ 0,\ 0, 0]^T$ in Eqs. (6.22) and (6.23), respectively; consequently, it is theoretically possible to continue the integration through this point to obtain a physically acceptable result. However, it proved difficult to traverse the sonic point in such a way as to be on the precise trajectory leading to the complete combustion state. The incomplete steady structure reasonably agrees with the structure predicted by the unsteady analysis in the region prior to the gas sonic point, though the numerical method once again has difficulty capturing the thin drag relaxation layer located immediately behind the solid shock. The location of the gas sonic point ($\hat{\zeta} \sim -5.5\ mm$) predicted by both the steady and unsteady analysis reasonably agree. Notably, both the steady and unsteady analysis predict the onset of full-scale combustion, occurring at the location where ϕ_2 is a maximum, in the absence of a gas shock. Here, the increase in gas pressure necessary to initiate full-scale combustion is due to the combined effect of slow exothermic heat release, interphase drag, interphase heat transfer, and material compaction induced by the shocked solid flow.

Lastly, the predicted variation in $\hat{\tau}_{DDT}$ and $\hat{\xi}_{DDT}$ with $\hat{\beta}$ are shown in Fig. 7.25. Though both $\hat{\tau}_{DDT}$ and $\hat{\xi}_{DDT}$ increase slightly with $\hat{\beta}$, interphase drag is seen to have little influence on both of these quantities outside of a small interval where relatively small changes are predicted. For the cases considered in this study, material compaction is seen to have a greater influence on $\hat{\tau}_{DDT}$ and $\hat{\xi}_{DDT}$ than interphase drag.

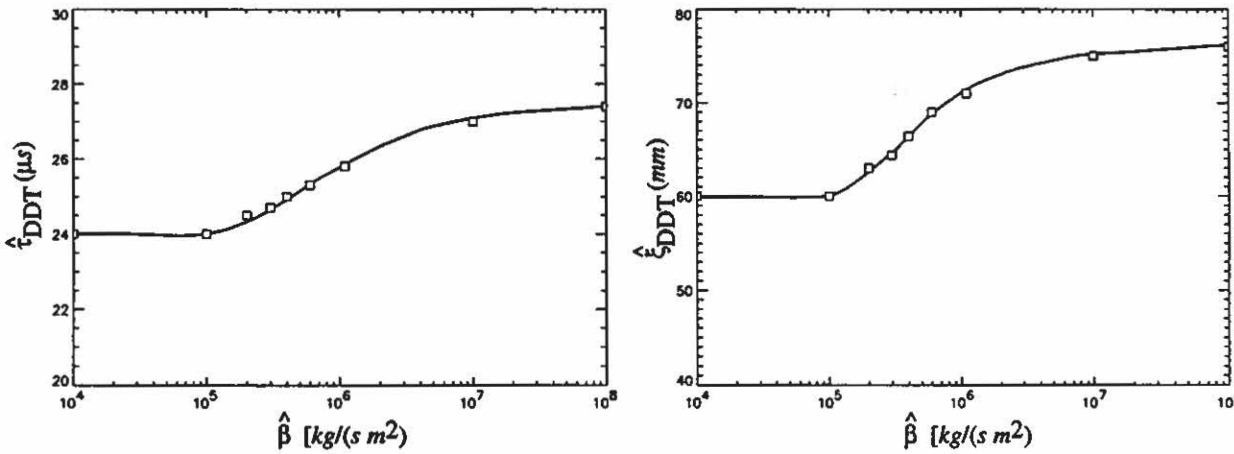

Figure 7.25: Predicted variation in time and distance to detonation for Case II identified in TABLE 6.2.

7.3 Effect of Ambient Mixture Density

Results of the steady analysis showed that *shocked gas-unshocked solid* CJ detonations do not exist for ambient mixture densities $\hat{\rho}_a < 486\ kg/m^3$. In this section, we demonstrate that two-shock detonation structures also evolve for ambient mixture densities less than this minimum value. In particular, it is shown that a CJ detonation structure having a lead solid shock and a trailing gas shock evolves for $\hat{\rho}_a = 400\ kg/m^3$. Though we only consider this single case, it is plausible to expect, based on the results of the previous section, that as $\hat{\rho}_a$ decreases there exists a continuous transition from *shocked gas-unshocked solid* CJ detonation structures, to *shocked gas-shocked solid* CJ detonation structures, and possibly to *unshocked gas-shocked solid* CJ detonation structures. Values for the model parameters and ambient conditions used for this simulation are given in TABLE 6.1 ($\phi_{2o} = 0.229$ for this case). The computational domain was defined for $0 \leq \hat{\xi} \leq 210\ cm$, and consisted of $N = 3000$ evenly spaced nodes. The CPU time for this simulation was approximately twelve hours.

The predicted velocity history of the gas and solid are shown in Fig. 7.26. Here, a solid shock propagating at speed 3081.1 m/s evolves for early time in response to the moving piston. Combustion is initiated at approximately $\hat{\tau} = \mu s$. Subsequently, the combustion wave accelerates, undergoes a transition to detonation, and relaxes to a steady two-shock CJ detonation propagating at speed 4592.1 m/s. Once again, the two-shock structure of the detonation wave is barely noticeable in the spatial profile for $\hat{u}_1$ at $\hat{\tau} = 500\ \mu s$.

The compaction front and burn front trajectories are shown in the $\hat{x}$-$\hat{\tau}$ plane of Fig. 7.27. The predicted time, $\hat{\tau}_{DDT}$, and distance, $\hat{\xi}_{DDT}$, associated with transition to detonation are approximately 170 μs and 460 mm, respectively. The value for $\hat{\xi}_{DDT}$ is substantially higher than those predicted in the previous sections for $\hat{\rho}_a = 1200\ kg/m^3$. This result is consistent with the experimental results of Bernecker

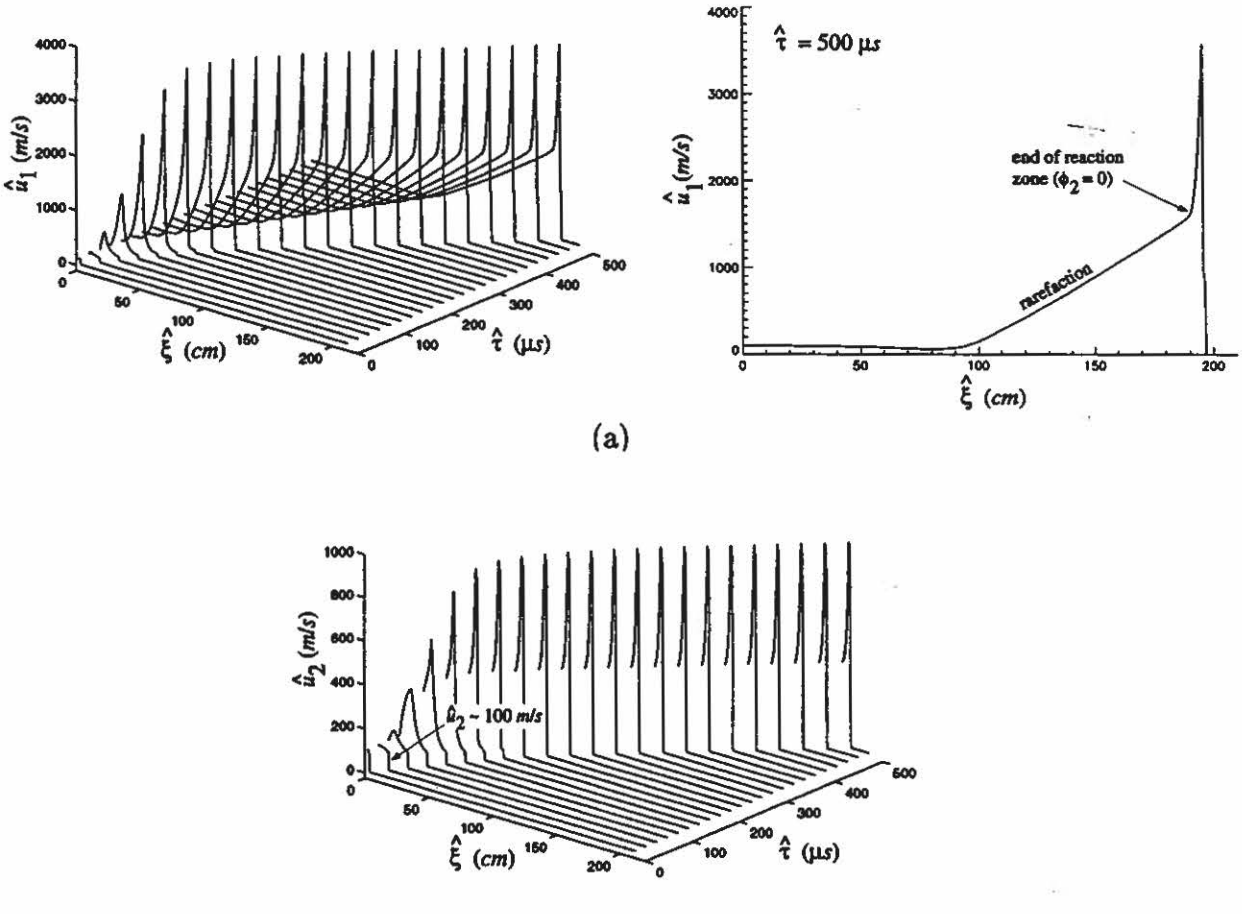

(a)

(b)

Figure 7.26: Predicted time histories for $\hat{\rho}_a = 400\ kg/m^3$: (a) gas velocity and (b) solid velocity.

and Price [15] which show that transition length increases with decreasing ambient mixture density. The predicted variation in the distance between the compaction front (associated with the lead solid shock) and the burn front (associated with the trailing gas shock), $\Delta\hat{x}_s$, with time is shown in Fig. 7.28. Here, it is seen that $\Delta\hat{x}_s$ relaxes to approximately 16 mm as steady detonation is approached.

The predicted variation in the gas and solid velocity, pressure, and Mach number squared, and in the solid volume fraction, throughout the reaction zone at $\hat{\tau} = 500\ \mu s$ are shown in Fig. 7.29. The location of both the lead solid shock and the trailing gas

Quantity	*Unsteady Analysis*	*Steady End State Analysis*
$\hat{\rho}_1$ final	619 kg/m^3	619 kg/m^3
$\hat{u}_1$ final	1617 m/s	1617 m/s
$\hat{P}_1$ final	2.98 GPa	2.98 GPa
M_1^2 final	1.00	1.00
$\hat{D}_{CJ}$	4592 m/s	4593 m/s

TABLE 7.4: COMPARISON OF THE PREDICTED GAS END STATE WITH THE CJ VALUES GIVEN BY THE STEADY DETONATION END STATE ANALYSIS FOR $\hat{\rho}_a = 400\ kg/m^3$

shock are clearly evident in this figure. Combustion is initiated by the solid shock, but significant combustion is again predicted to occur only behind the gas shock. As such, a compaction region exists between the two shocks. The gas and solid velocity, pressure, and Mach number squared change abruptly across their respective shocks, and are continuous in the compaction region between the shocks, and in the combustion region located between the gas shock and the end of the reaction zone. The solid volume fraction is continuous throughout the wave. Also, it is noted here that the solid Mach number squared increases from its subsonic value behind the solid shock, to unity within the reaction zone at $\hat{\xi} = 193.6\ cm$, and to approximately 1.2 at complete reaction. The predicted reaction zone length is 633 mm. Though this structure is qualitatively similar to the two-shock CJ structure predicted in Subection 7.2.1 for $\hat{\rho}_a = 1200\ kg/m^3$, the maximum pressures and velocities predicted here are substantially smaller, and the reaction zone length is substantially larger, than the corresponding values reported in that subsection.

Lastly, a comparison of the numerically predicted gas end state and detonation wave speed with the CJ values obtained from the equilibrium end state analysis for $\hat{\rho}_a = 400\ kg/m^3$ is given in TABLE 7.4. The good agreement between these values indicates that a *shocked gas-shocked solid* CJ detonation has evolved.

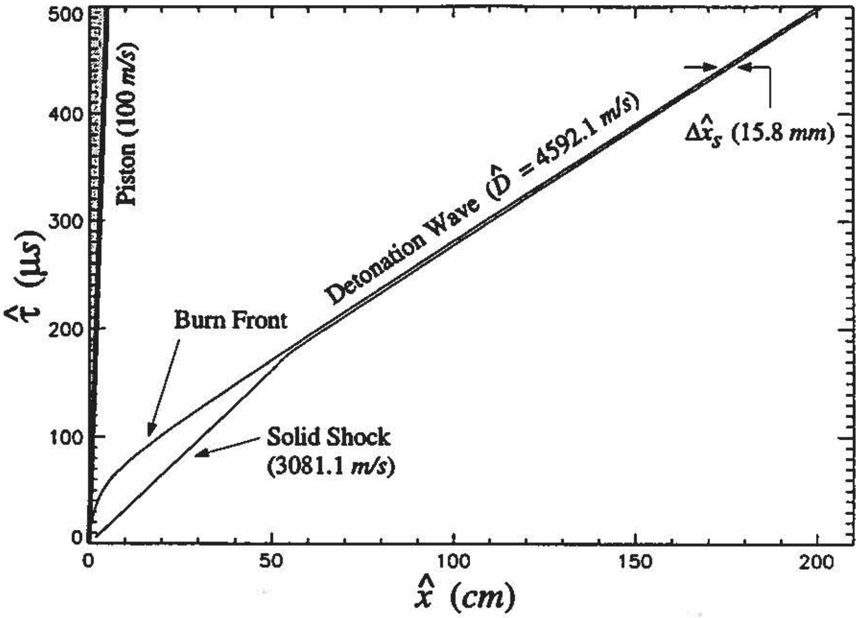

Figure 7.27: Predicted compaction wave and burn front trajectories for $\hat{\rho}_a = 400$ kg/m^3.

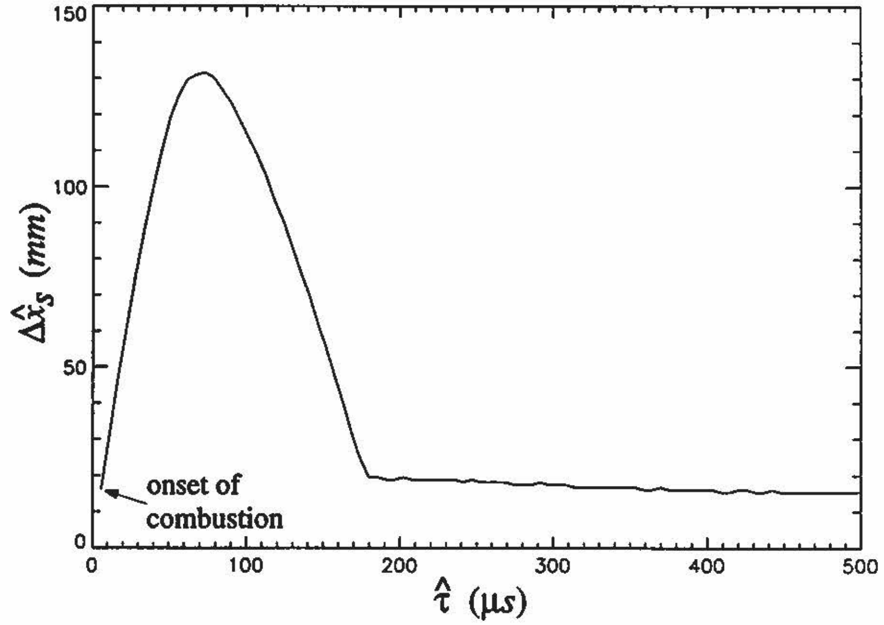

Figure 7.28: Predicted time history for the distance between the lead solid shock and the trailing gas for $\hat{\rho}_a = 400$ kg/m^3.

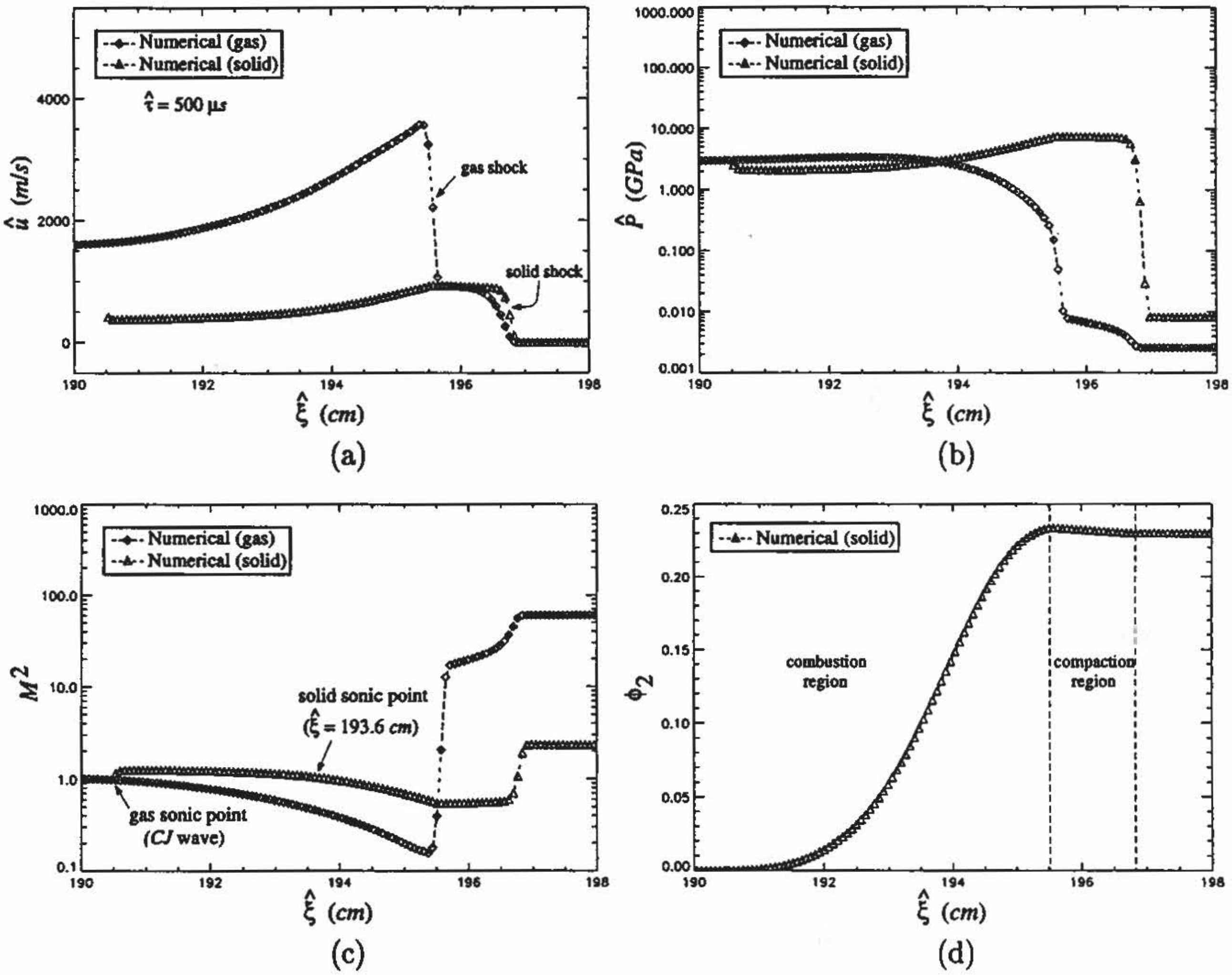

Figure 7.29: Predicted *shocked gas-shocked solid CJ* detonation structure for $\hat{\rho}_a = 400\ kg/m^3$: (a) gas and solid velocity; (b) gas and solid pressure; (c) gas and solid Mach number squared (relative to the wave); and (d) solid volume fraction.

8

CONCLUSIONS AND RECOMMENDATIONS

8.1 Steady Analysis

Steady two-phase detonations were analyzed in terms of their end states and reaction zone structure. The end state analysis identified three classes of potential two-phase detonation solutions: CJ detonations, strong detonations, and weak detonations. Of these three classes, CJ and weak detonations do not require energy input from a moving piston to sustain their propagation and are thus self-propagating waves. Given initial conditions at the detonation front, a detailed analysis of the spatial reaction zone structure determined the accessibility of the CJ and weak detonation end states.

The structure analysis identified both CJ and weak detonations having a *shocked gas* and an *unshocked solid* structure. No other self-propagating detonation structures were identified, though the analysis given here does not preclude their existence. This work is not the first to predict these CJ structures, as they have been previously predicted and analyzed by Powers, Stewart, and Krier [91, 95]. However, this work is the first to predict and analyze steady two-phase weak detonation structures.

The end state and steady wave speed for a weak detonation, if it exists, are dependent on reaction zone structure; thus, given a particular set of system parameters, one must integrate the steady model equations to determine these quantities. In this study, a phase space technique was used to identify steady weak detonation structures. It was shown that a weak detonation solution trajectory originating from a *shocked gas* and *unshocked solid* initial state must traverse a saddle point in the ϕ_1-$\hat{P}_1$ phase plane prior to terminating at a weak detonation end state. At the location of the saddle point, the gas velocity relative to the wave is locally sonic; at the end state, the gas velocity is supersonic. The weak detonation solution trajectory corresponds to a unique value of wave speed, $\hat{D}_W$, which is greater than the CJ wave speed for the ambient material, $\hat{D}_{CJ}$. For steady wave speeds greater than $\hat{D}_W$, strong solutions are predicted, and for waves speeds less than $\hat{D}_W$, non-physical solutions are predicted as turning points are reached in the ϕ_1-$\hat{P}_1$ phase plane, beyond which the solutions become double-valued functions of position. Similar phase space topologies exist for steady one-phase weak detonations [34].

The phase space topology for a steady CJ detonation structure is less complicated than that of a steady weak detonation, as a CJ solution trajectory does not traverse an interior singularity prior to terminating at the CJ end state. In contrast to weak detonations, the CJ end state and steady wave speed are independent of reaction zone structure, and can be uniquely determined by a simple equilibrium end state analysis. A CJ solution trajectory originating from a *shocked gas* and *unshocked solid* initial state terminates at the CJ end state for a unique value of wave speed, $\hat{D}_{CJ}$; at the CJ end state, the gas velocity relative to the wave is locally sonic. For wave speeds greater than $\hat{D}_{CJ}$, strong solutions are predicted, and for wave speeds less than $\hat{D}_{CJ}$, non-physical solutions are predicted.

Existence criteria for *shocked gas-unshocked solid* CJ and weak detonations were determined based on a parametric study of the steady model. For a physically relevant ambient mixture density ($\hat{\rho}_a = 1200\ kg/m^3$), *shocked gas-unshocked solid* CJ and weak detonations do not exist for large values of the drag coefficient, $\hat{\beta}$, or for large values of the heat transfer coefficient, $\hat{h}$. For such values, the drag and heat transfer rates are sufficient to drive the unshocked solid flow to a solid sonic state within the reaction zone. In this event, the solutions are non-physical as the solid variables are double-valued functions of position.

Provided that $\hat{\beta}$ and $\hat{h}$ are sufficiently small to admit *shocked gas-unshocked solid* structures, a bifurcation from weak detonations to CJ detonations occurs with increasing compaction viscosity, $\hat{\mu}_c$. As the value of $\hat{\mu}_c$ increases, the compaction rate decreases, and the gas sonic point located within the reaction zone structure of weak detonations approaches the end of the reaction zone. The bifurcation point corresponds to the critical of $\hat{\mu}_c$ at which the gas sonic point first reaches the end of the reaction zone.

Consequently, the existence of steady *shocked gas-unshocked solid* weak detonations depends on low drag and heat transfer rates, and high material compaction rates. The existence of steady *shocked gas-unshocked solid* CJ detonations depends on low drag and heat transfer rates, and low material compaction rates.

Also, the existence of steady *shocked gas-unshocked solid* CJ detonations is influenced by the ambient mixture density. Powers, Stewart, and Krier [91, 95] were the first to show that these CJ structures do not exist for ambient mixtures densities less than a minimum critical value. For such a value, the unshocked solid flow is once again driven to a sonic state within the reaction zone, resulting in the prediction of a non-physical solution. Though not considered in the this study, it is likely that a similar existence criterion holds for *shocked gas-unshocked solid* weak detonations.

8.2 Unsteady Analysis

Numerical simulations of piston-initiated DDT predicted the evolution of self-propagating detonation for values of the system parameters used in the steady analysis. The simulations were performed using a new high-resolution numerical method which demonstrated an ability to accurately capture strong shocks without the generation of spurious oscillations, and to accurately resolve fine-scale detonation structure. Comparisons of fully-resolved detonation structures with results given by the steady analysis clarified several previously unresolved issues.

First, it was shown that both *shocked gas-unshocked solid* CJ and weak detonation structures identified by the steady analysis evolve from piston-initiated DDT events. Which type of detonation evolves was found to depend on the existence criteria identified by the steady analysis. By considering increasing values of $\hat{\mu}_c$, while holding all other system parameters fixed (Case I identified in Table 6.2), the simulations predict a bifurcation from weak to CJ detonation structures very near the bifurcation point identified by the steady analysis. Consequently, a significant contribution of this work was in demonstrating for the first time that the CJ wave speed is not the unique wave speed for a self-propagating two-phase detonation.

Second, it was shown that detonation structures having a *shocked solid* evolve for parameter values in which the steady analysis predicts non-physical solutions due to solid sonic states occurring within the reaction zone of *unshocked solid* structures. In particular, by considering increasing values of $\hat{\beta}$, while holding all other system parameters fixed (Case II identified in Table 6.2), the unsteady analysis predicts a bifurcation from *shocked gas-unshocked solid* weak structures, to *shocked gas-unshocked solid* CJ structures, to *shocked gas-shocked solid* CJ structures, and finally to *unshocked gas-shocked solid* CJ structures. Also, it was shown that *shocked solid* structures evolve for ambient mixture densities less than the minimum value required for a steady *shocked gas-unshocked solid* CJ structure to exists. This dependency of detonation structure on both the drag rate and ambient mixture density has not been previously demonstrated. In addition to the detonation structures predicted by this study, other structures likely exist for different combinations of parameter values. In particular, as weak detonations are structure dependent, it is likely that the slightest modeling modification will affect the existence of these detonations. Nonetheless, this study has demonstrated a large variety of detonation structures admitted by two-phase continuum DDT models.

Close examination of numerically predicted detonation structures having a lead solid shock reveals a thin relaxation layer immediately behind the shock. Within this layer, the *unshocked* gas velocity rapidly equilibrates with the *shocked* solid velocity. The steady analysis estimates the width of the relaxation layer to be approximately 30 μm for the physically relevant value $\hat{\beta} = 1.1 \times 10^6 \ kg/(s \ m^2)$, and also indicates that the width of the layer decreases with increasing $\hat{\beta}$. The unsteady analysis shows the width of this layer to be small compared to the reaction zone length for this same value of $\hat{\beta}$ ($\sim 12 \ mm$). The presence of such fine-scale structure within the reaction zone brings up two important issues concerning numerical resolution and the validity of the continuum modeling approach.

First, the best shock-capturing methods to date require at least three computational cells to resolve a shock; this gives rise to an artificial shock structure. If the width of the drag relaxation layer behind the solid shock is on the order of three computational cell lengths, or smaller, then the artificial shock structure will overwhelm this fine-scale structure. A prohibitively large number of computational cells would be needed within the reaction zone to fully resolve the drag relaxation layer. For example, based on the values quoted in the previous paragraph, and assuming an even distribution of computational cells, approximately 2500 computational cells would be needed within the reaction zone to fully resolve all length scales. For the simulations performed in this study, the number of computational cells within the reaction zone ranged from 50-100, whereas previous DDT studies have typically used from 6-20 cells within the reaction zone.

Second, if the fine-scale structure occurring within the reaction zone is smaller than the characteristic size of a single solid particle, such as for the case described here, the fundamental premise of the continuum modeling approach is violated. As such, the appropriateness of continuum models for analyzing detonation in these systems is questionable, provided that the small lengths scales identified are physically relevant. However, due to modeling complexities, alternative modeling approaches are also certain to have many limitations.

As stated earlier, the primary objective of this work was to predict and analyze two-phase detonation structures by numerically simulating piston-initiated DDT, and to compare the predicted structures with results given by a steady detonation analysis. As such, the forms for the constitutive relations used in this study were chosen mostly for simplicity, and not to accurately model all experimentally observed features characteristic of piston-initiated DDT. Nevertheless, the numerical simulations reasonably predicted most experimentally observed features including the formation and propagation of a lead compaction wave, the induction period prior to the onset of significant combustion, and the final transition to detonation. The simulations did not predict the slow build-up of combustion observed during the early stages of DDT, nor did they predict the formation for an inert solid plug just prior to the onset of detonation. To this end, a number of modeling improvements can be made to obtain better predictive capabilities.

As this work addressed two-phase detonation structure, values for the combustion rate parameters were assumed constant, and were chosen to model high-rate combustion associated with detonation. These values proved much too large to properly account for low-rate combustion during the early stages of DDT. The combustion rate parameters should depend on the local solution, enabling low-rate combustion to be modeled under relatively mild conditions, and high-rate combustion to be modeled under detonation conditions. In fact, several recent DDT modeling studies have adopted such a strategy [59, 109]. Furthermore, experiments suggest that the formation of the inert solid plug, which is believed to be significant in effecting transition to detonation, is largely due to the coalescence of compression waves generated by the acceleration of this initial low-rate combustion process. Thus, it follows that the first step toward properly addressing inert plug formation is to accurately model low-rate combustion occurring during the early stages of DDT.

One of the most uncertain aspects of this model is the evolution equation used to predict the induction period prior to the onset of full-scale combustion. The values for the rate parameters used with this equation were chosen such that the numerically predicted induction time matched that observed in a single piston-initiated DDT experiment ($\hat{v}_p = 100\ m/s$) [80]. At a minimum, values for the rate parameters should be more judiciously chosen such that predictions for induction time match experimentally observed induction times for a range of piston velocities. To this end, one could choose to match the data reported by Sandusky and Bernecker [105]. However, as the functional form of the forcing term in this equation was chosen *ad hoc*, it would be appropriate to first choose a functional form based on stronger physical arguments.

Much work remains concerning the modeling of DDT in granular energetic solids. Though two-phase continuum models have demonstrated an ability to predict results commensurate with a number of DDT experiments, the development of models having good predictive capabilities is contingent upon accurate sub-scale modeling. The proper way to account for sub-scale processes, such as those responsible for the formation of "hot spots," within the framework of these models remains unclear. Also, better constitutive relations are needed to model the combustion, drag, heat transfer, and material compaction rates over the wide range of conditions associated with DDT. Due to a lack of experimental data, it is common practice to use empirical relations valid under less extreme conditions to describe these rate-dependent processes under detonation conditions. Furthermore, all prior modeling studies, including this study, have not rationally accounted for solid granule break-up, though it is well-accepted that substantial break-up occurs during DDT. Rate-dependent particle break-up could be rationally accounted for within the framework of the model used in this study. Such issues should be sorted out based on one-dimensional modeling before attacking complicated, but very important, multi-dimensional DDT problems.

A

DERIVATION OF THE SOUND SPEED RELATIONS

A general expression for the gas sound speed is derived in this appendix using standard thermodynamic relations. Though not shown here, an identical expression for the solid sound speed is derived using the same approach.

Given the functional dependency $\hat{P}_1 = \hat{P}_1(\hat{\rho}_1, \hat{e}_1)$ [Eq. (2.22)], a differential change in $\hat{P}_1$ is expressed as

$$d\hat{P}_1 = \left.\frac{\partial \hat{P}_1}{\partial \hat{\rho}_1}\right|_{\hat{e}_1} d\hat{\rho}_1 + \left.\frac{\partial \hat{P}_1}{\partial \hat{e}_1}\right|_{\hat{\rho}_1} d\hat{e}_1. \tag{A.1}$$

The Gibbs equation for a gas of fixed composition is given by

$$\hat{T}_1 d\hat{s}_1 = d\hat{e}_1 - \frac{\hat{P}_1}{\hat{\rho}_1^2} d\hat{\rho}_1, \tag{A.2}$$

Equation (A.1) is solved for $d\hat{e}_1$, and the result is substituted into Eq. (A.2) to obtain

$$\hat{T}_1 d\hat{s}_1 = \frac{1}{\left.\frac{\partial \hat{P}_1}{\partial \hat{e}_1}\right|_{\hat{\rho}_1}} d\hat{P}_1 - \left(\frac{\hat{P}_1}{\hat{\rho}_1^2} + \frac{\left.\frac{\partial \hat{P}_1}{\partial \hat{\rho}_1}\right|_{\hat{e}_1}}{\left.\frac{\partial \hat{P}_1}{\partial \hat{e}_1}\right|_{\hat{\rho}_1}} \right) d\hat{\rho}_1. \tag{A.3}$$

Setting $d\hat{s}_1 = 0$ in this equation, and solving the result for $d\hat{P}_1/d\hat{\rho}_1|_{\hat{s}_1}$ gives an expression for $\hat{c}_1^2$:

$$\hat{c}_1^2 = \left.\frac{d\hat{P}_1}{d\hat{\rho}_1}\right|_{\hat{s}_1} = \frac{\hat{P}_1}{\hat{\rho}_1}\Gamma_1 + \left.\frac{\partial \hat{P}_1}{\partial \hat{\rho}_1}\right|_{\hat{e}_1}, \tag{A.4}$$

where the Grüneisen coefficient Γ_1 is given by

$$\Gamma_1 = \frac{1}{\hat{\rho}_1} \left.\frac{\partial \hat{P}_1}{\partial \hat{e}_1}\right|_{\hat{\rho}_1}.$$

Equation A.4 is the desired result.

B

CHARACTERISTIC FORM OF THE MODEL EQUATIONS

The characteristic form of the model equations is given in this appendix. It is possible to express the equations in characteristic form since they constitute a hyperbolic system. As such, the partial differential equations can be reduced to ordinary differential equations which hold along characteristic curves in the (ξ, τ) plane.

To this end, Eq. (3.8) is left multiplied by each of the left eigenvectors $\mathbf{l}^{(j)}$ $(j = 1, \ldots, 9)$ [Eqs. (3.35-3.43)] to obtain a system of eight characteristic equations:

$$\mathbf{l}^{(j)} \cdot \left(\frac{\partial \mathbf{q}}{\partial \tau} + \bar{\bar{\mathbf{A}}}(\mathbf{q}) \frac{\partial \mathbf{q}}{\partial \xi} \right) = \mathbf{l}^{(j)} \cdot \mathbf{g}(\mathbf{q}). \tag{B.1}$$

Using the relation $\mathbf{l}^{(j)} \cdot \bar{\bar{\mathbf{A}}} = \lambda^{(j)} \mathbf{l}^{(j)}$ in Eq. (B.1), we obtain

$$\mathbf{l}^{(j)} \cdot \left(\frac{\partial \mathbf{q}}{\partial \tau} + \lambda^{(j)} \frac{\partial \mathbf{q}}{\partial \xi} \right) = \mathbf{l}^{(j)} \cdot \mathbf{g}(\mathbf{q}). \tag{B.2}$$

This system of equations gives the time rate of change in the conserved variables along characteristic curves in the (ξ, τ) plane, i.e.

$$\mathbf{l}^{(j)} \cdot \frac{d\mathbf{q}}{d\tau} = \mathbf{l}^{(j)} \cdot \mathbf{g}(\mathbf{q}) \qquad \text{on} \qquad \frac{d\xi}{d\tau} = \lambda^{(j)}. \tag{B.3}$$

The characteristic equations defined by Eq. (B.3) are:

<u>Gas Entropy Mode</u> $(\lambda, \mathbf{r}, \mathbf{l})^{(1)}$

$$\rho_1 \phi_1 T_1 \frac{ds_1}{d\tau_{1o}} - P_1 \frac{d\phi_1}{d\tau_{1o}} = \left[e_2 - e_1 + \frac{1}{2}(v_2 - v_1)^2 - \frac{P_1}{\rho_1} \right] C_m + (v_2 - v_1) C_d + C_e, \tag{B.4}$$

<u>Gas Acoustic Modes</u> $(\lambda, \mathbf{r}, \mathbf{l})^{(2)}$, $(\lambda, \mathbf{r}, \mathbf{l})^{(3)}$

$$\begin{aligned}\frac{1}{\rho_1 c_1^2}\frac{dP_1}{d\tau_{1\pm}} \pm \frac{1}{c_1}\frac{dv_1}{d\tau_{1\pm}} + \frac{1}{\rho_1\phi_1 c_1^2}\left(P_1 + \frac{\rho_1\eta_1(v_2-v_1)}{v_2-v_1\mp c_1}\right)\frac{d\phi_1}{d\tau_{1\pm}} \\ = \frac{1}{\rho_1\phi_1 c_1^2}\left\{\left[\frac{\Gamma_1}{2}(v_2-v_1)^2 + \Gamma_1(e_2-e_1) \pm c_1(v_2-v_1)\right.\right. \\ \left. + \eta_1\left(\frac{\rho_2(v_2-v_1)\mp c_1(\rho_2-\pi_5\rho_1)}{\rho_2(v_2-v_1\mp c_1)}\right) + \frac{P_1}{\rho_1}\right] C_m \\ \left. + \left[\Gamma_1(v_2-v_1)\pm c_1\right] C_d + \Gamma_1 C_e \right\} \\ \mp \frac{\pi_7\eta_1\phi_2}{c_1(v_2-v_1\mp c_1)}\left(P_2 - \pi_5 P_1 - f\right) \mp \frac{1}{c_1}\frac{dv_p}{d\tau}(\tau),\end{aligned} \tag{B.5}$$

Solid Entropy Mode $(\lambda, \mathbf{r}, \mathbf{l})^{(4)}$

$$\rho_2\phi_2 T_2\frac{ds_2}{d\tau_{2o}} - P_2\frac{d\phi_2}{d\tau_{2o}} = \pi_5\frac{P_2}{\rho_2}C_m - \pi_5 C_e, \tag{B.6}$$

Solid Acoustic Modes $(\lambda, \mathbf{r}, \mathbf{l})^{(5)}$, $(\lambda, \mathbf{r}, \mathbf{l})^{(6)}$

$$\begin{aligned}\frac{1}{\rho_2 c_2^2}\frac{dP_2}{d\tau_{2\pm}} \pm \frac{1}{c_2}\frac{dv_2}{d\tau_{2\pm}} + \frac{P_2}{\rho_2\phi_2 c_2^2}\frac{d\phi_2}{d\tau_{2\pm}} \\ = \frac{1}{\rho_2\phi_2 c_2^2}\left(-\pi_5\frac{P_2}{\rho_2}C_m \mp \pi_5 c_2 C_d - \pi_5\Gamma_2 C_e\right) \\ - \frac{\pi_7\eta_2\phi_1}{c_2^2}\left(P_2 - \pi_5 P_1 - f\right) \mp \frac{1}{c_2}\frac{dv_p}{d\tau}(\tau),\end{aligned} \tag{B.7}$$

Compaction Mode $(\lambda, \mathbf{r}, \mathbf{l})^{(7)}$

$$\frac{d\phi_2}{d\tau_{2o}} = \pi_7\phi_1\phi_2\left(P_2 - \pi_5 P_1 - f\right) - \pi_5\frac{C_m}{\rho_2}, \tag{B.8}$$

Particle Number Density Mode $(\lambda, \mathbf{r}, \mathbf{l})^{(8)}$

$$\frac{dn}{d\tau_{2o}} - \frac{n}{\rho_2}\frac{d\rho_2}{d\tau_{2o}} - \frac{n}{\phi_2}\frac{d\phi_2}{d\tau_{2o}} = \pi_5\frac{n}{\rho_2\phi_2}C_m, \tag{B.9}$$

Ignition Variable Mode $(\lambda, \mathbf{r}, \mathbf{l})^{(9)}$

$$\frac{dI}{d\tau_{2o}} = C_I, \tag{B.10}$$

where the differential operators are given by

$$\begin{aligned}\frac{d}{d\tau_{io}} &= \frac{\partial}{\partial\tau} + v_i\frac{\partial}{\partial\xi} \quad \text{on} \quad \frac{d\xi}{d\tau} = v_i, \\ \frac{d}{d\tau_{i\pm}} &= \frac{\partial}{\partial\tau} + (v_i \pm c_i)\frac{\partial}{\partial\xi} \quad \text{on} \quad \frac{d\xi}{d\tau} = v_i \pm c_i.\end{aligned}$$

The piston acceleration term $\frac{dv_p(\tau)}{d\tau}$ in Eqs. (B.5) and (B.7) is a prescribed function of time, and is thus considered a forcing term in these equations. It is noted that in the limit as $v_2 \rightarrow v_1 \pm c_1$, the characteristic equation associated with the corresponding forward or backward gas acoustic mode degenerates into the characteristic equation associated with the compaction mode. In these limits, the model equations become parabolic and the characteristic equations can no longer be used to construct a solution of the problem. It is seen from Eq. (B.5) that the sonic singularity is removed for $\eta_1 \equiv 0$.

C

CLASSIFICATION OF THE CHARACTERISTIC FIELDS

An analysis is given in this appendix for classifying the characteristic fields identified in Appendix B. Following Lax [68], the j^{th} characteristic field is classified as genuinely nonlinear if

$$\nabla_q \lambda^{(j)} \cdot \mathbf{r}^{(j)} \neq 0 \qquad \text{for all } \mathbf{q}, \tag{C.1}$$

and linearly degenerate if

$$\nabla_q \lambda^{(j)} \cdot \mathbf{r}^{(j)} \equiv 0 \qquad \text{for all } \mathbf{q}. \tag{C.2}$$

In these expressions, the gradient operator is defined by $\nabla_q = [\partial()/\partial q_1, \ldots, \partial()/\partial q_9]$.

The following expressions are obtained for the directional derivatives using the eigenvalues given by Eq. (3.22) and the right eigenvectors given by Eqs. (3.23-3.31):

$$\begin{aligned}
&\nabla_q \lambda^{(1)} \cdot \mathbf{r}^{(1)} \equiv 0, && \nabla_q \lambda^{(2)} \cdot \mathbf{r}^{(2)} = \frac{1}{\rho_1 \phi_1} \frac{\partial}{\partial \rho_1} (\rho_1 c_1)\bigg|_{s_1}, \\
&\nabla_q \lambda^{(3)} \cdot \mathbf{r}^{(3)} = -\frac{1}{\rho_1 \phi_1} \frac{\partial}{\partial \rho_1} (\rho_1 c_1)\bigg|_{s_1}, && \nabla_q \lambda^{(4)} \cdot \mathbf{r}^{(4)} \equiv 0, \\
&\nabla_q \lambda^{(5)} \cdot \mathbf{r}^{(5)} = \frac{1}{\rho_2 \phi_2} \frac{\partial}{\partial \rho_2} (\rho_2 c_2)\bigg|_{s_2}, && \nabla_q \lambda^{(6)} \cdot \mathbf{r}^{(6)} = -\frac{1}{\rho_2 \phi_2} \frac{\partial}{\partial \rho_2} (\rho_2 c_2)\bigg|_{s_2}, \\
&\nabla_q \lambda^{(7)} \cdot \mathbf{r}^{(7)} \equiv 0, && \nabla_q \cdot \mathbf{r}^{(8)} \equiv 0, \\
&\nabla_q \lambda^{(9)} \cdot \mathbf{r}^{(9)} \equiv 0.
\end{aligned} \tag{C.3}$$

where

$$\frac{\partial}{\partial \rho_1} (\rho_1 c_1)\bigg|_{s_1} = \frac{1}{2\rho_1^3 c_1} \frac{\partial^2 P_1}{\partial \mu_1^2}\bigg|_{s_1}, \qquad \frac{\partial}{\partial \rho_2} (\rho_2 c_2)\bigg|_{s_2} = \frac{1}{2\rho_2^3 c_2} \frac{\partial^2 P_2}{\partial \mu_2^2}\bigg|_{s_2}. \tag{C.4}$$

Here, $\mu_1 (= 1/\rho_1)$ and $\mu_2 (= 1/\rho_2)$ are the specific volume for the gas and the solid, respectively. Thus, the gas entropy field, $(\lambda, \mathbf{r}, \mathbf{l})^{(1)}$, the solid entropy field, $(\lambda, \mathbf{r}, \mathbf{l})^{(4)}$, the compaction field, $(\lambda, \mathbf{r}, \mathbf{l})^{(7)}$, the number density field, $(\lambda, \mathbf{r}, \mathbf{l})^{(8)}$, and the ignition variable field, $(\lambda, \mathbf{r}, \mathbf{l})^{(9)}$, are linearly degenerate characteristic fields. Since ρ_1, ϕ_1, c_1, and ρ_2, ϕ_2, c_2 are non-negative quantities, the gas acoustic fields, $(\lambda, \mathbf{r}, \mathbf{l})^{(2)}$ and $(\lambda, \mathbf{r}, \mathbf{l})^{(3)}$, and the solid acoustic fields, $(\lambda, \mathbf{r}, \mathbf{l})^{(5)}$ and $(\lambda, \mathbf{r}, \mathbf{l})^{(6)}$, are genuinely nonlinear characteristic fields provided that $\left.\dfrac{\partial^2 P_1}{\partial \mu_1^2}\right|_{s_1} \neq 0$ and $\left.\dfrac{\partial^2 P_2}{\partial \mu_2^2}\right|_{s_2} \neq 0$, respectively. These requirements for genuine nonlinearity are identical to those obtained by Embid and Baer [31] for the two-phase model proposed by Baer and Nunziato [5]. Furthermore, these requirements are the standard convexity conditions derived for the Euler equations of gas dynamics [28].

The expressions given by Eq. (C.4) are derived as follows. Here, only the expression for the gas is considered; the expression for the solid is derived in a similar manner. First, the expression on the left hand side of Eq. (C.4) is expanded by direct application of the chain rule

$$\left.\frac{\partial}{\partial \rho_1}(\rho_1 c_1)\right|_{s_1} = c_1 + \rho_1 \left.\frac{\partial c_1}{\partial \rho_1}\right|_{s_1}. \tag{C.5}$$

Next, the definition for the gas sound speed $c_1^2 = \partial P_1/\partial \rho_1|_{s_1}$ is differentiated with respect to ρ_1, and the resulting expression is solved for $\partial c_1/\partial \rho_1|_{s_1}$ to obtain

$$\left.\frac{\partial c_1}{\partial \rho_1}\right|_{s_1} = \frac{1}{2c_1} \left.\frac{\partial^2 P_1}{\partial \rho_1^2}\right|_{s_1}. \tag{C.6}$$

Since $\mu_1 = \dfrac{1}{\rho_1}$, we have that $\dfrac{\partial}{\partial \rho_1} = -\dfrac{1}{\rho_1^2}\dfrac{\partial}{\partial \mu_1}$; consequently, we obtain the following relation:

$$\left.\frac{\partial^2 P_1}{\partial \rho_1^2}\right|_{s_1} = \frac{1}{\rho_1^4} \left.\frac{\partial^2 P_1}{\partial \mu^2}\right|_{s_1} + \frac{2}{\rho_1^3} \left.\frac{\partial P_1}{\partial \mu_1}\right|_{s_1}. \tag{C.7}$$

Making the substitution

$$\left.\frac{\partial P_1}{\partial \mu_1}\right|_{s_1} = -\rho_1^2 \left.\frac{\partial P_1}{\partial \rho_1}\right|_{s_1} = -\rho_1^2 c_1^2,$$

in Eq. (C.7), we obtain

$$\left.\frac{\partial^2 P_1}{\partial \rho_1^2}\right|_{s_1} = \frac{1}{\rho_1^4} \left.\frac{\partial^2 P_1}{\partial \mu^2}\right|_{s_1} - \frac{2}{\rho_1} c_1^2. \tag{C.8}$$

Thus, substituting Eq. (C.6) into Eq. (C.5), using the relation given in Eq. (C.8), and simplifying, the desired result is obtained:

$$\left.\frac{\partial}{\partial \rho_1}(\rho_1 c_1)\right|_{s_1} = \frac{1}{2\rho_1^3 c_1} \left.\frac{\partial^2 P_1}{\partial \mu^2}\right|_{s_1} . \tag{C.9}$$

D

DERIVATION OF THE EIGENVECTOR EXPANSION COEFFICIENTS

The eigenvector expansion coefficients $\alpha^{(j)}$ $(j = 1, \ldots, 9)$ [Eqs. (4.30-4.38)] associated with the solution of the linear two-phase Riemann problem are derived in this appendix.

To this end, we choose the $\alpha^{(j)}$ such that each component of the vector equation

$$\delta(\mathbf{q}) = \sum_{j=1}^{9} \alpha^{(j)} \mathbf{r}^{(j)} \tag{D.1}$$

is satisfied to within $O[\delta(q_j)^2]$, and such that each component of the vector equation

$$\delta(\mathbf{f}) = \sum_{j=1}^{9} \alpha^{(j)} \lambda^{(j)} \mathbf{r}^{(j)} \tag{D.2}$$

is satisfied to within $O[\delta(f_j)^2]$, where the difference operator is defined by $\delta(\bullet) \equiv (\bullet)_R - (\bullet)_L$. Substituting the expressions for $\mathbf{r}^{(j)}$ $(j = 1, \ldots, 9)$ [Eqs. (3.23-3.31)] into Eq. (D.1), and fully expanding the resulting system of equations gives

$$\begin{aligned}
\delta\left(\rho_1\phi_1\right) &= \alpha^{(1)} + \alpha^{(2)} + \alpha^{(3)} + \alpha^{(7)} \frac{\rho_1\eta_1}{\rho_2\phi_2\left((v_2 - v_1)^2 - c_1^2\right)}, && \text{(D.3)}\\
\delta\left(\rho_1\phi_1 v_1\right) &= \alpha^{(1)} v_1 + \alpha^{(2)}\left(v_1 + c_1\right) + \alpha^{(3)}\left(v_1 - c_1\right) \\
&\quad + \alpha^{(7)} \frac{\rho_1\eta_1 v_2}{\rho_2\phi_2\left((v_2 - v_1)^2 - c_1^2\right)}, && \text{(D.4)}\\
\delta\left(\rho_1\phi_1\left(e_1 + v_1^2/2\right)\right) &= \alpha^{(1)}\left(H_1 - c_1^2/\Gamma_1\right) + \alpha^{(2)}\left(H_1 + v_1 c_1\right) \\
&\quad + \alpha^{(3)}\left(H_1 - v_1 c_1\right) + \alpha^{(7)} \frac{\rho_1\eta_1\left(H_1 + v_1 v_2 - v_1^2/2\right)}{\rho_2\phi_2\left((v_2 - v_1)^2 - c_1^2\right)}, && \text{(D.5)}\\
\delta\left(\rho_2\phi_2\right) &= \alpha^{(4)} + \alpha^{(5)} + \alpha^{(6)}, && \text{(D.6)}\\
\delta\left(\rho_2\phi_2 v_2\right) &= \alpha^{(4)} v_2 + \alpha^{(5)}\left(v_2 + c_2\right) + \alpha^{(6)}\left(v_2 - c_2\right), && \text{(D.7)}\\
\delta\left(\rho_2\phi_2\left(e_2 + v_2^2/2\right)\right) &= \alpha^{(4)}\left(H_2 - c_2^2/\Gamma_2\right) + \alpha^{(5)}\left(H_2 + v_2 c_2\right) \\
&\quad + \alpha^{(6)}\left(H_2 - v_2 c_2\right) + \alpha^{(7)} \eta_2/(\phi_2\Gamma_2), && \text{(D.8)}
\end{aligned}$$

$$\delta\left(\rho_2\phi_2^2\right) = \alpha^{(4)}\phi_2 + \alpha^{(5)}\phi_2 + \alpha^{(6)}\phi_2 + \alpha^{(7)}, \tag{D.9}$$

$$\delta(n) = \alpha^{(5)}n/(\rho_2\phi_2) + \alpha^{(6)}n/(\rho_2\phi_2) + \alpha^{(8)}. \tag{D.10}$$

$$\delta\left(\rho_2\phi_2 I\right) = \alpha^{(5)}I + \alpha^{(6)}I + \alpha^{(9)}. \tag{D.11}$$

With the assumption that $\mathbf{q}_L$ is close to $\mathbf{q}_R$, the left hand sides of Eqs. (D.4), (D.5), (D.7), (D.8), (D.9), and (D.11) can be approximated by the following expressions valid to $O(\delta^2)$, respectively:

$$\begin{aligned}
\delta\left(\rho_1\phi_1 v_1\right) &\sim v_1\delta\left(\rho_1\phi_1\right) + \rho_1\phi_1\delta(v_1),\\
\delta\left(\rho_1\phi_1\left(e_1 + v_1^2/2\right)\right) &\sim \left(e_1 + v_1^2/2\right)\delta\left(\rho_1\phi_1\right) + \rho_1\phi_1\delta(e_1) + \rho_1\phi_1 v_1\delta(v_1),\\
\delta\left(\rho_2\phi_2 v_2\right) &\sim v_2\delta\left(\rho_2\phi_2\right) + \rho_2\phi_2\delta(v_2),\\
\delta\left(\rho_2\phi_2\left(e_2 + v_2^2/2\right)\right) &\sim \left(e_2 + v_2^2/2\right)\delta\left(\rho_2\phi_2\right) + \rho_2\phi_2\delta(e_2) + \rho_2\phi_2 v_2\delta(v_2),\\
\delta\left(\rho_2\phi_2^2\right) &\sim \phi_2\delta\left(\rho_2\phi_2\right) + \rho_2\phi_2\delta(\phi_2),\\
\delta\left(\rho_2\phi_2 I\right) &\sim \rho_2\phi_2\delta(I) + I\delta\left(\rho_2\phi_2\right).
\end{aligned}$$

Substituting these expressions into Eqs. (D.3-D.11), and solving the resulting coupled system of equations for $\alpha^{(1)}, \alpha^{(2)}, \ldots, \alpha^{(9)}$ gives

$$\alpha^{(1)} = \delta\left(\rho_1\phi_1\right) - \frac{1}{c_1^2}\delta\left(P_1\phi_1\right) - \frac{\rho_1\eta_1}{c_1^2}\delta(\phi_1), \tag{D.12}$$

$$\alpha^{(2)} = \frac{1}{2c_1^2}\delta\left(P_1\phi_1\right) + \frac{\rho_1\phi_1}{2c_1}\delta(v_1) + \left(\frac{v_2 - v_1}{v_2 - (v_1 + c_1)}\right)\frac{\rho_1\eta_1}{2c_1^2}\delta(\phi_1), \tag{D.13}$$

$$\alpha^{(3)} = \frac{1}{2c_1^2}\delta\left(P_1\phi_1\right) - \frac{\rho_1\phi_1}{2c_1}\delta(v_1) + \left(\frac{v_2 - v_1}{v_2 - (v_1 - c_1)}\right)\frac{\rho_1\eta_1}{2c_1^2}\delta(\phi_1), \tag{D.14}$$

$$\alpha^{(4)} = \delta\left(\rho_2\phi_2\right) - \frac{1}{c_2^2}\delta\left(P_2\phi_2\right), \tag{D.15}$$

$$\alpha^{(5)} = \frac{1}{2c_2^2}\delta\left(P_2\phi_2\right) + \frac{\rho_2\phi_2}{2c_2}\delta(v_2), \tag{D.16}$$

$$\alpha^{(6)} = \frac{1}{2c_2^2}\delta\left(P_2\phi_2\right) - \frac{\rho_2\phi_2}{2c_2}\delta(v_2), \tag{D.17}$$

$$\alpha^{(7)} = \rho_2\phi_2\delta(\phi_2), \tag{D.18}$$

$$\alpha^{(8)} = \delta(n) - \frac{n}{\rho_2\phi_2 c_2^2}\delta\left(P_2\phi_2\right), \tag{D.19}$$

$$\alpha^{(9)} = \rho_2\phi_2\delta(I) + I\delta\left(\rho_2\phi_2\right) - \frac{I}{c_2^2}\delta\left(P_2\phi_2\right). \tag{D.20}$$

It is easily checked by directly substituting the expressions for $\lambda^{(j)}$ [Eq. (3.22)], $\mathbf{r}^{(j)}$ [Eqs. 3.23-3.31)], and $\alpha^{(j)}$ [Eqs. (D.12-D.20)] into Eq. (D.2) that the required identities are satisfied to within $O[\delta(f_j)^2]$.

E

EXACT SOLUTION OF THE LINEAR RIEMANN PROBLEM

In this appendix, the exact solution of the linear two-phase Riemann problem is re-expressed in a form more suitable for the development of the approximate Riemann solution valid for arbitrary initial data $\mathbf{q}_L$ and $\mathbf{q}_R$.

To this end, the solution is re-expressed in terms of the quantities ϕ_1, v_1, e_1, ϕ_2, v_2, e_2, n, I, and the new quantities $(\rho_1\phi_1)$, $(P_1\phi_1)$, $(\rho_2\phi_2)$, and $(P_2\phi_2)$. These new quantities are introduced using the identities

$$\rho_i = \frac{(\rho_i\phi_i)}{\phi_i}, \qquad P_i = \frac{(P_i\phi_i)}{\phi_i} \qquad (i = 1, 2) \tag{E.1}$$

Also, it is necessary to relate the thermodynamic derivatives $\partial P_i/\partial\rho_i|_{e_i}$ and $\partial P_i/\partial e_i|_{\rho_i}$ $(i = 1, 2)$ to derivatives expressed in terms of these newly defined quantities. As such, we use the thermodynamic relations

$$P_1 = P_1(\rho_1, e_1), \qquad P_2 = P_2(\rho_2, e_2), \tag{E.2}$$

whose functional forms are obtained from specific thermal and caloric equations of state for each phase. Expressions relating the quantities $P_i\phi_i$ to the quantities $\rho_i\phi_i$, ϕ_i, and e_i $(i = 1, 2)$ are uniquely determined by substituting the expressions given in Eq. (E.1) into Eq. (E.2); the functional forms of the resulting expressions are

$$P_1\phi_1 = F_1(\rho_1\phi_1, \phi_1, e_1), \qquad P_2\phi_2 = F_2(\rho_2\phi_2, \phi_2, e_2), \tag{E.3}$$

where F_i $(i = 1, 2)$ are used to denote the functional relationships. Now, assuming differential changes in the state of the system, we have from Eqs. (E.2) and (E.3) that (for $i = 1, 2$)

$$d(P_i) = \left.\frac{\partial P_i}{\partial \rho_i}\right|_{e_i} d(\rho_i) + \left.\frac{\partial P_i}{\partial e_i}\right|_{\rho_i} d(e_i), \tag{E.4}$$

$$d(P_i\phi_i) = \left.\frac{\partial F_i}{\partial(\rho_i\phi_i)}\right|_{\phi_i,e_i} d(\rho_i\phi_i) + \left.\frac{\partial F_i}{\partial\phi_i}\right|_{(\rho_i\phi_i),e_i} d(\phi_i) + \left.\frac{\partial F_i}{\partial e_i}\right|_{(\rho_i\phi_i),\phi_i} d(e_i), \qquad \text{(E.5)}$$

where the operator $d(\bullet)$ denotes a differential change in the enclosed quantity. Expanding the differential operators $d(P_i\phi_i)$ and $d(\rho_i\phi_i)$ in Eq. (E.5) and solving for $d(P_i)$, equating the resulting expression to Eq. (E.4), and collecting like terms gives

$$\left(\left.\frac{\partial F_i}{\partial(\rho_i\phi_i)}\right|_{\phi_i,e_i} - \left.\frac{\partial P_i}{\partial\rho_i}\right|_{e_i}\right) d(\rho_i) + \frac{1}{\phi_1}\left(\rho_i \left.\frac{\partial F_i}{\partial(\rho_i\phi_i)}\right|_{\phi_i,e_i} + \left.\frac{\partial F_i}{\partial\phi_i}\right|_{(\rho_i\phi_i),e_i} - P_i\right) d(\phi_i)$$
$$+ \left(\frac{1}{\phi_i}\left.\frac{\partial F_i}{\partial e_i}\right|_{(\rho_i\phi_i),e_i} - \left.\frac{\partial P_i}{\partial e_i}\right|_{\rho_i}\right) d(e_i) = 0, \qquad (i = 1, 2). \qquad \text{(E.6)}$$

Since we consider arbitrary differential changes in the state of the system [i.e., $d(\rho_i) \neq 0$, $d(\phi_i) \neq 0$, and $d(e_i) \neq 0$], then in general this expression is only satisfied if the coefficients of the $d(\bullet)$ are identically zero. Thus, the following relations are obtained:

$$\left.\frac{\partial P_i}{\partial\rho_i}\right|_{e_i} = \left.\frac{\partial F_i}{\partial(\rho_i\phi_i)}\right|_{\phi_i,e_i}, \qquad \text{(E.7)}$$

$$\rho_i\left(\left.\frac{\partial P_i}{\partial\rho_i}\right|_{e_i} - \frac{P_i}{\rho_i}\right) = \rho_i\eta_i = -\left.\frac{\partial F_i}{\partial\phi_i}\right|_{(\rho_i\phi_i),e_i}, \qquad \text{(E.8)}$$

$$\left.\frac{\partial P_i}{\partial e_i}\right|_{\rho_i} = \frac{1}{\phi_i}\left.\frac{\partial F_i}{\partial e_i}\right|_{(\rho_i\phi_i),\phi_i}. \qquad \text{(E.9)}$$

Using the relationships given in Eqs. (E.1), (E.3), and (E.7-E.9), the solution of the linear Riemann problem [Eqs. (4.23) and (4.27), with the quantity $\nu_{jR} - \nu_{jL}$ replaced by $\alpha^{(j)}$] is expressed in the following equivalent form in terms of the newly defined quantities:

$$\mathbf{q}(\xi,\tau) = \mathbf{q}_L + \sum_{\lambda^{(j)}<\xi/\tau} \alpha^{(j)}\mathbf{r}^{(j)} = \mathbf{q}_R - \sum_{\lambda^{(j)}\geq\xi/\tau} \alpha^{(j)}\mathbf{r}^{(j)}, \qquad \text{(E.10)}$$

$$\mathbf{f}(\xi,\tau) = \mathbf{f}_L + \sum_{\lambda^{(j)}<\xi/\tau} \alpha^{(j)}\lambda^{(j)}\mathbf{r}^{(j)} = \mathbf{f}_R - \sum_{\lambda^{(j)}\geq\xi/\tau} \alpha^{(j)}\lambda^{(j)}\mathbf{r}^{(j)}, \qquad \text{(E.11)}$$

where

$$\lambda^{(1),(2),\ldots,(9)} = v_1,\ v_1 + c_1,\ v_1 - c_1,\ v_2,\ v_2 + c_2,\ v_2 - c_2,\ v_2,\ v_2,\ v_2, \qquad \text{(E.12)}$$

$$\mathbf{r}^{(1)} = \left[1,\ v_1,\ H_1 - c_1^2/\Gamma_1,\ 0,\ 0,\ 0,\ 0,\ 0,\ 0\right]^T, \tag{E.13}$$

$$\mathbf{r}^{(2)} = [1,\ v_1 + c_1,\ H_1 + v_1 c_1,\ 0,\ 0,\ 0,\ 0,\ 0,\ 0]^T, \tag{E.14}$$

$$\mathbf{r}^{(3)} = [1,\ v_1 - c_1,\ H_1 - v_1 c_1,\ 0,\ 0,\ 0,\ 0,\ 0,\ 0]^T, \tag{E.15}$$

$$\mathbf{r}^{(4)} = \left[0,\ 0,\ 0,\ 1,\ v_2,\ H_2 - c_2^2/\Gamma_2,\ \phi_2,\ 0,\ 0\right]^T, \tag{E.16}$$

$$\mathbf{r}^{(5)} = [0,\ 0,\ 0,\ 1,\ v_2 + c_2,\ H_2 + v_2 c_2,\ \phi_2,\ n/\left(\rho_2\phi_2\right),\ I]^T, \tag{E.17}$$

$$\mathbf{r}^{(6)} = [0,\ 0,\ 0,\ 1,\ v_2 - c_2,\ H_2 - v_2 c_2,\ \phi_2,\ n/\left(\rho_2\phi_2\right),\ I]^T, \tag{E.18}$$

$$\begin{aligned} \mathbf{r}^{(7)} = \Bigg[& -\frac{F_{1_{\phi 1}}}{(\rho_2\phi_2)\left((v_2 - v_1)^2 - c_1^2\right)},\ -\frac{F_{1_{\phi 1}} v_2}{(\rho_2\phi_2)\left((v_2 - v_1)^2 - c_1^2\right)}, \\ & -\frac{F_{1_{\phi 1}}\left(H_1 + v_1 v_2 - v_1^2\right)}{(\rho_2\phi_2)\left((v_2 - v_1)^2 - c_1^2\right)},\ 0,\ 0,\ -\frac{F_{2_{\phi 2}}}{(\rho_2\phi_2)\Gamma_2},\ 1,\ 0,\ 0\Bigg]^T, \end{aligned} \tag{E.19}$$

$$\mathbf{r}^{(8)} = [0,\ 0,\ 0,\ 0,\ 0,\ 0,\ 0,\ 1,\ 0]^T, \tag{E.20}$$

$$\mathbf{r}^{(9)} = [0,\ 0,\ 0,\ 0,\ 0,\ 0,\ 0,\ 0,\ 1]^T, \tag{E.21}$$

$$\alpha^{(1)} = \delta\left(\rho_1\phi_1\right) - \frac{1}{c_1^2}\delta\left(P_1\phi_1\right) + \frac{F_{1_{\phi 1}}}{c_1^2}\delta(\phi_1), \tag{E.22}$$

$$\alpha^{(2)} = \frac{1}{2c_1^2}\delta\left(P_1\phi_1\right) + \frac{(\rho_1\phi_1)}{2c_1}\delta(v_1) - \left(\frac{v_2 - v_1}{v_2 - (v_1 + c_1)}\right)\frac{F_{1_{\phi 1}}}{2c_1^2}\delta(\phi_1), \tag{E.23}$$

$$\alpha^{(3)} = \frac{1}{2c_1^2}\delta\left(P_1\phi_1\right) - \frac{(\rho_1\phi_1)}{2c_1}\delta(v_1) - \left(\frac{v_2 - v_1}{v_2 - (v_1 - c_1)}\right)\frac{F_{1_{\phi 1}}}{2c_1^2}\delta(\phi_1), \tag{E.24}$$

$$\alpha^{(4)} = \delta\left(\rho_2\phi_2\right) - \frac{1}{c_2^2}\delta\left(P_2\phi_2\right), \tag{E.25}$$

$$\alpha^{(5)} = \frac{1}{2c_2^2}\delta\left(P_2\phi_2\right) + \frac{(\rho_2\phi_2)}{2c_2}\delta(v_2), \tag{E.26}$$

$$\alpha^{(6)} = \frac{1}{2c_2^2}\delta\left(P_2\phi_2\right) - \frac{(\rho_2\phi_2)}{2c_2}\delta(v_2), \tag{E.27}$$

$$\alpha^{(7)} = (\rho_2\phi_2)\delta(\phi_2), \tag{E.28}$$

$$\alpha^{(8)} = \delta(n) - \frac{n}{(\rho_2\phi_2)c_2^2}\delta\left(P_2\phi_2\right), \tag{E.29}$$

$$\alpha^{(9)} = \rho_2\phi_2\delta(I) + I\delta(\rho_2\phi_2) - \frac{I}{c_2^2}\delta(P_2\phi_2), \tag{E.30}$$

and ϕ_1, c_1, c_2, H_1, H_2, Γ_1, and Γ_2 are given by

$$\phi_1 = 1 - \phi_2, \tag{E.31}$$

$$c_1^2 = \frac{(P_1\phi_1)}{(\rho_1\phi_1)^2}F_{1_{e1}} + F_{1_{\rho 1\phi 1}}, \qquad c_2^2 = \frac{(P_2\phi_2)}{(\rho_2\phi_2)^2}F_{2_{e2}} + F_{2_{\rho 2\phi 2}}, \tag{E.32}$$

$$H_1 = e_1 + \frac{v_1^2}{2} + \frac{(P_1\phi_1)}{(\rho_1\phi_1)}, \qquad H_2 = e_2 + \frac{v_2^2}{2} + \frac{(P_2\phi_2)}{(\rho_2\phi_2)}, \tag{E.33}$$

$$\Gamma_1 = \frac{1}{(\rho_1\phi_1)} F_{1_{e1}}, \qquad \Gamma_2 = \frac{1}{(\rho_2\phi_2)} F_{2_{e2}}. \tag{E.34}$$

In these equations, the quantities $F_{i_{\rho i\phi i}}$, $F_{i_{\phi i}}$, and $F_{i_{ei}}$ $(i = 1, 2)$ denote the derivatives $\left.\frac{\partial F_i}{\partial(\rho_i\phi_i)}\right|_{\phi_i, e_i}$, $\left.\frac{\partial F_i}{\partial\phi_i}\right|_{(\rho_i\phi_i), e_i}$, and $\left.\frac{\partial F_i}{\partial e_i}\right|_{(\rho_i\phi_i), \phi_i}$ $(i = 1, 2)$, respectively.

F

AVERAGES FOR THE APPROXIMATE RIEMANN SOLUTION

In this appendix, Eqs. (4.39-4.62) are solved for the average quantities $\widetilde{\rho_1\phi_1}$, $\tilde{v}_1$, $\tilde{e}_1$, $\tilde{H}_1$, $\tilde{F}_{1_{\rho 1\phi 1}}$, $\tilde{F}_{1_{\phi 1}}$, $\tilde{F}_{1_{e1}}$, $\widetilde{\rho_2\phi_2}$, $\tilde{\phi}_2$, $\tilde{v}_2$, $\tilde{e}_2$, $\tilde{H}_2$, $\tilde{F}_{2_{\rho 2\phi 2}}$, $\tilde{F}_{2_{\phi 2}}$, $\tilde{F}_{2_{e2}}$, $\tilde{n}$, and $\tilde{I}$. To this end, it is convenient to first substitute the expressions given by Eqs. (4.41-4.50) into Eq. (4.39), and to fully expand the resulting expressions:

$$\Delta\left(\rho_1\phi_1\right) = \tilde{\alpha}^{(1)} + \tilde{\alpha}^{(2)} + \tilde{\alpha}^{(3)} - \frac{\tilde{\alpha}^{(7)}\tilde{F}_{1_{\phi 1}}}{\widetilde{\rho_2\phi_2}[(\tilde{v}_2-\tilde{v}_1)^2-\tilde{c}_1^2]}, \tag{F.1}$$

$$\begin{aligned}\Delta\left(\rho_1\phi_1 v_1\right) &= \tilde{\alpha}^{(1)}\tilde{v}_1 + \tilde{\alpha}^{(2)}\left(\tilde{v}_1+\tilde{c}_1\right) + \tilde{\alpha}^{(3)}\left(\tilde{v}_1-\tilde{c}_1\right) \\ &\quad - \frac{\tilde{\alpha}^{(7)}\tilde{v}_2\tilde{F}_{1_{\phi 1}}}{\widetilde{\rho_2\phi_2}[(\tilde{v}_2-\tilde{v}_1)^2-\tilde{c}_1^2]},\end{aligned} \tag{F.2}$$

$$\begin{aligned}\Delta\left(\rho_1\phi_1\left(e_1+v_1^2/2\right)\right) &= \tilde{\alpha}^{(1)}\left(\tilde{H}_1-\tilde{c}_1^2/\tilde{\Gamma}_1\right) + \tilde{\alpha}^{(2)}\left(\tilde{H}_1+\tilde{v}_1\tilde{c}_1\right) + \tilde{\alpha}^{(3)}\left(\tilde{H}_1-\tilde{v}_1\tilde{c}_1\right) \\ &\quad - \frac{\tilde{\alpha}^{(7)}(\tilde{H}_1+\tilde{v}_1\tilde{v}_2-\tilde{v}_1^2)\tilde{F}_{1_{\phi 1}}}{\widetilde{\rho_2\phi_2}[(\tilde{v}_2-\tilde{v}_1)^2-\tilde{c}_1^2]}\end{aligned} \tag{F.3}$$

$$\Delta\left(\rho_2\phi_2\right) = \tilde{\alpha}^{(4)} + \tilde{\alpha}^{(5)} + \tilde{\alpha}^{(6)}, \tag{F.4}$$

$$\Delta\left(\rho_2\phi_2 v_2\right) = \tilde{\alpha}^{(4)}\tilde{v}_2 + \tilde{\alpha}^{(5)}\left(\tilde{v}_2+\tilde{c}_2\right) + \tilde{\alpha}^{(6)}\left(\tilde{v}_2-\tilde{c}_2\right), \tag{F.5}$$

$$\begin{aligned}\Delta\left(\rho_2\phi_2\left(e_2+v_2^2/2\right)\right) &= \tilde{\alpha}^{(4)}\left(\tilde{H}_2-\tilde{c}_2^2/\tilde{\Gamma}_2\right) + \tilde{\alpha}^{(5)}\left(\tilde{H}_2+\tilde{v}_2\tilde{c}_2\right) \\ &\quad + \tilde{\alpha}^{(6)}\left(\tilde{H}_2-\tilde{v}_2\tilde{c}_2\right) - \frac{\tilde{\alpha}^{(7)}\tilde{F}_{2_{\phi 2}}}{\widetilde{\rho_2\phi_2}\tilde{\Gamma}_2},\end{aligned} \tag{F.6}$$

$$\Delta\left(\rho_2\phi_2^2\right) = \tilde{\alpha}^{(4)}\tilde{\phi}_2 + \tilde{\alpha}^{(5)}\tilde{\phi}_2 + \tilde{\alpha}^{(6)}\tilde{\phi}_2 + \tilde{\alpha}^{(7)}, \tag{F.7}$$

$$\Delta(n) = \tilde{\alpha}^{(5)}\tilde{n}/\widetilde{\rho_2\phi_2} + \tilde{\alpha}^{(6)}\tilde{n}/\widetilde{\rho_2\phi_2} + \tilde{\alpha}^{(8)}, \tag{F.8}$$

$$\Delta(\rho_2\phi_2 I) = \tilde{\alpha}^{(5)}\tilde{I} + \tilde{\alpha}^{(6)}\tilde{I} + \tilde{\alpha}^{(9)}. \tag{F.9}$$

Likewise, we substitute the expressions given by Eqs. (4.41-4.50) into Eq. (4.40) and fully expand the resulting expressions:

$$\Delta\left(\rho_1\phi_1 v_1\right) = \tilde{\alpha}^{(1)}\tilde{v}_1 + \tilde{\alpha}^{(2)}\left(\tilde{v}_1+\tilde{c}_1\right) + \tilde{\alpha}^{(3)}\left(\tilde{v}_1-\tilde{c}_1\right)$$

$$-\frac{\tilde{\alpha}^{(7)}\tilde{v}_2\tilde{F}_{1_{\phi 1}}}{\widetilde{\rho_2\phi_2}[(\tilde{v}_2-\tilde{v}_1)^2-\tilde{c}_1^2]}, \tag{F.10}$$

$$\begin{aligned}
\Delta\left(\rho_1\phi_1 v_1^2+P_1\phi_1\right) &= \tilde{\alpha}^{(1)}\tilde{v}_1^2+\tilde{\alpha}^{(2)}\left(\tilde{v}_1+\tilde{c}_1\right)^2+\tilde{\alpha}^{(3)}\left(\tilde{v}_1-\tilde{c}_1\right)^2 \\
&\quad -\frac{\tilde{\alpha}^{(7)}\tilde{v}_2^2\tilde{F}_{1_{\phi 1}}}{\widetilde{\rho_2\phi_2}[(\tilde{v}_2-\tilde{v}_1)^2-\tilde{c}_1^2]}, \qquad \text{(F.11)}\\
\Delta\left(\rho_1\phi_1 v_1\left(e_1+v_1^2/2+P_1/\rho_1\right)\right) &= \tilde{\alpha}^{(1)}\tilde{v}_1\left(\tilde{H}_1-\tilde{c}_1^2/\tilde{\Gamma}_1\right)+\tilde{\alpha}^{(2)}\left(\tilde{v}_1+\tilde{c}_1\right)\left(\tilde{H}_1+\tilde{v}_1\tilde{c}_1\right) \\
&\quad +\tilde{\alpha}^{(3)}\left(\tilde{v}_1-\tilde{c}_1\right)\left(\tilde{H}_1-\tilde{v}_1\tilde{c}_1\right) \\
&\quad -\frac{\tilde{\alpha}^{(7)}\left(\tilde{H}_1+\tilde{v}_1\tilde{v}_2-\tilde{v}_1^2\right)\tilde{F}_{1_{\phi 1}}}{\widetilde{\rho_2\phi_2}[(\tilde{v}_2-\tilde{v}_1)^2-\tilde{c}_1^2]}, \qquad \text{(F.12)}\\
\Delta\left(\rho_2\phi_2 v_2\right) &= \tilde{\alpha}^{(4)}\tilde{v}_2+\tilde{\alpha}^{(5)}\left(\tilde{v}_2+\tilde{c}_2\right)+\tilde{\alpha}^{(6)}\left(\tilde{v}_2-\tilde{c}_2\right), \qquad \text{(F.13)}\\
\Delta\left(\rho_2\phi_2 v_2^2+P_2\phi_2\right) &= \tilde{\alpha}^{(4)}\tilde{v}_2^2+\tilde{\alpha}^{(5)}\left(\tilde{v}_2+\tilde{c}_2\right)^2+\tilde{\alpha}^{(6)}\left(\tilde{v}_2-\tilde{c}_2\right)^2, \qquad \text{(F.14)}\\
\Delta\left(\rho_2\phi_2 v_2\left(e_2+v_2^2/2+P_2/\rho_2\right)\right) &= \tilde{\alpha}^{(4)}\tilde{v}_2\left(\tilde{H}_2-\tilde{c}_2^2/\tilde{\Gamma}_2\right)+\tilde{\alpha}^{(5)}\left(\tilde{v}_2+\tilde{c}_2\right)\left(\tilde{H}_2+\tilde{v}_2\tilde{c}_2\right) \\
&\quad +\tilde{\alpha}^{(6)}\left(\tilde{v}_2-\tilde{c}_2\right)\left(\tilde{H}_2-\tilde{v}_2\tilde{c}_2\right)-\frac{\tilde{\alpha}^{(7)}\tilde{F}_{2_{\phi 2}}}{\widetilde{\rho_2\phi_2}\tilde{\Gamma}_2}, \qquad \text{(F.15)}\\
\Delta\left(\rho_2\phi_2^2 v_2\right) &= \tilde{\alpha}^{(4)}\tilde{v}_2\tilde{\phi}_2+\tilde{\alpha}^{(5)}\left(\tilde{v}_2+\tilde{c}_2\right)\tilde{\phi}_2 \\
&\quad +\tilde{\alpha}^{(6)}\left(\tilde{v}_2-\tilde{c}_2\right)\tilde{\phi}_2+\tilde{\alpha}^{(7)}\tilde{v}_2, \qquad \text{(F.16)}\\
\Delta\left(v_2 n\right) &= \tilde{\alpha}^{(5)}\left(\tilde{v}_2+\tilde{c}_2\right)\tilde{n}/\widetilde{\rho_2\phi_2} \\
&\quad +\tilde{\alpha}^{(6)}\left(\tilde{v}_2-\tilde{c}_2\right)\tilde{n}/\widetilde{\rho_2\phi_2}+\tilde{\alpha}^{(8)}\tilde{v}_2, \qquad \text{(F.17)}\\
\Delta(\rho_2\phi_2 I v_2) &= \tilde{\alpha}^{(5)}\left(\tilde{v}_2+\tilde{c}_2\right)\tilde{I}+\tilde{\alpha}^{(6)}\left(\tilde{v}_2-\tilde{c}_2\right)\tilde{I}+\tilde{\alpha}^{(9)}\tilde{v}_2. \qquad \text{(F.18)}
\end{aligned}$$

Equations (F.4-F.9) and (F.13-F.18) are first solved for $\widetilde{\rho_2\phi_2}$, $\tilde{\phi}_2$, $\tilde{v}_2$, $\tilde{e}_2$, $\tilde{H}_2$, $\tilde{n}$, and $\tilde{I}$ in Section F.1. Next, Eqs. (F.1-F.3) and (F.10-F.12) are solved for $\widetilde{\rho_1\phi_1}$, $\tilde{v}_1$, $\tilde{e}_1$, and $\tilde{H}_1$ in Section F.2. Lastly, expressions for $\tilde{F}_{1_{\rho 1\phi 1}}$, $\tilde{F}_{1_{\phi 1}}$, $\tilde{F}_{1_{e1}}$, $\tilde{F}_{2_{\rho 2\phi 2}}$, $\tilde{F}_{2_{\phi 2}}$, and $\tilde{F}_{2_{e2}}$ are postulated in Section F.3 to complete the construction of the approximate solution.

F.1 Averages for the Solid Quantities

In this section, Eqs. (F.4-F.9) and Eqs. (F.13-F.18) are solved for $\widetilde{\rho_2\phi_2}$, $\tilde{\phi}_2$, $\tilde{v}_2$, $\tilde{e}_2$, $\tilde{H}_2$, $\tilde{n}$, and $\tilde{I}$. It is noted that by substituting the expressions for $\tilde{\alpha}^{(4)}$, $\tilde{\alpha}^{(5)}$, $\tilde{\alpha}^{(6)}$, and $\tilde{\alpha}^{(8)}$ [Eqs. (4.54-4.56) and (4.58), respectively] into Eqs. (F.4) and (F.8), that the latter two equations are identically satisfied by any averages we care to define. Also, it is noted that Eqs. (F.5) and (F.13) are identical expressions. Therefore, only Eqs. (F.5-F.7), (F.9), and (F.14-F.18) can be considered when determining the required average quantities for the solid phase. To this end, the following relations will prove useful:

$$\tilde{\alpha}^{(4)} + \tilde{\alpha}^{(5)} + \tilde{\alpha}^{(6)} = \Delta(\rho_2\phi_2), \tag{F.19}$$

$$\tilde{\alpha}^{(5)} + \tilde{\alpha}^{(6)} = \frac{1}{\tilde{c}_2^2}\Delta(P_2\phi_2), \tag{F.20}$$

$$\tilde{\alpha}^{(5)} - \tilde{\alpha}^{(6)} = \frac{\widetilde{\rho_2\phi_2}}{\tilde{c}_2}\Delta(v_2). \tag{F.21}$$

First, we rearrange terms in Eq. (F.5) to get

$$\Delta\left(\rho_2\phi_2v_2\right) = \tilde{v}_2\left(\tilde{\alpha}^{(4)} + \tilde{\alpha}^{(5)} + \tilde{\alpha}^{(6)}\right) + \tilde{c}_2\left(\tilde{\alpha}^{(5)} - \tilde{\alpha}^{(6)}\right).$$

Substituting the expressions given by Eqs. (F.19) and (F.21) into the above equation, we obtain

$$\Delta\left(\rho_2\phi_2v_2\right) = \tilde{v}_2\Delta\left(\rho_2\phi_2\right) + \widetilde{\rho_2\phi_2}\Delta(v_2).$$

This equation can be solved for $\widetilde{\rho_2\phi_2}$ to give

$$\widetilde{\rho_2\phi_2} = \frac{\Delta\left(\rho_2\phi_2v_2\right) - \tilde{v}_2\Delta\left(\rho_2\phi_2\right)}{\Delta(v_2)}. \tag{F.22}$$

Next, we expand the left hand side of Eq. (F.14) and rearrange terms on the right hand side of this same equation to get

$$\Delta\left(\rho_2\phi_2v_2^2\right)+\Delta\left(P_2\phi_2\right) = \tilde{v}_2^2\left(\tilde{\alpha}^{(4)} + \tilde{\alpha}^{(5)} + \tilde{\alpha}^{(6)}\right)+2\tilde{v}_2\tilde{c}_2\left(\tilde{\alpha}^{(5)} - \tilde{\alpha}^{(6)}\right)+\tilde{c}_2^2\left(\tilde{\alpha}^{(5)} + \tilde{\alpha}^{(6)}\right).$$

Substituting the expressions given by Eqs. (F.19-F.21) into this equation and simplifying the result gives

$$\Delta\left(\rho_2\phi_2v_2^2\right) = \tilde{v}_2^2\Delta\left(\rho_2\phi_2\right) + 2\widetilde{\rho_2\phi_2}\tilde{v}_2\Delta(v_2). \tag{F.23}$$

Substituting the expression for $\widetilde{\rho_2\phi_2}$ [Eq. (F.22)] into Eq. (F.23) and rearranging terms yields the following quadratic equation for $\tilde{v}_2$:

$$\Delta\left(\rho_2\phi_2\right)\tilde{v}_2^2 - 2\Delta\left(\rho_2\phi_2v_2\right)\tilde{v}_2 + \Delta\left(\rho_2\phi_2v_2^2\right) = 0.$$

This equation has two solutions given by

$$\tilde{v}_2 = \frac{\Delta\left(\rho_2\phi_2 v_2\right) \pm \sqrt{[\Delta(\rho_2\phi_2 v_2)]^2 - \Delta(\rho_2\phi_2)\Delta(\rho_2\phi_2 v_2^2)}}{\Delta(\rho_2\phi_2)}.$$

Performing the difference operations $\Delta(\bullet)$ $[\equiv (\bullet)_R - (\bullet)_L]$ in these solutions and simplifying the result gives the following expression for the solution corresponding to positive (+) root:

$$\tilde{v}_2 = \frac{\sqrt{\rho_{2L}\phi_{2L}}\,v_{2L} - \sqrt{\rho_{2R}\phi_{2R}}\,v_{2R}}{\sqrt{\rho_{2L}\phi_{2L}} - \sqrt{\rho_{2R}\phi_{2R}}}.$$

Likewise, the following expression is obtained for the solution corresponding to the negative (−) root:

$$\boxed{\tilde{v}_2 = \frac{\sqrt{\rho_{2L}\phi_{2L}}\,v_{2L} + \sqrt{\rho_{2R}\phi_{2R}}\,v_{2R}}{\sqrt{\rho_{2L}\phi_{2L}} + \sqrt{\rho_{2R}\phi_{2R}}}.} \tag{F.24}$$

Clearly, in order to obtain a physically meaningful average we must choose the solution corresponding to the negative root. Now, substituting this expression for $\tilde{v}_2$ into Eq. (F.22) and simplifying the result yields

$$\boxed{\widetilde{\rho_2\phi_2} = \sqrt{\rho_{2L}\rho_{2R}\phi_{2L}\phi_{2R}}.} \tag{F.25}$$

Next, we multiply Eq. (F.7) by $\tilde{v}_2$ and subtract the result from Eq. (F.16) to obtain

$$\begin{aligned} \Delta\left(\rho_2\phi_2^2 v_2\right) - \tilde{v}_2\left(\rho_2\phi_2^2\right) &= \tilde{\phi}_2\tilde{c}_2\left(\tilde{\alpha}^{(5)} - \tilde{\alpha}^{(6)}\right) \\ &= \widetilde{\rho_2\phi_2}\,\tilde{\phi}_2\Delta(v_2). \end{aligned}$$

This equation can be solved for $\tilde{\phi}_2$ to give

$$\tilde{\phi}_2 = \frac{\Delta\left(\rho_2\phi_2^2 v_2\right) - \tilde{v}_2\Delta\left(\rho_2\phi_2^2\right)}{\widetilde{\rho_2\phi_2}\,\Delta(v_2)}.$$

Since exact expressions for the averages $\tilde{v}_2$ and $\widetilde{\rho_2\phi_2}$ are known, this equation for $\tilde{\phi}_2$ reduces to

$$\boxed{\tilde{\phi}_2 = \frac{\sqrt{\rho_{2L}\phi_{2L}}\,\phi_{2L} + \sqrt{\rho_{2R}\phi_{2R}}\,\phi_{2R}}{\sqrt{\rho_{2L}\phi_{2L}} + \sqrt{\rho_{2R}\phi_{2R}}}.} \tag{F.26}$$

Similarly, we multiply Eq. (F.9) by $\tilde{v}_2$, and subtract the result from Eq. (F.18) to obtain

$$\begin{aligned}\Delta\left(\rho_2\phi_2 I v_2\right) - \tilde{v}_2\Delta\left(\rho_2\phi_2 I\right) &= \tilde{I}\tilde{c}_2\left(\alpha^{(5)} - \alpha^{(6)}\right)\\ &= \widetilde{\rho_2\phi_2}\tilde{\phi}_2\Delta(v_2).\end{aligned}$$

Solving this equation for $\tilde{I}$, substituting in the definitions for $\tilde{v}_2$ and $\widetilde{\rho_2\phi_2}$, and simplifying the result gives

$$\boxed{\tilde{I} = \frac{\sqrt{\rho_{2L}\phi_{2L}}I_L + \sqrt{\rho_{2R}\phi_{2R}}I_R}{\sqrt{\rho_{2L}\phi_{2L}} + \sqrt{\rho_{2R}\phi_{2R}}}.} \tag{F.27}$$

Next, we multiply Eq. (F.8) by $\tilde{v}_2$ and subtract the result from Eq. (F.17) to obtain

$$\begin{aligned}\Delta\left(v_2 n\right) - \tilde{v}_2\Delta(n) &= \frac{\tilde{c}_2\tilde{n}}{\widetilde{\rho_2\phi_2}}\left(\tilde{\alpha}^{(5)} - \tilde{\alpha}^{(6)}\right)\\ &= \tilde{n}\Delta(v_2).\end{aligned}$$

Solving this equation for $\tilde{n}$, substituting in the definition for $\tilde{v}_2$, and simplifying the result gives

$$\boxed{\tilde{n} = \frac{\sqrt{\rho_{2L}\phi_{2L}}n_R + \sqrt{\rho_{2R}\phi_{2R}}n_L}{\sqrt{\rho_{2L}\phi_{2L}} + \sqrt{\rho_{2R}\phi_{2R}}}.} \tag{F.28}$$

Now, we consider Eqs. (F.6) and (F.15). Expanding the left hand side of Eq. (F.6) and rearranging terms on the right hand side of this same equation yields

$$\begin{aligned}\Delta\left(\rho_2\phi_2 e_2\right) + \Delta\left(\rho_2\phi_2 v_2^2/2\right) = \tilde{H}_2\left(\tilde{\alpha}^{(4)} + \tilde{\alpha}^{(5)} + \tilde{\alpha}^{(6)}\right) - \frac{\tilde{\alpha}^{(4)}\tilde{c}_2^2}{\tilde{\Gamma}_2}\\ + \tilde{v}_2\tilde{c}_2\left(\tilde{\alpha}^{(5)} - \tilde{\alpha}^{(6)}\right) - \frac{\tilde{\alpha}^{(7)}\tilde{F}_{2_{\phi 2}}}{\widetilde{\rho_2\phi_2}\tilde{\Gamma}_2}.\end{aligned} \tag{F.29}$$

Substituting the expressions given by Eqs. (F.19) and (F.21), and the expressions for $\tilde{\alpha}^{(4)}$ [Eq. (4.33)] and $\tilde{\alpha}^{(7)}$ [Eq. (4.36)] into Eq. (F.29), using the second expression in Eq. (4.61) to replace $\tilde{H}_2$ in favor of $\widetilde{\rho_2\phi_2}$, $\tilde{v}_2$, $\widetilde{P_2\phi_2}$, and $\tilde{e}_2$, and recognizing that the second term on the left hand side of Eq. (F.29) is simply the expression given in Eq. (F.23) divided by two, we obtain the following expression after performing some simple algebra:

$$\Delta\left(\rho_2\phi_2 e_2\right) - \tilde{e}_2\Delta(\rho_2\phi_2) = \left(\frac{\widetilde{P_2\phi_2}}{\widetilde{\rho_2\phi_2}} - \frac{\tilde{c}_2^2}{\tilde{\Gamma}_2}\right)\Delta(\rho_2\phi_2) + \frac{1}{\tilde{\Gamma}_2}\Delta(P_2\phi_2) - \frac{\tilde{F}_{2_{\phi 2}}}{\tilde{\Gamma}_2}\Delta(\phi_2). \quad \text{(F.30)}$$

Now, upon using the second expression in Eq. (4.60) to replace $\tilde{c}_2^2$ in Eq. (F.30) in favor of $\widetilde{\rho_2\phi_2}$, $\widetilde{P_2\phi_2}$, $\tilde{F}_{2_{\rho 2\phi 2}}$, and $\tilde{F}_{2_{e2}}$, using the second expression in Eq. (4.62) to replace $\tilde{\Gamma}_2$ in Eq. (F.30) in favor of $\widetilde{\rho_2\phi_2}$ and $\tilde{F}_{2_{e2}}$, subtracting the term $\widetilde{\rho_2\phi_2}\Delta(e_2)$ from both sides of Eq. (F.30), and simplifying the result, we obtain

$$\begin{aligned}\Delta(\rho_2\phi_2 e_2) - \tilde{e}_2\Delta(\rho_2\phi_2) - \widetilde{\rho_2\phi_2}\Delta(e_2)& \\ = \frac{\widetilde{\rho_2\phi_2}}{\tilde{F}_{2_{e2}}}\Delta(P_2\phi_2) - \frac{\widetilde{\rho_2\phi_2}\tilde{F}_{2_{\rho 2\phi 2}}}{\tilde{F}_{2_{e2}}}\Delta(\rho_2\phi_2) - \frac{\widetilde{\rho_2\phi_2}\tilde{F}_{2_{\phi 2}}}{\tilde{F}_{2_{e2}}}\Delta(\phi_2) - \widetilde{\rho_2\phi_2}\Delta(e_2). \quad &\text{(F.31)}\end{aligned}$$

At this point, a number of assumptions can be made in order to define $\tilde{F}_{2_{\rho 2\phi 2}}$, $\tilde{F}_{2_{\phi 2}}$, $\tilde{F}_{2_{e2}}$, and $\tilde{e}_2$. Following the analysis of Glaister [37], it is plausible to choose

$$\Delta\left(\rho_2\phi_2 e_2\right) - \tilde{e}_2\left(\rho_2\phi_2\right) - \widetilde{\rho_2\phi_2}\Delta(e_2) = 0, \quad \text{(F.32)}$$

in which case the right hand side of Eq. (F.31) reduces to

$$\Delta\left(P_2\phi_2\right) - \tilde{F}_{2_{\rho 2\phi 2}}\Delta(\rho_2\phi_2) - \tilde{F}_{2_{\phi 2}}\Delta(\phi_2) - \tilde{F}_{2_{e2}}\Delta(e_2) = 0. \quad \text{(F.33)}$$

Equation (F.32) can then be solved for $\tilde{e}_2$:

$$\tilde{e}_2 = \frac{\Delta(\rho_2\phi_2 e_2) - \widetilde{\rho_2\phi_2}\Delta(e_2)}{\Delta(\rho_2\phi_2)}.$$

In this equation, we replace the term $\widetilde{\rho_2\phi_2}$ with the expression given by Eq. (F.25) and simplify the result to get

$$\boxed{\tilde{e}_2 = \frac{\sqrt{\rho_{2L}\phi_{2L}}e_{2L} + \sqrt{\rho_{2R}\phi_{2R}}e_{2R}}{\sqrt{\rho_{2L}\phi_{2L}} + \sqrt{\rho_{2R}\phi_{2R}}}.} \quad \text{(F.34)}$$

It remains to define the quantities $\tilde{F}_{2_{\rho 2\phi 2}}$, $\tilde{F}_{2_{\phi 2}}$, and $\tilde{F}_{2_{e2}}$ such that Eq. (F.33) is identically satisfied. Definitions for these quantities are postulated in a following section.

Lastly, we multiply Eq. (F.6) by $\tilde{v}_2$, subtract the result from Eq. (F.15), and simplify the resulting expression to get

$$\begin{aligned}\Delta\left(\rho_2\phi_2 v_2\left(e_2+v_2^2/2+P_2/\rho_2\right)\right) - \tilde{v}_2\Delta\left(\rho_2\phi_2\left(e_2+v_2^2/2\right)\right)& \\ = \tilde{c}_2\tilde{H}_2\left(\tilde{\alpha}^{(5)}-\tilde{\alpha}^{(6)}\right)+\tilde{v}_2\tilde{c}_2^2\left(\tilde{\alpha}^{(5)}+\tilde{\alpha}^{(6)}\right).&\end{aligned} \tag{F.35}$$

Upon substituting the expressions given by Eqs. (F.20) and (F.21) into Eq. (F.35), re-expressing the left hand side of Eq. (F.35) in terms of the total enthalpy of the solid H_2 $(= e_2 + v_2^2/2 + P_2/\rho_2)$, and simplifying the result, we obtain

$$\Delta\left(\rho_2\phi_2 v_2 H_2\right) - \tilde{v}_2\Delta\left(\rho_2\phi_2(H_2-P_2/\rho_2)\right) = \widetilde{\rho_2\phi_2}\tilde{H}_2\Delta(v_2)+\tilde{v}_2\Delta(P_2\phi_2). \tag{F.36}$$

Now, expanding the second term on the left hand side of this equation and canceling the appropriate terms gives

$$\Delta\left(\rho_2\phi_2 v_2 H_2\right) - \tilde{v}_2\Delta\left(\rho_2\phi_2 H_2\right) = \widetilde{\rho_2\phi_2}\tilde{H}_2\Delta(v_2).$$

This equation is solved for $\tilde{H}_2$ yielding

$$\tilde{H}_2 = \frac{\Delta(\rho_2\phi_2 v_2 H_2) - \tilde{v}_2\Delta(\rho_2\phi_2 H_2)}{\widetilde{\rho_2\phi_2}\Delta(v_2)}.$$

Since $\widetilde{\rho_2\phi_2}$, $\tilde{\phi}_2$, and $\tilde{v}_2$ are all known quantities, this expression for $\tilde{H}_2$ reduces to

$$\boxed{\tilde{H}_2 = \frac{\sqrt{\rho_{2L}\phi_{2L}}H_{2L}+\sqrt{\rho_{2R}\phi_{2R}}H_{2R}}{\sqrt{\rho_{2L}\phi_{2L}}+\sqrt{\rho_{2R}\phi_{2R}}}.} \tag{F.37}$$

In summary, definitions for the solid phase average quantities $\widetilde{\rho_2\phi_2}$, $\tilde{\phi}_2$, $\tilde{v}_2$, $\tilde{e}_2$, $\tilde{H}_2$, $\tilde{n}$, and $\tilde{I}$ are given by Eqs. (F.25), (F.26), (F.24), (F.34), (F.37), (F.28), and (F.27), respectively.

F.2 Averages for the Gas Quantities

In this section, Eqs. (F.1-F.3) and Eqs. (F.10-F.12) are solved for $\widetilde{\rho_1\phi_1}$, $\tilde{v}_1$, $\tilde{e}_1$, and $\tilde{H}_1$. It is noted, by substituting the expressions for $\tilde{\alpha}^{(1)}$, $\tilde{\alpha}^{(2)}$, $\tilde{\alpha}^{(3)}$, and $\tilde{\alpha}^{(7)}$ into Eq.

(F.1), that Eq. (F.1) is satisfied by any averages we care to define; also, Eqs. (F.2) and (F.10) are identical expressions. Therefore, only Eqs. (F.2), (F.3), (F.11), and (F.12) can be used to determine the required averages for the gas phase. In defining these average quantities, the following relations will prove useful:

$$\tilde{\alpha}^{(1)} + \tilde{\alpha}^{(2)} + \tilde{\alpha}^{(3)} = \Delta(\rho_1\phi_1) - \frac{\tilde{F}_{1_{\phi_1}}}{(\tilde{v}_2 - \tilde{v}_1)^2 - \tilde{c}_1^2}\Delta(\phi_1), \tag{F.38}$$

$$\tilde{\alpha}^{(2)} + \tilde{\alpha}^{(3)} = \frac{1}{\tilde{c}_1^2}\Delta(P_1\phi_1) - \frac{(\tilde{v}_2 - \tilde{v}_1)^2\tilde{F}_{1_{\phi_1}}}{\tilde{c}_1^2[(\tilde{v}_2 - \tilde{v}_1)^2 - \tilde{c}_1^2]}\Delta(\phi_1), \tag{F.39}$$

$$\tilde{\alpha}^{(2)} - \tilde{\alpha}^{(3)} = \frac{\widetilde{\rho_1\phi_1}}{\tilde{c}_1}\Delta(v_1) - \frac{(\tilde{v}_2 - \tilde{v}_1)\tilde{F}_{1_{\phi_1}}}{\tilde{c}_1[(\tilde{v}_2 - \tilde{v}_1)^2 - \tilde{c}_1^2]}\Delta(\phi_1). \tag{F.40}$$

First, we rearrange Eq. (F.2) to get

$$\Delta\left(\rho_1\phi_1 v_1\right) = \tilde{v}_1\left(\tilde{\alpha}^{(1)} + \tilde{\alpha}^{(2)} + \tilde{\alpha}^{(3)}\right) + \tilde{c}_1\left(\tilde{\alpha}^{(2)} - \tilde{\alpha}^{(3)}\right) - \frac{\tilde{\alpha}^{(7)}\tilde{v}_2\tilde{F}_{1_{\phi_1}}}{\widetilde{\rho_2\phi_2}[(\tilde{v}_2 - \tilde{v}_1)^2 - \tilde{c}_1^2]}.$$

By substituting the expressions given by Eqs. (F.38) and (F.40) and the expression for $\tilde{\alpha}^{(7)}$ [Eq. (4.36)] into the above equation, and simplifying the resulting expression [recognizing that $\Delta(\phi_2) = -\Delta(\phi_1)$], we obtain

$$\Delta\left(\rho_1\phi_1 v_1\right) = \tilde{v}_1\Delta\left(\rho_1\phi_1\right) + \widetilde{\rho_1\phi_1}\Delta(v_1).$$

This equation is solved for $\widetilde{\rho_1\phi_1}$ to obtain

$$\widetilde{\rho_1\phi_1} = \frac{\Delta\left(\rho_1\phi_1 v_1\right) - \tilde{v}_1\Delta\left(\rho_1\phi_1\right)}{\Delta(v_1)}. \tag{F.41}$$

Also, expanding the left hand side of Eq. (F.11) and rearranging the terms on the right hand side of this same equation gives

$$\begin{aligned}\Delta\left(\rho_1\phi_1 v_1^2\right) + \Delta\left(P_1\phi_1\right) = {} & \tilde{v}_1^2\left(\tilde{\alpha}^{(1)} + \tilde{\alpha}^{(2)} + \tilde{\alpha}^{(3)}\right) + 2\tilde{v}_1\tilde{c}_1\left(\tilde{\alpha}^{(2)} - \tilde{\alpha}^{(3)}\right) \\ & + \tilde{c}_1^2\left(\tilde{\alpha}^{(2)} + \tilde{\alpha}^{(3)}\right) - \frac{\tilde{\alpha}^{(7)}\tilde{v}_2^2\tilde{F}_{1_{\phi_1}}}{\widetilde{\rho_2\phi_2}[(\tilde{v}_2 - \tilde{v}_1)^2 - \tilde{c}_1^2]}.\end{aligned}$$

Now, substituting in the expressions given by Eqs. (F.38-F.40), and the expression for $\tilde{\alpha}^{(7)}$ [Eq. (4.36)] into the above expression, the following result is obtained upon simplifying:

$$\Delta\left(\rho_1\phi_1 v_1^2\right) = \tilde{v}_1^2\Delta\left(\rho_1\phi_1\right) + 2\widetilde{\rho_1\phi_1}\tilde{v}_1\Delta(v_1). \tag{F.42}$$

Substituting the expression for $\widetilde{\rho_1\phi_1}$ [Eq. (F.41)] into this expression and rearranging terms results in a quadratic equation for $\tilde{v}_1$:

$$\tilde{v}_1^2 \Delta\left(\rho_1\phi_1\right) - 2\tilde{v}_1 \Delta\left(\rho_1\phi_1 v_1\right) + \Delta\left(\rho_1\phi_1 v_1^2\right) = 0.$$

This equation has two solutions given by

$$\tilde{v}_1 = \frac{\Delta\left(\rho_1\phi_1 v_1\right) \pm \sqrt{[\Delta(\rho_1\phi_1 v_1)]^2 - \Delta(\rho_1\phi_1)\Delta(\rho_1\phi_1 v_1^2)}}{\Delta(\rho_1\phi_1)}.$$

Once again, the negative root leads to the physically relevant solution

$$\boxed{\tilde{v}_1 = \frac{\sqrt{\rho_{1L}\phi_{1L}}v_{1L} + \sqrt{\rho_{1R}\phi_{1R}}v_{1R}}{\sqrt{\rho_{1L}\phi_{1L}} + \sqrt{\rho_{1R}\phi_{1R}}}.} \tag{F.43}$$

With $\tilde{v}_1$ known, Eq. (F.41) reduces to

$$\boxed{\widetilde{\rho_1\phi_1} = \sqrt{\rho_{1L}\rho_{1R}\phi_{1L}\phi_{1R}}.} \tag{F.44}$$

Next, we consider Eqs. (F.3) and (F.12). Expanding the left hand side of Eq. (F.3) and rearranging terms on the right hand side of this same equation yields

$$\begin{aligned} \Delta(\rho_1\phi_1 e_1) + \Delta(\rho_1\phi_1 v_1^2/2) = \tilde{H}_1\left(\tilde{\alpha}^{(1)} + \tilde{\alpha}^{(2)} + \tilde{\alpha}^{(3)}\right) - \frac{\tilde{\alpha}^{(1)}\tilde{c}_1^2}{\tilde{\Gamma}_1} \\ + \tilde{v}_1\tilde{c}_1\left(\tilde{\alpha}^{(2)} - \tilde{\alpha}^{(3)}\right) - \frac{\tilde{\alpha}^{(7)}(\tilde{H}_1 + \tilde{v}_1\tilde{v}_2 - \tilde{v}_1^2)\tilde{F}_{1_{\phi 1}}}{\widetilde{\rho_2\phi_2}[(\tilde{v}_2 - \tilde{v}_1)^2 - \tilde{c}_1^2]}. \end{aligned} \tag{F.45}$$

Substituting the expressions given by Eqs. (F.38) and (F.40), and the expressions for $\tilde{\alpha}^{(1)}$ [Eq. (4.30)] and $\tilde{\alpha}^{(7)}$ [Eq. (4.36)] into Eq. (F.45), using the first expression in Eq. (4.61) to replace $\tilde{H}_1$ in favor of $\widetilde{\rho_1\phi_1}$, $\tilde{v}_1$, $\widetilde{P_1\phi_1}$, and $\tilde{e}_1$, recognizing that the second term on the left hand side of Eq. (F.45) is simply the expression given in Eq. (F.42) divided by two, and using the equality $\Delta(\phi_2) = -\Delta(\phi_1)$, we obtain the following expression after performing some simple algebra:

$$\Delta(\rho_1\phi_1 e_1) - \tilde{e}_1\Delta(\rho_1\phi_1) = \left(\frac{\widetilde{P_1\phi_1}}{\widetilde{\rho_1\phi_1}} - \frac{\tilde{c}_1^2}{\tilde{\Gamma}_1}\right)\Delta(\rho_1\phi_1) + \frac{1}{\tilde{\Gamma}_1}\Delta(P_1\phi_1) - \frac{\tilde{F}_{1_{\phi 1}}}{\tilde{\Gamma}_1}\Delta(\phi_1). \tag{F.46}$$

Now, using the first expression in Eq. (4.60) to replace $\tilde{c}_1^2$ in Eq. (F.46) in favor of $\widetilde{\rho_1\phi_1}$, $\widetilde{P_1\phi_1}$, $\tilde{F}_{1_{\rho1\phi1}}$, and $\tilde{F}_{1_{e1}}$, using the first expression in Eq. (4.62) to replace $\tilde{\Gamma}_1$ in Eq. (F.46) in favor of $\widetilde{\rho_1\phi_1}$ and $\tilde{F}_{1_{e1}}$, subtracting the term $\widetilde{\rho_1\phi_1}\Delta(e_1)$ from both sides of Eq. (F.46), and simplifying the result, we obtain

$$\begin{aligned}\Delta(\rho_1\phi_1 e_1)-&\tilde{e}_1\Delta(\rho_1\phi_1) - \widetilde{\rho_1\phi_1}\Delta(e_1)\\ &= \frac{\widetilde{\rho_1\phi_1}}{\tilde{F}_{1_{e1}}}\Delta(P_1\phi_1) - \frac{\widetilde{\rho_1\phi_1}\tilde{F}_{1_{\rho1\phi1}}}{\tilde{F}_{1_{e1}}}\Delta(\rho_1\phi_1) - \frac{\widetilde{\rho_1\phi_1}\tilde{F}_{1_{\phi1}}}{\tilde{F}_{1_{e1}}}\Delta(\phi_1) - \widetilde{\rho_1\phi_1}\Delta(e_1).\end{aligned} \tag{F.47}$$

Here, as was done for the solid phase analysis, we choose

$$\Delta\left(\rho_1\phi_1 e_1\right) - \tilde{e}_1\left(\rho_1\phi_1\right) - \widetilde{\rho_1\phi_1}\Delta(e_1) = 0, \tag{F.48}$$

in which case Eq. (F.47) reduces to

$$\Delta\left(P_1\phi_1\right) - \tilde{F}_{1_{\rho1\phi1}}\Delta(\rho_1\phi_1) - \tilde{F}_{1_{\phi1}}\Delta(\phi_1) - \tilde{F}_{1_{e1}}\Delta(e_1) = 0. \tag{F.49}$$

Substituting the expression for $\widetilde{\rho_1\phi_1}$ [Eq. (F.41)] into Eq. (F.48), and solving the resulting expression for $\tilde{e}_1$ yields

$$\boxed{\tilde{e}_1 = \frac{\sqrt{\rho_{1L}\phi_{1L}}e_{1L} + \sqrt{\rho_{1R}\phi_{1R}}e_{1R}}{\sqrt{\rho_{1R}\phi_{1R}} + \sqrt{\rho_{1R}\phi_{1R}}}.} \tag{F.50}$$

Similar to the solid phase analysis, it is necessary to define the quantities $\tilde{F}_{1_{\rho1\phi1}}$, $\tilde{F}_{1_{\phi1}}$, and $\tilde{F}_{1_{e1}}$ such that Eq. (F.49) is identically satisfied. Definitions for these quantities are postulated in the following section.

Lastly, we multiply Eq. (F.3) by $\tilde{v}_1$, subtract the result from Eq. (F.12), and simplify the result to get

$$\begin{aligned}&\Delta\left(\rho_1\phi_1 v_1\left(e_1 + v_1^2/2 + P_1/\rho_1\right)\right) - \tilde{v}_1\Delta\left(\rho_1\phi_1\left(e_1 + v_1^2/2\right)\right)\\ &\quad= \tilde{c}_1\tilde{H}_1\left(\tilde{\alpha}^{(2)} - \tilde{\alpha}^{(3)}\right) + \tilde{v}_1\tilde{c}_1^2\left(\tilde{\alpha}^{(2)} + \tilde{\alpha}^{(3)}\right) - \frac{\tilde{\alpha}^{(7)}(\tilde{v}_2 - \tilde{v}_1)(\tilde{H}_1 + \tilde{v}_1\tilde{v}_2 - \tilde{v}_1^2)\tilde{F}_{1_{\phi1}}}{\widetilde{\rho_2\phi_2}[(\tilde{v}_2 - \tilde{v}_1)^2 - \tilde{c}_1^2]}.\end{aligned} \tag{F.51}$$

Upon substituting the expressions given by Eqs. (F.39) and (F.40), and the expression for $\tilde{\alpha}^{(7)}$ [Eq. (4.36)] into Eq. (F.51), re-expressing the left hand side of Eq. (F.51) in terms of the total enthalpy of the gas H_1 $(= e_1 + v_1^2/2 + P_1/\rho_1)$, and simplifying the result, we obtain

$$\Delta\left(\rho_1\phi_1 v_1 H_1\right) - \tilde{v}_1\Delta\left(\rho_1\phi_1(H_1 - P_1/\rho_1)\right) = \widetilde{\rho_1\phi_1}\tilde{H}_1\Delta(v_1) + \tilde{v}_1\Delta(P_1\phi_1). \qquad \text{(F.52)}$$

Expanding the second term on the left hand side of this equation and canceling like terms gives

$$\Delta\left(\rho_1\phi_1 v_1 H_1\right) - \tilde{v}_1\Delta\left(\rho_1\phi_1 H_1\right) = \widetilde{\rho_1\phi_1}\tilde{H}_1\Delta(v_1).$$

Since $\widetilde{\rho_1\phi_1}$ and $\tilde{v}_1$ are known quantities, this equation can be solved for $\tilde{H}_1$ to give

$$\boxed{\tilde{H}_1 = \frac{\sqrt{\rho_{1L}\phi_{1L}}H_{1L} + \sqrt{\rho_{1R}\phi_{1R}}H_{1R}}{\sqrt{\rho_{1L}\phi_{1L}} + \sqrt{\rho_{1R}\phi_{1R}}}.} \qquad \text{(F.53)}$$

In summary, the required gas phase average quantities $\widetilde{\rho_1\phi_1}$, $\tilde{v}_1$, $\tilde{e}_1$, and $\tilde{H}_1$ are given by Eqs. (F.44), (F.43), (F.50), and (F.53), respectively.

F.3 Averages for the Thermodynamic Derivatives

In this section, definitions for $\tilde{F}_{1_{\rho1\phi1}}$, $\tilde{F}_{2_{\rho2\phi2}}$, $\tilde{F}_{1_{\phi1}}$, $\tilde{F}_{2_{\phi2}}$, $\tilde{F}_{1_{e1}}$, and $\tilde{F}_{2_{e2}}$ are are postulated such that Eqs. (F.33) and (F.49) are identically satisfied. These approximations are all that is needed to complete the approximate Riemann solution. For convenience, Eqs. (F.33) and (F.49) are given below in a slightly rearranged form:

$$\Delta\left(P_1\phi_1\right) = \tilde{F}_{1_{\rho1\phi1}}\Delta(\rho_1\phi_1) + \tilde{F}_{1_{\phi1}}\Delta(\phi_1) + \tilde{F}_{1_{e1}}\Delta(e_1), \qquad \text{(F.54)}$$

$$\Delta\left(P_2\phi_2\right) = \tilde{F}_{2_{\rho2\phi2}}\Delta(\rho_2\phi_2) + \tilde{F}_{2_{\phi2}}\Delta(\phi_2) + \tilde{F}_{2_{e2}}\Delta(e_2). \qquad \text{(F.55)}$$

Since each of these equations contains the three average derivatives, these averages cannot be uniquely defined. As such, the methodology proposed by Glaister [37] is adopted in which artificial states are introduced in order to define the averages.

The following approximations for $\tilde{F}_{1_{\rho1\phi1}}$, $\tilde{F}_{1_{\phi1}}$, and $\tilde{F}_{1_{e1}}$ are proposed:

$$\tilde{F}_{1_{\rho1\phi1}} = \left\{\frac{1}{4}\left[F_1(\rho_{1R}\phi_{1R}, \phi_{1R}, e_{1R}) + F_1(\rho_{1R}\phi_{1R}, \phi_{1R}, e_{1L}) + F_1(\rho_{1R}\phi_{1R}, \phi_{1L}, e_{1L})\right.\right.$$

$$
\begin{aligned}
&+F_1(\rho_{1R}\phi_{1R}, \phi_{1L}, e_{1R})] - \frac{1}{4}\left[F_1(\rho_{1L}\phi_{1L}, \phi_{1R}, e_{1R}) + F_1(\rho_{1L}\phi_{1L}, \phi_{1L}, e_{1R})\right.\\
&\left.\left.+F_1(\rho_{1L}\phi_{1L}, \phi_{1R}, e_{1L}) + F_1(\rho_{1L}\phi_{1L}, \phi_{1L}, e_{1L})\right]\right\} / \Delta(\rho_1\phi_1),\\
&\qquad\qquad\qquad\qquad\qquad\qquad \text{if } \Delta(\rho_1\phi_1) \neq 0, \qquad \text{(F.56)}
\end{aligned}
$$

$$
\begin{aligned}
\tilde{F}_{1_{\phi 1}} = &\left\{\frac{1}{2}\left[F_1(\rho_{1R}\phi_{1R}, \phi_{1R}, e_{1R}) + F_1(\rho_{1L}\phi_{1L}, \phi_{1R}, e_{1L})\right] + \frac{1}{2}\left[F_1(\rho_{1R}\phi_{1R}, \phi_{1L}, e_{1R})\right.\right.\\
&\left.\left.+F_1(\rho_{1L}\phi_{1L}, \phi_{1L}, e_{1L})\right]\right\} / \Delta(\phi_1), \qquad\qquad \text{if } \Delta(\phi_1) \neq 0, \qquad \text{(F.57)}
\end{aligned}
$$

$$
\begin{aligned}
\tilde{F}_{1_{e1}} = &\left\{\frac{1}{4}\left[F_1(\rho_{1R}\phi_{1R}, \phi_{1R}, e_{1R}) + F_1(\rho_{1L}\phi_{1L}, \phi_{1L}, e_{1R}) + F_1(\rho_{1R}\phi_{1R}, \phi_{1L}, e_{1R})\right.\right.\\
&\left.+F_1(\rho_{1L}\phi_{1L}, \phi_{1R}, e_{1R})\right] - \frac{1}{4}\left[F_1(\rho_{1R}\phi_{1R}, \phi_{1L}, e_{1L}) + F_1(\rho_{1R}\phi_{1R}, \phi_{1R}, e_{1L})\right.\\
&\left.\left.+F_1(\rho_{1L}\phi_{1L}, \phi_{1R}, e_{1L}) + F_1(\rho_{1L}\phi_{1L}, \phi_{1L}, e_{1L})\right]\right\} / \Delta(e_1),\\
&\qquad\qquad\qquad\qquad\qquad\qquad \text{if } \Delta(e_1) \neq 0. \qquad \text{(F.58)}
\end{aligned}
$$

Similarly, the following approximations for $\tilde{F}_{2_{\rho 2\phi 2}}$, $\tilde{F}_{2_{\phi 2}}$, and $\tilde{F}_{2_{e2}}$ are proposed:

$$
\begin{aligned}
\tilde{F}_{2_{\rho 2\phi 2}} = &\left\{\frac{1}{4}\left[F_2(\rho_{2R}\phi_{2R}, \phi_{2R}, e_{2R}) + F_2(\rho_{2R}\phi_{2R}, \phi_{2R}, e_{2L}) + F_2(\rho_{2R}\phi_{2R}, \phi_{2L}, e_{2L})\right.\right.\\
&\left.+F_2(\rho_{2R}\phi_{2R}, \phi_{2L}, e_{2R})\right] - \frac{1}{4}\left[F_2(\rho_{2L}\phi_{2L}, \phi_{2R}, e_{2R}) + F_2(\rho_{2L}\phi_{2L}, \phi_{2L}, e_{2R})\right.\\
&\left.\left.+F_2(\rho_{2L}\phi_{2L}, \phi_{2R}, e_{2L}) + F_2(\rho_{2L}\phi_{2L}, \phi_{2L}, e_{2L})\right]\right\} / \Delta(\rho_2\phi_2),\\
&\qquad\qquad\qquad\qquad\qquad\qquad \text{if } \Delta(\rho_2\phi_2) \neq 0, \qquad \text{(F.59)}
\end{aligned}
$$

$$
\begin{aligned}
\tilde{F}_{2_{\phi 2}} = &\left\{\frac{1}{2}\left[F_2(\rho_{2R}\phi_{2R}, \phi_{2R}, e_{2R}) + F_2(\rho_{2L}\phi_{2L}, \phi_{2R}, e_{2L})\right] + \frac{1}{2}\left[F_2(\rho_{2R}\phi_{2R}, \phi_{2L}, e_{2R})\right.\right.\\
&\left.\left.+F_2(\rho_{2L}\phi_{2L}, \phi_{2L}, e_{2L})\right]\right\} / \Delta(\phi_2), \qquad\qquad \text{if } \Delta(\phi_2) \neq 0, \qquad \text{(F.60)}
\end{aligned}
$$

$$
\begin{aligned}
\tilde{F}_{2_{e2}} = &\left\{\frac{1}{4}\left[F_2(\rho_{2R}\phi_{2R}, \phi_{2R}, e_{2R}) + F_2(\rho_{2L}\phi_{2L}, \phi_{2L}, e_{2R}) + F_2(\rho_{2R}\phi_{2R}, \phi_{2L}, e_{2R})\right.\right.\\
&\left.+F_2(\rho_{2L}\phi_{2L}, \phi_{2R}, e_{2R})\right] - \frac{1}{4}\left[F_2(\rho_{2R}\phi_{2R}, \phi_{2L}, e_{2L}) + F_2(\rho_{2R}\phi_{2R}, \phi_{2R}, e_{2L})\right.\\
&\left.\left.+F_2(\rho_{2L}\phi_{2L}, \phi_{2R}, e_{2L}) + F_2(\rho_{2L}\phi_{2L}, \phi_{2L}, e_{2L})\right]\right\} / \Delta(e_2),\\
&\qquad\qquad\qquad\qquad\qquad\qquad \text{if } \Delta(e_2) \neq 0. \qquad \text{(F.61)}
\end{aligned}
$$

In Eqs. (F.56-F.61), the functions $F_1(\rho_1\phi_1, \phi_1, e_1)$ and $F_2(\rho_2\phi_2, \phi_2, e_2)$ are obtained from the thermodynamic state relations for each phase. In the event that $\Delta(\rho_i\phi_i)$, $\Delta(\phi_i)$, or $\Delta(e_i)$ ($i = 1, 2$) vanish, then we take the appropriate limits of Eqs. (F.56-F.61) (i.e., as $\Delta(\rho_i\phi_i) \rightarrow 0$, $\Delta(\phi_i) \rightarrow 0$, or $\Delta(e_i) \rightarrow 0$) to obtain the following expressions, respectively:

$$\begin{aligned}\tilde{F}_{1_{\rho 1\phi 1}} = {} & \frac{1}{4}\left[\frac{\partial F_1}{\partial(\rho_1\phi_1)}(\rho_1\phi_1, \phi_{1R}, e_{1R}) + \frac{\partial F_1}{\partial(\rho_1\phi_1)}(\rho_1\phi_1, \phi_{1R}, e_{1L})\right. \\ & \left. + \frac{\partial F_1}{\partial(\rho_1\phi_1)}(\rho_1\phi_1, \phi_{1L}, e_{1R}) + \frac{\partial F_1}{\partial(\rho_1\phi_1)}(\rho_1\phi_1, \phi_{1L}, e_{1L})\right], \\ & \text{if } \Delta(\rho_1\phi_1) = 0, \qquad \text{(F.62)}\end{aligned}$$

$$\tilde{F}_{1_{\phi 1}} = \frac{1}{2}\left[\frac{\partial F_1}{\partial \rho_1}(\rho_{1R}\phi_{1R}, \phi_1, e_{1R}) + \frac{\partial F_1}{\partial \rho_1}(\rho_{1L}\phi_{1L}, \phi_1, e_{1L})\right], \text{ if } \Delta(\phi_1) = 0, \text{ (F.63)}$$

$$\begin{aligned}\tilde{F}_{1_{e1}} = {} & \frac{1}{4}\left[\frac{\partial F_1}{\partial e_1}(\rho_{1R}\phi_{1R}, \phi_{1R}, e_1) + \frac{\partial F_1}{\partial e_1}(\rho_{1R}\phi_{1R}, \phi_{1L}, e_1)\right. \\ & \left. + \frac{\partial F_1}{\partial e_1}(\rho_{1L}\phi_{1L}, \phi_{1R}, e_1) + \frac{\partial F_1}{\partial e_1}(\rho_{1L}\phi_{1L}, \phi_{1L}, e_1)\right], \text{ if } \Delta(e_1) = 0, \quad \text{(F.64)}\end{aligned}$$

$$\begin{aligned}\tilde{F}_{2_{\rho 2\phi 2}} = {} & \frac{1}{4}\left[\frac{\partial F_2}{\partial(\rho_2\phi_2)}(\rho_2\phi_2, \phi_{2R}, e_{2R}) + \frac{\partial F_2}{\partial(\rho_2\phi_2)}(\rho_2\phi_2, \phi_{2R}, e_{2L})\right. \\ & \left. + \frac{\partial F_2}{\partial(\rho_2\phi_2)}(\rho_2\phi_2, \phi_{2L}, e_{2R}) + \frac{\partial F_2}{\partial(\rho_2\phi_2)}(\rho_2\phi_2, \phi_{2L}, e_{2L})\right], \\ & \text{if } \Delta(\rho_2\phi_2) = 0, \qquad \text{(F.65)}\end{aligned}$$

$$\tilde{F}_{2_{\phi 2}} = \frac{1}{2}\left[\frac{\partial F_2}{\partial \rho_2}(\rho_{2R}\phi_{2R}, \phi_2, e_{2R}) + \frac{\partial F_2}{\partial \rho_2}(\rho_{2L}\phi_{2L}, \phi_2, e_{2L})\right], \text{ if } \Delta(\phi_2) = 0, \text{ (F.66)}$$

$$\begin{aligned}\tilde{F}_{2_{e2}} = {} & \frac{1}{4}\left[\frac{\partial F_2}{\partial e_2}(\rho_{2R}\phi_{2R}, \phi_{2R}, e_2) + \frac{\partial F_2}{\partial e_2}(\rho_{2R}\phi_{2R}, \phi_{2L}, e_2)\right. \\ & \left. + \frac{\partial F_2}{\partial e_2}(\rho_{2L}\phi_{2L}, \phi_{2R}, e_2) + \frac{\partial F_2}{\partial e_2}(\rho_{2L}\phi_{2L}, \phi_{2L}, e_2)\right], \text{ if } \Delta(e_2) = 0, \quad \text{(F.67)}\end{aligned}$$

It is easily checked by direct substitution that the expressions given by Eqs. (F.56-F.67) identically satisfy Eqs. (F.54) and (F.55). Though these definitions for the derivatives appear complicated, they can generally be reduced when the equations of state are specified, and the reduced forms can be directly implemented into a computer algorithm. For example, using the virial equation of state for the gas given in Appendix G, and the non-ideal Tait equation of state for the solid-given in Appendix H, we obtain the relations

$$\begin{aligned} F_1(\rho_1\phi_1, \phi_1, e_1) &= \pi_{11}(\rho_1\phi_1)\left[1 + \pi_{12}\frac{(\rho_1\phi_1)}{\phi_1}\right] e_1, \\ F_2(\rho_2\phi_2, \phi_2, e_2) &= (\pi_{13} - 1)\,(\rho_2\phi_2)\,(e_2 - \pi_{15}) - \pi_{13}\pi_{14}\phi_2. \end{aligned}$$

Exact expressions for the thermodynamic derivatives are obtained from these relations:

$$\left.\frac{\partial F_1}{\partial(\rho_1\phi_1)}\right|_{\phi_1,e_1} = \pi_{11}\left[1 + 2\pi_{12}\frac{(\rho_1\phi_1)}{\phi_1}\right] e_1, \tag{F.68}$$

$$\left.\frac{\partial F_1}{\partial\phi_1}\right|_{(\rho_1\phi_1),e_1} = -\pi_{11}\pi_{12}\frac{(\rho_1\phi_1)^2}{\phi_1^2}e_1, \tag{F.69}$$

$$\left.\frac{\partial F_1}{\partial e_1}\right|_{(\rho_1\phi_1),\phi_1} = \pi_{11}(\rho_1\phi_1)\left[1 + \pi_{12}\frac{(\rho_1\phi_1)}{\phi_1}\right], \tag{F.70}$$

$$\left.\frac{\partial F_2}{\partial(\rho_2\phi_2)}\right|_{\phi_2,e_2} = (\pi_{11} - 1)\,(e_2 - \pi_{15}), \tag{F.71}$$

$$\left.\frac{\partial F_2}{\partial\phi_2}\right|_{(\rho_2\phi_2),e_2} = -\pi_{13}\pi_{14}, \tag{F.72}$$

$$\left.\frac{\partial F_2}{\partial e_2}\right|_{(\rho_2\phi_2),\phi_2} = (\pi_{13} - 1)\,(\rho_2\phi_2). \tag{F.73}$$

Now, using the relation for F_1, the definitions given by Eqs. (F.56-F.58) and (F.62-F.64) reduce to

$$\begin{aligned} \tilde{F}_{1_{\rho 1\phi 1}} &= \pi_{11}\left(1 + 2\pi_{12}\frac{\phi_{1L} + \phi_{1R}}{\phi_{1L}\phi_{1R}}\frac{\rho_{1L}\phi_{1L} + \rho_{1R}\phi_{1R}}{2}\right)\left(\frac{e_{1L} + e_{1R}}{2}\right), \\ \tilde{F}_{1_{\phi 1}} &= -\frac{\pi_{11}\pi_{12}}{2}\left[\frac{(\rho_{1L}\phi_{1L})^2}{\phi_{1L}\phi_{1R}}e_{1L} + \frac{(\rho_{1R}\phi_{1R})^2}{\phi_{1L}\phi_{1R}}e_{1R}\right], \\ \tilde{F}_{1_{e1}} &= \pi_{11}\left[\frac{\rho_{1L}\phi_{1L} + \rho_{1R}\phi_{1R}}{2} + \pi_{12}\frac{\phi_{1L} + \phi_{1R}}{\phi_{1L}\phi_{1R}}\left(\frac{(\rho_{1L}\phi_{1L})^2 + (\rho_{1R}\phi_{1R})^2}{4}\right)\right]. \end{aligned}$$

Using the relation for F_2, the definitions given by Eqs. (F.59-F.61) and (F.65-F.67) reduce to

$$\begin{aligned}
\tilde{F}_{2_{\rho 2 \phi 2}} &= (\pi_{13} - 1)\left(\frac{e_{2L} + e_{2R}}{2} - \pi_{15}\right), \\
\tilde{F}_{2_{\phi 2}} &= -\pi_{13}\pi_{14}, \\
\tilde{F}_{2_{e2}} &= (\pi_{13} - 1)\left(\frac{\rho_{2L}\phi_{2L} + \rho_{2R}\phi_{2R}}{2}\right).
\end{aligned}$$

These expressions for the average gas and solid derivatives are globally valid since identical expressions are obtained using the definitions given by Eqs. (F.62-F.67). Furthermore, these averages appear reasonable when compared to the exact expressions given in Eqs. (F.68-F.73).

G

VIRIAL EQUATION OF STATE FOR THE GAS

The gas phase is described by a virial state equation. The thermal and caloric equations of state are

$$\hat{P}_1 = \hat{\rho}_1 \hat{R} \hat{T}_1 \left(1 + \hat{b}\hat{\rho}_1\right), \tag{G.1}$$

$$\hat{e}_1 = \hat{c}_{v1o} \hat{T}_1, \tag{G.2}$$

where the constants $\hat{R}$, $\hat{c}_{v1o}$, and $\hat{b}$ are the gas constant, specific heat at constant volume, and virial coefficient, respectively. These state relations are non-dimensionalized using the scaled variables defined in Eq. (2.45) to obtain

$$P_1 = \pi_{11} \rho_1 T_1 \left(1 + \pi_{12} \rho_1\right), \tag{G.3}$$

$$e_1 = T_1, \tag{G.4}$$

where

$$\pi_{11} = \frac{\hat{R}}{\hat{c}_{v1o}}, \qquad \pi_{12} = \hat{b}\hat{\rho}_{1o}. \tag{G.5}$$

Using Eq. (G.4) to replace T_1 in favor of e_1 in Eq. (G.3) gives

$$P_1 = \pi_{11} \rho_1 e_1 \left(1 + \pi_{12} \rho_1\right). \tag{G.6}$$

The following thermodynamic derivatives are obtained from this expression:

$$\left.\frac{\partial P_1}{\partial \rho_1}\right|_{e_1} = \pi_{11} \left(1 + 2\pi_{12} \rho_1\right) e_1, \tag{G.7}$$

$$\left.\frac{\partial P_1}{\partial e_1}\right|_{\rho_1} = \pi_{11} \rho_1 \left(1 + \pi_{12} \rho_1\right). \tag{G.8}$$

Using these derivatives, the Grüneisen coefficient, Γ_1, is given by

$$\Gamma_1 \equiv \frac{1}{\rho_1} \left.\frac{\partial P_1}{\partial e_1}\right|_{\rho_1} = \pi_{11} \left(1 + \pi_{12} \rho_1\right), \tag{G.9}$$

and the non-dimensional gas sound speed squared, c_1^2, is given by

$$\begin{aligned}
c_1^2 &\equiv \frac{P_1}{\rho_1}\Gamma_1 + \left.\frac{\partial P_1}{\partial \rho_1}\right|_{e_1} \\
&= \pi_{11}\left[\left(1+\pi_{12}\rho_1\right)\frac{P_1}{\rho_1} + \left(1+2\pi_{12}\rho_1\right)e_1\right] \\
&= \pi_{11}T_1\left[1+2\pi_{12}\rho_1+\pi_{11}\left(1+\pi_{12}\rho_1\right)^2\right].
\end{aligned} \tag{G.10}$$

Here, Eq. (G.3) was used to eliminate P_1 in favor of ρ_1 and T_1, and Eq. (G.4) was used to eliminate e_1 in favor of T_1 to obtain the last expression of Eq. (G.10).

H

TAIT EQUATION OF STATE FOR THE SOLID

The solid phase is described by a Tait equation of state. The thermal and caloric equations of state are

$$\hat{P}_2 = (\gamma_2 - 1)\hat{c}_{v2o}\hat{\rho}_2\hat{T}_2 - \frac{\hat{\rho}_{2o}\hat{\sigma}}{\gamma_2}, \tag{H.1}$$

$$\hat{e}_2 = \hat{c}_{v2o}\hat{T}_2 + \frac{\hat{\rho}_{2o}\hat{\sigma}}{\gamma_2\hat{\rho}_2} + \hat{q}, \tag{H.2}$$

where the constants $\hat{\rho}_{2o}$, γ_2, $\hat{c}_{v2o}$, $\hat{\sigma}$, and $\hat{q}$ are the ambient solid density, Tait parameter, specific heat at constant volume, non-ideal solid parameter, and the chemical energy, respectively. These state relations are non-dimensionalized using the scaled variables defined in Eq. (2.45) to obtain

$$P_2 = (\pi_{13} - 1)\,\rho_2 T_2 - \pi_{14}, \tag{H.3}$$

$$e_2 = T_2 + \frac{\pi_{14}}{\rho_2} + \pi_{15}, \tag{H.4}$$

where

$$\pi_{13} = \gamma_2, \qquad \pi_{14} = \frac{\hat{\sigma}}{\gamma_2\hat{c}_{2o}^2}, \qquad \pi_{15} = \frac{\hat{q}}{\hat{c}_{2o}^2}. \tag{H.5}$$

Using Eq. (H.4) to replace T_2 in favor of e_2 in Eq. (H.3) gives

$$P_2 = (\pi_{13} - 1)\,\rho_2\,(e_2 - \pi_{15}) - \pi_{13}\pi_{14}. \tag{H.6}$$

The following thermodynamic derivatives are obtained from this expression:

$$\left.\frac{\partial P_2}{\partial \rho_2}\right|_{e_2} = (\pi_{13} - 1)\,(e_2 - \pi_{15})\,, \tag{H.7}$$

$$\left.\frac{\partial P_2}{\partial e_2}\right|_{\rho_2} = (\pi_{13} - 1)\,\rho_2. \tag{H.8}$$

Using these derivatives, the Grüneisen coefficient, Γ_2, is given by

$$\Gamma_2 \equiv \frac{1}{\rho_2} \left. \frac{\partial P_2}{\partial e_2} \right|_{\rho_2} = \pi_{13} - 1, \tag{H.9}$$

and the non-dimensional solid sound speed squared, c_2^2, is given by

$$\begin{aligned} c_2^2 &\equiv \frac{P_2}{\rho_2}\Gamma_2 + \left. \frac{\partial P_2}{\partial \rho_2} \right|_{e_2} \\ &= (\pi_{13} - 1)\left(\frac{P_2}{\rho_2} + e_2 - \pi_{15}\right) \\ &= \pi_{13}\,(\pi_{13} - 1)\,T_2. \end{aligned} \tag{H.10}$$

Here, Eq. (H.3) was used to eliminate P_2 in favor of ρ_2 and T_2, and Eq. (H.4) was used to eliminate e_2 in favor of ρ_2 and T_2 to obtain the last expression of Eq. (H.10).

I

INTRAGRANULAR STRESS RELATION

The intragranular stress $\hat{f}(\phi_2)$ [Eq. (2.14)] used in this study to model compaction of the granular material is given by

$$\hat{f} = \left(\hat{P}_{2o} - \hat{P}_{1o}\right) \frac{\phi_2^2}{\phi_{2o}^2} \frac{(2-\phi_{2o})^2}{(2-\phi_2)^2} \frac{\ln\frac{1}{1-\phi_2}}{\ln\frac{1}{1-\phi_{2o}}}. \tag{I.1}$$

This stress relation, which was used by Powers et al. [93] to analyze steady compaction waves in porous HMX, is similar in form to the analytical expression used by Carroll and Holt [25] to model dynamic pore collapse in solids due to plastic deformation. This relation is constructed such that 1) it is a monotonically increasing function of ϕ_2, and 2) the difference between the solid and gas pressure balances the intragranular stress for the ambient state [i.e., $\hat{P}_{2o} - \hat{P}_{1o} = \hat{f}(\phi_{2o})$]. The first of these conditions is motivated by experiments which show that an increasing hydrostatic stress $(\hat{P}_2 - \hat{P}_1)$ is necessary to balance an increased intragranular stress $(\hat{f})$ resulting from compaction of the porous material (increasing ϕ_2). The second condition specifies that the ambient mixture is an equilibrium state since the first term on the right hand side of the dynamic compaction equation, Eq. (2.7), vanishes for the ambient state. The variation in the quantity $\dfrac{\hat{f}}{\hat{P}_{2o} - \hat{P}_{1o}}$ with ϕ_2 is shown is Fig. I.1.

Equation (I.1) can be expressed in terms of the non-dimensional variable f defined in Eq. (2.45) to give

$$f = \pi_{16} \frac{\phi_2^2}{\phi_{2o}^2} \frac{(2-\phi_{2o})^2}{(2-\phi_2)^2} \frac{\ln\frac{1}{1-\phi_2}}{\ln\frac{1}{1-\phi_{2o}}}, \tag{I.2}$$

where

$$\pi_{16} = \frac{\hat{P}_{2o} - \hat{P}_{1o}}{\hat{\rho}_{2o}\hat{c}_{2o}^2}. \tag{I.3}$$

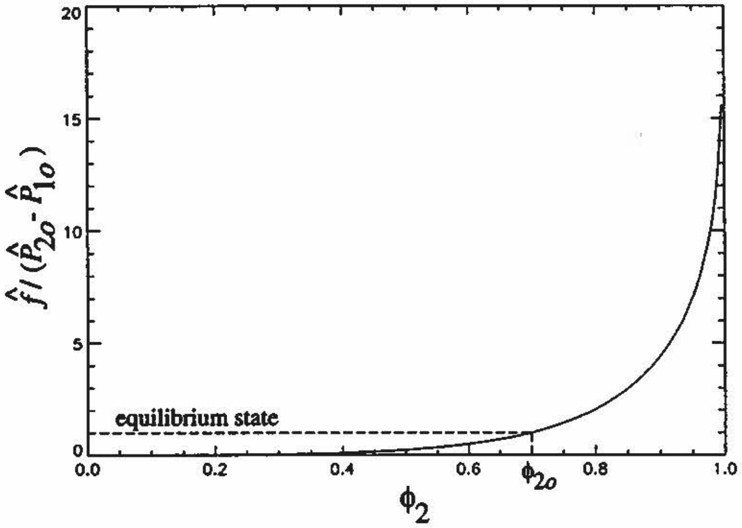

Figure I.1: Variation in the intragranular stress with solid volume fraction for $\phi_{2o} = 0.7$.

LIST OF REFERENCES

[1] Anton, H., *Elementary Linear Algebra*, John Wiley, New York, 1987.

[2] Asay, B., and Hantel, L., Major Thrust Areas for Examination of Deflagration-to-Detonation Transition in Granular and Damaged Explosives, M-8-91-61, Los Alamos National Laboratory, Los Alamos, New Mexico, 1991.

[3] Baer, M. R., Numerical Studies of Dynamic Compaction of Inert and Energetic Granular Materials, *Journal of Applied Mechanics*, 55: 36-43, 1988.

[4] Baer, M. R., and Nunziato, J. W., A Theory for Deflagration-to-Detonation Transition (DDT) in Granular Explosives, SAND 82-0293, Sandia National Laboratories, 1983.

[5] Baer, M. R., and Nunziato, J. W., A Two-Phase Mixture Theory for the Deflagration to Detonation Transition (DDT) in Reactive Granular Materials, *International Journal of Multiphase Flow*, 12: 861-889, 1986.

[6] Baer, M. R., Benner, R. E., Gross, R. J., and Nunziato, J. W., Modeling and Computation of Deflagration-to-Detonation Transition (DDT) in Reactive Granular Materials, *Lectures in Applied Mathematics*, 24: 1-30, 1986.

[7] Baer, M. R., Gross, R. J., Nunziato, J. W., and Igel, E. A., An Experimental and Theoretical Study of Deflagration-to-Detonation Transition (DDT) in the Granular Explosive, CP, *Combustion and Flame*, 65: 15-30, 1986.

[8] Baer, M. R., and Nunziato, J. W., Compressive Combustion of Granular Materials Induced by Low-Velocity Impact, In: *Proceedings of the Ninth (International) Symposium on Detonation*, Portland, Oregon, 744-754, 1989.

[9] Barkve, T., The Riemann Problem for a Nonstrictly Hyperbolic System Modeling Nonisothermal, Two-Phase Flow in a Porous Medium, *SIAM Journal on Applied Mathematics*, 49(3): 784-798, 1989.

[10] Bdzil, J. B., and Son, S. F., Engineering Models of Deflagration to Detonation Transition, LA-12794-MS, Los Alamos National Laboratory, Los Alamos, New Mexico, 1995.

[11] Bear, J. *Dynamics of Fluids in Porous Media*, Elsevier, New York, 1972.

[12] Bell, J. B., Colella, P., and Trangenstein, J. A., Higher Order Godunov Methods for General Systems of Hyperbolic Conservation Laws, *Journal of Computational Physics*, 82: 362-397, 1989.

[13] Bement, L. J., and Schimmel, M. L., Investigation of the Super*Zip Separation Joint, NASA Technical Memorandum 4031, 1988.

[14] Bernecker, R. R., and Price, D., Studies in the Transition from Deflagration to Detonation in Granular Explosives – I: Experimental Arrangement and Behavior of Explosives Which Fail to Exhibit Detonation, *Combustion and Flame*, 22: 111-118, 1974.

[15] Bernecker, R. R., and Price, D., Studies in the Transition from Deflagration to Detonation in Granular Explosives – II: Transitional Characteristics and Mechanisms Observed in 91/9 RDX/Wax, *Combustion and Flame*, 22: 119-129, 1974.

[16] Bernecker, R. R., Sandusky, H. W., and Clairmont, A. R., Deflagration-to-Detonation Transition Studies of Porous Explosive Charges in Plastic Tubes, In: *Proceedings of the Seventh Symposium (International) on Detonation*, 119-138, 1981.

[17] Bernecker, R. R., Sandusky, H. W., and Clairmont, A. R., Deflagration-to-Detonation Transition (DDT) Studies of a Double-Based Propellant, In: *Proceedings of the Eighth Symposium (International) on Detonation*, 658-668, 1985.

[18] Bilicki, Z., Dafermos, C., Kestin, J., Majda, G., and Zeng, D. L., Trajectories and Singular Points in Steady-State Models of Two-Phase Flows, *International Journal of Multiphase Flow*, 13: 511-533, 1987.

[19] Boris, J. P., and Book, D. L., Flux-Corrected Transport I: Shasta, a Fluid Transport Algorithm that Works, *Journal of Computational Physics*, 11: 38-69, 1973.

[20] Boris, J. P., Book, D. L., and Hain, K., Flux-Corrected Transport II: Generalizations of the Method, *Journal of Computational Physics*, 18: 248-283, 1975.

[21] Boure, J. A., and Delhaye, J. M., General Equations and Two-Phase Flow Modeling, In: *Handbook of Multiphase Systems* (Hetsroni), McGraw-Hill, New York, Volume 1, 36-95, 1982.

[22] Butler, P. B., Lembeck, M. F., and Krier, H., Modeling of Shock Development and Transition to Detonation Initiated by Burning in Porous Propellant Beds, *Combustion and Flame*, 46: 75-93, 1982.

[23] Butler, P. B., and Krier, H., Analysis of Deflagration to Detonation Transition in High-Energy Solid Propellants, *Combustion and Flame*, 63: 31-48, 1986.

[24] Campbell, A. W., Deflagration-to-Detonation Transition in Granular HMX, LA-UR 80-2016, Los Alamos National Laboratory, Los Alamos, New Mexico, 1980.

[25] Carroll, M. M., and Holt, A. C., Static and Dynamic Pore-Collapse Relations for Ductile Porous Materials, *Journal of Applied Physics*, 43: 1626-1635, 1972.

[26] Chakravarthy, S. R., and Osher, S., Computing with High-Resolution Upwind Schemes for Hyperbolic Equations, In: *Lectures in Applied Mathematics*, 22: 57-86, 1985.

[27] Coperthwaite, M., and Zwisler, W. H., "TIGER" Computer Code Documentation, Report PYV-1281, Stanford Research Institute, 1974.

[28] Courant, R., and Friedrichs, K. O., *Supersonic Flow and Shock Waves*, John Wiley, New York, 1948.

[29] Doering, W., On Detonation Processes in Gases, *Annalen der Physik*, 43: 421-436, 1943.

[30] Drew, D. A., Mathematical Modeling of Two-Phase Flow, *Annual Review of Fluid Mechanics*, 15: 261-291, 1983.

[31] Embid, P., and Baer, M., Mathematical Analysis of a Two-Phase Continuum Mixture Theory, *Continuum Mechanics and Thermodynamics*, 4: 279-312, 1992.

[32] Embid. P., Hunter, J., and Majda, A., Simplified Asymptotic Equations for the Transition to Detonation in Reactive Granular Materials, *SIAM Journal on Applied Mathematics*, 52(5): 1199-1237, 1992.

[33] Embid, P., and Majda, A., An Asymptotic Theory for Hot Spot Formation and Transition to Detonation for Reactive Granular Materials, *Combustion and Flame*, 89: 17-36, 1992.

[34] Fickett, W., and Davis, W. C., *Detonation*, University of California Press, Berkeley, 1979.

[35] Fletcher, C. A. J., *Computational Techniques for Fluid Dynamics*, Volume II, Springer-Verlag, Berlin, 1991.

[36] Freistuhler, H., and Pitman, E. B., A Numerical Study of a Rotationally Degenerate Hyperbolic System. Part 1. The Riemann Problem, *Journal of Computational Physics*, 100: 306-321, 1992.

[37] Glaister, P., An Approximate Linearized Riemann Solver for the Euler Equations for Real Gases, *Journal of Computational Physics*, 74: 382-408, 1988.

[38] Glaister, P., An Approximate Linearized Riemann Solver for the Three-Dimensional Euler Equations for Real Gases Using Operator Splitting, *Journal of Computational Physics*, 77: 361-383, 1988.

[39] Glaister, P., An Efficient Riemann Solver for Unsteady Flows with Non-Ideal Gases, *Computers and Mathematical Applications*, 24(3): 77-93, 1992.

[40] Godunov, S. K., A Difference Scheme for Numerical Computation of Discontinuous Solutions of Hydrodynamic Equations, *Sbornik Mathematics*, 47: 271-306, 1959.

[41] Gokhale, S. S., and Krier, H., Modeling of Unsteady Two-Phase Reactive Flow in Porous Beds of Propellant, *Progress in Energy and Combustion Science*, 8: 1-39, 1982.

[42] Green, L. G., James, E., Lee, E. L., Chambers, E. S., Tarver, C. M., Westmoreland, C., Weston, A., and Brown, B., Delayed Detonation in Propellants from Low-Velocity Impact, In: *Proceedings of the Seventh Symposium (International) on Detonation*, 256-264, 1981.

[43] Griffiths, N., and Groocock, J. M., Burning to Detonation of Solid Explosives, *Journal of the Chemical Society* (London), 814: 4154-4162, 1960.

[44] Grismer, M. J., A Numerical Investigation of Oblique Detonations with Applications to Propulsion, Ph.D. Dissertation, University of Notre Dame, 1994.

[45] Harten, A., and Hyman, J. M., Self-Adjusting Grid Methods for One-Dimensional Hyperbolic Conservation Laws, *Journal of Computational Physics*, 50: 235-269, 1983.

[46] Harten, A., Hyman, J. M., and Lax, P. D., On Finite Difference Approximation and Entropy Conditions for Shocks, *Communication in Pure and Applied Mathematics*, 29: 297-322, 1976.

[47] Hassanizadeh, M., and Gray, W. G., General Conservation Equations for Multi-Phase Systems: 1. Averaging Procedure, In: *Flow Through Porous Media, Progress in Engineering Sciences*, CML Publications, 1-14, 1983.

[48] Hassanizadeh, M., and Gray, W. G., General Conservation Equations for Multi-Phase Systems: 2. Mass, Momenta, Energy, and Entropy Equations, In: *Flow Through Porous Media, Progress in Engineering Sciences*, CML Publications, 17-29, 1983.

[49] Hindmarsh, A. C., ODEPACK, a Systematized Collection of ODE Solvers, In: *Scientific Computing*, North-Holland, Amsterdam, 55-64, 1983.

[50] Hirsch, C., *Numerical Computation of Internal and External Flows*, Volume 1, John Wiley and Sons, New York, 1990.

[51] Hirsch, C., *Numerical Computation of Internal and External Flows*, Volume 2, John Wiley and Sons, New York, 1990.

[52] Hoffman, S. J., and Krier, H., Fluid Mechanics of Deflagration-to-Detonation Transition in Porous Explosives and Propellants, *AIAA Journal*, 19(12): 1571-1579, 1981.

[53] Isaacson, E., and Temple, B., Nonlinear Resonance in Systems of Conservation Laws, *SIAM Journal on Applied Mathematics*, 52(5): 1260-1278, 1992.

[54] Jeffrey, A., *Quasilinear Hyperbolic Systems and Waves*, Pitman, Boston, 1976.

[55] Johansson, C. H., and Persson, P. A., *Detonics of High Explosives*, Academic, London, 1970.

[56] Kang, J., Butler, P. B., and Baer, M. R., A Thermomechanical Analysis of Hot Spot Formation in Condensed-Phase, Energetic Materials, *Combustion and Flame*, 89: 117-139, 1992.

[57] Keyfitz, B. L., Some Elementary Connections Among Nonstrictly Hyperbolic Conservation Laws, *Contemporary Mathematics*, 60: 67-77, 1987.

[58] Keyfitz, B. L, and Kranzer, H. C., The Riemann Problem for a Class of Hyperbolic Conservation Laws Exhibiting a Parabolic Degeneracy, *Journal of Differential Equations*, 47: 35-65, 1983.

[59] Kober, E. M., Bdzil, J. B., and Son, S. F., Modeling DDT in Granular Explosives with a Multi-Dimensional Hydrocode, LA-UR 95-2812, Los Alamos National Laboratory, Los Alamos, New Mexico, 1995.

[60] Krier, H., Rajan, S., and Van Tassell, W. F., Flame-Spreading and Combustion in Packed Beds of Propellant Grains, *AIAA Journal*, 14(3): 301-309, 1976.

[61] Krier, H., and Mozaffarian, A., Two-Phase Reactive Particle Flow Through Normal Shock Waves, *International Journal of Multiphase Flow*, 4: 65-79, 1978.

[62] Krier, H., and Gokhale, S. S., Modeling of Convective Mode Combustion Through Granulated Propellant to Predict Detonation Transition, *AIAA Journal*, 16(2): 177-183, 1978.

[63] Krier, H., and Kezerle, J. A., A Separated Two-Phase Flow Analysis to Study Deflagration-to-Detonation Transition (DDT) in Granulated Propellant, In: *Proceedings of the Seventeenth Symposium (International) on Combustion*, 23-34, 1979.

[64] Kuo, K. K., Vichnevetsky, R., and Summerfield, M., Theory of Flame Front Propagation in Porous Propellant Charges Under Confinement, *AIAA Journal*, 11: 444-451, 1973.

[65] Kuo, K. K., and Summerfield, M., Theory of Steady-State Burning of Gas-Permeable Propellants, *AIAA Journal*, 12: 49-56, 1974.

[66] Kuo, K. K., and Summerfield, M., High Speed Combustion of Mobile Granular Solid Propellants: Wave Structure and the Equivalent Rankine-Hugoniot Relation, In: *Proceedings of the Fifteenth Symposium (International) on Combustion*, 515-527, 1975.

[67] Kuo, K. K., Koo, J. H., Davis, T. R., and Coates, G. R., Transient Combustion in Mobile Gas Permeable Propellants, *Acta Astronautica*, 3: 573-591, 1976.

[68] Lax, P. D., Hyperbolic Systems of Conservation Laws II, *Communications in Pure and Applied Mathematics*, 10: 537-566, 1957.

[69] Lax, P. D., *Hyperbolic Systems of Conservation Laws and the Mathematical Theory of Shock Waves*, Regional Conference Series in Applied Mathematics, Society for Industrial and Applied Mathematics, 11, 1973.

[70] Lax, P. D., and Wendroff, B., Systems of Conservations Laws, *Communications in Pure and Applied Mathematics*, 13: 217-237, 1960.

[71] Lee, E., Finger, M., and Collins, W., JWL Equation of State Coefficients for High Explosives, UCID-16189, Lawrence Livermore Radiation Laboratory Report, Livermore, California, 1973.

[72] LeVeque, R. J., *Numerical Methods for Conservation Laws*, Birkhauser Verlag, Boston, 1992.

[73] Lichtenberg, A. J., and Lieberman, M. A., *Regular and Chaotic Dynamics*, Springer-Verlag, New York, 1992.

[74] Liu, T. P., Admissible Solutions of Hyperbolic Conservation Laws. *Memoirs of the American Mathematical Society*, Providence, 240, 1981.

[75] Luebcke, P. E., Dickson, P. M., and Field, J. E., Deflagration-to-Detonation Transition in Granular Pentaerythritol Tetranitrate, *Journal of Applied Physics*, 79(7): 3499-3503, 1996.

[76] Mader, C. L., FORTRAN BKW, LA-3704, Los Alamos National Laboratory, Los Alamos, New Mexico, 1973.

[77] Mader, C. L., *Numerical Modeling of Detonations*, University of California Press, Berkeley, 1979.

[78] Marsh, S. P., *LASL Shock Hugoniot Data*, University of California Press, Berkeley, 1980.

[79] McAfee, J. M., and Campbell, A. W., An Experimental Study of the Deflagration to Detonation Transition in Heavily Confined HMX, LA-CP 86-19, Los Alamos National Laboratory, Los Alamos, New Mexico, 1986.

[80] McAfee, J. M., Asay, B. W., Campbell, W., and Ramsay, J. B., Deflagration to Detonation Transition in Granular HMX, In: *Proceedings of the Ninth Symposium (International) on Detonation*, 265-278, 1989.

[81] McAfee, J. M., Asay, B. W., and Bdzil, J. B., Deflagration-to-Detonation in Granular HMX: Ignition, Kinetics, and Shock Formation, LA-UR 93-1754, Los Alamos National Laboratory, Los Alamos, New Mexico, 1993.

[82] Menikoff, R., Errors When Shock Waves Interact Due to Numerical Shock Width, *SIAM Journal on Scientific Computing*, 15(5): 1227-1242, 1994.

[83] Menikoff, R., Numerical Anomalies Mimicking Physical Effects, LA-UR 95-2628, Los Alamos National Laboratory, Los Alamos, New Mexico, 1995.

[84] Menikoff, R., Bdzil, J., Son, S. F., Kapila, A. K., and Stewart, D. S., Two-Phase Models of DDT Part I: Review of Modeling Issues, LA-UR-96-979, Los Alamos National Laboratory, Los Alamos, New Mexico, 1995.

[85] Menikoff, R., and Lackner, K. S., Anomalous Physical Effects from Artificial Numerical Length Scales, LA-UR 95-2135, Los Alamos National Laboratory, Los Alamos, New Mexico, 1995.

[86] Nunziato, J. W., Initiation and Growth-to-Detonation in Reactive Mixtures, In: *Shock Waves in Condensed Matter*-1983, Elsevier, New York, 1984.

[87] Oleinik, O. A., Discontinuous Solutions of Non-linear Differential Equations, *Uspekhi Matematicheskikh Nauk*, 12: 3-73, 1957; *American Mathematical Society. Translations*, 26(2): 195-172.

[88] Osher, S., Numerical Solution of Singular Perturbation Problems and Hyperbolic Systems of Conservation Laws, In: *Mathematical Studies*, North-Holland, New York, 47-61, 1981.

[89] Osher, S., and Solomon, F., Upwind Difference Schemes for Hyperbolic Systems of Conservation Laws, *Mathematics of Computation*, 38: 339-374, 1982.

[90] Passman, S. L., Nunziato, J. W., and Walsh, E. K., A Theory of Multiphase Mixtures, In: *Rational Thermodynamics* (Truesdell), Springer-Verlag, New York, 287-325, 1984.

[91] Powers, J. M., *Theory of Detonation Structure for Two-Phase Materials*, Ph.D. Thesis, University of Illinois at Urbana-Champaign, 1988.

[92] Powers, J. M., Stewart, D. S., and Krier, H., Two-Phase Steady Detonation Analysis, *Progress in Astronautics and Aeronautics, Dynamics of Explosions*, 14: 341-361, 1988.

[93] Powers, J. M., Stewart, D. S., and Krier, H., Analysis of Steady Compaction Waves in Porous Materials, *Journal of Applied Mechanics*, 56: 15-24, 1989.

[94] Powers, J. M., Stewart, D. S., and Krier, H., Theory of Two-Phase Detonation – Part I: Modeling, *Combustion and Flame*, 80: 264-279, 1990.

[95] Powers, J. M., Stewart, D. S., and Krier, H., Theory of Two-Phase Detonation – Part II: Structure, *Combustion and Flame*, 80: 280-303, 1990.

[96] Powers, J. M., and Gonthier, K. A., Reaction Zone Structure for Strong, Weak Overdriven, and Weak Underdriven Oblique Detonations, *Physics of Fluids A*, 4(9): 2082-2089.

[97] Price, D., and Bernecker, R. R., Sensitivity of Porous Explosives to Transition from Deflagration to Detonation, *Combustion and Flame*, 25: 91-100, 1975.

[98] Price, D., and Bernecker, R. R., Effect of Wax on the Deflagration-to-Detonation Transition of Porous Explosives, In: *Behavior of Dense Media Under High Dynamic Pressure*, Commissariat a l'Energie Atomique, Paris, 149-159, 1978.

[99] Ramshaw, J. D., and Trapp, J. A., Characteristics, Stability, and Short-Wavelength Phenomena in Two-Phase Flow Equation Systems, *Nuclear Science and Engineering*, 66: 93-102, 1978.

[100] Roe, P. L., Approximate Riemann Solvers, Parameter Vectors, and Difference Schemes, *Journal of Computational Physics*, 43: 357-372, 1981.

[101] Roe, P. L., Sonic Flux Formulae, *SIAM Journal on Scientific and Statistical Computing*, 13(2): 611-630, 1992.

[102] Roe, P. L., Some Contributions to the Modeling of Discontinuous Flows, In: *Proceedings of the 1983 AMS-SIAM Summer Seminar on Large Scale Computing in Fluid Mechanics, Lectures in Applied Mathematics*, SIAM, Philadelphia, 22: 163-193, 1985.

[103] Roe, P. L., and Pike, J., Efficient Construction and Utilization of Approximate Riemann Solutions, In: *Computing Methods in Applied Sciences and Engineering VI*, North-Holland, New York, 499-518, 1984.

[104] Sandusky, H. W., and Liddiard, T. P., Dynamic Compaction of Porous Beds, Report NSWC TR 83-246, Naval Surface Weapons Center, 1985.

[105] Sandusky, H. W., and Bernecker, R. R., Compressive Reaction in Porous Beds of Energetic Material, In: *Proceedings of the Eighth Symposium (International) on Detonation*, 881-891, 1985.

[106] Saurel, R., Larini, M., and Loraud, J. C., Ignition and Growth of a Detonation by a High Energy Plasma, *Shock Waves*, 2:19-29, 1992.

[107] Saurel, R., Larini, M., and Loraud, J. C., Numerical Modeling of Deflagration-to-Detonation Transition Produced by Laser Impact on Granular Explosive, *Computational Fluid Dynamics Journal*, 1(2): 155-174, 1992.

[108] Shames, I. H., *Mechanics of Fluids*, McGraw-Hill, New York, 1992.

[109] Son, S. F., Asay, B. W., and Bdzil, J. B., Inert Plug Formation in the DDT of Granular Energetic Materials, LA-UR 95-2872, Los Alamos National Laboratory, Los Alamos, New Mexico, 1995.

[110] Son, S. F., Asay, B. W., Bdzil, J. B., and Kober, E. M., Reaction Rate Modeling in the Deflagration to Detonation Transition of Granular Energetic Materials, Presented at the MRS Meeting, Boston, Massachusetts, 1995.

[111] Stewart, D. S., Asay, B., and Prasad, K., Simplified Modeling of Transition to Detonation in Porous Energetic Materials, *Physics of Fluids*, 6(7): 2515-2533, 1994.

[112] Strang, G., On the Construction and Comparison of Difference Schemes, *SIAM Journal on Numerical Analysis*, 5(3): 506-517, 1968.

[113] Sweby, P. K., High Resolution Schemes Using Flux Limiters for Hyperbolic Conservation Laws, *SIAM Journal on Numerical Analysis*, 21(5): 995-1011, 1984.

[114] Temple, B., Global Solution of the Cauchy Problem for a Class of 2×2 Nonstrictly Hyperbolic Conservation Laws, *Advances in Applied Mathematics*, 3: 335-375, 1982.

[115] Thompson, K. W., Time Dependent Boundary Conditions for Hyperbolic Systems, *Journal of Computational Physics*, 68: 1-24, 1987.

[116] Truesdell, C., and Toupin, R., The Classical Field Theories, *Handbuch der Physik*, Springer, Berlin, II: 226, 1960.

[117] Truesdell, C., and Noll, N., The Nonlinear Field Theories of Mechanics, *Handbuch der Physik*, Springer, Berlin, III, 1965.

[118] Van Albada, G. D., Van Leer, B., and Roberts, W. W., A Comparative Study of Computational Methods in Cosmic Gas Dynamics, *Astronomy and Astrophysics*, 108: 76-84, 1982.

[119] Van Leer, B., Towards the Ultimate Conservative Difference Scheme, II: Monotonicity and Conservation Combined in a Second Order Scheme, *Journal of Computational Physics*, 14: 361-370, 1974.

[120] von Neumann, J., and Richtmyer, R. D., A Method for the Numerical Calculation of Hydrodynamic Shocks, *Journal of Applied Physics*, 21: 232-237, 1950.

[121] von Neumann, J., Theory of Detonation Waves, In: *John von Neumann Collected Works*, Macmillan Press, New York, 203-218, 1963.

[122] White, F. M., *Viscous Fluid Flow*, McGraw-Hill, Inc., New York, 1974.

[123] Whitham, G. B., *Linear and Nonlinear Waves*, John Wiley, New York, 1974.

[124] Wiggins, S., *Introduction to Applied Nonlinear Dynamical Systems and Chaos*, Springer-Verlag, New York, 1990.

[125] Williams, F. A., Barrere, M., and Huang, N. C., *Aspects of Solid Propellant Rockets*, NATO AGARDograph, Vol. 116.

[126] Williams, W. O., Foundations of Mixture Theory, In: *Rational Thermodynamics* (Truesdell), Springer-Verlag, New York, 344-352, 1984.

[127] Woodward, P., and Collela, P., The Numerical Simulation of Two-Dimensional Fluid Flow with Strong Shocks, *Journal of Computational Physics*, 54(1): 115-173, 1984.

[128] Yanenko, N. N., *The Method of Fractional Steps*, Springer-Verlag, New York, 1971.

[129] Zalesak, S. T., Fully Multidimensional Flux-Corrected Transport Algorithms for Fluids, *Journal of Computational Physics*, 31: 335-362, 1979.

[130] Zauderer, E., *Partial Differential Equations of Applied Mathematics*, John Wiley, New York, 1989.

[131] Zeldovich, Ya. B., On the Theory of the Propagation of Detonation in Gaseous Systems, *Zhurnal Eksperimental'noi i Teoreticheskoi Fiziki*, 10: 542-568, 1940. (English translation: NACA TM 1261, 1960.)

[132] Zeldovich, Y. B., and Raizer, Y. P., *Elements of Gasdynamics and the Classical Theory of Shock Waves*, Academic Press, New York, 1968.